ENERGY MANAGEMENT OF DYNAMIC WIRELESS POWER TRANSFER

SYSTEMS FOR ELECTRIC VEHICLE APPLICATIONS

by

Ahmed N. Azad

A dissertation submitted in partial fulfillment
of the requirements for the degree

of

DOCTOR OF PHILOSOPHY

in

Electrical Engineering

Approved:

_____   _____
Zeljko Pantic, Ph.D.   Regan Zane, Ph.D.
Major Professor   Committee Member

_____   _____
Doran Baker, Ph.D.   Randall Christensen, Ph.D.
Committee Member   Committee Member

_____   _____
Ziqi Song, Ph.D.   Richard S. Inouye, Ph.D.
Committee Member   Vice Provost for Graduate Studies

UTAH STATE UNIVERSITY
Logan, Utah

2019

ABSTRACT

Energy Management of Dynamic Wireless Power Transfer Systems for Electric Vehicle
Applications

by

Ahmed N. Azad, Doctor of Philosophy

Utah State University, 2019

Major Professor: Zeljko Pantic, Ph.D.
Department: Electrical and Computer Engineering

Wireless Power Transfer (WPT) technology is becoming widespread as a method for efficient, reliable, low-maintenance, and clean power transmission. With the gradual depletion of fossil fuel, EVs are expected to replace the conventional gasoline vehicles, eventually. As a result, roadway electrification is increasingly gaining more attention. EV-charging is one of the main applications of WPT as it provides a safe, contactless, robust, and environment-friendly method for charging. At present, most commercial wireless chargers for EVs involves Stationary WPT (SWPT). However, range limitations and long charging time issues cannot be fully resolved with SWPT only. Consequently, Dynamic WPT (DWPT) has recently been employed to eliminate this issue by charging EVs periodically with bursts of energy emitted from road-embedded transmitter pads. However, these intermittent bursts of energy can hamper grid-side regulation and potentially cause grid-instability, which calls for intelligent grid-side energy management. Secondly, DWPT power bursts received at the EV side could affect EV battery lifetime, which calls for energy management at EV side, similarly. This dissertation aims to design a DWPT system for EV applications with intelligent energy management at the grid side, as well as the EV side. Firstly, a *vehicle detection system* is proposed and implemented which accurately detects the arrival of the vehicle on

a charging pad. The proposed system also measures other relevant real-time information (both from vehicle-side and road-side) as well as communicates these measurements to the DWPT charger, implementing a safe and efficient DWPT system. Secondly, a bidirectional grid-side energy buffering method is proposed with distributed energy storage units installed throughout the DWPT transmitter grid. These Supercapacitor (SC)-based energy storage units operate in conjecture of an intelligent controller which ensures reduced pulsations at the grid while not compromising the desired power transfer to/from EVs. Finally, at the EV side, a hybrid energy storage system (HESS) containing a battery and an SC unit is proposed, where the SC unit acts as an energy buffer for pulsating DWPT/drivetrain power. Also, an Energy Management System (EMS) is proposed which intelligently captures the pulsating DWPT power while significantly reducing the peak transient power faced by the battery, thereby facilitating longer battery life.

(232 pages)

PUBLIC ABSTRACT

Energy Management of Dynamic Wireless Power Transfer Systems for Electric Vehicle

Applications

Ahmed N. Azad

Wireless power transfer is a method of transferring electric power from a transmitter to a receiver without requiring any physical connection between the two. Dynamic Wireless Power Transfer (DWPT) entails having the transmitters buried under the roadway and the receiver unit being installed on the Electric Vehicle (EV). In this method, EVs are charged while driving over the transmitters as they receive bursts of electric energy at the time of significant alignment between transmitters and receivers. Compared to the stationary charging method which involves parking the EV for long hours for a full charge, the dynamic charging method (i.e., DWPT) offers convenience as the vehicle gets charged while driving. It also facilitates extended driving range of EVs. Despite offering these advantages, DWPT causes a few significant issues. DWPT charging results in a transient power profile both at grid side and EV side, which not only hampers grid-side regulation but also affects EV-battery longevity. To address these two issues, both grid-side and EV-side energy management are needed to be employed to protect the grid and the vehicle from sudden exposure to harmful power transients. In this dissertation, the grid-side and EV-side energy management methods have been investigated. Firstly, a detection system to safely detect the vehicle on charging lane is proposed. This detection system is used to facilitate safe and efficient operation of DWPT chargers on EV roadways. Secondly, A novel DWPT system is proposed, which reduces the grid-side power transients with minimal additional hardware requirements. Finally, an EV-side energy management system is proposed which reduces the exposure of EV batteries to pulsating DPWT-power, thereby helping batteries to last longer.

To the memory of my late father Md. Abul Kalam Azad

ACKNOWLEDGMENTS

I would like to extend my sincere gratitude to my advisor Prof. Zeljko Pantic for his guidance, tolerance, and encouragement. Being his first PhD student, I have been fortunate enough to have his utmost support and nurturing. His knowledge, vision, and confidence inspired me to push through the hardest obstacles.

I am also deeply indebted to Prof. Regan Zane for his extensive professional guidance throughout my graduate study. I would also like to thank my committee members, Prof. Doran Baker, Prof. Randall Christensen and Prof. Ziqi Song for providing their valuable support and for reviewing my work.

I am grateful to Utah State University Power Electronics Lab (UPEL) for the academic and financial support which made the completion of my PhD program possible. I deeply appreciate our lab manager Ryan Bohm, for providing the safety-training and equipment-support. I would like to acknowledge all my colleagues at UPEL for their wonderful collaboration. I strongly thank Reza Tavakoli and Ujjwal Pratik who I had the pleasure to discuss and be a co-author with.

Finally, I would like to thank my family, especially my mother and my wife for their unconditional love and support throughout my graduate career.

Ahmed Nasim Azad

CONTENTS

LIST OF TABLES

LIST OF FIGURES

ACRONYMS

BFL	Battery Facing Load
CPT	Capacitive Power Transfer
DWPT	Dynamic Wireless Power Transfer
EMS	Energy Management System
ESR	Equivalent Series Resistance
EV	Electric Vehicle
FFFB	FeedForward FeedBack
IPT	Inductive Power Transfer
LGM	LonGitudinal Misalignment
LPT	Low Power Excitation
LTM	LaTeral Misalignment
MV	Magnetic Vector
OCV	Open Circuit Voltage
PLL	Phase Locked Loop
RC	Receiver Coil
RSC	Road Side Controller
SAE	Society of Automotive Engineers
SC	Supercapacitor
SCFL	SC Facing Load
SOC	State of Charge
SWPT	Stationary Wireless Power Transfer
TC	Transmitter Coil
TU	Transmitter Unit
VDS	Vehicle Detection System
WPT	Wireless Power Transfer

CHAPTER 1

INTRODUCTION

1.1   Wireless Power Transfer: History & Evolution

Efficient, safe and convenient electric power transmission could be considered one of the important factors that are contributing to the advancement of modern civilization. With the growing demand for electric power for utility and portable consumer electronics, this need for convenient power transfer is increasingly becoming more emphasized on. Conventional methods of power transfer involve closed-loop wired connection between the source and the load. Contactless, or Wireless Power Transfer (WPT), on the other hand, has the capability to exchange power between a source and a load that is physically separated.

Electrical engineers have been inspired by the idea of transmitting power wirelessly for more than a century. In the 1910s, Nikola Tesla was the first who presented the concept of transmitting power wirelessly using Faraday's law of induction [4]. Although his invention named as Wardenclyffe Tower, designed for wireless power transmission, was eventually not successful, his vision has shaped his successors' motivation to develop the technology. With the passage of time, WPT has been gradually transformed into a worldwide multi-billion dollar commercial industry [5]. High-efficiency operation up to 90% or more, reliability, and robustness are some of the most prominent features of WPT [6]. In addition, environmentally inert operation in the face of adverse environmental conditions such as moisture, dirt, or chemical exposure has facilitated a virtually maintenance-free operation which adds to its popularity [7], especially in EV applications. For the last few decades, WPT has found applications in electric household appliances such as cellphone chargers [8]-[10], biomedical implants such as artificial hearts [11]-[13], etc. These are some examples of low power applications of WPT. Medium/high power applications of WPT are predominantly found in electric vehicle charging systems [14]-[17].

The general classification of WPT technologies can be illustrated using Fig. 1.1. Based on the relative distance between the power source and the load, the wireless power transfer methods can largely be divided into two categories, namely near-field and far-field transfer, as depicted in Fig. 1.1. Near-field transfer corresponds to the case where the distance between source and load is less compared to $\lambda/2\pi$ (λ being the signal-wavelength), whereas far-field transfer corresponds to higher source-to-load distances.
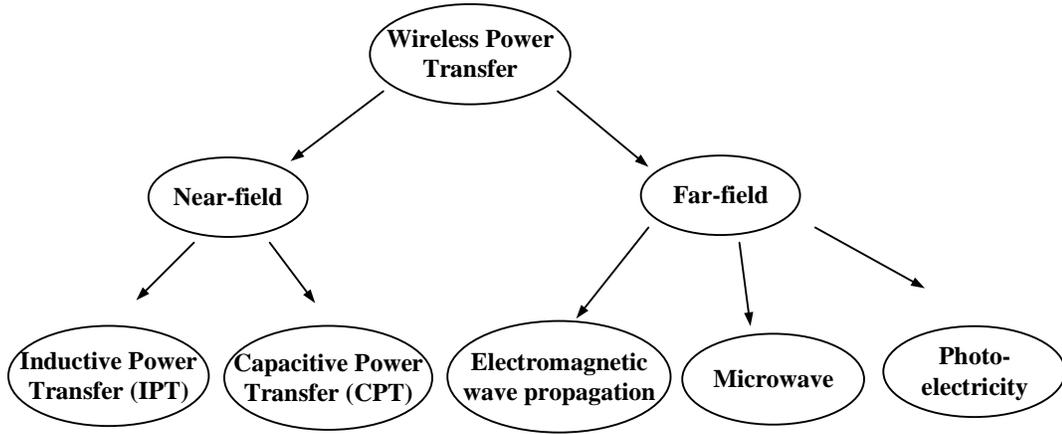
Fig. 1.1: Classification of WPT technologies.

Near-field WPT can be divided into two general categories depending on the type of field (electric, or magnetic) responsible for the wireless power transmission, namely Inductive Power Transfer (IPT) and Capacitive Power Transfer (CPT). In the case of IPT, power is transferred via magnetic field coupling, whereas in the case of CPT, power is transferred via electric field coupling. CPT applications are limited by air's maximum electric field intensity (30kV/cm). Also, compared with the magnetic permeability of air, the electric permittivity is much lower in value, consequently making capacitive coupling harder to achieve without frequencies in MHz range and kilovolts of voltage between coupler plates. High voltage rating of components, lower power density, and high-frequency operational requirements are some of the other deficiencies of CPT.

The far-field transfer takes place where the distance between source and load is much

larger compared to the signal wavelength. High directivity of transmitting antenna is required in far-field transfer to ensure efficient power transfer. High directivity can be achieved through increasing the operating frequency at a higher level (up to microwave or visual spectrum). This high-frequency operation, however, raises health and safety concerns. This safety issue combined with low efficiency makes the far-field method impractical for many applications.

Among the existing methods of wireless power transfer, the inductive method (IPT) is considered by far to be the most secure and productive for wireless power transfer in consumer electronics and biomedical industry [18], [19]. The preferred method for Electric Vehicle (EV) charging applications is also predominantly the inductive method [5], although, most recently there have been some deployments of CPT in EV applications [20]. Recently, IPT deployment in-vehicle charging infrastructure has been investigated by B. J. Limb et al, and this WPT technology is proven to be economically and environmentally viable as the replacement of gasoline-driven vehicle infrastructure [21]. Thereby, the IPT-type WPT charging in EV roadway infrastructures will be the scope of this dissertation, too.

1.2 Successive Developments & Challenges of WPT Deployment in EV

Prior to delineating the scope of this dissertation, the two different varieties of IPT-type WPT commonly applied in EV applications, along with their respective advantages and disadvantages are discussed as follows.

1.2.1 Stationary WPT: Benefits & Challenges

Due to the gradual depletion of fossil fuel all over the world, the automotive industry is slowly leaning towards electrified transportation. EVs offer a noise-free, clean, and Zero-Emission(ZE) alternative with higher fuel economy, compared to the conventional gas-driven vehicles that can have efficiency as low as 14% [22]. The application of WPT in the EV industry can largely be attributed to the added degree of freedom and protection it provides to users. Stationary WPT charging stations are suitable for harsh environment charging, and are resilient to the potential hazards associated with high power charger cable plug-in.

The charging process, if fully automatized, provides additional convenience.

Even with these benefits, stationary WPT is unable to solve two issues that are standing in the way of EVs' progress, preventing EVs to compete with gasoline vehicles. Firstly, the size and cost of EV batteries are significant which makes EVs more expensive than their gasoline counterparts. Also, the charging stations are not ubiquitous, meaning the accessibility to charger outlets is still limited. This fact, combined with the battery's limited driving range, creates the so-called "range anxiety". Because of range anxiety, users are often reluctant to buy EVs. Moreover, the recharging time of an EV battery unit can be significantly longer compared to the refueling time of a gasoline vehicle. Short charging time of EVs would require very high charging current which would be detrimental to battery life. Also, designing converters at high current level would be difficult and make the converter hardware bulky and expensive. Due to these reasons, 6-8 hours full-recharge time is typically required for EV batteries. From Idaho National Lab's (INL) recent study [23], about 85% of EV owners charge their cars at home. It suggests that EVs are generally charged overnight.

1.2.2 Dynamic WPT: Benefits & Challenges

To eliminate the problems associated with the stationary WPT systems, Dynamic WPT (DWPT) systems have been proposed. In case of DWPT charging, the vehicle could be charged as it drives over the buried transmitter coils embedded in roadways. As opposed to hours-long stationary charging while the vehicle can not move, DWPT could facilitate "opportunity charging" while the vehicle is on the move, which not only would eliminate the long recharge time issue but also would extend the vehicle range, thereby eliminating the range anxiety. Moreover, if the electrified roadways are made ubiquitous, it could help reduce the battery size and cost, simultaneously making the All-Electric Range (AER) of EVs to be virtually infinite. However, despite eliminating some bottlenecks of EV deployment, DWPT introduces two new issues that demand adequate attention.

Firstly, a significant issue with DWPT is that the power pulsations at the EV battery at the moment of power transfer. Unlike stationary systems in which case a constant power is delivered to the vehicle during charging, the DWPT charging method may produce

an intermittent profile of the power delivered to the vehicle. It leads to oversized power hardware at the vehicle side, and it can be harmful to battery health and lifetime. To convert intermittent input power into a smooth charging power for vehicle batteries, the use of Supercapacitor (SC) is heavily employed in EVs. SC has significantly higher power density than the EV battery which enables it to handle short bursts of energy. Different Hybrid Energy Storage Systems (HESS) containing both batteries and SCs have been proposed in the literature. For example, direct paralleling of SC with a battery, active paralleling of SC with a battery facing load (BLFL), active paralleling of SC with SC facing load (SCFL) have been proposed and compared in [24]. In [15], a novel HESS has been proposed with active paralleling of SC and battery to the EV, offering additional flexibilities (free selection of battery and SC voltage levels) at the cost of additional converter requirement. Recently, topologies have been proposed with energy storage in the vehicle-side compensation tank which eliminates the need for any DC-DC converter at the EV-side at the expense of complicated control strategies [25].

The second issue regarding DWPT is that grid-side power pulsations resulted from the vehicle alignment are inevitable in dynamic wireless charging [26]. This problem is virtually nonexistent in case of stationary charging but would become more and more prominent with the expansion of DWPT. One reason behind this is that most of the stationary EV charging happens overnight. About 40% generators in the USA experience low load overnight as reported by the Electric Power Research Institute (EPRI), which makes it easier for the grid to absorb the EV load overnight [27]. Above all, stationary charging requires a fairly uniform profile of power intake by the vehicles, and it does not result in any perceivable power fluctuation at the grid.

However, in the case of dynamic charging, it is more likely that the vehicle would be charged mostly at day time during peak hours when most people commute to work. During this peak time, supplying EVs from the grid could put significant pressure on the grid itself. The power fluctuation problem would be increased, causing voltage and frequency fluctuations at the grid-side, thereby making the situation even worse. These grid-side issues are

worsened in case of microgrids [28], which have become more widespread in remote areas where the central grid is nonexistent or rudimentary. Since the capacity of an islanded microgrid is smaller than the grid capacity, it cannot be treated as an infinite bus, thereby, a more stringent supply-demand balancing restrictions apply in order to ensure frequency regulation and/or grid stability. To make the situation even more aggravated, the renewable energy generators which predominantly supplies microgrid systems, are dependent on ambient operation conditions (e.g. wind flow, sunlight, etc.) which fluctuate throughout the day. As a result, microgrids power generation profiles are naturally intermittent. This fact, combined with the intermittent nature of DWPT power loads, could cause high-frequency oscillations in microgrids [29], the effect of which could be more serious than in case of a central grid. So, for dynamic WPT applications, it is of paramount importance to employ energy buffering both at the centralized grid-side and microgrids.

Oak Ridge National Lab (ORNL) has investigated the grid-side impacts of DWPT [30], [26]. In [26], Lithium capacitors (LiC)s are actively paralleled with the grid side to provide a satisfactory 81% reduction of grid pulsations. However, the employment of a high-power bidirectional converter at the power transmitter side increases the cost and complexity at the grid-side. A convenient solution with minimal additional hardware requirements to address the grid-side issue is still to be developed.

1.2.3 Bidirectional Dynamic WPT: Benefits & Challenges

Comparing the SWPT's and DWPT's advantages and disadvantages, it can be summarized that, DWPT provides some important benefits that the SWPT can not provide. However, DWPT significantly increases the power transients at the grid-side and the EV-side, whereas SWPT does not cause those issues.

Combining the advantages of stationary and dynamic WPT while simultaneously minimizing their downsides would provide the ultimate solution for the EV industry. Bidirectional WPT could serve as an excellent potential to achieve this goal. Bidirectional WPT would facilitate establishing a Vehicle-to-Grid (V2G) system [31], capable of supplementing the grid with some extra power from EV batteries if needed. It would, on average,

help keep the Area Control Error (ACE) low, which is beneficial to the grid [27]. With intelligently controlled, optimally sized, distributed energy storage at grid-side, grid voltage and frequency regulations could also be maintained. These bidirectionally charged storage units could also act as energy buffers, capable of transferring energy from one vehicle to the next, essentially facilitating a more advanced Vehicle-to-Vehicle (V2V) charging system [32]. Above all, bidirectional power transfer capability would serve a greater benefit to facilitate Distributed Generation (DG) systems/Green Energy (GE) systems by offering additional storage to utilize the unpredictable nature of the generated energy. The V2G charging can also serve a renewable-energy-powered Distributed Generation (DG) network [33], [34] where the power generation could be highly stochastic due to fluctuating climate conditions. This case where the EV storage is used to supplement an existing battery storage system is commonly referred to as "Living and Mobility" [26]. The state of California could be used as an example where the "Living and Mobility" concept could be employed. California produces about 40% of its electricity from solar power plants. However, since they can not manage access energy due to lack of battery storage, surplus renewable energy sometimes becomes a liability on their part; consequently, they have to pay other states (ex: Arizona) to take their surplus energy [35]. If V2G and G2V (Grid-to-Vehicle) bidirectional infrastructure were to be implemented, the EV battery storage capability could help to absorb some part of the excess energy produced when needed, also give back some power to the grid at times there is not enough solar power available at the grid.

While this is an example of V2G charging as a form of secondary energy reserve in DG units, there are many ancillary benefits offered by V2G, if integrated into conventional grids [36]. Among them, peak load shaving [37], load balancing [38], frequency and active/reactive power regulation [39], power reserve support [40] are some examples. Above all, V2G helps with grid stability, efficiency, and reliability [41]. Moreover, there are perceivable economic aspects of V2G infrastructure [42]. A conventional G2V charging tends to increase the grid power demand which would require additional investment in power generation and distribution infrastructure. Opposite to G2V, the V2G charging would help

to reduce this additional cost. In the United States, V2G charging has potential to save an equivalent of 6.5 million barrels of oil per day, whereas the net return from V2G is estimated in the range from \$90-\$4000 per year per vehicle [36], [37]. Due to environmental and economic benefits provided by G2V and V2G charging, a bidirectional DWPT infrastructure capable of facilitating them has been proposed and investigated in [43].

However, V2G charging has some disadvantages as well. The V2G charging still can cause a transient EV power profile and consequently cause the battery degradation and reduced lifespan [42]. It has been claimed that if the cost of EV battery capacity depreciation is considered, the profit from V2G use would significantly reduce [36]. Moreover, the V2G cannot eliminate the power grid-side pulsations, and a bidirectional DWPT infrastructure capable of grid-side energy management is still needed.

1.3 Scope of This Dissertation

Upon discussing the different types of WPT systems available in EV industry along with their respective advantages and disadvantages, this dissertation presents a systematic analysis and design methodology to address some of the existing issues present in the EV industry in the areas of DWPT applications. The focus of this research has been primarily concentrated on effective energy management of inherently transient DWPT power profiles to mitigate some of the adverse impacts DWPT tends to inflict upon the grid and the EV. The following chapters of this dissertation are arranged as follows:

Chapter 2 : Chapter 2 describes the detailed overview of the DWPT charging infrastructure in electrified roadways. Starting from a basic DWPT unit as a building block, an elaborate description is provided in order to depict how these units collectively build up a larger EV grid infrastructure and also how that infrastructure is integrated within an even larger electric grid. The impact of different designs and operation scenarios of electrified roadways on the grid and the EVs are investigated to delineate the issues that are addressed by this thesis. Consequently, steady-state power transfer analysis of both unidirectional and bidirectional DWPT charging is carried out. Possible control variables to control the power transfer are identified, which will be used to design the DWPT controller in successive

chapters.

Chapter 3 : Chapter 3 presents a comprehensive *vehicle detection system* for energy management on DWPT-charged EVs. The successful operation of DWPT systems largely depends on the timely detection of the oncoming vehicle. Moreover, various other information such as vehicle misalignment with the charging track, vehicle speed, presence of harmful objects on the charging track, etc. can be incorporated with the DWPT system controller for safe and efficient energy management. The presented vehicle detection system accurately measures and communicates all these real-time information with a DWPT system. A simulation model of the proposed VDS system is discussed, followed by hardware implementation. The designed hardware prototype is tested with a 25-kW DWPT charger system of an E-bus. The integrated operation of the detection system along with the DWPT charger is carried out, and the role of the proposed detection system in improving the energy management and safety of DWPT system is experimentally validated.

Chapter 4 : Chapter 4 addresses the discussed grid-side issues corresponding to DWPT charging. An SC-based grid-side energy buffering unit is proposed which can be inserted into existing grid-side infrastructure with no additional power electronic requirement. A control strategy of the grid-side inverter is introduced to intelligently control the buffering unit so that the grid-side power pulsations due to G2V and V2G charging are minimized. Two controllers are proposed and designed, which work together to regulate the track current and manage the energy buffering unit to control the grid-side power fluctuations while simultaneously ensuring the full-capacity power delivery to the vehicle. Detailed modeling of the proposed DWPT system is carried out using General State-Space Averaging (GSSA) method, and the controller design method is discussed in detail. A simulation model of the full system is built, and the simulation results are compared with a conventional DWPT system to evaluate the benefits of the proposed system. This chapter also contains a detailed description of the hardware setup built in order to validate the proposed design. A bidirectional DWPT system prototype is developed as a downscaled version of an EV charging system. The detailed hardware-development stages and controller-design stages

are discussed. Experimental tests to evaluate DWPT charging scenarios are presented and evaluated. Finally, the experimental results are compared with the corresponding simulation results to validate the effectiveness of the design.

Chapter 5 : This chapter addresses the discussed EV-side issues corresponding to DWPT charging. An actively controlled hybrid energy storage system containing a battery and SC unit is proposed to ensure that batteries are not exposed to high charging or discharging currents that could affect the longevity of EV batteries. SC is used as an energy buffer, absorbing both the highly transient part of the incoming DWPT charging profile and the transient load profile of EV drivetrain caused by rapid acceleration/deceleration of the vehicle. An energy management system is designed to control the hybrid energy storage and provide various other important features, such as regenerative braking capability, bus voltage regulation, voltage/current protection, etc. Different DWPT profiles and drive cycle powertrain are modeled and tested with the proposed EV storage system in a simulation environment. The simulation results are discussed, and the effectiveness of the proposed system is summarized.

Chapter 6 : Finally, Chapter 6 outlines all the conclusions reached from this dissertation. The salient features of the designed DWPT systems are summarized along with their advantages and disadvantages. The research contributions and its potential to address the issues in EV roadways and EV storage systems are listed. Possible future research directions are discussed at the end.

CHAPTER 2

DWPT SYSTEMS FOR EV APPLICATIONS: OVERVIEW AND ANALYSIS

In this chapter, an overview of the DWPT systems deployed in EV applications is presented. Section 2.1 discusses a single DWPT charging unit architecture. On a larger scale, these units are arranged together to create a DWPT system infrastructure for EV roadways, which has been discussed in Section 2.2. Section 2.3 and Section 2.4 provides a detailed mathematical analysis of unidirectional and bidirectional DWPT systems, respectively. The presented mathematical analysis serves as the background for the work presented in subsequent chapters of this dissertation. The chapter summary is given in Section 2.5.

2.1 Basic DWPT Unit for EV Charging

Fig. 2.1 depicts a typical grid-powered DWPT system for EV roadways. Generally, any WPT system can be identified as the association of two physically detached subsystems. One is called *primary* or *transmitter* and the other one is generally called *secondary*, *receiver* or *pickup*. The primary side sources the power to be transmitted, and the secondary is responsible for receiving the wirelessly transmitted power. The main component of primary is a High Frequency (HF) inverter, which takes a DC input (in case the supply is the AC utility grid, that AC voltage should be rectified and power-factor-corrected to generate a stable DC grid which will be used as the DWPT system input) and converts it into a very high frequency AC signal. The power transfer capacity of a DWPT system is highly dependent on the frequency of operation, which justifies the use of HF inverter. In order to prevent the increased VA rating of the inverter circuitry as a result of supplying the mostly-reactive coil current, a compensation circuit is needed at the primary side [44]. Additionally, a compensation network at the secondary side is also employed to enhance the power transfer capability [44], [45]. Different types of compensation topologies can be

employed to achieve different additional design goals [46].
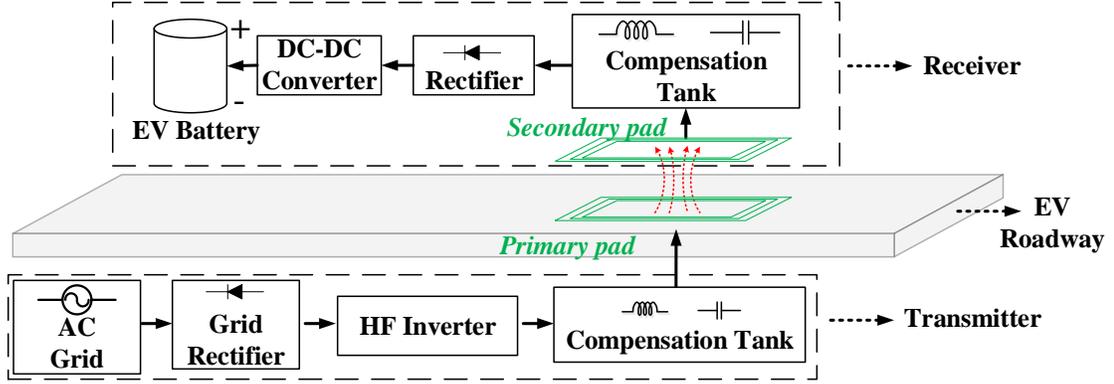
Fig. 2.1: A typical grid-powered DWPT system.

It is important for the coils to have a low loss to enhance the power transfer capability of the system. Because of the skin-effect, the effective cross-sectional area of typical power cable would decrease at higher frequencies, consequently increasing its resistance. Although multi-strand cable would help to mitigate the skin-effect, current crowding at high frequency would affect the current distribution in conductor strands, thereby increasing the effective resistance and consequently, decreasing the DWPT efficiency. That is why, typical WPT applications require employing specially-manufactured, very heavily stranded wires namely "Litz wires" which provide exceptionally low resistance at high frequencies [47].

Due to a relatively large air gap between coils, the coil leakage inductances are higher, and the coupling is lower, forming a loosely coupled transformer having a coupling factor of 0.1-0.5 [48]. Due to the mutual coupling between the primary and secondary coil, alternating current at the primary coil (also referred to as track current) would induce an AC voltage through the secondary coil. In order to charge an EV battery, this AC voltage needs to be processed to a DC voltage. It is accomplished by a rectifier following the secondary coil and compensation arrangement. Finally, in order to implement smooth battery charging control (such as Constant Current-Constant Voltage commonly known as CC-CV control), this rectified DC voltage can be further processed and controlled by a DC-DC converter (as

shown in Fig. 2.1) before deilvering the power to the EV battery.

2.2 DWPT Charging Infrastructure

The previous section discusses the unit DWPT system, whereas multiple of these units can be combined to form a DWPT infrastructure. Such an infrastructure could be envisioned as an array of DWPT transmitter units installed in the EV roadway, and a fleet of EV capable of receiving the DWPT charging while traveling through the road. A conceptual diagram illustrating a dynamic charging system for electrified transportation is presented in Fig. 2.2.
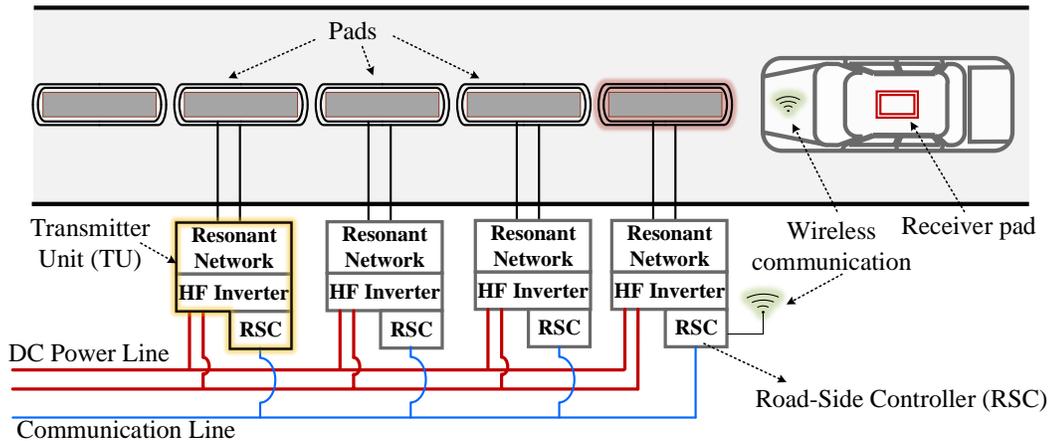
Fig. 2.2: An illustration of a dynamic charging system for electric vehicles with pads and transmitter units.

The road lane contains an array of elongated pads, which are individually powered from corresponding Transmitter Units (TUs). Each TU is powered from a DC grid section, and it consists of an HF inverter, followed by a compensation (matching) resonant network which supplies the corresponding pad with a high-frequency alternating current, and a Road-Side Controller (RSC). The RSC is a microcontroller-based system that controls the pad activation and synchronizes its operation with adjacent pads. All RSC units are connected via a central communication line, so that synchronized operation of the whole section is facilitated. The communication line is typically made of optical fibers. For this particular

application, Control Area Network (CAN) communication protocol is proposed for data exchange. Synchronized energizing and de-energizing of coils in consecutive pads causes seamless power delivery to a moving vehicle.

Groups of TUs and pads are further organized hierarchically into sections, as illustrated in Fig. 2.3 . The size of a section can vary, depending on the rating of the DC power source supplying the section, and the frequency of electrified vehicles driving through the section. All TUs in a section share a common DC bus, and it should be sized to support the most demanding charging scenario for that particular section. As illustrated in Fig. 2.3 , power for the DC grid can be provided by the ac power grid or generated locally from renewable energy sources.
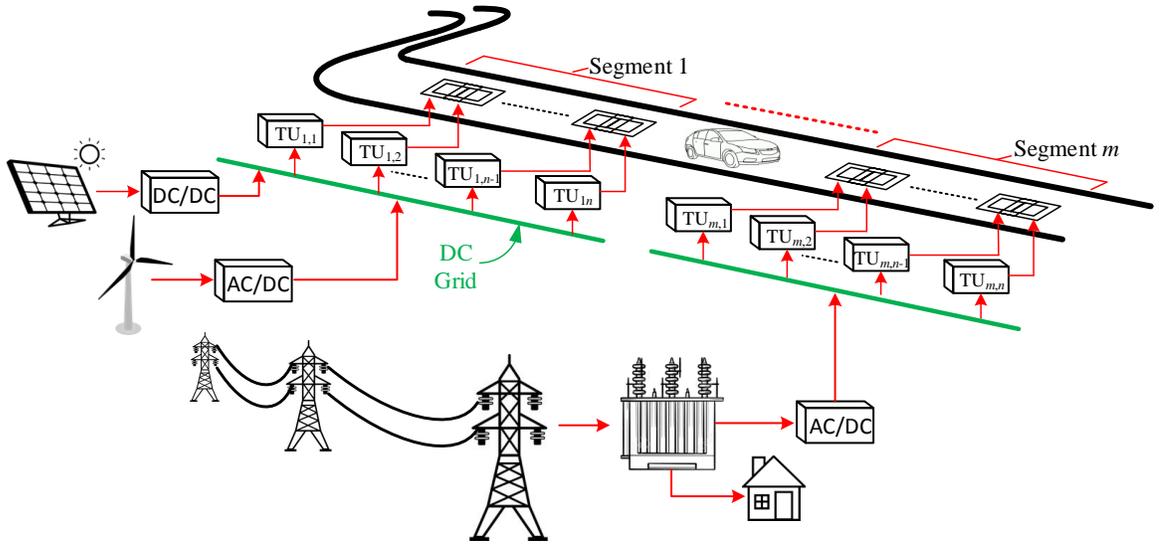
Fig. 2.3: Dynamic charging system at a large scale with illustrated sectional organization.

Different coil types have been proposed for DWPT, although the single-loop elongated rail [49], [50] and circular or squared lumped coil designs [51] have been dominating in practical applications, so far. The single-rail structure provides a constant power input from the grid for a longer period of time and requires less independent power electronic units per length of the electrified section. However, that comes at the cost of high rail current, difficult compensation, lower efficiency, and safety concerns about the uncovered

but energized pad portion. Due to the relatively low local coupling between the vehicle and the single-turn primary coil, high current is needed to deliver the required power. That leads to very high reactive power, causing difficulty in designing capacitor compensation blocks. This is typically resolved by using distributed compensation along the rail, which, in turn, increases the complexity of the coil design. A high primary rail current results in more losses in the primary pads than it is identified in other coil designs. Finally, it is difficult to magnetically shield the part of the pad that is not covered by the vehicle, which raises significant health concerns. Contrariwise, the lumped coil structure is more efficient and magnetically safer [52]. It also increases reliability, because failure in one pad does not hamper the system operation much since a single pad typically occupies a small area [53]. However, these systems require distributed power electronic units and the power profile is inherently more transient.

In an attempt to improve the power profile by increasing the system's misalignment tolerance, different bipolar coil designs have been proposed, such as BPP [53], DDP [54], and DDQP [55]. They provide better features than their unipolar counterpart CP [56], but at the price of additional hardware complexity. Similarly, different control algorithms can be employed to reduce the power profile transients, both for unipolar systems [1], [57] and for bipolar systems [54]. To balance the pad construction and control complexity, an elongated pad structure can be employed with longer coils of rectangular shape. The increased dimensions with respect to lumped coils provide an inherent improvement of the power profile, with an assumption that the decoupled coils are controlled in a timely manner. In the analysis that follows, the elongated pads will be considered as the pad structure of choice.

The pulsating nature of the power input to a charged vehicle can be eliminated by intelligent design and activation of transmitter pads. By reducing pad-to-pad distance, and by smoothly transitioning the excitation from one pad to another, the power sag between two pulses can be eliminated. To make the transition smooth, pads are overlapped in a controlled fashion, as illustrated in Fig. 2.4. That way, zero-coupling between successive

coils is established (similar to a BPP structure in [53]), so that the decoupled operation of each coil is possible. Since the coils' mutual inductance if nullified, the pads can be controlled and energized so that a seamless power transition between two successive pads is achieved. In the zone between two pads, both pads are kept active to jointly provide the requested power, as illustrated in Fig. 2.4.
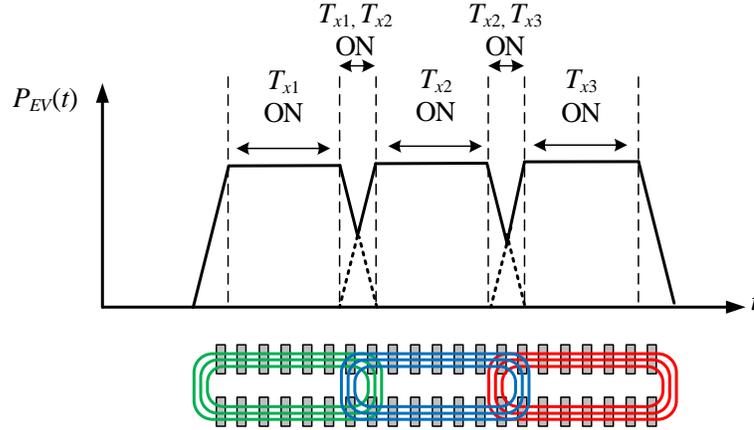
Fig. 2.4: Power transfer profiles from overlapped, sequentially-activated pads.

Fig. 2.5 presents the vehicle power profiles corresponding to two different spacing scenarios between successive transmitter pads.If the pad-to-pad distance is relatively high, as shown in Fig. 2.5(a), the vehicle receives a pulse-train shaped power profile P_{EV1}. However, when the pads are overlapped as in Fig. 2.5(b), the pad excitations can be controlled in such a way that the vehicle receives almost sag-less power P_{EV1}. As illustrated in Fig. 2.5(b), the average P_{2avg} and maximum power P_{2max} are much closer in value for the overlapped pad structure compared to the separated pad structure, making the hardware specification less demanding. That way, the later structure achieves a more uniform power profile at the expense of a more complicated controller and pad structures. From this analysis, one can conclude that the pad design proposed in Fig. 2.5(b) effectively solves the problem of intermittent power at the vehicle side.
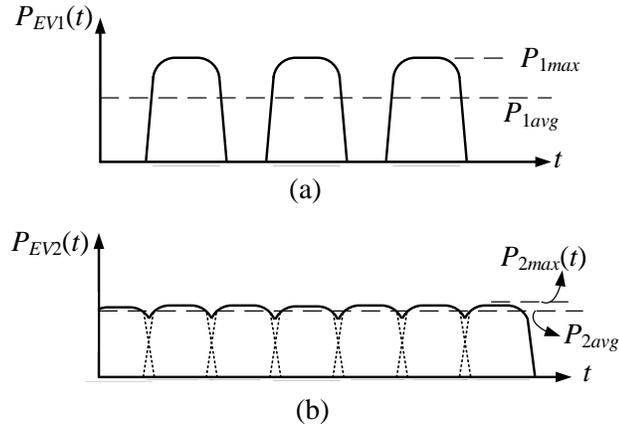
Fig. 2.5: The profile of the power received at the vehicle (a) when pads are further apart (b) when pads are partially overlapped.

A similar problem of intermittent power can be identified at the transmitter side (at the inverter input), but it cannot be solved by redesigning the coils structure since it is inherent to the dynamic charging process. The TU input power profile (the input power to individual inverter units) nonetheless remains intermittent and pulsating, as illustrated in Fig. 2.6.
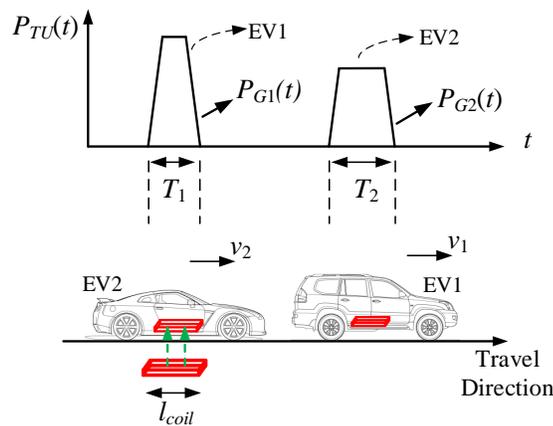
Fig. 2.6: The power profile at the TU input.

As can be observed from Fig. 2.6, after vehicle $EV1$ leaves the charging pad, the power

transfer will drop, which will be a signal to the RSC to terminate charging. When the next vehicle $EV2$ is detected, the RSC will reenergize the coil again and transfer power to $EV2$. In a general case of different power demands and different velocities (v_1 and v_2), the TU power profile would be different for the two vehicles as illustrated with $P_{G1}(t)$ and $P_{G2}(t)$ in Fig. 2.6. The width of the power pulse is determined by the speed of the vehicles and the pad size, while its magnitude is controlled by the vehicle which is demanding more or less power. The inverter input filtering capacitance does not have the capability to smoothen the TU input power profile, and the TU would demand the same or very similar power profile from the DC grid section, causing the "segmented current" and power to vary in a similar manner. These power profiles can be known *a priori* only in terms of statistical quantities, such are mean values and power variances.

When a significant number of EVs are performing in-motion charging on an electrified roadway, even a somewhat smooth power intake from each of them can result in significant power fluctuations at the grid-side. To illustrate the grid-side impact of DWPT charging, a segment power profile is considered, as illustrated in Fig. 2.7. In this scenario, a segment having length L_{seg}=400 m, consisting of an array of TUs, each rated at P_{1max}=25 kW is considered. For simplicity, a fleet of 5 EV is considered to be moving along the segment, with each car having the same speed v=20 m/s, same length L_v=5 m and the same car-to-car following distance of 40 m. In this scenario, the maximum instantaneous power demand from the segment $P_{seg,max}$ is 125 kW, whereas the average power $P_{seg,avg}$ would be significantly lower. These relations generally hold, irrespective of different vehicle speeds and number of vehicles on the segment. Moreover, the value of $P_{seg,max}$ would increase as the number of vehicle present on a segment at a given moment increases. For example, for the segment in question, in the high traffic scenario where the vehicle-to-vehicle distance is small, there could be a staggering number of 80 vehicles on the segment, which would demand an absolute maximum value of $P_{seg,max}$ equal to 2 MW. On a larger scale, several segment power profile P_{seg} are summed up to result in a grid power profile P_{grid}.
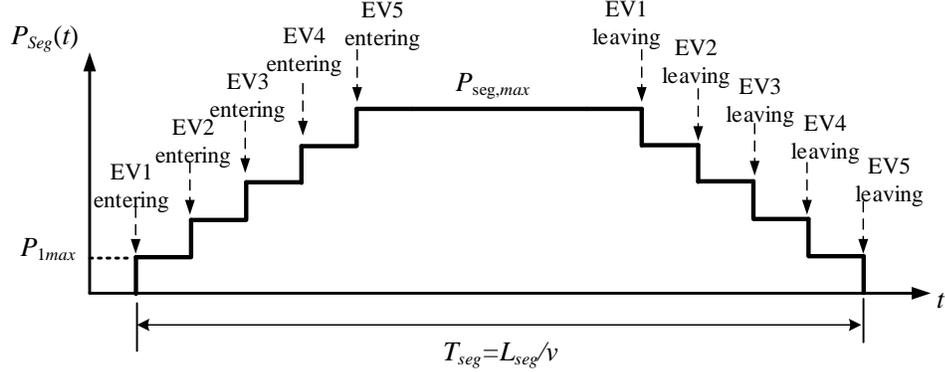
Fig. 2.7: The input power profile of one segment.

When designing a segment, cables must be rated at the absolute maximum power rating, although in practice, the average power demand would be lower. In other words, the system design would be oversized. Additionally, a gradual expansion of the segment size would be difficult, as the inclusion of new units would require even higher cable rating than before. As a possible solution for the discussed problems, intelligent energy buffering at the grid side is proposed in this work to decrease or eliminate the gap between $P_{seg,max}$ and $P_{seg,avg}$. In other words, it makes it possible to design a segment with reduced rating compared to $P_{seg,max}$ and makes it easier to expand the segment size. Using the aforementioned energy buffering, the grid power profile would be downscaled in a similar way, effectively reducing the volume and cost of the grid-side hardware.

2.3   DWPT Unit Steady State Analysis

Fig. 2.8 depicts a typical grid-powered DWPT unit circuit diagram. The AC utility grid power is rectified and then smoothed by a power factor correction unit to reduce the current harmonic distortion at the grid side. The core element of the primary is the HF inverter, which converts the DC input into a high-frequency AC signal. In a general case, the inverter output voltage is controlled by means of phase-shift modulation. The inverter is followed by a compensation network. In this dissertation, an LCC compensation circuit is selected due to its ability to produce a controlled, load-independent current through the primary coil, to act as a current source to secondary electronics, and to adjust the load

power factor at the output of the inverter. The primary compensation circuit parameters contain a series inductor L_{ps}, a parallel capacitor C_{pp} and a series capacitor C_{ps}. Similarly, the secondary compensation network contains a series inductor L_{ss}, a parallel capacitor C_{sp}, and a series capacitor C_{ss}.
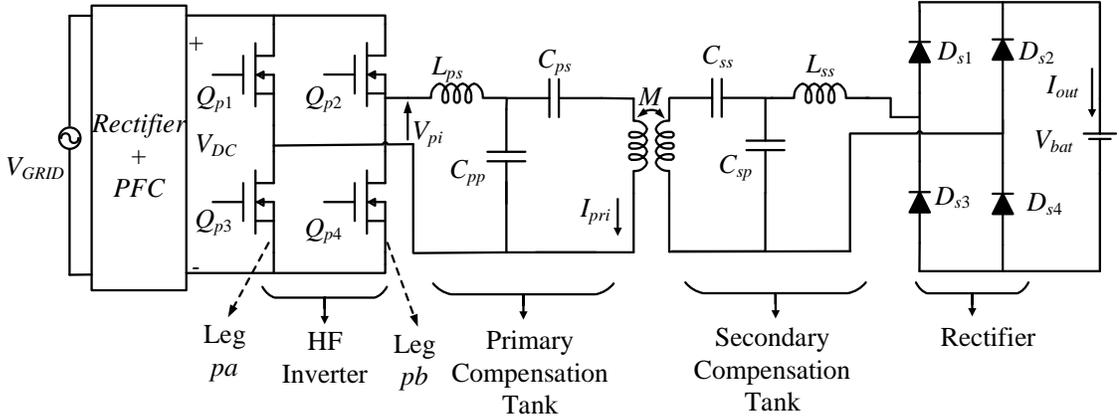
Fig. 2.8: A typical circuit for DWPT-charging of EVs.

The inverter switching is set to match the resonant frequency of the primary compensation tank. Consequently, a sinusoidal current at switching frequency flows through the primary coil (also referred to as a track current) causing an alternating magnetic field around the primary coil and through the secondary coil. According to Faraday's law, the AC magnetic field induces an AC voltage across the secondary coil. That induced voltage is sent through a secondary compensation network prior to being rectified by means of a diode bridge rectifier. The rectifier output could be further processed by a DC-DC converter (not shown in Fig. 2.8) before delivering DC power to the load. The load can be a battery (as shown in Fig. 2.8) which corresponds to a battery charging application, in which case $V_{out} = V_{bat}$ and the output DC power is directly controlled by the amount of current supplied to the battery ($P_{out} = I_{bat}V_{bat}$). If the output voltage varies linearly with the output DC current, resistive element R_{load} is an adequate load model. The mentioned parts of the system are discussed in detail in the text that follows.

Typical inverter waveforms for the symmetric phase-shift modulation are shown in Fig. 2.9. In this example, the inverter legs pa and pb are operated with the phase shift ϕ_p with respect to each other. The inverter outputs a square-wave AC voltage. Assuming that the resonant tank eliminates higher harmonics, harmonic analysis can be adapted to study the power transfer through the system. The RMS value of the first harmonic of the inverter output voltage $V_{pi,1,rms}$ is presented in (2.1). ϕ_p is considered to be the control input of the inverter and the primary. By controlling ϕ_p, the first harmonic of the inverter output voltage will be controlled, which in essence controls the track current. Effectively, the inverter could be represented as a ϕ_p-dependent voltage source approximated with the first harmonic after ignoring the high-frequency harmonics, as follows:

$$V_{pi,1,rms} = \frac{2\sqrt{2}}{\pi} V_{DC} \sin \frac{\phi_p}{2} \tag{2.1}$$
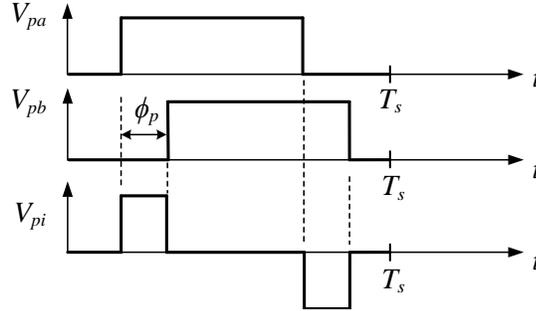
Fig. 2.9: Time waveforms of the phase-shifted voltages of inverter legs and the inverter output voltage.

If the load is modeled as a battery voltage V_{bat}, the equivalent AC load will be a voltage source, too:

$$V_{out} = \frac{2\sqrt{2}}{\pi} V_{bat} \tag{2.2}$$

If the resistor R_{load} is a more suitable load model, then the AC equivalent load can be calculated as:

$$R_{ac} = \frac{8}{\pi^2} R_{load} \tag{2.3}$$

Fig. 2.10 represents an equivalent circuit with simplified inverter and two load models, as described.

(a)

(b)
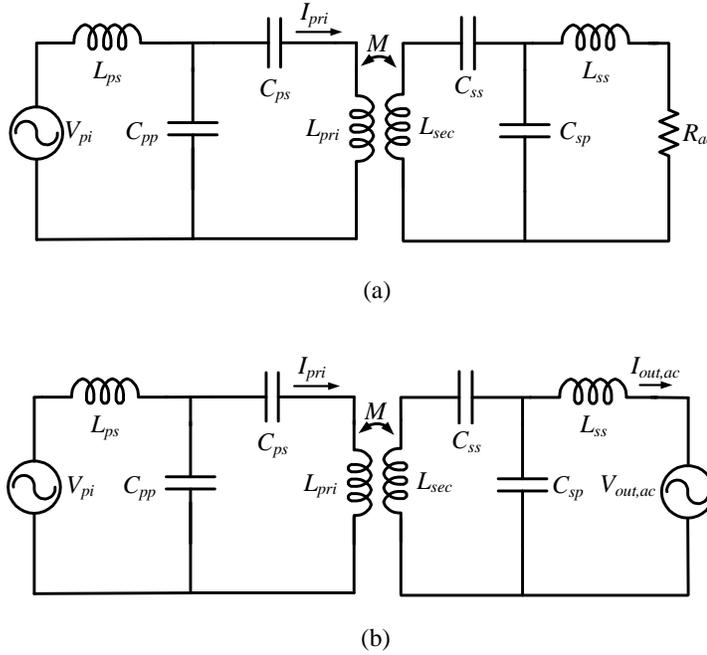
Fig. 2.10: Simplified equivalent WPT circuit with (a) resistive load model (b) battery load model.

In order to simplify the system analysis, the coupling between the primary and the secondary coils can be replaced by the current dependent voltage source V_{oc} and the secondary impedance referred to the primary side $\boldsymbol{Z_r}$, as shown in Fig. 2.11. Here, the effect of the load at the secondary is included in the primary circuit as a reflected impedance $\boldsymbol{Z_r}$. Similarly, the effect of the primary magnetic field on secondary is modeled with a voltage source $\boldsymbol{V_{oc}}$. This voltage source acts as a power supply for the secondary circuit and its value is proportional to primary coil current $\boldsymbol{I_{pri}}$ and the coils' mutual inductance M:

$$\boldsymbol{V_{oc}} = j\omega_s M \boldsymbol{I_{pri}} \tag{2.4}$$

The $\boldsymbol{V_{oc}}$ source could be converted to a current source with the help of source-transformation theory, as shown in Fig. 2.12. Now, the secondary compensation network tuning conditions are chosen such that L_{sec}, C_{sp} and C_{ss} are in resonance, i.e.,
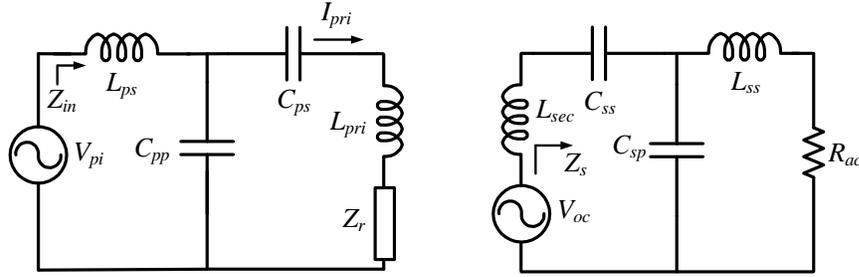
Fig. 2.11: The simplified equivalent circuit after coupling between primary and secondary coils is replaced by V_{oc} and Z_r.

$$\omega_s L_{sec} - \frac{1}{\omega_s C_{sp}} - \frac{1}{\omega_s C_{ss}} = 0 \tag{2.5}$$

Furthermore, the L_{ss} and C_{sp} are also selected to be tuned:

$$\omega_s L_{ss} - \frac{1}{\omega_s C_{sp}} = 0 \tag{2.6}$$

From (2.5)-(2.6), it can be derived that:

$$\omega_s L_{ss} = \omega_s L_{sec} - \frac{1}{\omega_s C_{sp}} \tag{2.7}$$

Now, upon source transformation, an effective inductance L_{ss}, becomes parallelly connected with C_{sp}. Due to the condition (2.6), L_{ss} and C_{sp} together results in anti-resonance, effectively working together as an open circuit. Thereby, the current supplied to the load is essentially equal to the current of the current source:

$$\boldsymbol{I_{out,ac}} = \frac{\boldsymbol{V_{oc}}}{j\omega_s L_{ss}} \tag{2.8}$$
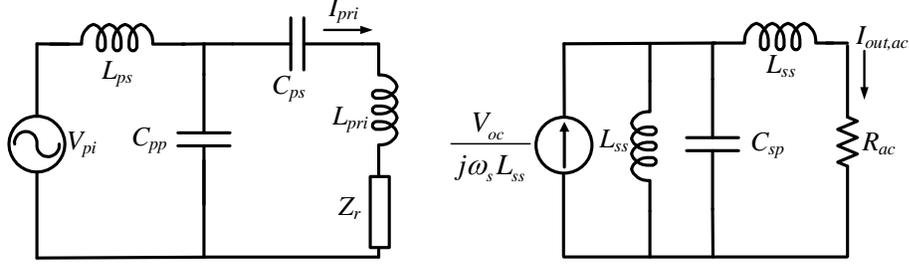
Fig. 2.12: Decoupled primary and source-transformed secondary equivalent circuit.

(2.8) can be also written as a linear function of the primary coil current after substituting (2.4) into (2.8):

$$\boldsymbol{I_{out,ac}} = \frac{\boldsymbol{V_{oc}}}{j\omega_s L_{ss}} = \frac{M}{L_{ss}}\boldsymbol{I_{pri}} \tag{2.9}$$

Furthermore, due to condition (2.8), the input impedance seen by the voltage source $\boldsymbol{V_{oc}}$ becomes resistive at resonant frequency:

$$\boldsymbol{Z_s} = \frac{\omega_s^2 L_{ss}^2}{R_{ac}} \tag{2.10}$$

Thereby, effectively, the system experiences a zero power-factor load. This condition is beneficial for reducing the reactive power rating of the system's primary side. Using (2.4) and (2.10), and referring $\boldsymbol{Z_s}$ to the primary side, the reflected load can be derived as:

$$\boldsymbol{Z_r} = \frac{\omega_s^2 M^2}{\boldsymbol{Z_s}} \tag{2.11}$$

From (2.10)-(2.11), it is evident that at the resonant frequency, $\boldsymbol{Z_r}$, is resistive:

$$\boldsymbol{Z_r} = \frac{M^2 R_{ac}}{L_{ss}^2} \tag{2.12}$$

As has been done at the secondary, the source transformation can be applied at the primary, too, converting voltage source $\boldsymbol{V_{pi}}$ and the series inductance L_{ps} into a current source and a parallelly-connected inductance, as shown in Fig. 2.13.
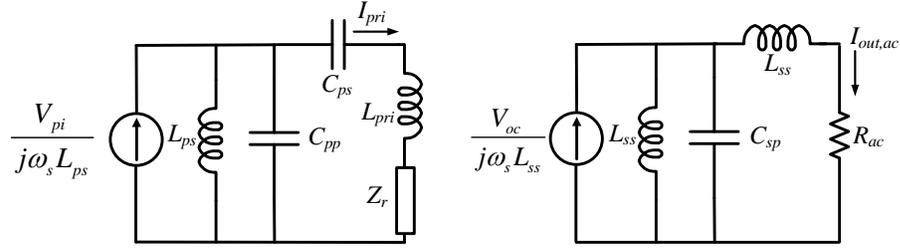
Fig. 2.13: Source-transformed primary and secondary equivalent circuit.

L_{ps} and C_{pp} as selected to be in resonance at the operation frequency as follows:

$$\omega_s L_{ps} - \frac{1}{\omega_s C_{pp}} = 0 \tag{2.13}$$

Consequently, following the source transformation, the L_{ps} is connected in parallel with C_{ps}. This parallelly-connected pair undergoes anti-resonance, effectively operating as an infinite impedance (open circuit) branch. Thereby, the current supplied to the coil is essentially equal to the transformed current source value. From Fig. 2.13, it is evident that primary coil current is independent of the $\boldsymbol{Z_r}$ value. In other words, LCC compensation in the primary results in a load-independent primary coil current, which is a desirable feature for many WPT applications. The expression of the primary current is then:

$$\boldsymbol{I_{pri}} = \frac{\boldsymbol{V_{pi}}}{j\omega_s L_{ps}} \tag{2.14}$$

Also, C_{pp} , C_{ps}, and L_{pri} are selected to be in series resonance:

$$\omega_s L_{pri} - \frac{1}{\omega_s C_{pp}} - \frac{1}{\omega_s C_{ps}} = 0 \tag{2.15}$$

Due to (2.6), the input impedance $\boldsymbol{Z_{in}}$ looking from the voltage $\boldsymbol{V_{pi}}$ becomes resistive,

similar to the secondary case, and thereby a zero-power factor of the total system can be achieved. This condition effectively reduces the VA rating of the inverter. The analytical expression of the input impedance is:

$$\boldsymbol{Z_{in}} = \frac{\omega_s{}^2 L_{ps}^2}{\boldsymbol{Z_r}} \tag{2.16}$$

Combining (2.12) and (2.16), the expression of zero-power-factor input impedance for a tuned primary and secondary compensation network is derived as:

$$\boldsymbol{Z_{in}} = \frac{\omega_s{}^2 L_{ps}^2 L_{ss}^2}{M^2 R_{ac}} \tag{2.17}$$

However, in practical implementations, a slightly lagging power factor is typically preferred. In this scenario, any compensation element could be slightly modified to achieve a lagging power factor condition. The delivered power can be calculated as the active power dissipated by $\boldsymbol{Z_r}$:

$$P_{out} = I_{pri}^2 Re(\boldsymbol{Z_r}) \tag{2.18}$$

Putting (2.2), (2.12) and (2.14) into (2.18), the transferred power for a tuned system is:

$$P_{out} = \frac{8}{\pi^2} \frac{M^2}{L_{ps}^2 L_{ss}^2} \frac{V_{dc}^2}{\omega_s^2} R_{ac} \sin^2(\frac{\phi_p}{2}) \tag{2.19}$$

The expression (2.19) is suitable when the load is modeled as a resistor, (Fig. 2.12(a)). In case the load is a battery, and it is modeled as a voltage source (Fig. 2.12 (b)), then the expression of power can be derived as:

$$P_{out} = I_{out,ac} V_{out,ac} \tag{2.20}$$

where $I_{out,ac}$ could be derived by combining (2.9) and (2.14) as follows:

$$I_{out,ac} = \frac{M\boldsymbol{V_{pi}}}{j\omega_s L_{ps} L_{ss}} \tag{2.21}$$

Substituting V_{out} from (2.2), and I_{out} from (2.21) into (2.20), the expression of output power is obtained as:

$$P_{out} = \frac{8}{\pi^2} \frac{M}{L_{ps} L_{ss}} \frac{V_{dc} V_{bat}}{\omega_s} \sin(\frac{\phi_p}{2}) \tag{2.22}$$

2.4 Bidirectional DPWT System Analysis

Bidirectional WPT (BWPT) systems have been reported in the past for aircraft applications [58], [59]. Since they offer some unique features appealing to EV applications ([31], [60], [61]) BWPT systems have been investigated for EV roadways in addition to the unidirectional counterpart. Fig. 2.14 illustrates a detailed block diagram of a typical bidirectional system for an EV application.
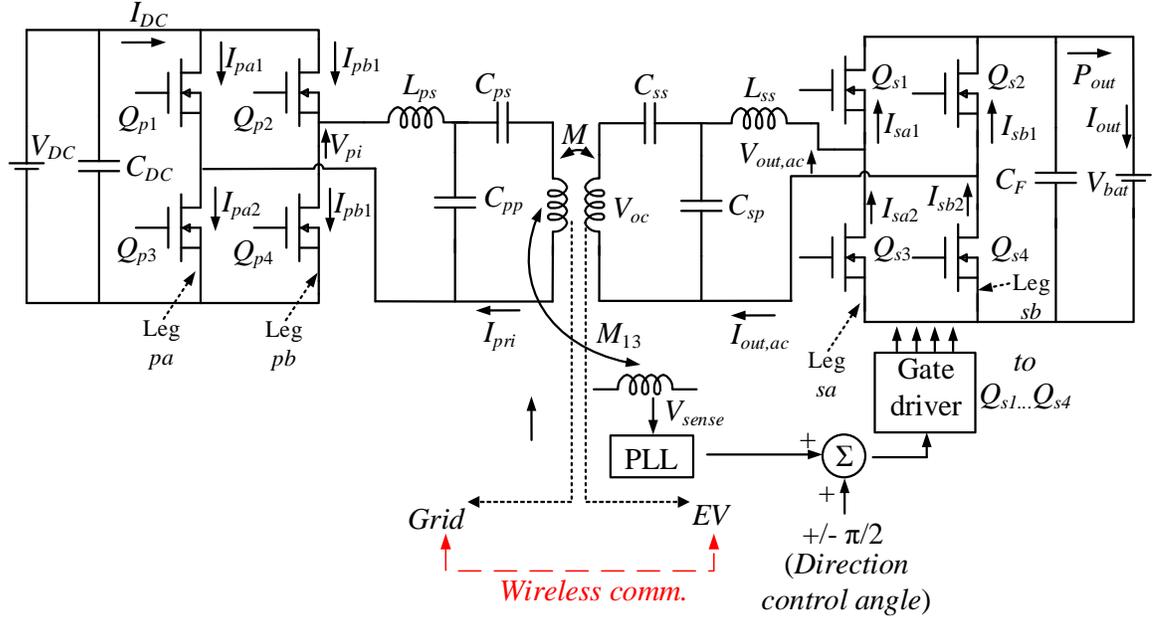
Fig. 2.14: A bidirectional DWPT system circuit diagram.

As can be observed from Fig. 2.14, the circuit structures of bidirectional and unidirectional systems are very similar. For simplified analysis, a constant voltage V_{DC} is adopted as the input of the system. V_{DC} supplies a high-frequency inverter, followed by an LCC compensation network and the primary coil arrangement. At the EV-side, the secondary circuitry consists of an LCC compensator, followed by an active rectifier which is the main difference between unidirectional and bidirectional systems. By controlling the active rectifier, the amount and direction of power transfer can be regulated, which would not be possible with a passive (diode) rectifier at the secondary.

In order to control the power flow direction, synchronization between the primary and secondary operations is needed. A Phase Locked Loop (PLL) and sensing coil arrangement have been proposed recently for primary-secondary synchronization [62]. Fig. 2.14 illustrates the deployment scheme of such an arrangement. Additionally, wireless communication between the grid side and EV side might be deployed to keep both sides coordinated and consequently, set the charging mode (V2G or G2V) and the power level.

A phasor diagram is shown in Fig. 2.15 to illustrate the effect of synchronization on power transfer amount and direction. Here, the locus of the active rectifier input voltage phasor $\boldsymbol{V_{out,ac}}$ at the secondary is drawn with respect to the primary inverter output voltage $\boldsymbol{V_{pi}}$ and induced open-circuit voltage $\boldsymbol{V_{oc,out}}$.
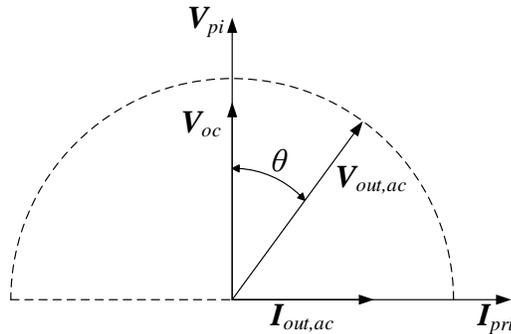
Fig. 2.15: Phasor diagram of voltage and currents associated with BWPT power transfer.

Combining (2.4) and (2.14), it can be shown that $\boldsymbol{V_{pi}}$ and $\boldsymbol{V_{oc}}$ are in phase as follows:

$$V_{oc} = \frac{MV_{pi}}{L_{ps}} \tag{2.23}$$

$\boldsymbol{I_{out,ac}}$ and $\boldsymbol{I_{pri}}$ are in phase, too, as suggested by (2.9). Furthermore, it can be observed from (2.21) that $\boldsymbol{I_{out,ac}}$ lags behind $\boldsymbol{V_{pi}}$ by 90°. Let us assume that $\boldsymbol{V_{out,ac}}$, at a particular load, is lagging by θ with respect to $\boldsymbol{V_{pi}}$. The equation for calculating the transferred power is:

$$P_{out} = Re(\boldsymbol{V_{out,ac}} \boldsymbol{I^*_{out,ac}}) \tag{2.24}$$

Finally, the expression for transferred power can be derived from (2.21) and (2.24) as:

$$P_{out} = \frac{MV_{pi}}{\omega_s L_{ps} L_{ss}} V_{out,ac} \sin\theta \tag{2.25}$$

From Fig. 2.15, it is evident that the active rectifier phase angle θ can be chosen as the variable to control the power flow direction and amount. When $\theta = 90°$, the power transfer is towards the vehicle and (2.25) reduces to (2.22). When $\theta = $ -90°, the power flow direction is reversed with the same magnitude. Finally, when $\theta = 0°$, the power transfer is terminated.

(2.25) describes the operation of the active rectifier in so-called synchronous rectification mode, i.e., where the rectifier legs operate in a complementary manner with a 180° phase shift between them. Alternatively, the phase-shift between the rectifier legs can be controlled in which case the phase-shift angle ϕ_s would serve as an additional power control variable. However, it should be noted that ϕ_s does not have the ability to change the power flow direction since it is limited to 0 to 180° range. Fig. 2.16 shows a representative set of waveforms containing the inverter and the rectifier leg voltages.
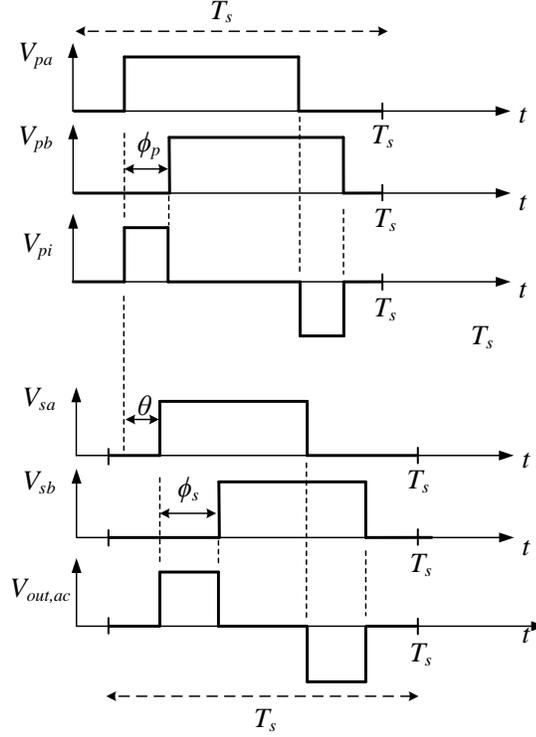
Fig. 2.16: Diagram of the phase-shift-modulated inverter voltages, active-rectifier voltages, showing the synchronization phase-shift angle θ between the inverter and the converter.

The relative position of ϕ_p, ϕ_s, and θ is designated with respect to each other. With the secondary phase-shift control, the modified form of (2.25) becomes:

$$P_{out} = \frac{MV_{pi}}{\omega_s L_{ps} L_{ss}} V_{out,ac,max} \sin(\frac{\phi_s}{2}) \sin\theta \tag{2.26}$$

where $V_{out,ac,max}$ is the maximum value of $\boldsymbol{V_{out,ac}}$ obtained for $\phi_s{=}0°$ (synchronous rectification mode).

A more general form of (2.26) including the phase-shift angle dependence of the inverter output voltage from (2.1), can be expressed as:

$$P_{out} = \frac{8}{\pi^2} \frac{MV_{dc} V_{bat}}{\omega_s L_{ps} L_{ss}} \sin(\frac{\phi_p}{2}) \sin(\frac{\phi_s}{2}) \sin\theta \tag{2.27}$$

From (2.27), it can be observed that either of ϕ_p, ϕ_s, or θ is capable of controlling the output power. However, in practical DWPT implementations, ϕ_p is not typically used for regulating power transfer, as its application would require information about the secondary-side charging states to be the delivered to the primary in real-time. Successful implementation of the primary-side control would require a very fast and reliable communication link to be established between the vehicle and each of TUs, which raises significant reliability concerns. Examples of primary-side and dual-side controls have been reported in the literature about SWPT systems, but not that often for DWPT systems. Instead, ϕ_p is implemented to control the primary coil current and typically maintain it at a preset reference value. Effectively, this decision turns a TU into a regulated current source supplying the primary coils, while the control over the power flow is left to the secondary-side control parameters ϕ_s and θ.

2.5 Summary

A DWPT transmitter unit contains one road-embedded power supply unit and one or more transmitter coil. Similarly, a single EV is considered to be a DWPT receiver unit. The power supply unit processes the grid power to generate high-frequency AC-current in the transmitter coil in order to transmit DWPT power to EVs. The power profile generated at the grid-side by a single DWPT pulse supplied to a single EV depends on coil geometry, vehicle velocity, transmitter coil activation control, distance between successive transmitter coils, etc. Multiple DWPT transmitter units together build up a larger DWPT segment infrastructure. The large-scale DWPT power profile at segment-level is dependent on the number of the vehicle entering and leaving a particular segment at any given period of time, along with the unit DWPT pulse profile. Different shape of the unit-level and segment-level DWPT power profile at the grid-side has been illustrated and compared, and their effect on grid-side DWPT hardware infrastructure has been discussed.

A representative circuit diagram of a single DWPT unit is presented in order to analyze the electrical system in detail. Compensation network tuning and other transformation methods are used, leading to the decomposition of this circuit into simplified equivalent cir-

cuits. Detailed analysis and formulation of transferred power are discussed. Consequently, a bi-directional DWPT system is proposed along with similar analysis, leading to the formulation of bi-directional power transfer. The role of synchronization between the DWPT transmitter and receiver has been analyzed in detail, and the control variables responsible for bi-directional power transfer control is identified.

CHAPTER 3

VEHICLE DETECTION SYSTEM FOR DWPT ENERGY MANAGEMENT

For DWPT applications, it is necessary to have a vehicle detection system capable of detecting the oncoming vehicle and, consequently, communicate the detection information to the Road-Side controller (RSC). In this way, the RSC can control the activation of the respective primary coil so that it is activated only at the time the vehicle arrives (or just about to arrive) on top of it. It facilitates the overall safety of operation, as no harmful magnetic field is projected to the road for indefinite amount of time. Similarly, it would help the system reduce the overall system losses, as the coil is only activated for a short period of time during which the actual DWPT charging takes place. Finally, the vehicle detection system could help any other type of control action that depends on the vehicle detection information to initiate its control strategy effectively.

However, an ideal Vehicle Detection System (VDS) should not only work as a vehicle detection sensor but also have some built-in intelligence to detect the misalignment of the vehicles secondary coil with respect to the primary coil. A minimum set of parameters identified for a VDS to assist successful operation in a DWPT system are identified as follows: vehicle presence at a given place, vehicle lateral-misalignment, and vehicle speed. The RSC can use this misalignment and speed information to adjust the transmitted power accordingly. That way, the vehicle would receive the same average power regardless of its misalignment, as long as the misalignment is within an acceptable range. A comprehensive VDS including all these minimum features is proposed in this chapter. The detection system has been successfully implemented on a DWPT-charged 22-ft electric bus (E-bus) and tested on an outdoor test track in a fully functional DWPT-charging environment. At the end of the chapter, the experimental results for the implemented hardware prototype are discussed and summarized.

3.1 Vehicle Detection Systems: A Literature Review

The concept of vehicle detection on roadways is not as new as DWPT technology itself. Primarily, investigation of vehicle detection methods [63], [64], [65] has been focused on traffic management applications. Recently, vehicle alignment detection systems have been implemented in stationary WPT applications. [66] shows that only 5% of drivers would perfectly align their vehicles with charging pads, which would lead to insufficient and inefficient wireless charging. It makes a detection system necessary for stationary EV charging systems. RF positioning method [67] and frequency tracking method [68], for instance, have been employed for EV alignment. The Society of Automotive Engineers (SAE) surveyed the industry representatives offering seven different alignment techniques, and based on results, identified two as adequate for stationary wireless charging: Low Power Excitation (LPE) and Magnetic Vector (MV) [69]. The LPE technique relies on existing magnetic assemblies on the vehicle and in the road, while the MV method uses auxiliary magnetic coil assemblies for generating and sensing magnetic fields.

For DWPT applications, one possible detection method involves using an RF link between the primary and secondary pads. However, the signal latency and attenuation of the high-frequency signal at the receiver make this method difficult. The authors in [70] considered segmenting the primary coil itself to make a DWPT detection system. Although it has the upside of not involving any additional sensor coils, the detection information is only available after the vehicle leaves the first coil segment. In addition, only one segment could be energized at a time. A three-coil detection system is proposed in [71] where the phase reversal of the induced voltage in the detection coils is used as the detection method. This DWPT detection system does not measure and report the vehicle misalignment/speed information which might be useful for a DWPT controller. To detect the vehicle, this algorithm requires a null-power-point between adjacent coils which may be non-existent in some recent design layouts [72].

As being independent of the charging system, the solution proposed in this chapter can be implemented no matter what the actual DWPT power profile is. Moreover, it would

work as an integral part of the RSC, facilitating an efficient DWPT operation.

3.2 DWPT System Limitations: Review & Proposed Solution

Some of the significant limitations faced by DWPT systems are discussed below, followed by the proposed VDS system description to detect and compensate for those limitations.

3.2.1 Lateral Misalignment (LTM)

DWPT is very sensitive to the alignment between the coils engaged in the energy exchange [73]. The misalignment between coils can naturally occur in the lateral direction with respect to the vehicle's traveling axis. An increase in misalignment leads to increased magnetic field leakage [74], which reduces mutual inductance M and magnetic coupling k between pads. The drop of power transfer happens very fast, proportional to M^2 [52], as the transferred DWPT power can be expressed as:

$$P_{out} = \omega_s \frac{M^2}{L_{sec}} I_{pri}^2 Q_L \tag{3.1}$$

where L_{sec} is secondary coil inductance, and Q_L is the loaded quality factor at secondary. When LTM occurs, those systems operating at the boundary of their power capacity will suffer the reduction in delivered power due to LTM. Vehicle LTM depends on the driver's driving habits, as well as road conditions. A standard deviation of misalignment of s_D=46 cm is measured for an average driver in [75]. In [1], the authors have shown that in this case, the expected received DWPT energy of an average vehicle would decrease by 46% compared to the energy of a perfectly aligned one. Additionally, misalignment can cause detuning of some primary and secondary impedance matching networks [76] and consequently cause an efficiency-drop when transferring the same power compared to an aligned case. To cope with this problem, complex tuning networks integrated into the compensation networks are sometimes used [77].

According to Eq. (3.1), it is possible to use I_{pri}, ω_s, or Q_L to control/regulate DWPT

power. However, in DWPT applications where multiple secondary coils are power by the same primary source, the ω_s is not preffered as the controlling parameter [1]. I_{pri} can be controlled by the variable phase-shift angle of the primary side inverter controller [1], [78]. Similarly, varying the duty ratio of a dc-dc converter at the secondary side can be used as a method to control Q_L [79]. In this way, the nominal power is maintained even when the vehicle is misaligned. This method has the obvious advantage that it does not require a system for LTM measurement. Nevertheless, it retains some serious drawbacks. Q_L is recommended to stay in the range from 3-7 to avoid multiple problems at the secondary. However, to cope with misalignment, Q_L may need to vary in a wide range. For example, to compensate for M reduction of 50%, the secondary would need to quadruple Q_L. Main disadvantages of high Q_L are: (i) high reactive current flowing through secondary compensation network elements causing elevated secondary loss, (ii) VA rating of secondary compensation network elements being proportional to Q_L, and (iii) a detrimental detuning effect that secondary can cause to primary if the secondary reactance is not compensated, as being now scaled up Q_L times. Therefore, Q_L variation is typically applied for a narrow range, fine control of the transferred power, rather than for misalignment effect correction.

These aforementioned methods for controlling DWPT power still suffer from other physical limitations and would work only for a limited LTM range, since there would be a maximum limit on the power electronics beyond which DWPT power can not be delivered. Thereby, in situations of high degrees of misalignments, a preferred method to eliminate the adverse effect of misalignment is to take corrective action by the EV driver who would align the vehicle to track the pads central line while driving. To perform this action, the driver should know the amount and direction of misalignment in real-time. Thereby, a Driver Information System (DIS) would be necessary which would display the LTM value to the driver in real-time. In addition, the actual misalignment information should be calculated and relayed to the driver as timely as possible. As studied in [34], the lateral vehicle acceleration depends on road type and conditions and vehicle type, and it is measured to vary in a broad range from 0.68 to 1.63 m/s^2 for most of the vehicles. If a lateral acceleration

is adopted to be a_L=1 m/s^2, the LTM equal the standard deviation s_D=46 cm would be eliminated in about 0.96 s, as calculated from the following equation:

$$t = \sqrt{\frac{2LTM}{a_L}} \tag{3.2}$$

A timely update of LTM information to the driver is necessary to allow correct decision-making. If it is required that information about LTM should be updated at least ten times during that period, the response of a DWPT-VDS in updating a DIS should be shorter than 96 ms.

3.2.2 Longitudinal Misalignment (LGM)

An LGM is a natural phenomenon that occurs when a DWPT-charged EV transitions from one primary pad to another, as well as before an EV enters the energized section. Similar to LTM, LGM also decreases M in Eq. (3.1), and consequently reduces the DWPT power transfer. Some attempts have been made to design and outline the primary pads in the way to provide a seamless (sag-less) power transfer during the transition [72]. However, it is more common to have periods of very low or no coupling between adjacent pads. To preserve good energy efficiency, all coils should be de-energized during the low coupling intervals, and a selected coil should be energized only when the coupling reaches a prede-termined threshold value. In that case, the RSC should be capable of detecting the vehicle before the secondary is directly on top of the primary coil, and then energizing the primary coil promptly. Attempts have been made to determine the vehicle longitudinal position [78]. If the RSC acquires information about the vehicle speed and if it can track the power de-livery to the secondary, it would be possible to estimate the moment when the next pad will be reached and when it should be energized. Ideally, a speed-measurement capability should thereby be included in a VDS, in addition to LTM measurement.

3.2.3 Operation With Foreign Object

If a metallic object appears on the electrified track at the time of charging, it may

cause a serious safety issue and environmental threat [80]. These objects can absorb energy from the magnetic field generated by the power transmitter, resulting in a parasitic power loss. Apart from reducing the power transfer efficiency, the heating of the foreign object can pose a significant fire hazard. Therefore, a Foreign Object Detection (FOD) system is needed as a part of the VDS to prevent power transfer in these situations.

WiTricity [81] proposes a FOD system employing the inductive detection method that senses power, frequency, current, voltage, etc. measurements to detect a foreign object. Their construction consists of a set of overlapped coils. Non-overlapped coil system for FOD has been proposed in [82] as an improved design for stationary WPT chargers. The Power Loss Detection (PLD) method presented in [83] is cost-effective and simpler as it omits additional bulky elements, such as heatsinks or thermocouples. However, this method is only proved to be effective for low power applications. The quality factor of a secondary coil decreases when a foreign metallic object is present on the primary side, and this can be used as a decisional parameter for a FOD as described in [84]. In general, the FOD solutions found in the literature are suitable for stationary WPT applications and involves activating the primary coil to detect the foreign object, which could still be dangerous. In order to ensure system efficiency, safety, and reliability, an ideal FOD-integrated VDS would, not only detect a foreign object on the road from a distance, but also respond to the objects presence by shutting off the charging immediately.

In addition, some other hazardous road conditions (perceivable to the driver as hazardous in terms of power transfer) might also be generally termed as "foreign object", if it also requires system-shutdown for safety considerations. Thereby, a Driver Feedback (DF) system, capable of causing emergency shutdown by means of drivers emergency signal sent to the DWPT controller, could also be included in the system in order to maintain safe and efficient DWPT operation.

3.2.4   Proposed Solution

In the light of the aforementioned limitations, a comprehensive Vehicular Detection System for DWPT applications (DWPT-VDS), operating on magnetic principles is pro-

posed, developed and optimized as a solution. The following functionalities are integrated into the DWPT-VDS: (i) a vehicle detection mechanism, (ii) measurement of the vehicle's LTM, (iii) vehicle speed measurement, (iv) Driver Information System (DIS), (v) Foreign Object Detection (FOD) System, (vi) Driver Feedback (DF) System. Fig. 3.1 shows the integrated block diagram of the proposed VDS system with the DWPT system.
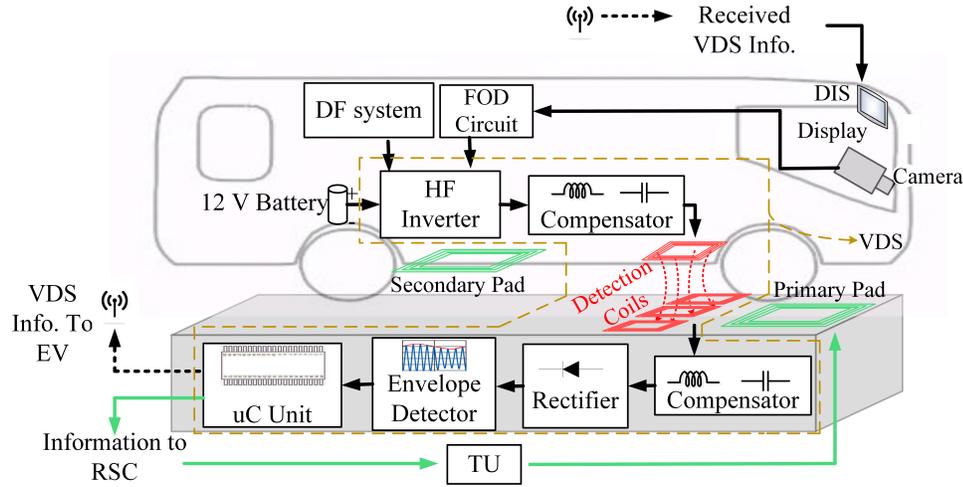
Fig. 3.1: Proposed DWPT system's operational block diagram with integrated DWPT-VDS.

When integrated into a DWPT charging system, the DWPT-VDS allows some critical functions, such as correcting the lateral position of the vehicle by the driver, extending the range of full power reception from a misaligned vehicle, as well as helping the RSC employ smooth-transitioning between adjacent pads. The DWPT-VDS system is designed to be an interoperable solution, capable of coping with variable vertical offsets caused by different vehicle ground clearances. A comprehensive study of different coil structures and algorithms for speed and misalignment estimation in a DWPT-VDS, along with their comparisons, are presented. The objective is to maximize the misalignment detection range for a given size of test coils and provide a robust solution for vehicles with different ground clearances. The reported misalignment information is incorporated within the main DWPT controller which adjusts the DWPT power accordingly so that the vehicle receives a uniform average power irrespective of its misalignment. Furthermore, a DIS visualizing speed and misalignment

information is also developed and tested to help the driver align the vehicle with the road-embedded primary coils. A FOD and a DF system are finally implemented and integrated with the DWPT-VDS to make it ideal for safe DWPT operation on EV roadways.

A *three-coil* DWPT-VDS system for vehicle misalignment and speed detection is selected, designed, and tested as part of a proof-of-concept design. The additional feature of vehicle speed measurement is experimentally demonstrated by the DWPT-VDS, which could be used by the DWPT controller to make time-critical activation decisions. The functionality of FOD and DF systems are also verified. The proposed method can operate equally in different types of DWPT charging systems, irrespective of the power coils type, shape, layout, etc. Although the proposed method is implemented for DWPT systems, it is equally applicable to stationary WPT applications or as part of a traffic detection system in general.

3.3 Vehicle Detection System (VDS) Configuration

The proposed DWPT-VDS system largely consists of two separate hardware components, named as *transmitter circuit* and *receiver circuit*. Depending on their relative location of the transmitter/receiver circuit hardware, two possible configurations for the DWPT-VDS are presented in Fig. 3.2(a) and (b). There are some advantages and disadvantages of both configurations, which are discussed below:

3.3.1 DWPT-RSDS

A detailed block diagram of DWPT-RSDS is given in Fig. 3.2(a). The *transmitter circuit* is mounted on the vehicle, and the *receiver circuit* is embedded in the road. The *transmitter circuit* is mounted underneath the front part of the vehicle (electric bus in this case) while the *receiver circuit* can be positioned in front of, at, or even behind the primary coil. In-depth details of the system hardware description, along with its integration to the main DWPT controller are given in the subsequent section. The operation of a DWPT-RSDS can be described as follows: the magnetic field generated by the transmitter coil (TC) of an approaching EV is sensed by the multiple road-embedded receiver coil (RC)

units, consequently processed to calculate LTM and speed. These pieces of information are immediately used by the roadside controller (RSC) unit to calculate the activation (energizing) time instant of the next primary coil and current reference for the same primary coil so that the nominal power is transferred despite the LTM. At the same time, wireless communication is used to transfer the collected information to the vehicle DIS to be displayed onscreen. The driver, thereby, is offered an alternative to align the vehicle and improve the DWPT performances.
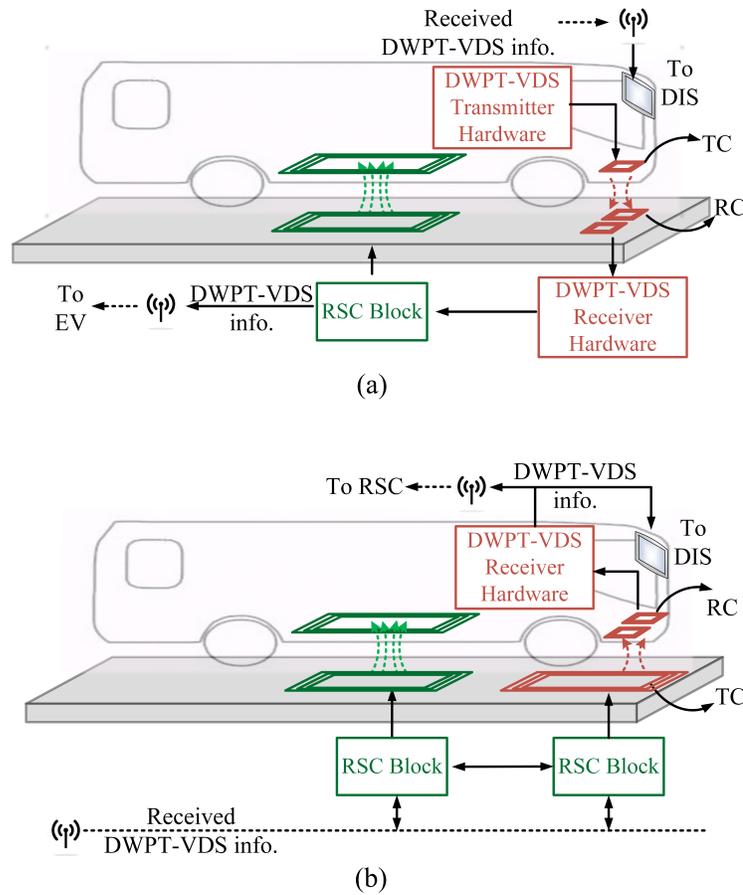
Fig. 3.2: System block diagram of (a) DWPT-RSDS (b) DWPT-VSDS.

The advantages of the DWPT-RSDS solution are multiple. Firstly, the vehicle (driver) in this case, has full control over the transmitter activation. That way, drivers can activate the transmitter unit and make the vehicle visible and susceptible to charging. Alternatively,

they can decide to deactivate it and travel through the electrified roadway section without receiving any power. Additionally, the speed, the presence, and LTM information are collected at the side where their application is time-critical and through a more reliable wired system. Later, they are delivered to the vehicle wirelessly, and as long as that action satisfies the latency criteria mentioned, the driver will be timely informed about the driving conditions. A significant disadvantage of the proposed solution is that it cannot utilize the existing, road embedded coil infrastructure for LTM detection since at least two side-by-side receiver coils are needed for sensing purposes. Consequently, detection units should be periodically incorporated into road-embedded modules, which makes the system more complicated and less reliable. How often a vehicle should be "re-detected", depends on the topology of the road infrastructure and the study of that goes beyond the scope of this dissertation.

3.3.2 DWPT-VSDS

In this configuration, the *transmitter circuit* is embedded underground, and the *receiver circuit* is placed underneath the vehicle (at the front), as shown in Fig. 3.2(b). In this setup, the primary coil itself could be used as the DWPT-VSDS transmitter instead of deploying an additional transmitter coil. In that case, this primary coil would generate the magnetic field, which will be then sensed by the vehicle-mounted receiver unit. Consequently, the DWPT controller would have the role of controlling the DWPT-VSDS. Wired underground communication allows the RSC to determine the moment when it should energize the primary pad for detection purposes. It is expected that DWPT will use different controlling strategy and different frequency when operating in vehicle-detection mode. The processed LTM and speed are delivered to DIS through wired communication and directly displayed on it, whereas the same information is relayed to the RSC via a high-speed RF link. The data are then utilized by the RSC to calculate the coil activation timing and current reference for the immediate next primary coil.

The advantage of this setup is, firstly, the inherent non-invasive nature of the system. The DWPT-VSDS is deployable in existing coil infrastructures without installing any ad-

ditional hardware periodically along the roadway, which entails less system complexity and lower cost. Secondly, since every primary coil can be used as a DWPT-VSDS transmitter, the update of the MLT and speed information is more frequent than in DWPT-RSDS case. Finally, the reliability of DIS is increased due to the wired connection between DIS and the receiver control unit. However, the latency and reliability issue of RF links could hamper the proper operation of RSCs, particularly at high vehicle speeds. Additionally, the vehicle driver does not have full control over detectability of the vehicle on the road, as it was the case in DWPT-RSDS systems.

3.4   VDS System Components

A DWPT-RSDS configuration is chosen for the implementation of the proposed DWPT-VDS system. The system components are discussed as follows:

3.4.1   Transmitter Circuit

The transmitter circuit consists of a high-frequency inverter, a compensation circuit, and a transmitter coil, as shown in Fig. 3.3. It takes its power for operation directly from the vehicle's 12-V internal battery, eliminating the need for an external power source. The proposed full-bridge inverter operates with 50% duty cycle at 95 kHz. The activation/deactivation of the transmitter circuit is dependent on the FOD system's input or through the vehicles Energy Management System (EMS) input. In addition, the driver can provide the same input with the help of a handheld remote clicker. Each of these inputs can switch-off the DWPT-VDS system if needed. The OFF state of the DWPT-VDS would make the vehicle "magnetically invisible" and charging would be prevented. For example, if the battery is full, the EMS might decide to deactivate the detection system and prevent any further charging. Similarly, if the driver perceives some unusual/hazardous situations on the road, he/she might want to deactivate the detection system with the remote control switch and prevent DWPT charging.
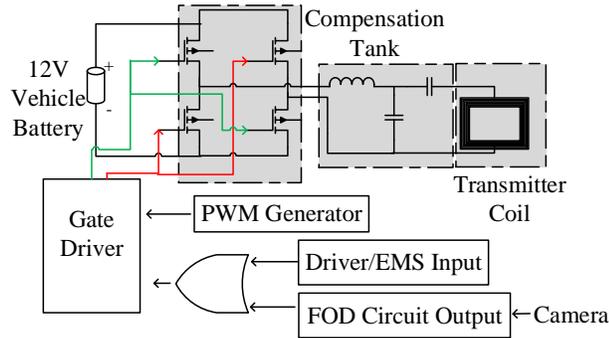
Fig. 3.3: VDS transmitter with integrated FOD and DF input.

The topology of this compensation network is important for efficient system operation. Different types of series and parallel compensation have been proposed in [85]. In [77], the LCC compensation network has been employed. This topology makes the resonant frequency almost independent of the load and mostly unaffected by the coils coupling co-efficient. This topology results in improved LTM tolerance [76], which makes the detection range wider and improves the overall WPT efficiency [86]. Zero-voltage or current switching is also possible with the LCC structure [77] and [87].

3.4.2 Receiver Circuitry

The receiver circuit is shown in Fig. 3.4. It consists of receiver coils, followed by a series capacitive compensation network and a full-bridge rectifier.
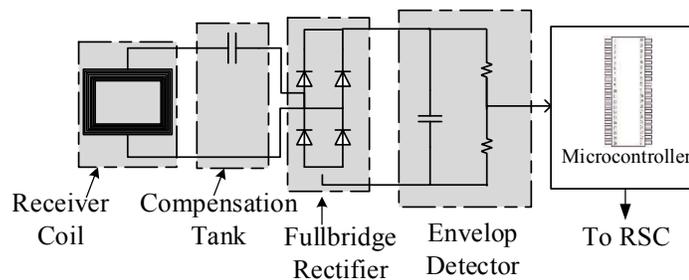
Fig. 3.4: VDS receiver circuitry.

Appropriate values of capacitors were placed at each rectifier output to properly capture

envelopes and reject the harmonic noise without introducing much delay. These envelopes are processed by a microcontroller unit. Finally, the calculated LTM and speed information are sent to the RSC, which controls the power level used to charge the vehicle.

3.4.3 Integrated DWPT Controller

The proposed DWPT-VDS works as an integral part of the DWPT controller (RSC type) implemented in [1], where a DWPT charging system is designed for an E-bus. [1] proposes an optimum, real-time control over the primary coil current, so that the zone of nominal energy transferred to the vehicle is extended for laterally misaligned vehicles, still allowing efficient operation of the system. The controller operation significantly depends on LTM information provided by the detection system, which justifies the necessity of the DWPT-VDS as an integral part of the combined DWPT system. The successful operation of the control algorithm is dependent upon accurate detection of LTM. If LTM is precisely known, it becomes possible to adjust the reference of the primary track current as follows, so that transferred average power is maintained:

$$I_{pri}^* = I_{pri,nom} \frac{M_{max}}{M(f(LTM))} \tag{3.3}$$

where $I_{pri,nom}$ is the nominal value of the primary coil current, and M_{max} is the maximum possible mutual inductance between primary and secondary coil. The control objective is to maintain a constant level of transferred energy regardless of varying LTM. To illustrate, the variation of power-transfer with different misalignment scenarios, given in Fig. 3.5 can be helpful. For a reported LTM value, and assuming constant vehicle speed, the transferred energy can be calculated by integrating the corresponding LTM curve. It is evident that with an increased amount of LTM, the power envelope becomes smaller, causing the transferred energy to decrease. In other words, for higher LTMs, the power transfer must be increased accordingly to fulfill the control objective, which is, to match the maximum transferred energy corresponding to the most aligned case (LTM=0). From Fig. 3.5 and Eq. (3.1), one can calculate the required increase in coil current needed to transfer the same amount of

energy while having a random LTM. This strategy is implemented in the DWPT controller for this application.
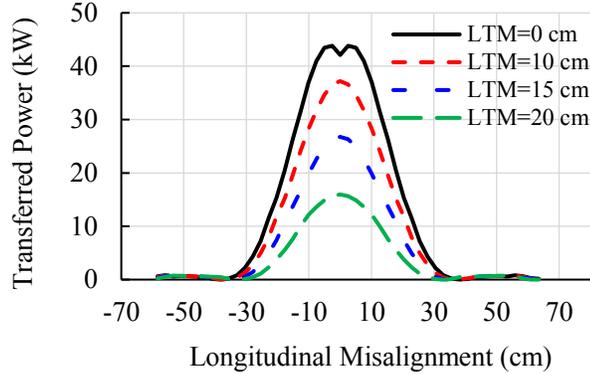
Fig. 3.5: DWPT power profile for various LTMs [1].

As mentioned before, there are two common approaches to regulate the DWPT power to compensate for the reduction of M, namely primary coil current control and secondary duty-cycle control. The proposed current control method is simulated to be more efficient for the circuit in [1] and for the typical range (0.1-0.25) of coupling co-efficient. Finally, the secondary duty-cycle control requires a Buck converter to operate in a wide input voltage range while ensuring the same output voltage, which can affect Buck converters efficiency. Contrariwise, the current control method allows the secondary buck converter to continue operating at the optimum efficiency point.

3.5 VDS System Design Optimization

In order to optimize the size and complexity of the proposed DWPT-VDS system, four different layouts of detection coils are investigated. The configurations are classified as single-coil, double-coil, and three-coil structures. A three-coil structure can be arranged so that the coils are positioned in-line or they form a triangle. The latter layout has the advantage of measuring the vehicle speed at the price of more space occupied in the road. Those four configurations are shown in Fig. 3.6. Rectangular coil shapes are selected over the circular coils to better fit the available space underneath the bus and in the road.
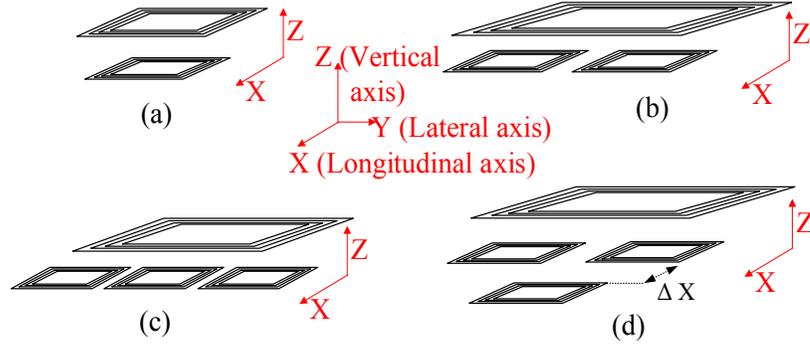
Fig. 3.6: (a) single-coil design (b) double-coil design (c) inline three-coil design and (d) triangular three-coil design.

The envelopes of the signals induced in the detection coils are used as an input to the detection algorithm. Regardless of the selected design or layout, the detected coil voltage envelope for every coil is a bell-shaped curve along the longitudinal axis (x-axis in Fig. 3.6) with a maximum reached when the coils are aligned longitudinally. This makes it easier to make the LTM decision based on the maxima of each signal envelope at the longitudinally aligned point.

3.5.1 Single-coil Design

Fig. 3.6(a) shows the single-coil design. To begin the detection algorithm analysis, the mutual inductance profile between the transmitter-receiver coil needs to be derived. A common approach to calculate the mutual inductance between two current-carrying filaments is by means of Neumann's formula:

$$M = \frac{\mu_0}{4\pi} \int \int \frac{d\boldsymbol{s} d\boldsymbol{s}'}{r} \tag{3.4}$$

where, r is the distance between the line elements $d\boldsymbol{s}$ and $d\boldsymbol{s}$, and μ_0 is the permeability of space. This basic formula could be extended to calculate the mutual inductance between two rectangular coils, such as those shown in Fig. 3.6(a). The derivation of the mutual inductance expression is presented in Section A.1. Using the presented method, the mutual inductance profile between the primary and the secondary detection coil is simulated. The simulation result is shown in Fig. 3.7. The measured detection voltage is directly pro-
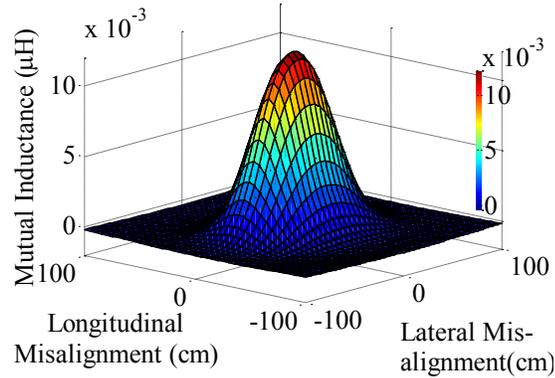
Fig. 3.7: 3D mutual inductance profile of a single-coil design.

portional to the mutual inductance for a constant TC current. Consequently, the mutual inductance profile could be used to develop a misalignment detection algorithm. Depending on the value of mutual inductance, the misalignment could be readily detected. However, if only the individual value of the mutual inductance is used, it might often result in an erroneous misalignment value. The mutual inductance value is sensitive to the vertical offset between the primary and the detection coils. Therefore, if the vehicle ground clearance is varied due to different weight-load conditions, it would change the mutual inductance values that would lead to a wrong result.

Fig. 3.8 shows the mutual inductance profile between the longitudinally aligned transmitter and receiver coils for three different vertical clearances. The three different levels consist of an average vehicle ground clearance and two other clearances at ± 2.5 cm from that level (which represents overloaded and under-loaded vehicle conditions). It is also evident that the same coupling could occur for different clearances, which makes it difficult to accurately measure the misalignment by using a single coil only. Additionally, a single coil could cover only a narrow misalignment detection range. Since the use of a single measured value of M is prone to produce misleading detection information, to make the algorithm less sensitive to height variations, the concept of multiple coils is considered, and the difference between detection signals instead of the actual individual signals is considered as well.
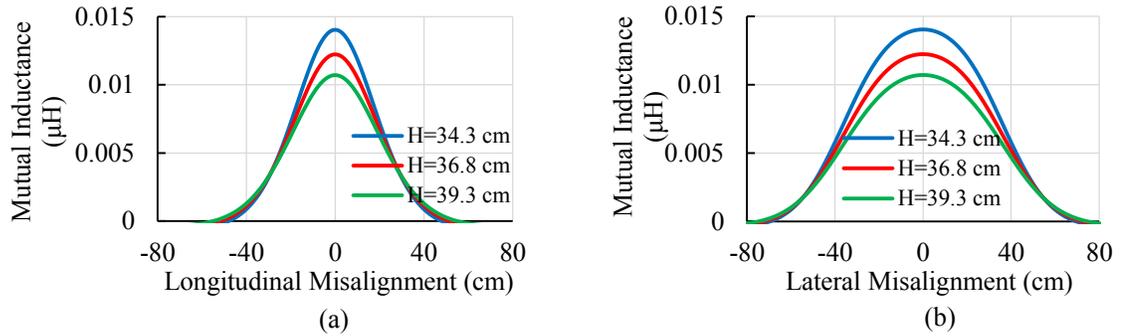
Fig. 3.8: Mutual inductance profile of a single-coil system for three different ground-clearances.

3.5.2 Double-coil Design

Fig. 3.6(b) demonstrates a double-coil system consisting of two identical shaped RCs. The double-coil system could use the mutual inductance difference between two coils to reduce the effect of height variations and other environmental variations. It could also result in a larger misalignment detection range. Fig. 3.9 demonstrates the improvement of using the double-coil mutual inductance difference over the single-coil measurement, by showing that the differential quantity has less variation than the individual quantity.
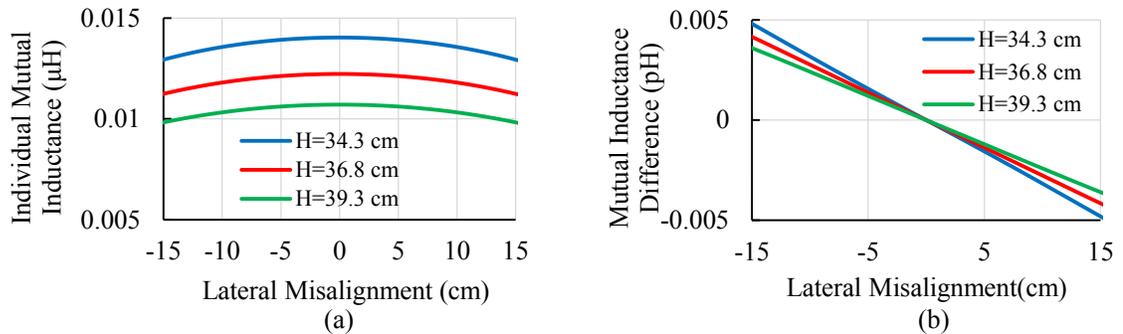
Fig. 3.9: Comparison between the single-coil individual mutual inductance and the double-coil mutual inductance difference variation with ground clearance.

Finding the optimum distance between the two coils to ensure the best detection range and accuracy is of paramount importance. Two extreme cases where the coils are too

close or too far away are illustrated in Fig. 3.10. If the coils are too close, the system would effectively behave as a single-coil system, and the detection range would be small consequently. If the coils are too far, there would be a "dead zone" with an unchanged difference value which cannot be interpreted by the detection algorithm, as there is no change in value with respect to misalignment in the dead zone.
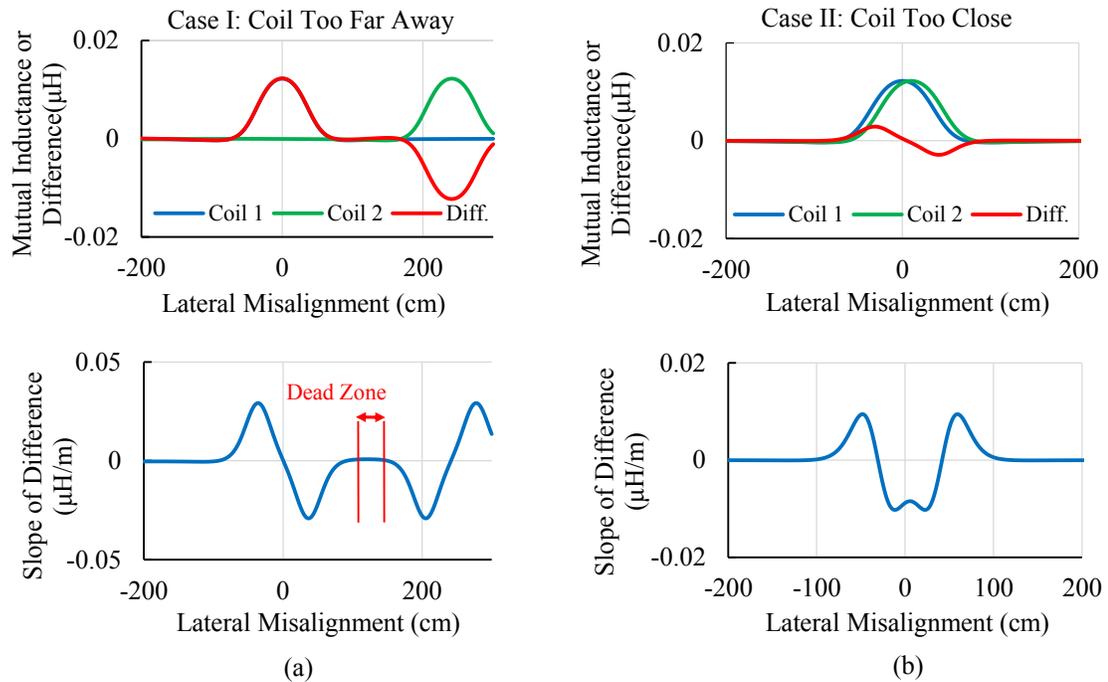
Fig. 3.10: The effect of distance between two coils of a double-coil design.

Low induced voltage values (corresponding to less than 10% of the maximum mutual inductance) could be corrupted by noise and might be hard to detect due to the voltage drop of the rectification diodes, thereby being prone to error. Therefore, a new variable named Field Width W_f is proposed as shown in Fig. 3.11(a). W_f represents the detectable region of the mutual inductance curve. By varying the center-to-center distance between the two coils, it is found that if the coil distance is less than W_f, then there would be no "dead zone". This rule is used as the highest limit of the center-to-center coils distance. In addition, if the coils are directly placed next to each other, the center-to-center distance is equal to coil's width, which sets the lower limit of the allowable distance. The optimum value should be

searched in between these maximum and minimum allowable distance values.
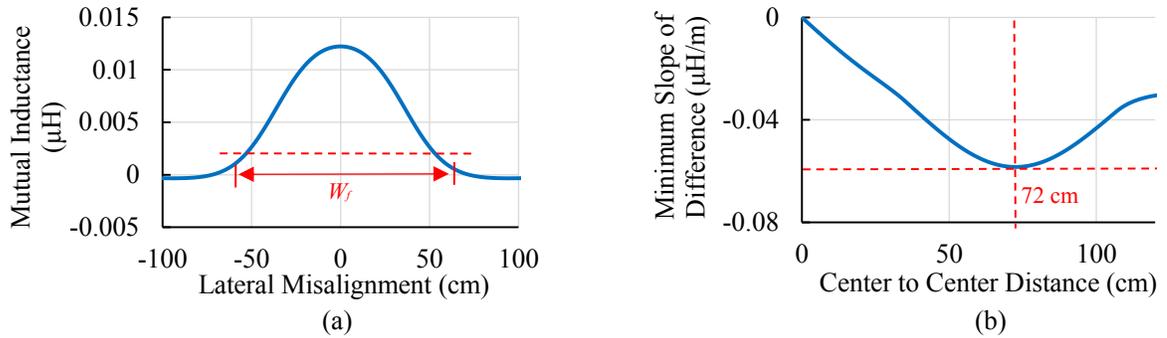
Fig. 3.11: (a) The effective zone for a given mutual inductance profile (b) Optimum operating zone selection for the double-coil system.

For finding out the optimum value and detectable range, the following criteria are chosen:

(i) In the optimum detectable range, the mutual inductance difference value should be unambiguous. That means that there should not be any identical values of the difference in case of two different misalignments. This condition narrows down the maximum possible detection zone to be between the centers of the coils. In addition, as in the W_f explanation, less than 10% of the maximum value cannot be accurately detected. This further narrows the optimum detectable range.

(ii) The mutual inductance difference swing should be maximized on both sides of the misalignment axis. This would ensure that a small change in misalignment would trigger a large change in the difference, resulting in a higher resolution of detection. This optimization could be achieved by varying the coil distance and finding the distance corresponding to the lowest possible minima value of the slope of the difference.

With this criterion, the optimized value of the center-to-center distance was found to be 72 cm, as suggested in Fig. 3.11(b). Fig. 3.12 shows the relative position of the optimum, minimum, and maximum center-to-center distances along with the optimum detectable range which was found to be from -21 cm to +21 cm. With respect to the size of the
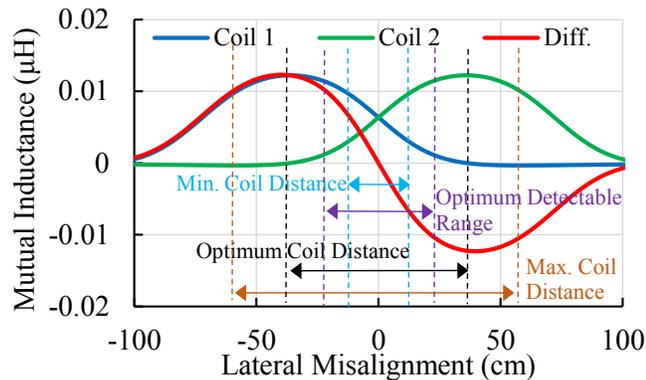
Fig. 3.12: Optimum operating zone location for a double-coil system.

detection coil of 27.6 cm, the optimum center-to-center distance represents about 260% of this width, and the optimum detection range is then approximately 170% of the coil width. These two parameters are scalable with the width of the detection coils, which could be one approach to increase the detection range. Alternatively, an additional detection coil can be used.

3.5.3   Three-coil Design

In order to increase the optimum detectable range, a third coil can be used in addition to the aforementioned double-coil system. Fig. 3.6(c) and (d) show two three-coil systems. The three-coil system could cover a wider area than the two coils, resulting in a wider and more accurate LTM detection range. If the center coil is displaced along the longitudinal axis, it will result in an additional speed detection capability of the design. A design of this type is shown in Fig. 3.6(d).

Fig. 3.13 demonstrates the mutual inductance profile of a three-coil system similar to the one selected for the experimental validation of the detection algorithm. It demonstrates that with a third coil inserted in the middle of the double-coil configuration, it is possible to increase the optimum detectable range in both directions from ±21 cm to ±58 cm. While the LTM is within ±21 cm, the misalignment can still be determined from *Coil 1* and *Coil 3*. However, when either *Coil 1* or *Coil 3* drops below 10% of the maximum in the positive or negative direction, *Coil 2* can be used to measure misalignment. Thereby, in

both directions, the 10% cutoff line of *Coil 2* determines the boundary of optimum detection range. That makes the optimum detectable range of the three-coil system equal to W_f of the central coil. Outside the W_f range, the measured signals can still be used for misalignment estimation, but they would be prone to variable vertical offset error, as explained in the case of single-coil design.
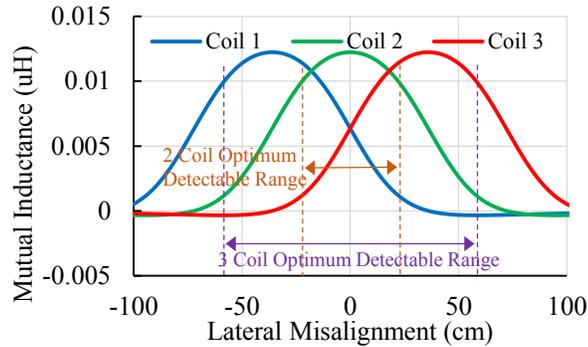
Fig. 3.13: Lateral mutual inductance profile for the three-coil system.

3.6   Simulation Results

After choosing the three-coil RC configuration for a DWPT-RSDS, a simulation model using ANSYS-MAXWELL was built to investigate the systems electromagnetic profiles more accurately, as shown in Fig. 3.14(a). The simulation output is shown in Fig. 3.14(b) where the lateral M profile for zero longitudinal misalignment is plotted.

(a)   (b)
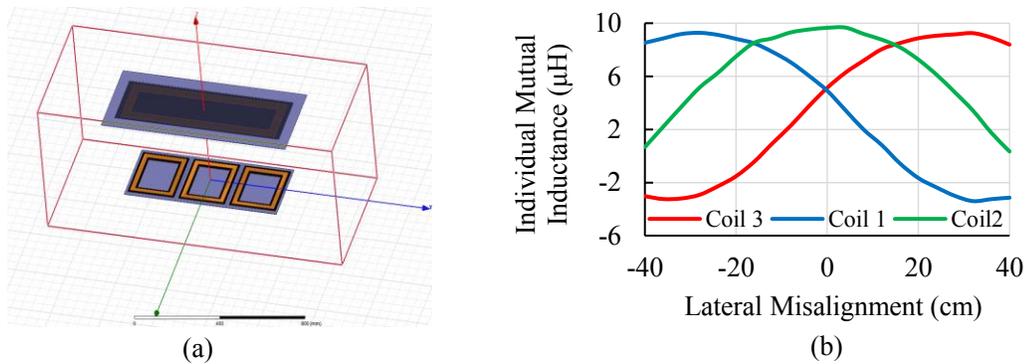
Fig. 3.14: (a) FEM simulation model of the three-coil detection system (b) Simulated lateral axis mutual inductance profiles.

Finite Element Method (FEM) is employed by the simulation model to model all aspects of the final design (adjacent detection coils, shielding metal plate, ferrite plates for field-shaping, and the number of turns deposited in a flat pattern). Those Maxwell simulation results were further incorporated into a MATLAB/Simulink model to simulate the electrical system in detail. For simplification purposes, the simulation is performed for a constant vehicle speed of 40 km/h. Fig. 3.15 summarizes the three coil voltages.
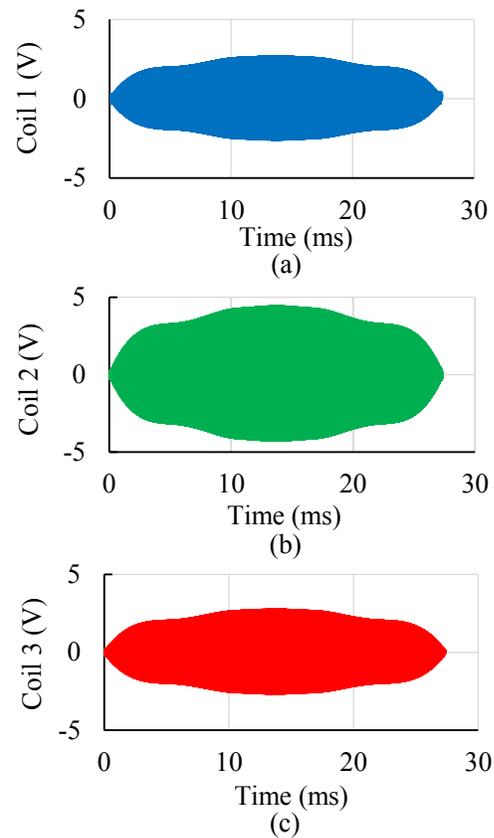
Fig. 3.15: MATLAB simulation results showing the detected coil voltages.

In the practical implementation, these voltage signals are further processed by the envelope detector and microcontroller unit to implement the detection algorithm; detected coil-voltage envelopes are shown in Fig. 3.16.
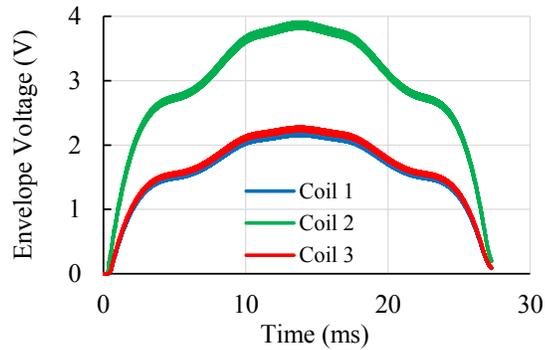
Fig. 3.16: Simulated coil voltage envelopes of the RCs.

3.7   Experimental Results

In this section, the implemented VDS setup and its integrated operation with a 25-kW DWPT system is discussed in detail.

3.7.1   DWPT-VDS System Hardware Setup

The transmitter circuit containing the inverter and the compensation network is mounted in a waterproof box. Fig. 3.17 shows the interior and exterior part of this mounting box, and the transmitter coil TC. The TC is sealed in a plastic enclosure and mounted underneath the bus along its central axis.

Fig. 3.17: Transmitter circuit hardware, and TC structure.

The receiver circuit is shown in Fig. 3.18 is designed to be embedded in the roadway, and it is mounted underneath the RC structure. The three-coil RC structure is mounted on a plywood board. The receiver coil and circuitry is contained in a waterproof box as shown in Fig. 3.18. Table 3.1 lists the system specifications for the implemented DWPT-VDS.

Fig. 3.18: Receiver circuit, and RC structure

Table 3.1: DWPT-VDS system specifications

System parameter	Value
Supply voltage	12 V
Operation frequency	95 kHz
TC current	1 A
TC Litz wire specification	5/5/28/40
TC number of turns	20
TC Mean Lenghth per Turn (MLT)	170 cm
TC outer dimension	75 cm x 20 cm
RC Litz wire specification	20/44
RC MLT	91.4 cm
RC outer dimensions	26.7 cm x 21.6 cm
RC number of turns	45

The existing DWPT charging system of the E-bus operates at a 20-kHz operation frequency. A proper selection of the VDS system's operating frequency is needed for efficient operation. To avoid interference between the two systems (including the impact of harmonics), the operation frequency of the detection system should be positioned far from the DWPT frequency. The frequency sweep characteristics of the TC is shown in Fig. 3.19 reveals that the coils ESR (Equivalent Series Resistance) increases with frequency, causing the coil's quality factor to drop eventually. To ensure an acceptable efficiency while being reasonably far from the DWPT frequency (20 kHz), the VDS operating frequency is chosen to be 95 kHz (at the position of $95/20 = 4.75^{th}$ harmonic), to ensure that it does not

significantly interfere with the DWPT system.
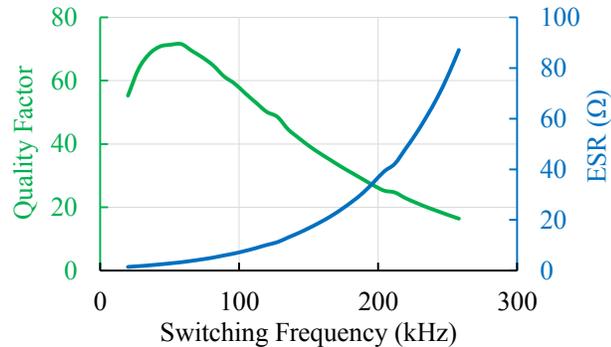
Fig. 3.19: VDS TC characteristics.

3.7.1.1 LTM Detection

After building the hardware setup as discussed, the coils'-characterization considering different misalignment conditions is carried out by measuring the induced coil voltages, which are proportional to the coils mutual inductance. The height/ground-clearance H between the TC and RCs was kept equal to what would be the actual clearance in road condition when the system with the secondary coils is buried in the road. The interpolated voltage curves of the three-coil system are shown in Fig. 3.20. The points are measured along the lateral axis, both positive and negative, with zero longitudinal misalignment between TC-RC structure. As one can see, each coil has a bell-shaped voltage profile with a peak corresponding to the perfect alignment between that RC and the TC. Since *Coil 2* is perfectly aligned with the TC at zero LTM, it has a peak at that point. In order to determine LTM, the voltage profile is divided into four regions, as shown in Fig. 3.20. These regions were determined by observing where the voltage curves crossed each other. Now, it could be determined which section the system is operating in, by simply subtracting the coil voltages from each other. This method allows for faster computation and higher accuracy. Once a region is determined, the voltages are used to determine the exact LTM. To get high accuracy, the line with the highest and steady slope was used in each region. In Region I, the voltage difference between *Coil 2* and *Coil 1* is used. Regions II and III

use the difference between *Coil 1* and *Coil 3*. In Region IV, the voltage difference between *Coil 2* and *Coil 3* is used. All characterization results are incorporated into the detection algorithm.
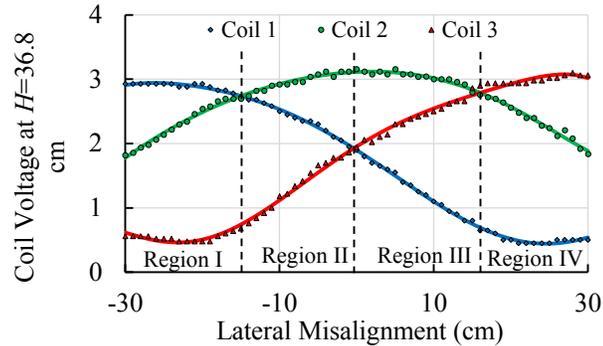
Fig. 3.20: Lateral voltage profile for the three-coil system obtained experimentally (dots) and interpolated curves (lines) with 1-cm resolution.

Fig. 3.21(a) highlights the relative location of main DWPT pads with respect to the RC structure. For proper operation, the vehicle should be driven over the RCs first and then the primary coil, which is ensured in this setup.
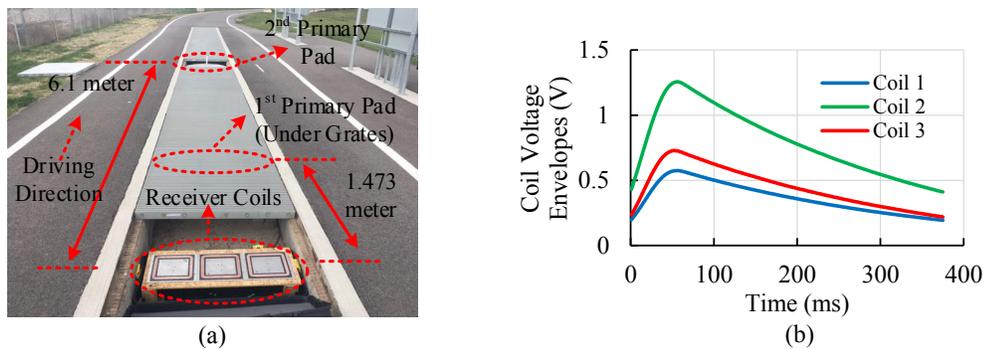
Fig. 3.21: (a) DWPT-VDS RC setup and primary coils installed in the road (b) The detected voltage envelopes of the RCs when the bus is moving at 24 km/h.

An example of RC envelope voltages detected by the microcontroller is shown in Fig. 3.21(b). The effect of vehicle height on the detection system was investigated, as well. Fig. 3.22 shows two different height levels H and associated induced voltage curves. It is

observable that the lower the height, the higher the induced voltage become.
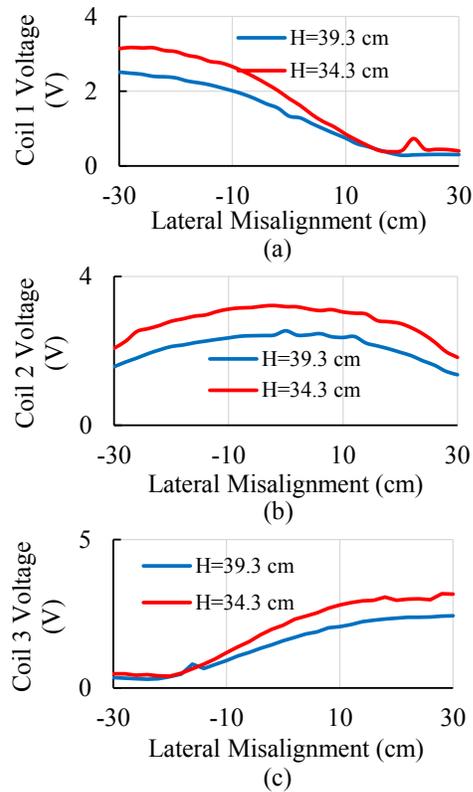
Fig. 3.22: Effect of different heights on induced coil voltages.

Upon installation on the bus and under the roadway, the system was tested. Using a step size of 2 cm, the LTM is tested for ± 30 cm from the centerline. This range was determined to be sufficient for this application. This test is done for different ground clearances (emulated by detection coils lifting or lowering instead of loading the bus), and the results are summarized in Table 3.2. The system reports an average absolute error of 0.0645 cm for nominal clearance. When the mechanical load changes, the clearance also changes. For a ± 2.5 cm variation of clearance, the reported misalignment error is observed to be roughly restricted within 1 cm.

Table 3.2: Experimental result of DWPT-VDS setup

Experimented LTM range (cm)	Misalignment step size (cm)	Ground clearance (cm)	Mean absolute error (cm)	maximum error (cm)
-30 to +30	2	34.3	1.0323	2
-30 to +30	2	36.83	0.0645	1
-30 to +30	2	39.37	0.6452	2

3.7.1.2 Speed Detection

To test the speed detection capability, the three-coil system arrangement requires slight modification. As shown in Fig. 3.6(d), the central coil of the three-coil arrangement is offsetted by a known value of ΔX. The central coils displacement plays a vital role in the speed detection algorithm. This displacement would lead to a delay in the captured voltage envelope of the central coil. Searching for the peaks of all three voltage profiles, the time delay of the central coil to reach its peak with respect to the other two coils peak voltages are sensed and recorded by the DWPT-VDS algorithm. With the known displacement (Δs=25.4 cm) and recorded time delay Δt (in ms), the calculated speed can be expressed as:

$$v[km/h] = 36\frac{\Delta s[cm]}{\Delta t[ms]} \tag{3.5}$$

Fig. 3.23 (a) shows the modified coil structure to add the speed detection capability to the DWPT-VDS. In this scenario, the central RC was displaced by 25.4 cm in the longitudinal direction. Fig. 3.23 (b) illustrates the captured voltage envelops and Δt, observed by the DWPT-VDS for the corresponding testing scenario. After detection, the calculated speed is displayed on a DIS display. The experimental results are shown in Section 3.7.4.
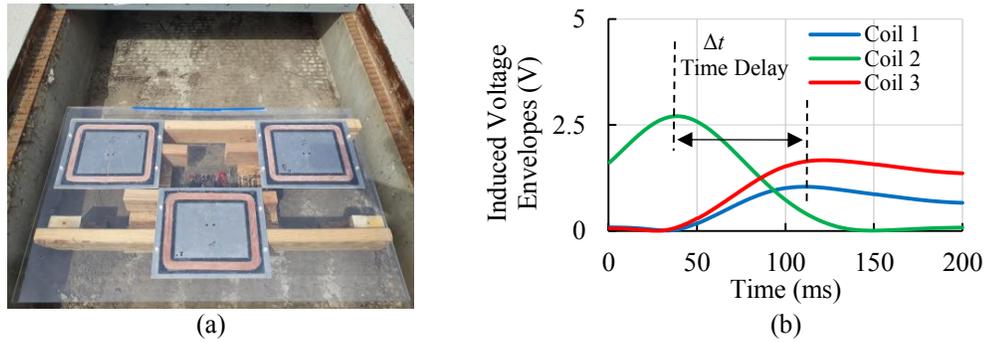
Fig. 3.23: (a) Three-coil DWPT-VDS setup for additional speed measurement capability (b) Detected RC voltage envelopes for the setup.

3.7.2 Integrated Operation of DWPT-VDS and RSC

The proposed DWPT-VDS system's functionality is tested in conjecture with an integrated RSC [1]. The nominal value of the primary current is selected to be 75 A such as the vehicle can receive nominal power at the most aligned case. The highest coil current value of 100 A is set by the hardware limitations. Fig. 3.24 (a) shows the current reference generated by the controller at various LTM. The primary currents correction ensures a 30% increase in transferred energy for the system presented in [1]. Fig. 3.24(b) depicts the improvement of transferred energy with the controller. It is evident that, when the vehicle is perfectly aligned, the transferred energy with the controller is equal to the energy transferred while there is no controller in action.
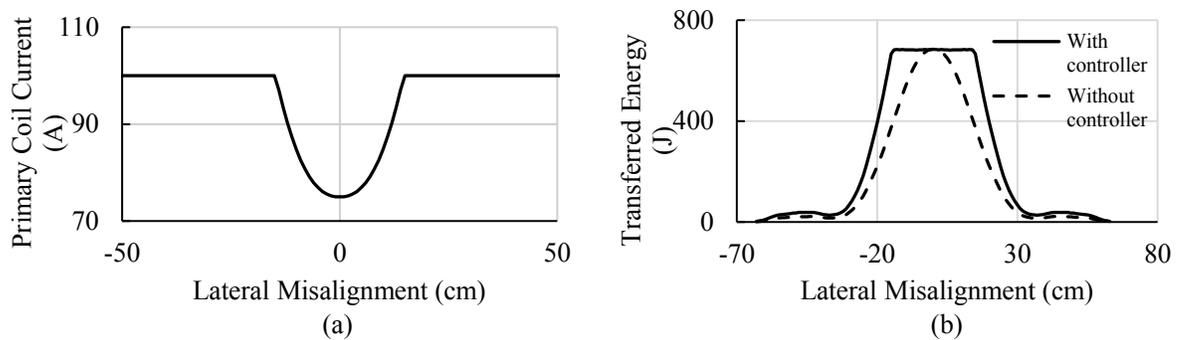
Fig. 3.24: (a) The primary coil current reference as a function of LTM (b) Energy-transfer comparison with and without the controller [1].

It is evident from Fig. 3.24(b) that the DWPT control algorithm significantly improves the transferred energy at higher LTM scenarios, thereby adapting the real road scenarios intelligently. By providing accurate misalignment information, the proposed DWPT-VDS system thereby contributes to the efficient operation of the DWPT system.

3.7.3 FOD System Performance

The FOD system detects selected types of foreign objects on the track from a distance using high-speed image processing, and transfers the detection information to the VDS-transmitter. The probabilistic Hough Transform [88] is applied by the image-processing unit to detect the charging lane borders in real-time. Consequently, foreign objects on road surfaces inside the charging lane are detected with 1-D Haar Wavelet Spikes [89], [90]. The details of the FOD algorithm is presented in [91], and is beyond the scope of this dissertation.

Fig. 3.25(a) shows the FOD system hardware unit. The FOD system consists of four Raspberry Pi (RPi) 3 Model B ARMv8 1GB RAM computers. An "RPi Camera Board v2" is attached to the master RPi computer (via the white camera cable shown in Fig. 3.25(a)), that is mounted on the bus windshield. Fig. 3.25(b) shows the experimental setup of FOD system mounted on the E-bus.

Fig. 3.25: (a) FOD system hardware (b) FOD system experimental setup mounted on the E-bus.

In principle, FOD accuracy increases with numbers of Central Processing Units (CPUs)

in that each CPU can be responsible for detecting specific features in smaller regions. However, higher CPU numbers require more power, better heat management, and packaging; it would also increase communication overhead. The current architecture processes 10 frames per second which is considered adequate for this given application.

Fig. 3.26 shows the FOD system performance where captured oscilloscope snapshots of the FOD system are summarized. Upon image-processing and subsequently detecting the foreign object, the FOD system outputs a digital signal (blue). This digital signal turns off the DWPT-VDS transmitter's gate driver (Fig. 3.3), and the TC-current (yellow) goes to zero. As a result, no RC voltages are detected at the receiver side, and effectively the vehicle is "invisible" to the DWPT-VDS and consequently, the DWPT system. After passing the object, the digital pulse gets automatically removed by the FOD system, which re-enables the DWPT-VDS. The DWPT-VDS output is directly connected to DWPT controller as an input to switch the DWPT charging ON/OFF.

(a)   (b)
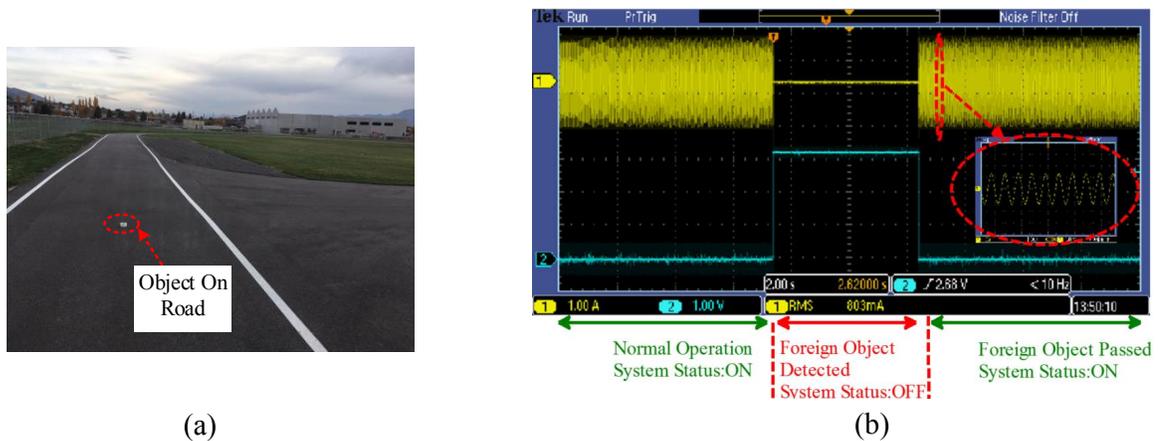
Fig. 3.26: (a) Foreign object on road and (b) corresponding signal detected at the hardware.

3.7.4   DIS Performance

Two XBEE wireless transceivers are installed at the RSC and the vehicle in order to create a wireless network to keep the driver informed about the measured DWPT-VDS information in real-time. The LTM and speed information are wirelessly transmitted (over

ZigBee protocol) and showed on a DIS display. The DIS display is placed beside the driver's seat. The default screen is shown in Fig. 3.27(a). The green line represents the center axis of the vehicle lane. In addition to displaying speed and misalignment information, the DIS also instructs the driver to move toward the center axis, thereby help to achieve the best alignment between primary and secondary coils. To illustrate, Fig. 3.27(b),(c) shows two cases of possible situations. In Fig. 3.27(b) case, the vehicle is misaligned towards the right, and consequently, the DIS displays an arrow pointing towards left, instructing the driver to go left to achieve full alignment. Similarly, in Fig. 3.27(c), the vehicle's LTM is in the opposite direction, resulting in a flipped direction of the arrow. The length of the arrow is proportional to the degree of misalignment as shown.

(a) (b) (c)
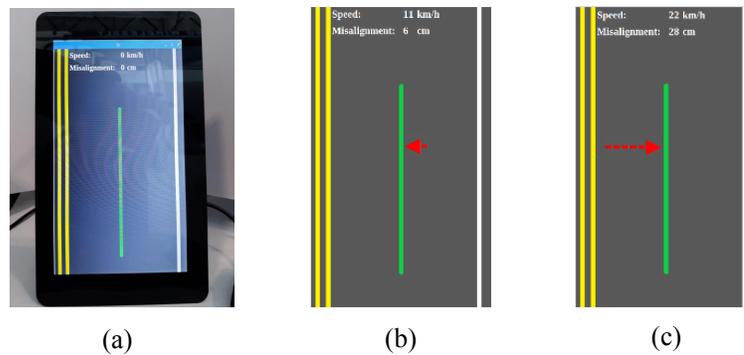
Fig. 3.27: (a) DIS display (b) Illustration of DIS operation assisting a driver to align the vehicle. The driver is informed to correct trajectory by 6 cm toward left (c) Similar scenario when the DIS suggests the driver to move 28 cm toward the right.

Fig. 3.28 depicts the testing scenario where a 25-kW DWPT-charged E-bus is being driven on the charging track, and the DIS is reporting the misalignment and speed while simultaneously instructing the driver to move towards the zero-misalignment (green) axis.
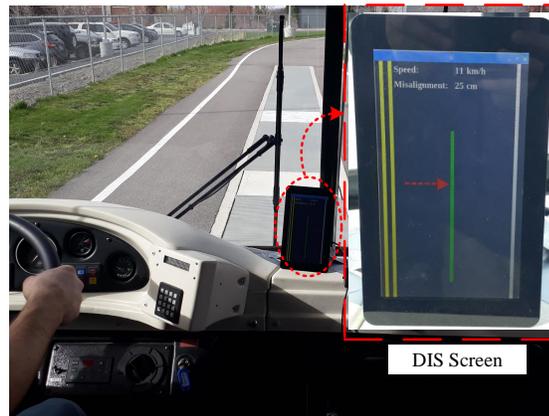
Fig. 3.28: Experimental setup of a DIS display on a 25-kW DWPT-charged E-bus in DWPT environment.

3.7.5   DF System Performance

For utilizing driver's feedback, an off-the-shelf handheld clicker is used to wirelessly transmit the driver's decision to the DWPT-VDS, in order to stop/start the DWPT charging. Fig. 3.29 shows the driver's remote clicker. Table 3.3 shows the various operating scenario of FOD and DF unit output, as well as resulting DWPT-VDS status. When either of FOD or DF signal wants to disable the DWPT-VDS system, the DWPT charging is automatically disabled.

Fig. 3.29: Driver's remote clicker.

Similar to the FOD input, the driver's input is taken as an enabling input to the

Table 3.3: DWPT system output with different FOD and DF signals

DF input	FOD System's input	DWPT-VDS and DWPT charging status
Charge	FO detected	Deativated
Charge	FO not detected	Activated
Stop	FO detected	Deativated
Stop	FO not detected	Deativated

DWPT-VDS transmitter's gate driver (Fig. 3.3). Consequently, similar waveforms as in Fig. 3.26(b) are produced when the driver decides to use the handheld clicker to deactivate the DWPT-VDS, and consequently, terminate the DWPT charging. The only difference between FOD and DF input is that the FOD signal is cleared automatically after passing the foreign object whereas the DF signal must be cleared manually in order to resume DWPT charging. The reason behind this is safety considerations. For example, if the driver thinks that the roadside conditions are not safe to charge, it should also be up to him/her to decide when it is safe to resume charging. In the case of a foreign object, the FOD system is intelligent enough to do that automatically.

3.7.6 Summary

An intelligent Vehicle Detection System (DWPT-VDS) for vehicle lateral-misalignment and speed detection in a DWPT system is proposed. The number of detection coils has been optimized with the objective to extended the detectible misalignment range and to achieve an accurate estimation that is immune to vehicle's ground-clearance variations. An optimized three-coil detection system is implemented, in conjunction with an existing DWPT-charged E-bus system. The reported misalignment information has been used to adjust the DWPT power level, and that way to compensate for vehicle misalignment. A triangular arrangement of the three detection coils is explored and tested in order to attain speed measurement. Moreover, a Driver Information System (DIS) is employed to display the DWPT-VDS information, suggesting the driver to take corrective action, if needed, and align the vehicle with the road-embedded charging pads. In addition, a Foreign Object Detection (FOD) system is implemented to safely and immediately terminate DWPT-charging

in case of the existence of harmful foreign objects is detected on the charging track. Finally, a driver-or-EMS-initiated shutdown of DWPT is also implemented and tested as a safety/protection feature. Robust DWPT-VDS system performance with an integrated DWPT controller is observed with satisfactory accuracy.

CHAPTER 4

GRID-SIDE ENERGY MANAGEMENT FOR EV-DWPT APPLICATIONS

DWPT charging of EV results in an inherently-transient power profile at the grid side. These transient profiles could potentially hamper the grid stability and regulation, especially in peak hours. In this chapter, this grid-side issue of DWPT charging on EV roadways is addressed. A DWPT system is proposed in Section 4.1 which, with the help of a grid-side *energy buffering unit*, reduces the peak transient power observed at the grid side while simultaneously ensuring fully-rated power transfer to the EV. The proposed energy buffering unit can be actively controlled by the grid-side inverter without requiring additional power electronics. The detailed analysis of the inverter operation in order to actively control the energy buffering unit is presented in Section 4.2. Section 4.3 describes the sequence of the operating phases the system undergoes before, during, and after a DWPT power cycle. Section 4.4 presents a method of optimally designing/selecting the energy buffering unit parameters for a given application. The system's controller structure and its design method are discussed in detail in Section 4.5. Section 4.6 presents the simulation results of a 25-kW DWPT system is built in a MATLAB Simulink environment to evaluate the performance of the proposed system. The system's performance is simulated and compared with a conventional DWPT system (of the same power rating) in order to prove the effectiveness of the proposed grid-side energy management. Section 4.8 discusses the development of a downscaled hardware prototype built to experimentally validate the proposed control method. The experimental results with the proposed control method are presented and compared with the results when the same system is operated conventionally (i.e., without the proposed controller). From the comparisons, the effectiveness of the grid-side energy buffering method is experimentally validated. Section 4.9 discusses the summary of the work presented in this chapter.

4.1   Proposed System Structure

Fig. 4.1 depicts the proposed topology of the DWPT system for grid-side energy management. DC voltage V_{DC} is the part of the DC grid network supplying a series of similar systems, while the DC power is obtained from a renewable DC source or rectifying an AC grid voltage, as explained in Section 2.2. By ensuring that this DC bus is protected from WPT high-frequency power pulsations, it would be ensured, in turn, that the AC or DC grids are effectively protected. The proposed system is designed to have the capability to protect grid from power pulsations without requiring any additional converter at the primary side.
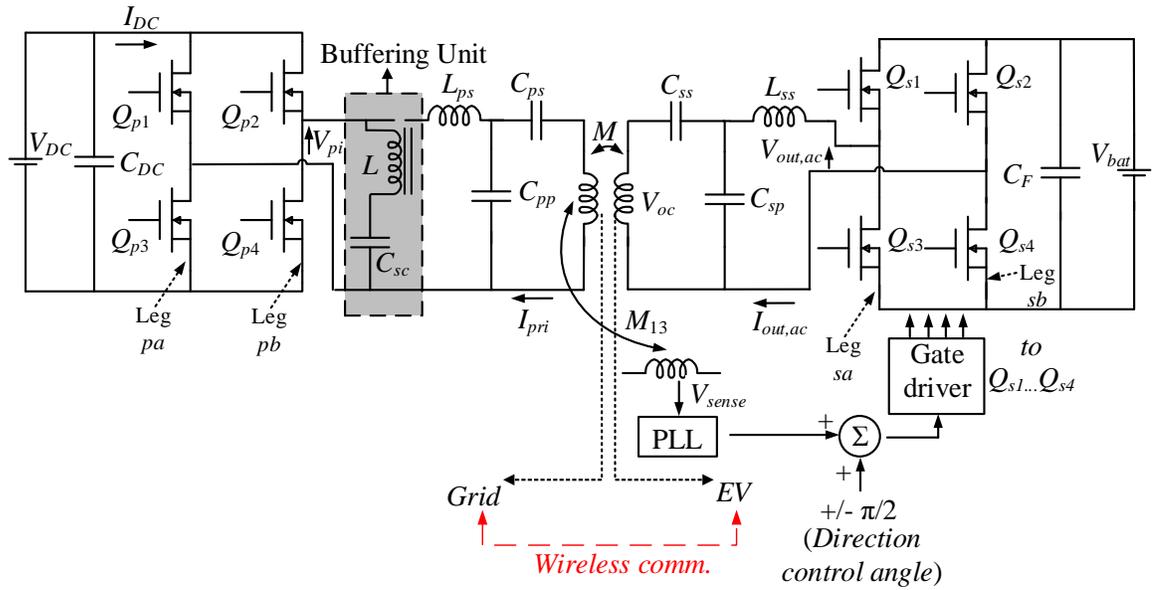
Fig. 4.1: The proposed DWPT system for grid-side energy management in EV-charging infrastructure.

To accomplish the minimal converter requirements, an additional circuit block, called a buffering unit is placed in between the H-bridge and the primary-side compensation network, as shown in Fig. 4.1. This circuit block consists of a current smoothing inductor L and a supercapacitor C_{SC}. Working together, the elements act as a unit offering roadside storage and energy buffering, given that inverter switching is controlled intelligently. The

components are chosen in such a way that the LC branch containing L and C_{SC} provides high impedance at all system harmonic frequencies except for the DC component of the inverter output voltage V_{pi}. Although similar type of circuit block has been proposed in [25], where it has been employed to protect the EV battery from DWPT power pulsations, the proposed topology is different is some fundamental aspects. For example, proposed topology does not require the use of a bypass capacitor, which reduces cost and improves efficiency due to the Equivalent Series Resistance (ESR) associated with the bypass capacitor. Also, in this system architecture, the proposed topology works with LCC compensation, as opposed to parallel compensation presented in [25]. Capacitors C_{pp} and C_{ps} ensure that the primary coil does not contain any DC current component which would have no contribution to the power transfer and also would require an oversized coil.

4.2   Grid-side Inverter Control Analysis

In order to accomplish the design goals, the primary-side inverter will be switched appropriately to work as a converter, or inverter, or both. In other words, V_{pi} will have AC or DC components, or both. In order to establish a mathematical background to understand this operation, the Fourier analysis has been carried out to calculate the inverter output voltage V_{pi}. The analysis results in both zero-frequency and AC harmonic components. Starting with a generic analysis, the generic Fourier expression $f(t)$ of a periodic signal with a fundamental angular frequency $\omega = 1$ is:

$$f(t) = \frac{a_0}{2} + \sum_{n=1,2,..}^{\infty} (a_n \cos nt + b_n \sin nt) \tag{4.1}$$

, where n is the order of signal harmonics and an and bn, are the Fourier coefficients. Let us consider an inverter leg that operates at a duty cycle D, supplied by a DC voltage V_{DC}. For this case, the Fourier coefficients can be represented as:

$$a_n = \frac{1}{\pi} \int_0^{2\pi D} V_{DC} \cos nt\, dt$$
$$b_n = \frac{1}{\pi} \int_0^{2\pi D} V_{DC} \sin nt\, dt \tag{4.2}$$

Solving (4.2), the coefficients can be calculated as:

$$a_0 = 2V_{DC}D$$
$$a_n = \frac{V_{DC}}{n\pi} \sin 2n\pi D \tag{4.3}$$
$$b_n = \frac{V_{DC}}{n\pi}(1 - \cos 2n\pi D)$$

Substituting (4.3) in (4.1), the Fourier representation of a single inverter leg is calculated and simplified as:

$$f(t) = V_{DC}D + \frac{2V_{DC}}{n\pi} \sum_{n=1,2,..}^{\infty} [\sin n\pi D(1 - \cos n\pi D)] \tag{4.4}$$

Now let us consider two inverter legs pa and pb are switching with a fundamental switching frequency of ω, but with different duty cycle D_a and D_b. Furthermore, let us consider there is a phase-shift of ϕ_p between the two legs. After substituting these conditions in (4.4), the inverter leg voltages can be calculated as:

$$V_{pa} = V_{DC}D_a + \frac{2V_{DC}}{n\pi} \sum_{n=1,2,..}^{\infty} [\sin n\pi D_a \cos(n(\omega t + \phi_p) - n\pi D_a)] \tag{4.5}$$

$$V_{pb} = V_{DC}D_b + \frac{2V_{DC}}{n\pi} \sum_{n=1,2,..}^{\infty} [\sin n\pi D_b \cos(n\omega t - n\pi D_b)] \tag{4.6}$$

The inverter output voltage is simply the difference between the two leg voltages, as follows:

$$V_{pi} = V_{pa} - V_{pb} \tag{4.7}$$

Combining (4.5)-(4.7), the inverter output voltage can be expressed as:

$$V_{pi} = V_{DC}(D_a - D_b) + \frac{2V_{DC}}{n\pi} \sum_{n=1,2,..}^{\infty} [\sin n\pi D_a \cos(n\omega t + n\phi_p - n\pi D_a) - \sin n\pi D_b \cos(n\omega t - n\pi D_b)]$$

(4.8)

From (4.8), it is evident that the inverter legs having unequal duty cycles produces an average output $V_{pi,0}$ expressed as:

$$V_{pi,0} = V_{DC}(D_a - D_b)$$

(4.9)

as well as a harmonic AC output $V_{pi,n}$ expressed as:

$$V_{pi,n} = \frac{2V_{DC}}{n\pi} \sum_{n=1,2,..}^{\infty} [\sin n\pi D_a \cos(n\omega t + n\phi_p - n\pi D_a) - \sin n\pi D_b \cos(n\omega t - n\pi D_b)] \quad (4.10)$$

(4.9) suggests that it is possible to control DC voltage component of V_{pi} by controlling D_a and D_b. Also, (4.10) suggests that by controlling D_a, D_b, and ϕ_p it is possible to control the AC component of V_{pi}. In other words, if the inverter legs are controlled intelligently, this average voltage output $V_{pi,0}$ could be utilized to control an energy buffering unit, and the harmonic AC output $V_{pi,n}$ could simultaneously supply AC load which is the DWPT load in this case.

Taking advantage of the aforementioned analysis, the primary-side inverter operation can be divided into three operational modes, which are described in detail as follows.

4.2.1   DC Mode Operation

In this operational mode, the inverter operates similar to a DC-DC converter. The simplified equivalent circuit for this operation is shown in Fig. 4.2. In this scenario, the inverter legs are operated in phase, but with different duty cycles ($D_a \neq D_b$). The inverter is operated at a frequency significantly different than the resonant frequency of the WPT

circuit. Since the compensation circuit is tuned for only one resonant frequency, it would provide high impedance at this different frequency. Consequently, the alternating current supplied to the rest of the compensation circuit can be neglected in the analysis that follows. Thereby, the inverter effectively has an LC branch at its output, containing C_{SC} and an inductance L. This inductor minimizes the SC current ripple. The inverter output voltage V_{pi} predominantly contains DC component, as shown in Fig. 4.3(a).
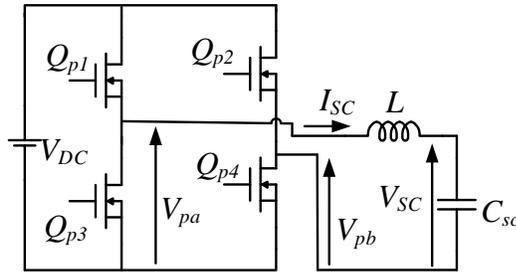
Fig. 4.2: Simplified equivalent circuit of primary circuit in DC mode operation.
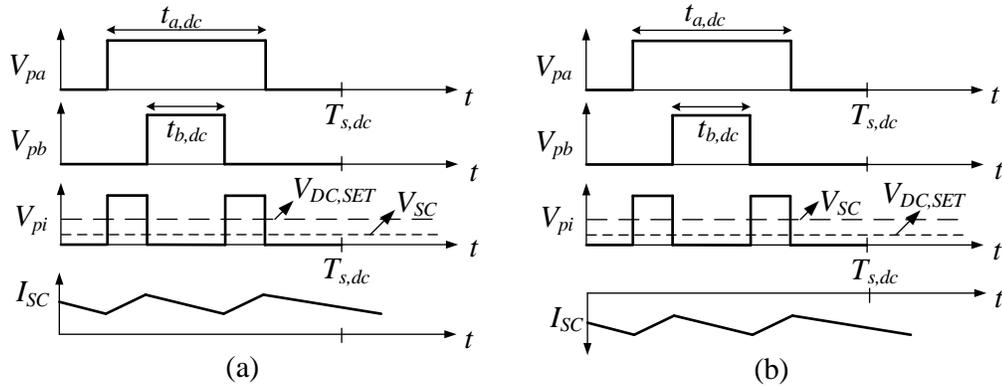
Fig. 4.3: (a) SC discharging and (b) SC charging during DC mode operation.

The duty cycle of the circuit is:

$$\Delta D_{conv} = \frac{t_{a,dc} - t_{b,dc}}{T_{s,dc}} \qquad (4.11)$$

where $T_{s,dc}$ is the switching period of the H-bridge; $t_{a,dc}$ and $t_{b,dc}$ are the conduction period of the inverter legs. The converter output $V_{DC,SET}$ can be easily calculated as $\Delta D_{conv}V_{DC}$. If $V_{DC,SET} > V_{SC}$, the converter operates as a Boost converter. The SC current I_{SC} will increase and eventually become positive, causing SC to charge slowly. Conversely, if $V_{SC} > V_{DC,SET}$ the converter operates as a Buck converter. The SC current would decrease and eventually become negative, discharging the SC and sending current back to the DC bus. In both cases, the SC voltage will eventually match the $V_{DC,SET}$. The SC discharging and charging scenario waveforms are shown in Fig. 4.3(a) and (b), respectively.

4.2.2 AC Mode Operation

In this mode, the H-bridge operates as a conventional phase-shifted inverter. The inverter legs operate with a phase-shift angle of ϕ_p between them. The legs are operated at the same duty cycle ($D_a = D_b$), with the switching frequency ($1/T_s$) equal to the resonant frequency of the WPT circuit, generating only an AC voltage at the output. The inverter circuit is shown in Fig. 4.4(a) and corresponding output waveforms are shown in Fig. 4.4(b).
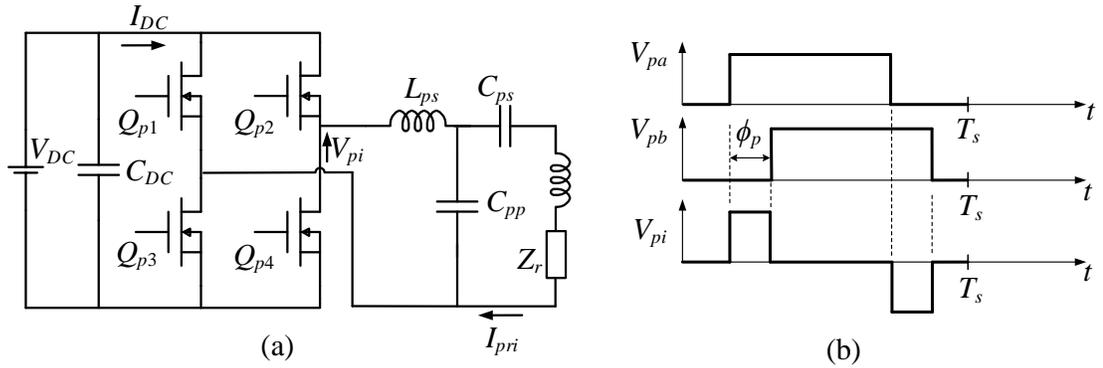
Fig. 4.4: (a) Primary equivalent circuit of AC mode operation (b) AC mode operational waveforms.

No energy is transferred to or from the buffering unit in this mode of operation.

4.2.3 Dual Mode Operation

The primary-side equivalent circuit for this mode is shown in Fig. 4.5(a). In this mode of operation, the H-bridge operates as an inverter which is capable of outputting both AC and DC components. The inverter legs are ϕ_p phase-shifted with unequal duty cycles ($D_a \neq D_b$), at the resonant operating frequency. Consequently, the output voltage contains both an average component and a harmonic component. The average component charges or discharges the SC, while the filtered harmonic component can supply the WPT load simultaneously. The inverter waveforms for this operation are shown in Fig. 4.5(b). The small-signal AC as well as DC analysis of the inverter and the buffering unit in *dual mode operation* is presented in detail in Section B.2.
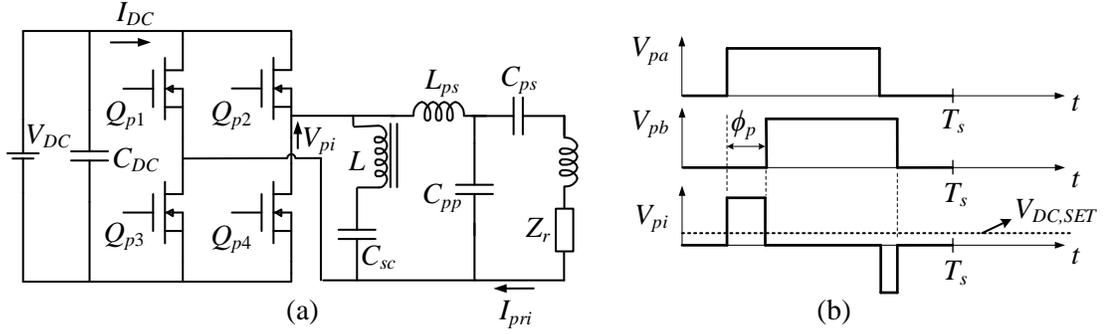
Fig. 4.5: (a) Primary equivalent circuit for dual mode operation (b) operational waveforms in dual mode.

4.3 System Operating Phases

While operating on electrified roadways, a DWPT system typically undergoes three characteristic operation phases. These phases are discussed as follows.

4.3.1 Precharge Phase

In this phase, the system precharges the SC and brings it to a predefined operating

voltage, to make it ready for the next DWPT charging cycle. During this phase, the inverter operates in *DC mode* described in Section 4.2.1. A *grid current controller* is designed and deployed to control the grid current during the *precharge phase*, consequently controlling the SC charging current, too. Depending on the predefined SC operating voltage and the charging current, the *precharge phase* can last up to a few minutes, especially at the initial start-up when the SC is completely depleted. The *grid current controller* design is discussed in Section 4.5.3.

4.3.2   Idle Phase

An *idle phase* is employed following the *precharge phase* during which the system awaits the arrival of the next EV. During this time, the SC is prevented from charging/discharging, being held at the nominal operating voltage level. In a possible deployment scenario, the DWPT system is awaiting a signal from a Vehicle Detection System (VDS) [57]. The VDS is an external sensory system which detects if there is any vehicle arriving at the primary coil, requesting G2V or V2G power transfer. Receiving such a signal terminates the *idle phase*, and the next phase termed as *charging phase* begins.

4.3.3   Charging Phase

This phase is reached as soon as the system gets a VDS signal indicating the arrival of an EV. Upon receiving this signal, the system initiates its controllers. To control the DPWT energy management at the grid side, two different controllers are employed. The first one is the *track current controller* which regulates the primary coil at a constant value. The second controller is the *grid current controller* previously introduced in *precharge phase*. The *grid current controller* ensures that the grid only supplies a constant level of power to deliver to the vehicle, whereas the SC unit supplies the predominantly pulsating transient portion of the DWPT power to the vehicle. The *grid current controller* also ensures that, in case of a V2G power transfer, the SC absorbs the transient part of the DPWT profile coming to the grid. In this scenario, the *grid current controller* maintains an average charging power to the grid, while protecting the grid from V2G power pulsations. The controller design

details are discussed in Section 4.5.

When the DWPT charging is over and the particular vehicle has departed, two different cases may take place. Firstly, if there is another vehicle arriving at the primary pad shortly after, the DWPT system gets another VDS signal. In this scenario, the system continues to run with the *charging phase*, controlling the grid and the track current. In an alternate case, where no vehicle is arriving shortly, there is no VDS signal received by the system yet. In this scenario, the system returns to the *precharge phase*. The *grid current controller* brings the SC to its nominal operating voltage. Upon reaching the nominal point, the system switches to *idle phase*, awaiting the next VDS signal for the upcoming vehicle. Alternatively, in case the system is still precharging the SC, and the VDS signal is received, the controller would start the *charging phase*, as long as the SC voltage is not beyond a predefined operating window. This operating window is necessary to implement as a protection feature, in order to ensure that SC unit is not overcharged or over-discharged.

4.4 Design Considerations for System Optimization

In this section, the procedure for optimally sizing the energy buffering unit for a given DWPT application is discussed in detail. In addition, the selection of proper operating frequency to precharge the buffering unit while reducing system losses is discussed as well.

4.4.1 Selection of SC Value

In this section, the optimum sizing of SC unit for a given system is analyzed and formulated with respect to various system parameters. The objective of this optimization is to select an optimum SC capacity and voltage that ensures optimum cost, reduced system loss, and ease of control while maintaining adequate power buffering in a continuous manner. During peak hours at an electrified roadway, EVs receive DWPT pulses almost continuously from TUs. In such a situation, the SC unit should be able to continue operating without depleting itself. In other words, SC energy capacity should be high enough to provide uninterrupted energy buffering for a large number of EVs. Let us consider a situation where multiple EVs follow each other on an electrified roadway. The operation parameters

are given in Table 4.1.

Table 4.1: Representative EV-roadway operating conditions

Parameter	Value
EV velocity, v	50 mph
Length of primary coil, l_{coil}	2 m
Single DWPT pulse time, T_{on}	89.5 ms
Time between two consecutive DWPT pulses, T_{off}	2 s
Single full cycle of DWPT charging per EV, T_{Total}	2.09 s
Charging duty cycle per EV, D_{Tr}	4.31%

The least amount of following distance between two consecutive EVs should correspond to the generally recommended "safe trailing distance" [92], [93]. With this constraint, the time between consecutive DWPT pulses can be taken as T_{off}=2 s. A constant value of the vehicle speed of v= 50 mph (22.35 m/s) is considered for the EVs in this example. In this scenario, for a given length of primary coil l_{coil}, the time required for one DWPT pulse can be determined as:

$$T_{on} = \frac{v}{l_{coil}} \tag{4.12}$$

A single "full DWPT cycle" consists of the DWPT pulse time T_{on}, added to the trailing time T_{off}, as follows:

$$T_{Total} = T_{on} + T_{off} \tag{4.13}$$

Fig. 4.6 illustrates the EV roadway operating conditions discussed above. Now, let us consider that the grid power is controlled to deliver an average value of P_{avg} throughout a DWPT cycle:

$$P_{avg} = \frac{P_{max}T_{on}}{T_{Total}} \tag{4.14}$$
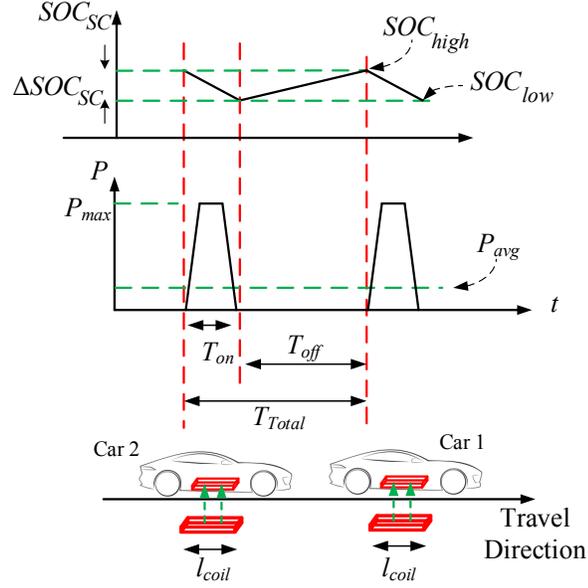
Fig. 4.6: Periodic DWPT power pulses at grid side and associated variation in SC SOC.

Consequently, the SC unit should be sized appropriately to supply the rest of power $(P_{max} - P_{avg})$ needed for a DWPT pulse during T_{on}. The SC energy E used to supply this DWPT pulse should be regained from the grid, to ensure its continuous operation. Now, upon supplying a DPWT pulse, the next pulse will occur after at least T_{off} time period. During this time, the *grid current controller* (explained in Section 4.5.3) precharges the SC unit adequately so that the SC could regain its lost energy E before the next vehicle comes. The proper sizing of SCs depends on all of the discussed parameters. It can be derived that, for a given SC voltage V_{sc}, the SOC of the SC is:

$$SOC_{SC} = \frac{V_{SC}^2}{V_{SC,Rated}} \tag{4.15}$$

where $V_{sc,Rated}$ is the voltage corresponding to a fully charged SC. Let us consider that, during operation, the optimum voltage and SOC swing window of the SC are V_{high} to V_{low} and SOC_{high} to SOC_{low}, respectively. Now, from (4.15), one can express V_{high} and V_{low} as follows:

$$V_{high}^2 = V_{SC,rated}^2 SOC_{high}$$
$$V_{low}^2 = V_{SC,rated}^2 SOC_{low} \qquad (4.16)$$

Within the specified SOC window, the amount of stored energy in a SC unit is:

$$E = \frac{1}{2}C_{SC}(V_{SC,high}^2 - V_{SC,low}^2) \qquad (4.17)$$

Combining (4.16) and (4.17), one can obtain:

$$E = \frac{1}{2}C_{SC}V_{SC,Rated}^2 \Delta SOC_{SC} \qquad (4.18)$$

where $\Delta SOC = SOC_{high} - SOC_{low}$ is the window of operation. SC unit energy E should be able to supply the power throughout the DWPT pulse time T_{on}:

$$E = (P_{max} - P_{avg})T_{on} \qquad (4.19)$$

Combining (4.14), (4.18) and (4.19), one can derive

$$\frac{1}{2}C_{SC}V_{SC,Rated}^2 \Delta SOC_{SC} = P_{max}(1 - \frac{T_{on}}{T_{Total}})T_{on} \qquad (4.20)$$

Substituting (4.14) into (4.20), it can be found that

$$C_{SC}V_{SC,Rated}^2 = \frac{2P_{max}v_{avg}}{\Delta SOC_{SC}l_{coil}}(1 - \frac{v_{avg}}{T_{Total}l_{coil}}) \qquad (4.21)$$

(4.21) describes the equation for selecting SC voltage and capacitance in terms of the allowable SOC window, EV speed, coil length, and the peak-DWPT power level. An alternative expression can be derived, which is more practical in determining the optimum SC size for a normalized system. For that, let us introduce a new variable:

$$F_{p,buffer} = (1 - \frac{P_{avg}}{P_{max}}) \qquad (4.22)$$

where $F_{p,buffer}$ is the factor of power buffering, i.e., the fraction of peak DWPT power that is supplied by the SC. The substitution of (4.22) into (4.20) results in:

$$C_{SC}V^2_{SC,Rated} = \frac{2F_{p,buffer}P_{max}T_{on}}{\Delta SOC_{SC}} \qquad (4.23)$$

After one DWPT pulse is over, the SC SOC hits SOC_{low} limit due to supplying a part of the DWPT power. Following a DWPT pulse, there is no vehicle demanding DWPT power for the following T_{off} period. Thereby, this period could be utilized to precharge SC to make it ready for the next DWPT power transfer. For precharging the SC, no more than P_{avg} power from the grid should be used in order to maintain an average power of P_{avg} even during the precharge period. In order to restore the lost energy E of SC during this precharging period, it can be derived that:

$$E = \frac{1}{2}C_{SC}V^2_{SC,Rated}\Delta SOC_{SC} = P_{avg}T_{off} \qquad (4.24)$$

$$C_{SC}V^2_{SC,Rated} = \frac{2(1 - F_{p,buffer})P_{max}T_{off}}{\Delta SOC_{SC}} \qquad (4.25)$$

From (4.23) and (4.25), optimum value of C_{SC} and $V_{SC,Rated}$ could be selected to support uninterrupted energy buffering from SC on EV roadways.

While (4.23) and (4.25) define guidelines for selecting the SC ratings, other system constraints should be taken into account to determine the optimum operating conditions for the SC unit for a given DWPT system. To illustrate the optimum operating zone of an SC, Fig. 4.7 depicts the different system constraints that would determine the optimum operating conditions of an SC. Different system voltage and current limits are plotted here. Four different levels of power-buffering ($F_{p,buffer}$) are considered for the SC unit, namely 25%, 50%, 75%, and 87.5%. 25% power-buffering would result in 25% of the peak-power reduction at the grid side. Similarly, 50% would increase SC utilization to suppress 50% of grid-power pulsation, respectively. The absolute maximum voltage limit of the system is V_{DC}, and the maximum current limit of the system depends on the maximum allowable

current of the inverter switches. These are the two absolute ratings, beyond which the system cannot operate at any time. Within these two limits, there are two additional limits which furthermore confine the system's optimum operation region. Firstly, the *track current controller*'s operation is hampered beyond a maximum voltage level, and thereby the system needs to operate within this limit to successfully maintain track regulation. This limiting factor is discussed in Section 4.5.4 in more detail. Secondly, the SC module defines a maximum allowable level of charging/discharging current for its safe operation. For a required power-buffering level, the SC operating current should be further decreased in order to reduce the switch-conduction losses in the inverter. The reason behind this is that the SC current increases the peak current at inverter switches.
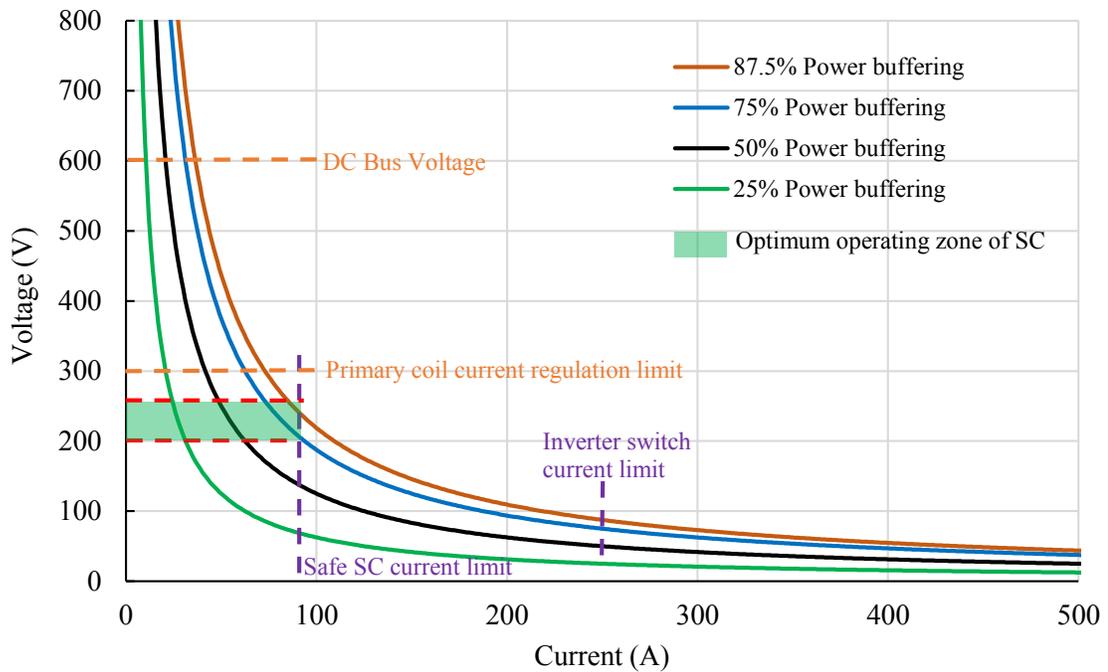
Fig. 4.7: Optimum operating region of SC unit.

Now, for a for the sake of formulation, the SC unit's operating current for buffering a 25-kW system can be approximately calculated as:

$$I_{SC,Fp} = \frac{F_{p,buffer}P_{max}}{V_{SC}} \tag{4.26}$$

Reducing this operating current of the SC unit helps to reduce the inverter switch current and, consequently, the associated switch-stresses. To compensate for the lowering of SC operating current, the SC operating voltage level should be made higher in order to maintain a desired level of power-buffering. However, higher voltages of SC also could be limited by a few factors, as well. The SC module's cost increases with a higher voltage rating. As a result, the SC voltage rating should also be selected carefully. Finally, depending on the optimum operating SOC swing ΔSOC_{SC}, the operating voltage window of SC should be selected. In Fig. 4.7, this SC voltage window shown is marked by the green box, which is the preferred operating window of SC for a given system. The width of the SC voltage window comes from the optimum allowable SOC range, defined in the earlier calculations. Keeping in mind the aforementioned analysis and constraints, representative optimum operating limits of SC unit are tabulated in Table 4.2, for a 25-kW DWPT charging system.

Table 4.2: Optimized SC operational specifications for a 25-kW DWPT system

Parameter	Value
Factor of power-buffering, $F_{p,buffer}$	75%
SC charging current, $I_{sc,Fp}$	80 A
SC rated voltage, $V_{sc,Rated}$	280 V
SC SOC maximum allowable limit, SOC_{max}	85%
SC SOC minimum allowable limit, SOC_{min}	70%
SC optimum operating SOC upper limit, SOC_{high}	80%
SC optimum operating SOC lower limit, SOC_{low}	75%
SC operating SOC window, ΔSOC_{SC}	5%
SC optimum operating voltage upper limit, V_{high}	250 V
SC optimum operating voltage limit, V_{low}	242 V
SC maximum allowable voltage, V_{max}	258 V
SC minimum allowable voltage, V_{min}	234 V
Minimum SC capacitance value, C_{SC}	0.86 F

A 75% peak-power reduction at the grid side is ensured by the SC unit. Rated SC operating current limit is chosen to be 80 A, and the nominal operating SOC window is selected from about 75% to 80%. With the constraint, the minimum value of SC can be calculated from (4.23) to be:

$$C_{SC} = \frac{2F_{p,buffer}P_{max}T_{on}}{\Delta SOC_{SC}V_{SC,Rated}^2} = 0.86 \text{ F} \tag{4.27}$$

In addition to the nominal operating voltage limits, a maximum and minimum operating voltage limits V_{max} and V_{min} should be employed beyond which limits the system will not be allowed to operate. These limits correspond to an absolute SC SOC limits of SOC_{max} and SOC_{min}, respectively. These absolute limits serve two purposes. Firstly, these limits serve over voltage/under voltage protection features for the SC. Secondly, this window also makes sure that the system continues to operate up to some limits when the T_{off} between two consecutive DWPT pulses is too small. This particular situation happens when the tailing distance between two successive vehicles is reduced. As an example, let us consider an extreme example where $T_{off}=0$ and a second vehicle immediately demands a DWPT pulse upon the departure of the first vehicle. At the end of the first DWPT pulse, the SC SOC will come down from 80% to around 75%. In a typical scenario ($T_{off} >0$), the grid controller will precharge the SC again and bring it to 80% before the following vehicle arrives. However, since $T_{off}=0$, the *precharge phase* is skipped, and the SC continues to normally operate, providing energy buffering for the second vehicle as long as it's SOC does not go below its absolute minimum operable limit. Similarly, when two consecutive V2G pulses take place with no T_{off} in between, the SC SOC goes momentarily higher, and for that scenario, the maximum operable limit comes into play again.

Instead of interpreting $T_{off}=0$ as the immediate arrival of a second vehicle, it can also be interpreted as the first vehicle is in standstill position. In this case as well, the SC will continue to provide energy bufffering as long as its maximum operating limits are not violated. The capability of SC to buffer such consecutive DWPT cycles ($T_{off}=0$) can be increased by increasing the value of C_{SC}.

From (4.27), it is evident that, with an appropriately sized energy buffering unit, it is possible to achieve a high level of energy buffering with a comparatively low value of capacitance. This conclusion, in fact, helps to have a wider range of selection of the suitable energy storage options for achieving desired power buffering. In the proposed system, a SC unit is proposed. However, any storage unit that satisfies the system requirements depicted in Fig. 4.7, will be a candidate for the energy buffer unit, for example, electrolytic capacitors [94], Lithium-ion Capacitors (LiCs) [95] etc.

4.4.2 Selection of Choke Inductance Value

Proper selection of the choke inductance L helps to smooth the charging/discharging current of SC, thereby facilitates better control of the SC unit. As described in Section B.3, the average component of the inverter voltage output is responsible for SC charging/discharging. The L-C branch containing the choke inductor and the SC provides high impedance to the high-frequency component of the inverter voltage V_{pi}. As a result, the L-C branch acts effectively as part of a switch-mode DC-DC converter. The inverter operates as a Buck converter while charging the SC, as suggested by (B.31) presented in the analysis at Section B.2.

The value of inductance is mostly determined by the allowed current ripple through the inductor L. In typical designs, up to 10%-15% current ripple in the DWPT operation is selected as a design objective. The current ripple calculation of L is derived in detail in Section B.3. For a maximum allowable peak-to-peak current ripple $\Delta i_{Lmax,pk-pk}$, at the operating frequency f_s and for converter duty cycle ΔD, the minimum value of inductance is found by a current ripple can be formulated from (B.37) as follows:

$$L_{min} = \frac{(V_{DC} - V_{SC})D_1 T_s}{\Delta i_{Lmax,pk-pk}} \tag{4.28}$$

where D_1 can be derived from the steady state operating value of the phase-shift angle ϕ_p as follows:

$$D_1 = \frac{\phi_p}{2\pi} \tag{4.29}$$

The lowest value of inductance is calculated from the maximum allowable current-ripple requirements of the system. (4.28) provides the guideline for selecting the lowest value of L for a given design. However, in order to facilitate smoother charging/discharging current for the SC, a higher value of L might be used which will effectively decrease the current ripple. This generally entails increasing the size and weight of the inductor. Nevertheless, it results in a favorable design in SC applications, since continuous exposure of SC in high ripple-current may cause overheating which tends to decrease its lifetime [96], [97]. However, there is an upper limit of the inductance beyond which it will not be suitable for the intended DWPT application. Since the SC provides the transient part of the DWPT pulse, the SC current should be able to smoothly follow the required DWPT load profile. Since the choke inductor L is in series with C_{SC}, the inductor should be able to change its current at a rate equal or faster than the change in current demanded by the DPWT power profile. In order to further illustrate the point, Fig. 4.8 shows a DWPT current profile I_{out}, and corresponding profile of I_L .
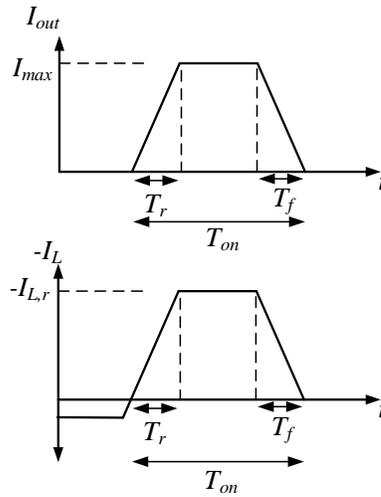
Fig. 4.8: Voltage and current across choke inductance during *charging phase*.

From Fig. 4.8, it can be observed that, before the arrival of the DWPT load the I_L is negative, which charges the SC. It is accomplished by the *grid current controller* as it precharges the SC with a constant current before the arrival of EV. As soon as the load arrives, the controller discharges the SC and I_L follows the load profile.

The load profile's rise time T_r and fall time T_f are considered equal for the sake of simplified formulation. In this scenario, either of these two time periods can be used to calculate the maximum value of L. The change in current during the rise time T_r of the load can be expressed as:

$$L \left| \frac{I_{L,r}}{T_r} \right| = |V_{L,r}| \tag{4.30}$$

where $V_{L,r}$ is the inductor voltage v_L during T_r. The value of $V_{L,r}$ is determined by the control action of the *grid current controller* as it applies a duty cycle change during this period of time, as expressed as:

$$|\Delta D_L| = \frac{|V_{L,r}|}{V_{DC}} \tag{4.31}$$

Combining (4.30) and (4.31), the maximum value of L for successful DWPT operation can be formulated as:

$$L_{max} = \frac{|\Delta D_{L,max}| V_{DC}}{\left| \frac{I_{L,r}}{T_r} \right|} \tag{4.32}$$

where $D_{L,max}$ is the maximum value of duty cycle that can be applied by the *grid current controller*, while still maintaining the system's integrated control over the track and grid. Theoretically, for any given point of time, its value can be determined by the following equation:

$$\Delta D_{max} = \frac{V_{SC}}{V_{DC}} + |\Delta D_{L,max}| \tag{4.33}$$

where ΔD_{max} is the theoretical limit of the duty cycle beyond which point the *track current*

controller cannot maintain the regulation of the primary coil current. The theoretical limit of duty cycle depends on the nominal inverter phase-shift angle ϕ_p which will be discussed in Section 4.5.4.

For a successful design, the value of L for a given system should be chosen within the range defined by (4.28) and (4.32) as follows:

$$L_{min} < L < L_{max} \tag{4.34}$$

4.4.3   Selection of the Precharge Mode Operating Frequency

During the initial system start-up and between the charging cycles of two consecutive vehicles, the SC is slowly charged to bring its operation voltage to a predefined value determined by the desired utilization of SC. During those intervals, it is important to have negligible current in the primary coil due to two reasons. Firstly, the primary coil typically possesses a considerable parasitic resistance which would result in unwanted losses in the system. Removing the coil current during the SC *precharge phase* improves efficiency. Secondly, current flowing through the primary coil during precharging of SC would cause safety concern due to the fact that the primary coil current generates excessive magnetic field above the road. Since the precharging occurs between the charging intervals when there is no car to cover and shield the transmitter magnetic field, humans and animals could be exposed to a harmful field level. While precharging, one way to prevent the primary coil current is to use a switch (relay) to disconnect the pad coil during this period. However, the relay's contact resistance would produce even more losses during the regular power delivery operation. In addition, the use of a relay would add to the system's control complexity. Thereby, the precharging frequency is carefully chosen so that the circuit branch containing the primary coil results in a high-impedance, and consequently, negligible current flows through the primary. For precharging, the *DC Mode* operation of the inverter is selected in order to have a significant average output voltage to charge the SC. However, due to the square-wave output shape of the inverter voltage, there would still be a significant number of higher frequency harmonics present in the voltage. It could be possible that some of

these harmonics would lie close to the resonant frequency of the primary compensation loops. In that case, if any of those high frequency component is strong enough, it might cause a perceivable current flowing through the primary coil and the compensation loops. To illustrate, Fig. 4.9 shows the magnitude of transconductances $\frac{I_{pri}}{V_{pi}}$ and $\frac{I_{LP}}{V_{pi}}$. Both of the transfer functions shows frequency-selective characteristics with two peaks at 75 kHz and 93 kHz, and both of them shows an attenuating trend for all the higher and lower frequencies. It can also be noticed from Fig. 4.9 that at frequencies lower than 75 kHz, the attenuation is approximately 20 dB/decade, whereas at frequencies higher than 93 kHz, the attenuation is 40 dB/decade. Consequently, the precharge frequency should be selected at a frequency higher than 93 kHz. In this scenario, all the higher order harmonics would be further apart from those two peaks at 75 kHz and 93 kHz, thereby ensuring negligible current at the primary coil. Also, operating at higher frequency would ensure more attenuation of harmonics compared to the lower frequencies. For this system, the precharge frequency is selected to be 140 kHz.
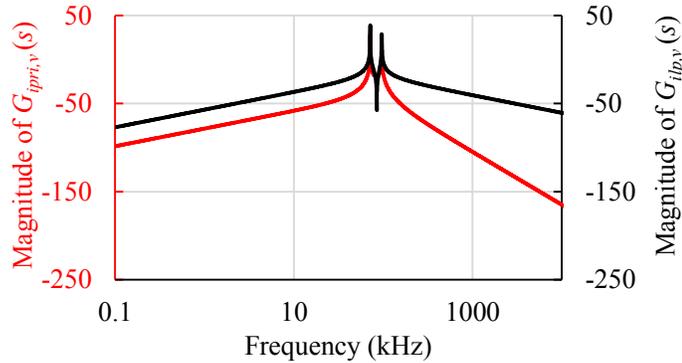
Fig. 4.9: Magnitude Bode plots of transconductances $\frac{I_{pri}}{V_{pi}}$ and $\frac{I_{Lps}}{V_{pi}}$.

4.5 Controller Design

In this section, the controller design procedure for the proposed system is discussed in detail. Prior to designing the controller stages, the system is adequately modeled using small-signal AC analysis. The bandwidth requirement of the controllers is identified. The

decoupling of the controller dynamics in order to successfully maintain system operation is discussed, as well.

4.5.1 Controller Operation Overview

For the proposed system, two different controllers are deployed to maintain system operation as shown in Fig. 4.10, namely the *track current controller* and the *grid current controller*. The control objective of a *track current controller* is to regulate primary coil current to closely match a selected reference. A well-regulated primary coil current is a desirable feature in many WPT systems, and consequently, this approach has been adopted in the proposed system as well. On the other hand, the *grid current controller's* objective is to regulate the grid current throughout the DWPT charging cycle.
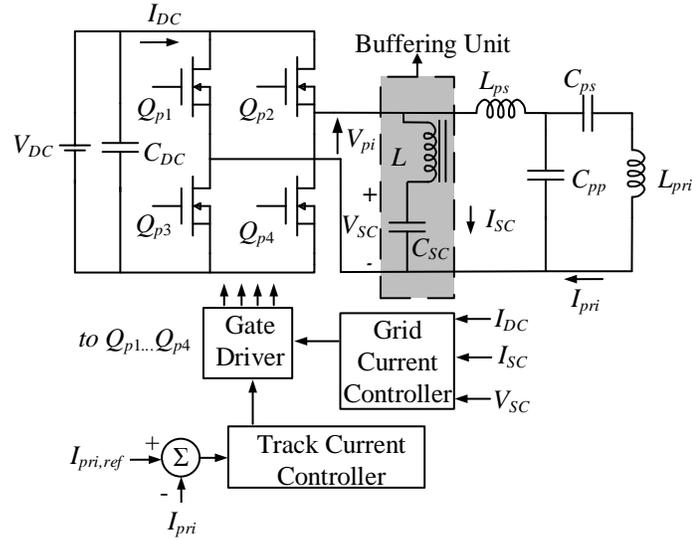
Fig. 4.10: The DWPT primary circuitry and proposed control system for grid-side energy management.

The objective is to design two fast controllers that operate together, maintaining both the track current and grid current regulation irrespective of unloaded, loaded, G2V, or V2G charging scenarios. It is important to ensure that the controllers do not affect each other's dynamics. That is why it is of paramount importance to choose the bandwidth of both

controllers appropriately.

In a typical case, these are the general considerations while choosing the controller bandwidths:

(i) Controller bandwidth should be lower than the system's operating frequency [98] .

(ii) Controller bandwidth should be faster than the DWPT load dynamics in order to produce the system response unaffected by the DWPT load transients.

(iii) If two feedback controllers are employed to work together with one controller nested inside the other, it is recommended that the outer-loop controller's bandwidth is lower than the that of the inner-loop controller.

From (ii), the bandwidth of both the controllers should be faster than the DWPT power profile's bandwidth. However, the DWPT pulse's time period and consequently, bandwidth can vary in a wide range depending on the coil geometry and the velocity of the vehicle. For example, for a l_{coil}=2 m, and v=80 mph, one DWPT pulse would take 55 ms. Higher v or lower l_{coil} would reduce the DWPT pulse width and thereby require faster response time from the controller. In other words, the DWPT pulse width depends on both the coil geometry and the vehicle speed, both of which vary with different system designs and operation scenarios. Ideally, the controllers should be faster compared to the range of DWPT profile bandwidths that can occur on EV roadways. For this application, a feedback controller of 1 kHz bandwidth is selected for the *track current controller*. The controller controls the inverter output voltage $V_{pi,1,rms}$ to regulate the primary coil current. Fig. 4.11(a) shows the inverter output voltage waveform and the $V_{pi,1,rms}$ to level when it is operating in conventional *AC mode*. This is the mode when the inverter operates when there is no SC-buffering unit present in the system. Fig. 4.12(a) shows the corresponding block diagram of the control loop of the system.
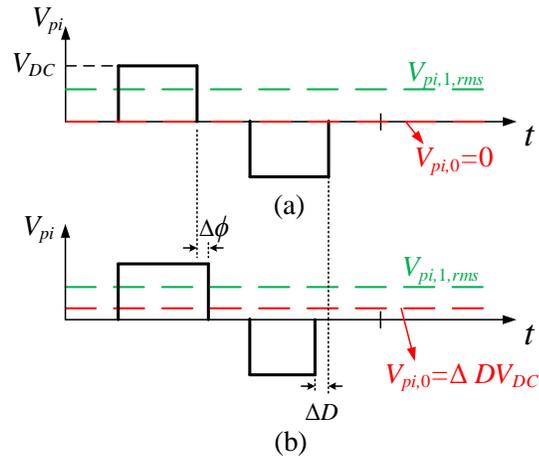
Fig. 4.11: Inverter output voltage with the *track current controller* (a) without the *grid current controller* (b) with the *grid current controller*.
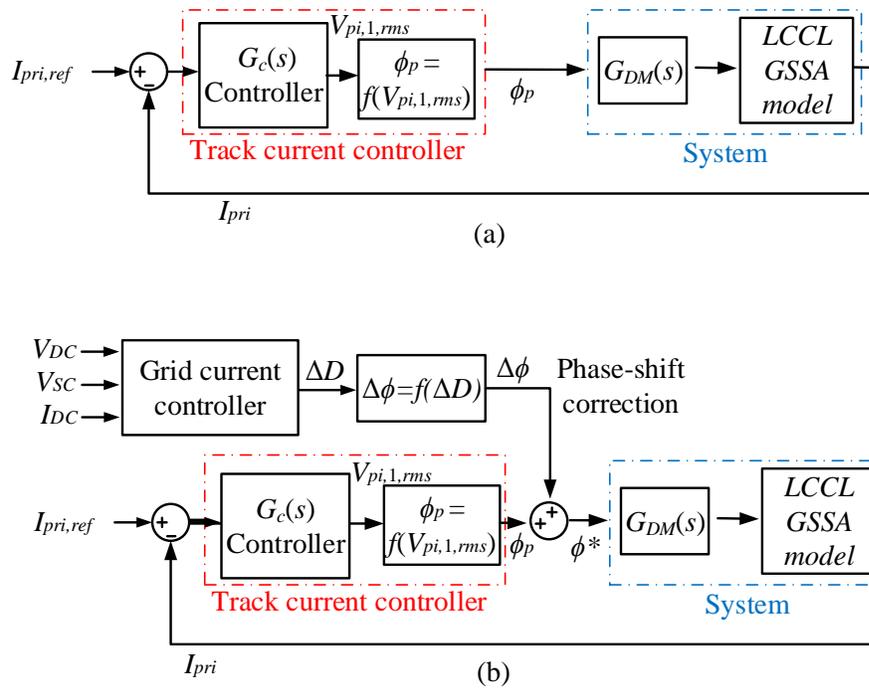
Fig. 4.12: (a) The block diagram of a *track current controller* (b) Combined system's block diagram with *track current controller* and the *grid current controller*.

However, upon inserting the SC-buffering unit into the system, an additional *grid current controller* (Fig. 4.12(b)) is designed and deployed to control the energy buffering operation of the SC unit, which in turn, controls the grid current. This controller controls the inverter output voltage average value of $V_{pi,0}$ to control the grid current. The inverter needs to operate in *dual mode* in order to facilitate the $V_{pi,0}$ output of the inverter in addition to $V_{pi,1,rms}$ value which is needed for the *track current controller*.

Fig. 4.11(b) shows the inverter output voltage waveform in this mode. Application of a finite ΔD duty cycle output by the *grid current controller* changes the inverter output waveform as can be observed by Fig. 4.11(b). This, in turn, changes the $V_{pi,1,rms}$ value of the inverter, which could upset the track current regulation if not corrected by appropriate controller action. In order to help the *track current controller* maintain a fast regulation of current, a feedforward correction term ($\Delta\phi$) should be added to ϕ_p calculated by the *track current controller* to help maintain constant $V_{pi,1,rms}$ value accordingly. This is illustrated in Fig. 4.11(b) where it is shown that a positive $\Delta\phi$ is added to the inverter output voltage waveform, as a corrective feedforward action after the grid current applies a ΔD duty cycle to output a finite $V_{pi,0}$ to control the grid current I_{DC}. With the application of $\Delta\phi$, the $V_{pi,1,rms}$ is still maintained at the same level as in Fig. 4.11(a). In this way, the two controllers' dynamics are decoupled and do not perceivably affect each other. Thereby, the bandwidth restriction suggested by requirement (iii) is mostly eliminated. This feature is especially attractive for DWPT application because the *grid current controller* bandwidth can be selected considering the DWPT load dynamics, without being limited by the *track current controller*. This freedom of setting the grid current controller bandwidth also makes it easier to install an SC buffering unit and associated controller as an add-on to an existing DWPT system without redesigning the *track current controller*.

As proposed, the *track current controller* and the *grid current controller* are designed for controlling the DWPT system to facilitate proposed power buffering at the grid side. The design of those controllers are discussed as follows:

4.5.2 Track Current Controller

The *track current controller* design objective is to regulate the primary coil current during both unloaded and loaded scenario. The loaded scenario corresponds to the situation when an EV undergoing G2V or V2G charging, whereas the unloaded scenario corresponds to the situation when the system is awaiting the arrival of an EV in the near future. The tuning of the primary-side compensation network plays an important role in the primary coil current calculations. Properly tuned compensation network acts as a filter, allowing fundamental harmonic of the H-bridge output voltage to pass through, and filtering other higher order harmonics. As a result, the fundamental harmonics of the H-bridge output predominantly contributes to the primary coil current, and (2.14) can be written as:

$$\boldsymbol{I_{pri}} = \frac{\boldsymbol{V_{pi,1,rms}}}{j\omega_s L_{ps}} \tag{4.35}$$

Also, if V_{DC} is considered to be constant, the H-bridge output voltage essentially depends only on the primary phase-shift angle ϕ_p, as from (2.1):

$$\boldsymbol{V_{pi,1,rms}} = \frac{2\sqrt{2}V_{DC}}{\pi} \sin(\frac{\phi_p}{2}) \tag{4.36}$$

Combining the considerations (4.35) and (4.36), it can be perceived that it is possible to regulate the primary coil current controlling ϕ_p only. That is why ϕ_p is chosen as the control variable for *track current controller*. In order to design the *track current controller*, the small-signal model of the WPT system needs to be derived. In this system, General State Space Averaging (GSSA) method [99] is used to derive the small-signal model. While modeling the system, a typical *AC mode* operation is considered where inverter legs are operating at constant duty cycles (D_a=D_b=0.5) and with the phase-shift modulation angle ϕ_p between the legs. The plant transfer function is taken to be the transconductance $G_{vi}(s)$ between the primary coil current I_{pri} and the fundamental harmonic of the H-bridge output voltage. The GSSA analysis of the system is discussed in Section B.1, where $G_{vi}(s)$ is derived. With the GSSA modeling approach, both unloaded and loaded $G_{vi}(s)$ are derived,

and the respective Bode plot magnitude responses are shown in Fig. 4.13. It can be observed that there is little difference between the loaded and unloaded cases. This suggests that either of the unloaded or loaded cases can be used to derive a controller design. For this system, the unloaded system is used for the controller design.
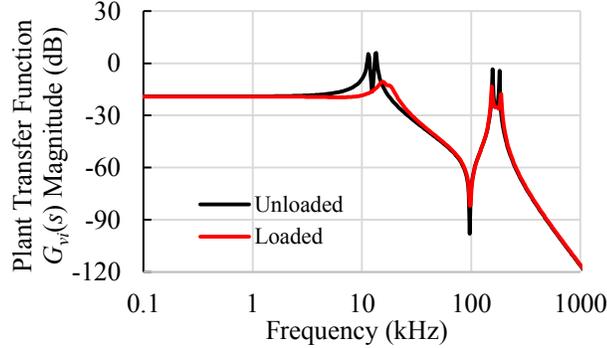
Fig. 4.13: Magnitude Bode plots of $G_{vi}(s)$ for unloaded and loaded systems.

The control loop block diagram is depicted earlier in Fig. 4.12(a). The effect of digital modulator and the inverter-delay have been modeled together as a transfer function $G_{DM}(s)$, similar to the approach shown in [99]. In Fig. 4.12(a), $G_{DM}(s)$ is the combined transfer function of the digital modulator $G_M(s)$ and the H-bridge delay $G_{H,delay}(s)$:

$$G_{DM}(s) = G_M(s)G_{H,delay}(s) \tag{4.37}$$

$G_M(s)$ is a steady-state gain term, nonlinearly dependent on ϕ_p as:

$$G_M(s) = \frac{\frac{2\sqrt{2}V_{DC}}{\pi}\sin(\frac{\phi_p}{2})}{\phi_p} \tag{4.38}$$

To linearize the control loop, this nonlinearity must be removed which has been accomplished by adding an extra computation step inside the *track current controller* to cancel out this non-linear term. Initially, the controller senses the primary coil current error signal and calculates the required $V_{pi,1,rms}$ needed for regulating I_{pri}. Afterward, it maps the result and finds the phase-shift angle that corresponds to that value, by solving:

$$\phi_p = 2\sin^{-1}\frac{V_{pi,1,rms}\pi}{2\sqrt{2}V_{DC}} \tag{4.39}$$

Successively, the digital modulator and the H-bridge inverter together convert the ϕ_p back into $V_{pi,1,rms}$. This way, the nonlinearity associated with $G_M(s)$ is removed, resulting in a linear control loop. $G_{H,delay}(s)$ is approximated as a first-order delay term. Upon applying a step change of phase-shift angle ϕ_p to the inverter, it takes some time to settle to a new $V_{pi,1,rms}$ value. $G_{H,delay}(s)$ models a simple approximation of that delay.

To illustrate, Fig. 4.14 shows two possible scenarios of step change of ϕ_p. A step change from ϕ_{lo} to ϕ_{hi} is shown in Fig. 4.14(a), and a step change from ϕ_{hi} to ϕ_{lo} is shown in Fig. 4.14(b). The corresponding inverter output voltage V_{pi} representing to the two values is shown in Fig. 4.14(c).
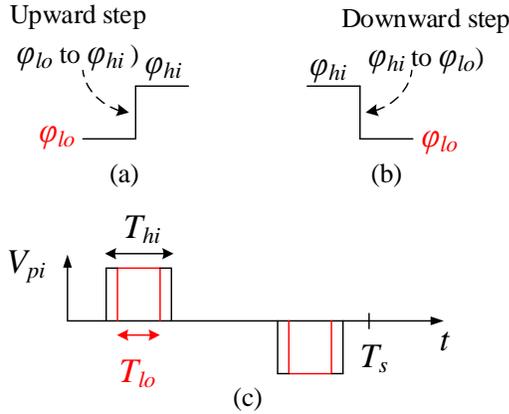
Fig. 4.14: (a) A step-up change in ϕ_p (b) a step-down change in ϕ_p (c) superimposed inverter outputs corresponding to two different conduction time periods resulted from the step change of (a) or (b).

The inverter's conduction time period T_{hi} corresponds to ϕ_{hi}, and T_{lo} corresponds to ϕ_{lo}. In [99], it has been proved that, in either case of step change, the time delay required

by the inverter to update the $V_{pi,1,rms}$ value corresponding to the step is:

$$T_D = \frac{T_s - T_{hi}}{2} \qquad (4.40)$$

where T_s is the operating period of the inverter, and T_{hi} is the time width of the larger angle during the step change. To approximate an optimum value of $G_{H,delay}(s)$, and consequently $G_{DM}(s)$, a step change to $T_{hi}=120°$ from $90°$ is used for calculation. T_D for this case is calculated to be 4.9 μs.

Fig. 4.15 shows how the simulated $V_{pi,1,rms}$ changes after the given angle step is applied to the inverter. An ideal RMS conversion block is used to calculate the inverter output voltage and simulate the effect of a step change. The $G_{DM}(s)$ that closely match the transient output voltage of the inverter during the step change can be found as:

$$G_M(s) = \frac{\frac{2\sqrt{2}V_{DC}}{\pi}\sin(\frac{\pi\phi_p}{360})}{\phi_p} \frac{30000e^{-sT_D}}{s+30000} \qquad (4.41)$$
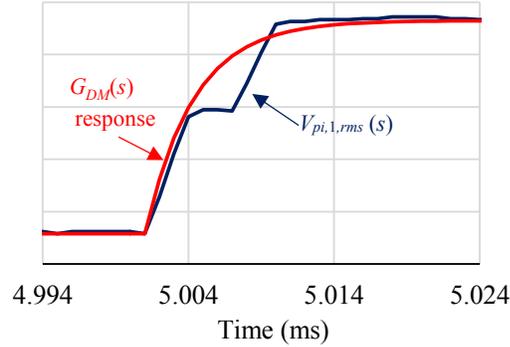
Fig. 4.15: Step response of $G_{DM}(s)$ and $V_{pi,1,rms}$ to a step change where $T_{hi}=120°$.

Consequently, the uncompensated loop gain of the system can be calculated as:

$$T_{i,un}(s) = G_{vi}(s)G_{DM}(s) \qquad (4.42)$$

The Bode plot gain of $T_{i,un}(s)$ is shown in Fig. 4.16. Upon deriving the $T_{i,un}(s)$, a

controller design is carried out to have a desired 1 kHz bandwidth and 60° phase margin. With these design constraints, the controller $G_{c(s)}$ transfer function is calculated as:

$$G_c(s) = \frac{7.898e8}{s(1 + \frac{s}{4000\pi})} \tag{4.43}$$
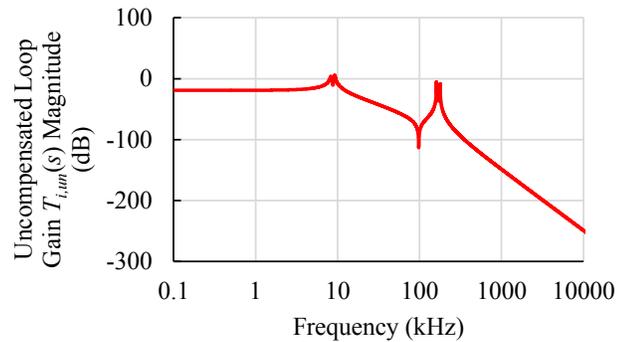
Fig. 4.16: The magnitude Bode plot of uncompensated loop gain $T_{i,un}(s)$.

The compensated loop gain can be represented as:

$$T_i(s) = G_c(s)T_{i,un}(s) \tag{4.44}$$

The magnitude and phase Bode plots of $G_c(s)$ are shown in Fig. 4.17. Fig. 4.18 shows the simulated track current regulation performance with a reference of 30 A. It is observed that the controller settles within 1 ms for both unloaded and loaded case. The magnitude and phase Bode plots of $T_i(s)$ are shown in Fig. 4.19.
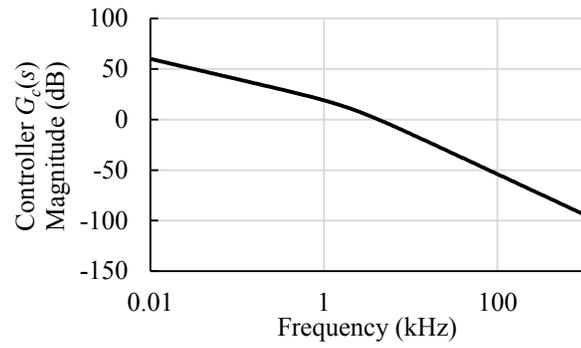
(a)
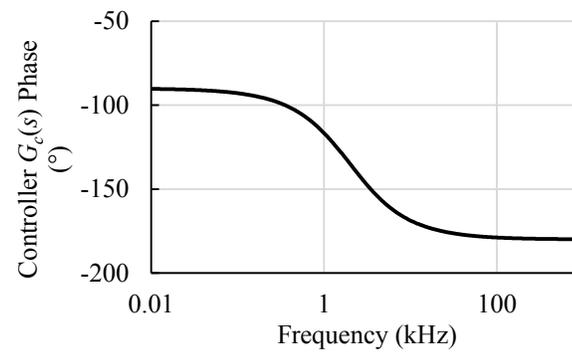
(b)

Fig. 4.17: Bode plots of the controller transfer function $G_c(s)$.
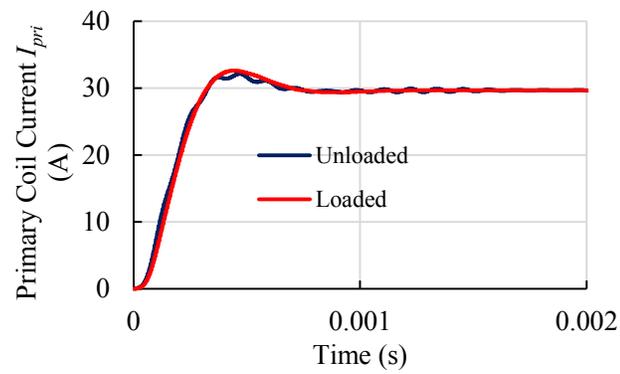
Fig. 4.18: The *track current controller* response to a 30-A step of reference.
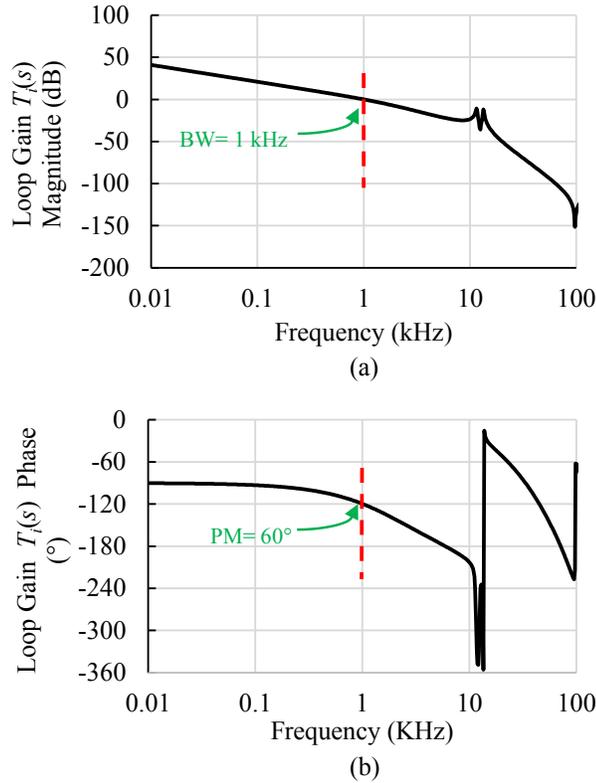
Fig. 4.19: Bode plots for the system loop gain $T_i(s)$.

4.5.3 Grid Current Controller

In the proposed system, the grid control objective is to regulate the grid current throughout the DWPT charging cycle. In effect, the *grid current controller* controls the sharing of DWPT profile between the grid and the SC unit in a manner that the grid current contribution can be maintained at an acceptable average level to ensure the grid stability. The objective is to design a fast *grid current controller* which operates well together with the *track current controller*, helping to maintain the track current while controlling the grid current. Moreover, this controller should not require any synchronization between the primary and the secondary while reacting fast enough to handle the DWPT dynamics for both G2V and V2G charging scenarios. Two different types of grid current control action are proposed. Those are discussed as follows:

4.5.3.1 Bang Bang Control

This type of controller is proposed for *grid current controller* in [100]. This type of control approach is fast and simple to implement. The controller action can be expressed as follows:

$$\Delta D = \begin{cases} \frac{V_{SC}}{V_{DC}} - D_{dec} & I_{sc} < I_{sc,lim} \\ \frac{V_{SC}}{V_{DC}} & I_{sc} = I_{sc,lim} \end{cases} \tag{4.45}$$

where the controller design parameter D_{dec} is a constant value of duty cycle decrement applied by the controller, $I_{sc,lim}$ is the operating current limit of the SC imposed by the controller, I_{sc} is the sensed value of SC current, V_{sc} is the sensed value of SC voltage. In this case, the controller applies D_{dec} until the I_{sc} reaches its set limit $I_{sc,lim}$. Upon reaching this limit, no further decremental duty cycle is applied (D_{dec}=0), and the SC maintains a constant level of $I_{sc,lim}$ current.

4.5.3.2 FFFB Control

This type of controller is proposed for *grid current controller* in [101].The controller action can be expressed as:

$$\Delta D = \frac{V_{SC}}{V_{DC}} + K_P(I_{DC,ref} - I_{DC}) \tag{4.46}$$

where I_{DC} is the sensed value of the grid current, $I_{DC,ref}$ is the desired value of the grid current to be maintained by the controller, and K_p is a proportional gain which is a controller design parameter. The first term in (4.46) is considered a feed-forward term, whereas the second term as a feedback term. By this control approach, the controller maintains a constant grid current reference $I_{DC,ref}$ throughout its operation time.

4.5.4 Decoupling of Track Current Controller and Grid Current Controller

Although ΔD=D_a-D_b=0 has been considered while designing the *track current controller*, in practice, the *grid current controller* applies a finite ΔD as its control action.

Nonzero ΔD would tend to change V_{pi}, and, consequently, I_{pri}. To prevent I_{pri} from drifting while a finite ΔD is applied, a phase-shift correction term $\Delta\phi$ is added to the *track current controller* output ($\phi^*=\phi_p+\Delta\phi$). To analytically find the correction relationship, one can consider a duty cycle perturbation ΔD added to D_b ($D_b^*=D_b+\Delta D$) for unchanged D_a value. In this scenario, the fundamental harmonic of the inverter output voltage before the perturbation can be represented as:

$$V_{pi,1,rms} = \frac{2V_{DC}}{\pi}\sqrt{A_1^2 + B_1^2} \tag{4.47}$$

where

$$A_1 = \sin\pi D_a \cos(\phi_p) - \sin(\pi D_a)$$
$$B_1 = -\sin\pi D_a \sin(\phi_p) \tag{4.48}$$

The inverter output voltage after the perturbation can be represented as:

$$V_{pi,1,rms}' = \frac{2V_{DC}}{\pi}\sqrt{A_2^2 + B_2^2} \tag{4.49}$$

where

$$A_2 = \sin\pi D_a \cos(\phi_p + \Delta\phi) - \sin(\pi D_a - \pi\Delta D)\cos\pi\Delta D$$
$$B_2 = -\sin\pi D_a \sin(\phi_p + \Delta\phi) + \sin(\pi D_a - \pi\Delta D)\sin\pi\Delta D \tag{4.50}$$

Equating (4.47) and (4.49) and solving, one can derive the phase-shift correction term $\Delta\phi$ as:

$$\Delta\phi = cos^{-1}\left(\frac{\frac{V_{pi,1,rms}^2\pi^2}{4V_{DC}^2} - \sin^2 C - \sin^2 D}{2\sin C \sin D}\right) - \phi_p + \pi\Delta D \tag{4.51}$$

where

$$C = \pi D_a$$

$$D = \pi D_a - \pi \Delta D$$
(4.52)

(4.51) takes a complex trigonometric form, which could be difficult for controllers to execute without causing computational delays. In order to help the controller operate faster in every iteration, a simplified curve-fitted expression is derived which accurately describes the relation between ΔD and $\Delta \phi$ around the quiescent point defined by operating ϕ_p and D_a. The locus of mapping function for constant D_a=0.5 and different operating value of ϕ_p is plotted in Fig. 4.20.
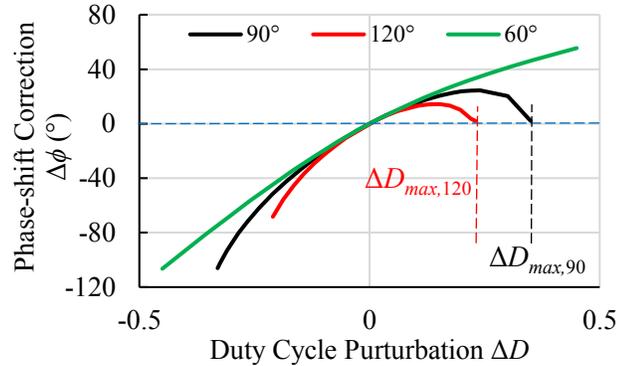
Fig. 4.20: The phase-shift correction function for constant D_a=0.5 and different ϕ_p values.

Previously, in Fig. 4.18 , and (4.46), it has been mentioned that there is a theoretical maximum limit of duty cycle ΔD_{max} beyond which, the track current control operation will be hampered. These limits, for different value of nominal ϕ_p is depicted in Fig. 4.20. Beyond these limits, the $\Delta \phi$ value calculated from (4.51) is complex, which indicates that there is no real value of correction angle $\Delta \phi$ practically applicable to provide requested fundamental of the inverter output voltage, causing the track current regulation to fail. Essentially, the location of these limits coincide with the intersection of the mapping function with the ΔD axis. For example, for ϕ_p =120°, this maximum duty cycle limit $\Delta D_{max,120}$ is 0.23. It is also observed from Fig. 4.20 that the value of ΔD_{max} increases with the decrease of ϕ_p.

Similarly, the mapping locus for constant $\phi_p=90°$ and different D_a values are plotted in Fig. 4.21 , where it can be observed that the ΔD_{max} limits increase with the decrease of D_a.
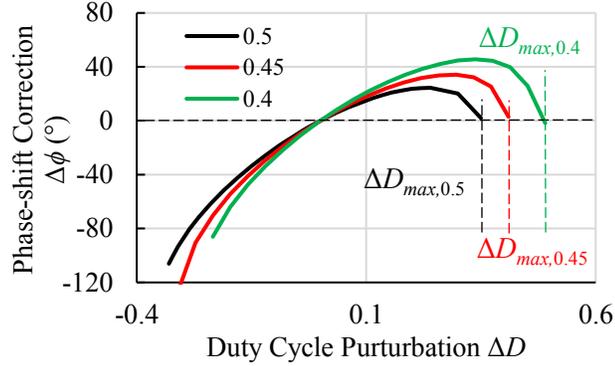
Fig. 4.21: The phase-shift correction function for constant $\Delta\phi=90°$ and different D_a.

For the proposed system, the quiescent operating points are $\phi_p =60°$, $D_a=0.5$. A simplified curve-fitting expression of the mapping function around this operating point can be derived as:

$$\Delta\phi = -127.26\Delta D + 179.87\Delta D - 0.6764 \tag{4.53}$$

Fig. 4.22 compares the analytical values of $\Delta\phi$ calculated from (4.51) , and the curve-fitted values found from (4.53), for different ΔD.
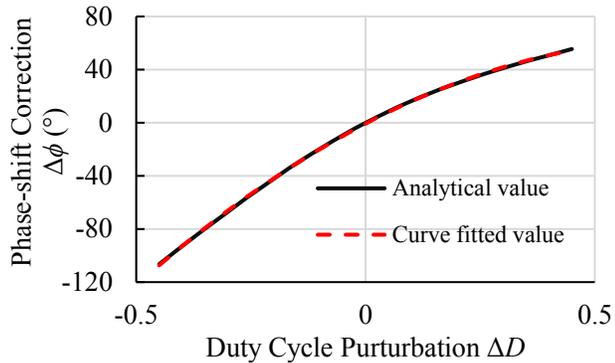
Fig. 4.22: $\Delta\phi$ vs. ΔD locus around the operating condition of $\phi_p =60°$ and $D_a=0.5$.

4.6 Simulation Results

In this section, a conventional DWPT system and the proposed system are simulated, and the simulation results are compared. For a fair comparison, the same power level of 25 kW is considered for both systems. Moreover, the DWPT power profile and the nominal primary coil current of both the systems are regulated to the same value. At first, the conventional 25 kW that employs a *track current controller* is simulated in G2V and V2G operating scenarios. Afterward, the simulations are repeated for the proposed system model. The proposed system model employs the designed *track current controller* and also the *grid current controller* which operates together along with the proposed buffering unit to implement the control strategy discussed earlier. During a DWPT power cycle, the system sequentially operates in the *precharge phase*, *idle phase*, and *charging phase*, as discussed previously in Section 4.3. The system's performances in each of these three operation phases are evaluated separately. While in the *precharge phase*, the *DC mode* operation of the inverter is employed and while in the *charging phase*, the *dual mode* operation is employed. Inverter's performances in both of these modes are simulated and discussed, as well. A complete DWPT cycle period (containing the three sequential phases) for both G2V and V2G cases are simulated, and consequently, the performances of the *track current controller* and the *grid current controller* are verified. The performances for two different power-buffering levels are investigated, too. Finally, the characteristics of the proposed model are compared with the conventional DWPT system.

4.6.1 Simulations of the Conventional DWPT System (No Buffering Unit Included)

A conventional DWPT system controlled by a *track current control* method is built using MATLAB Simulink environment. Generally, phase-shift modulation is a common method of controlling the coil current, and it has been selected for this system, too. The nominal value of the inverter phase-shift angle ϕ_p is a design parameter, and it is set to 120°. The selected value allows enough room for controlling the primary coil current in

both directions and produces the inverter output voltage of minimum harmonic content. Indeed, at this value, the ratio of the fundamental harmonic to higher-frequency harmonics is maximized, making the harmonics easier for filtering by the compensation network at the primary. The *track current controller* is designed to regulate the primary coil current at 30 A.

Table 4.3 summarizes all parameters of the modeled DWPT system, including the systems power ratings, tuned compensation network parameters, vehicle/coil dimensions, etc.

Table 4.3: Parameters of a 25-kW DWPT system

Parameter	Value
Segment length, L_{seg}	400 m
Vehicle length, l_v	5 m
Primary coil length, l_{coil}	2 m
Vehicle velocity, v	50 mph
TU rated power, P_{max}	25 kW
Grid voltage, V_{DC}	600 V
Battery voltage, V_{bat}	400 V
Rated primary coil current, I_{pri}	30 A
Rated operating frequency, f_s	85 kHz
Primary coil inductance, L_{pri}	200 μH
Secondary coil inductance, L_{sec}	200 μH
Primary series inductance, L_{ps}	29.2 μH
Secondary series inductance, L_{ss}	19.71 μH
Primary series capacitance, C_{ps}	9.15 nF
Primary parallel capacitance, C_{pp}	120 nF
Secondary series capacitance, C_{ss}	19.44 nF
Secondary parallel capacitance, C_{sp}	178 nF

With all these parameters in Table 4.3, the DWPT system is simulated for both G2V and V2G operation scenarios. The inverter voltage and the primary coil current waveforms are shown in Fig. 4.23.
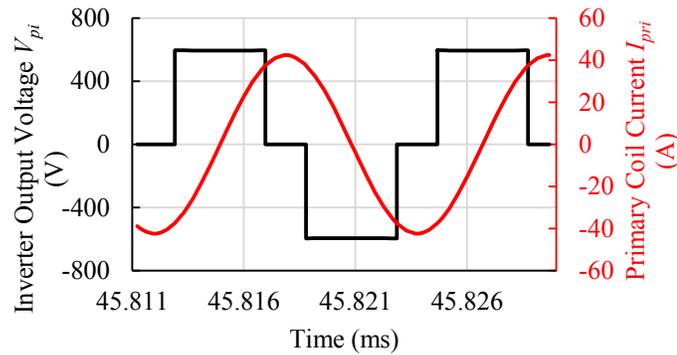
Fig. 4.23: Inverter output voltage V_{pi} and primary coil current I_{pri} waveforms.

Fig. 4.24(a) shows a representative output power P_{out} profile (at the EV side) of the 25-kW system in G2V *charging phase* for the vehicle moving at the speed of v=50 mph over a 2-m long pad. In this charging scenario, the power profile lasts for about 90 ms. The corresponding profiles of the input and output currents are shown in Fig. 4.24(b).
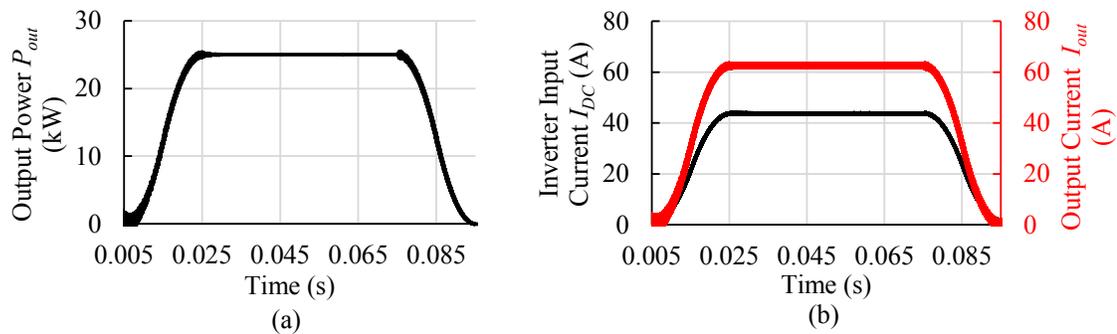
Fig. 4.24: (a) Output power P_{out} (b) inverter input current I_{DC} and inverter output current I_{out} for G2V charging operation.

The inverter switch currents while supplying the full 25-kW G2V power are shown in Fig. 4.25(a) and (b), whereas the corresponding switch currents at the active rectifier side are shown in Fig. 4.25(c) and (d).
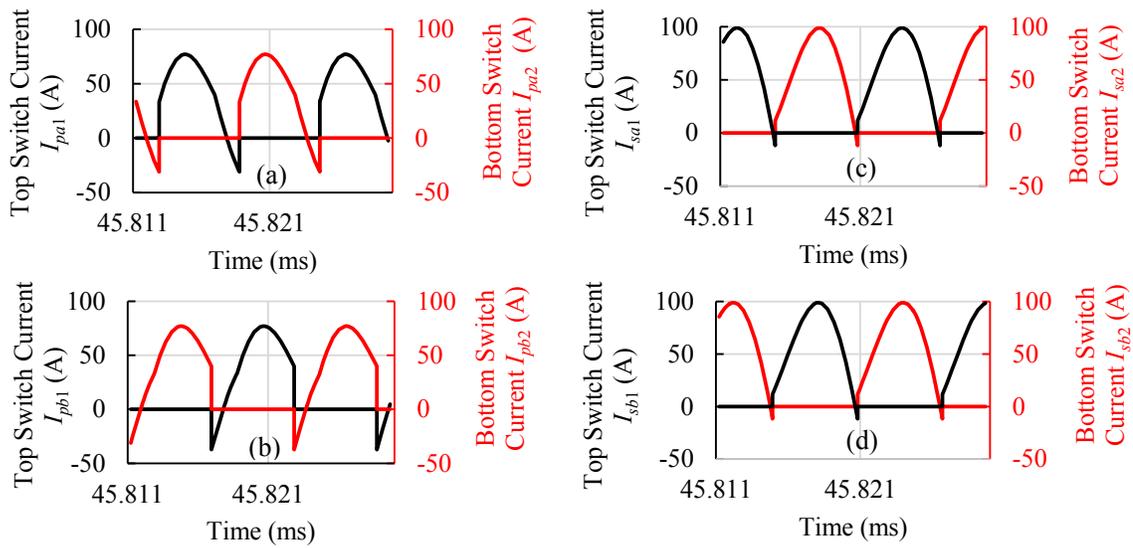
Fig. 4.25: Typical inverter switch currents for (a) leg pa and (b) leg pb, and rectifier switch currents for (c) leg sa and (b) leg sb while supplying the rated power of 25 kW to an EV.

For V2G operation, the same system is simulated with the output power P_{out} profile shown in Fig. 4.26(a). As shown, the negative P_{out} profile at the EV side represents the V2G power flow. The corresponding input current and output current waveforms are also shown in Fig. 4.26(b). The inverter switch currents and the active rectifier switch currents are shown in Fig. 4.27.
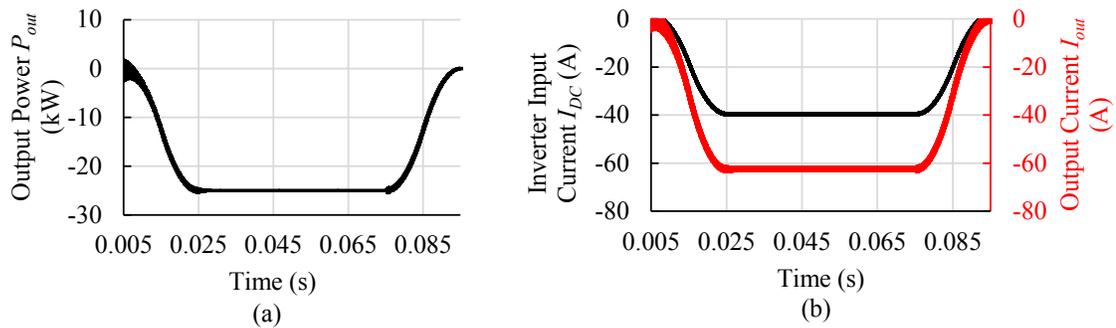
Fig. 4.26: (a) Output power P_{out} and (b) inverter input current I_{DC} and inverter output current I_{out} for V2G charging operation.
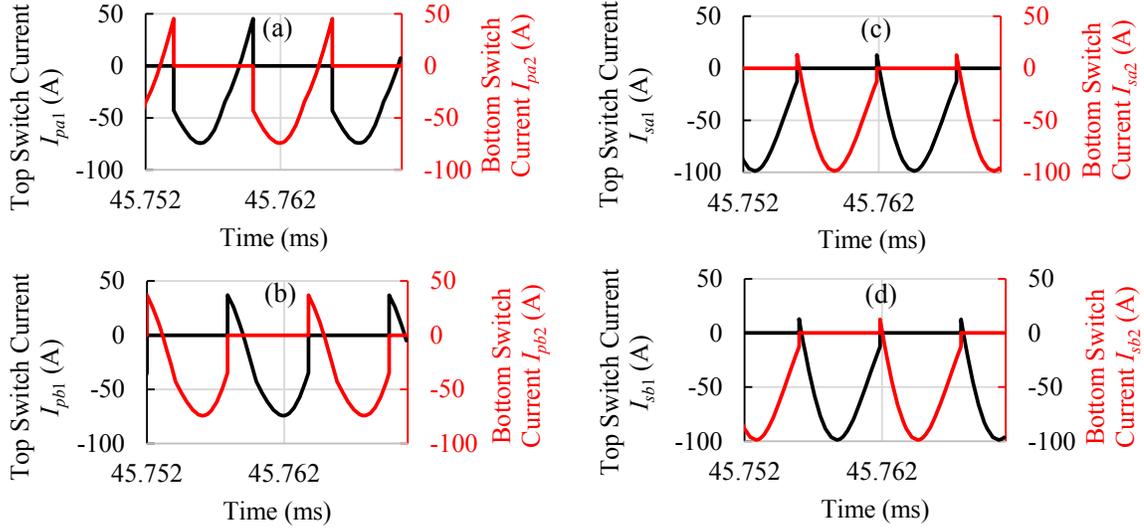
Fig. 4.27: Typical inverter switch currents for (a) leg *pa* and (b) leg *pb*, and rectifier switch currents for (c) leg *sa* and (b) leg *sb* while supplying the rated power of 25 kW to the grid.

4.6.2 Simulation of the Proposed DWPT System with Buffering Unit Included

A 25-kW DWPT system simulation model with the proposed energy buffer unit is built-in MATLAB Simulink environment. Table 4.4 is the extension of Table 4.3 providing the specifications of the system with the buffering unit deployed. Compared to the conventional system without the buffering unit, the nominal phase-shift angle is selected to be $\phi_p = 60°$ instead of 120°. It has been done to extend the controllable range of the inverter duty cycle to maintain track current regulation (as discussed in Section 4.5.4). This ϕ_p=120° operating point results in modified compensation parameters, which are also listed in Table 4.4. The capacitance of the SC buffering unit is selected to be 1 F for a targeted power buffering level of $F_{p,buffer}$=75% at the grid side.

The 25-kW system is simulated for different G2V and V2G operating scenarios, and the simulation results are presented to validate the system's functionality in *precharge*, *idle*, and *charging phase*s. These three phases, along with the *track current controller* and the *grid current controller*'s effectiveness for both G2V and V2G applications, are discussed in detail in the next subsections as follows.

Table 4.4: System parameters with the buffering unit

Parameter	Value
Primary series inductance, L_{ps}	16.85 H
Secondary series inductance, L_{ss}	19.71 H
Primary series capacitance, C_{ps}	19.14 nF
Primary parallel capacitance, C_{pp}	207.9 nF
Secondary series capacitance, C_{ss}	19.44 nF
Secondary parallel capacitance, C_{sp}	178 nF
Choke inductance, L	0.7 mH
Supercapacitance, C_{SC}	1 F

4.6.2.1 Precharge Phase Simulation

The *precharge phase* takes place at the initial startup of the system, and also at the end of a DWPT power transfer cycle. In this phase, the system operates in the *DC mode* to precharge the SC to the predefined operating voltage of 250 V. As discussed, the selected precharge frequency is chosen to be 140 kHz, i.e., greater than the operating frequency ($f_{prechg} > f_s$) to prevent perceivable primary coil current. The *track current controller* is deactivated in this phase, and the *grid current controller* maintains a constant grid current with its FFFB type control action, consequently, resulting in an approximately constant charging current for the SC. In order to determine the grid current set point at the *precharge phase*, $F_{p,buffer}$ factor plays an important role. The purpose of precharging is to replenish the SC energy used by the previous DWPT pulse before the next vehicle arrives so that the SC can continuously operate cycle after cycle. From the safe trailing distance rule, it is assumed that there is at least a distance corresponding to $T_{off}=2$ s between two consecutive vehicles. Thereby, the SC precharge current should be set in order to replenish the used SC energy (during the *charging phase* period T_{on}) in 2 s. With this consideration, the precharging current reference for the *precharging phase* can roughly be calculated as:

$$I_{DC,prechg,ref} = \frac{P_{max}F_{p,buffer}T_{on}}{V_{DC}T_{off}} \tag{4.54}$$

From (B.36), the precharge current is calculated as 1.5 A. With this reference current for

the *grid current controller*, a simulation is carried out of the *precharge phase* for the proposed 25-kW DWPT system. The inverter output voltage V_{pi} waveform shown in Fig. 4.28(a) verifies the *DC mode* operation. The primary coil current I_{pri} waveform during the *precharge phase* is depicted in Fig. 4.28(b).
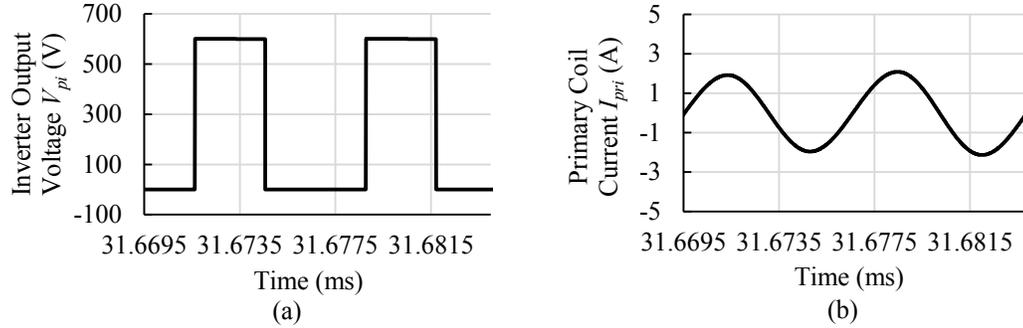
Fig. 4.28: (a) The inverter output voltage V_{pi} and (b) primary coil current I_{pri} waveforms during the *precharge phase*.

The grid current profile during the whole *precharging phase* is shown in Fig. 4.29(a), suggesting a successful grid current regulation at 1.5 A. In order to maintain the grid current regulation, the *grid current controller* applies an FFFB type control action ΔD determined by (4.46). The proportional gain K_p in (4.46) dedicated for the *precharge phase* is chosen to be $1/1200$ for this application.
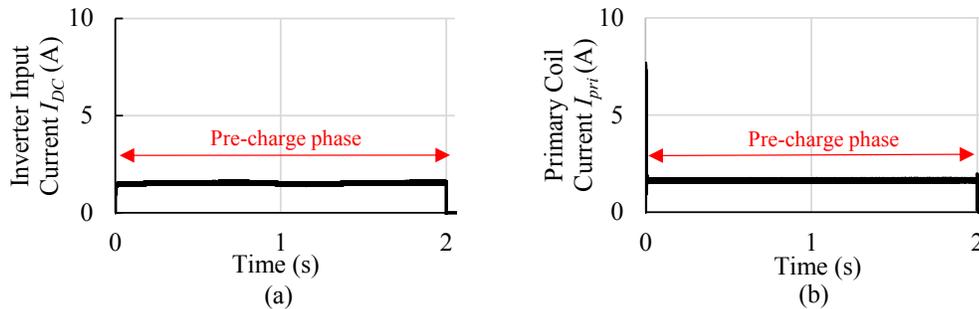
Fig. 4.29: (a) Grid current I_{DC}, and (b) primary coil current I_{pri} (RMS value) during the *precharge phase*.

Operating at f_{prechg} reduces the primary current level down to a very low value of

about 1 A throughout the *precharge phase*, as illustrated in Fig. 4.29(b). Fig. 4.30(a) and (b) shows the SC voltage and current during the *precharge phase*. It is also observed that perceivable SC current ripple(%) is present at the SC current. This is due to the fact that the choke inductance L is selected with a peak-to-peak ripple consideration based on the *charging phase* operating condition where the SC current level is much higher ($\geq$ 80 A). Another fact considered while selecting the inductance value is that smaller inductance ensures faster response of the buffering unit at DWPT load transients. Due to these reasons, the selected inductance results in a higher percentage of peak-to-peak ripple at very low current.

It is observed from Fig. 4.30(a) that the SC voltage V_{sc} linearly increases throughout the *precharge phase*. At $t = 2$ s when V_{sc} reaches 250 V, the *precharging phase* is terminated by the *grid current controller*. Consequently afterward, I_{sc} reduces down to zero and V_{sc} stays at the value of 250 V.
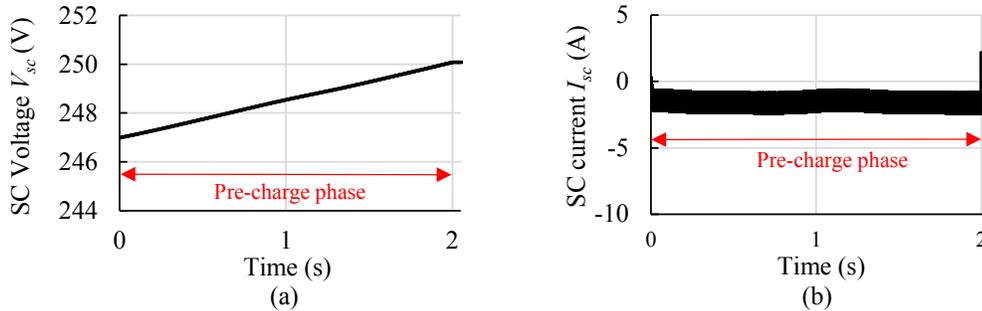
Fig. 4.30: (a) SC voltage V_{sc} and (b) SC current I_{sc} during the *precharge phase*.

4.6.2.2 Idle Phase Simulation

The *idle phase* is reached immediately after the *precharge phase* is over. A simulation scenario of the *idle phase* is depicted in Fig. 4.31. During this phase, the inverter is turned off to prevent further charging of the SC, and also to reduce system losses. As shown in Fig. 4.31(a), the grid current drops to zero as this phase begins. Also, since the inverter is turned off, the primary coil current drops to zero, too, as shown in Fig. 4.31(b). The *idle*

phase lasts until the initiation of the *charging phase*, which gets triggered by a VDS signal. For this simulation, the *idle phase* lasts from $t=2$ s to $t=2.1$ s. The SC voltage and current waveforms in Fig. 4.32 shows that the SC is resting idly at 250-V level, with a zero current throughout the *idle phase*.
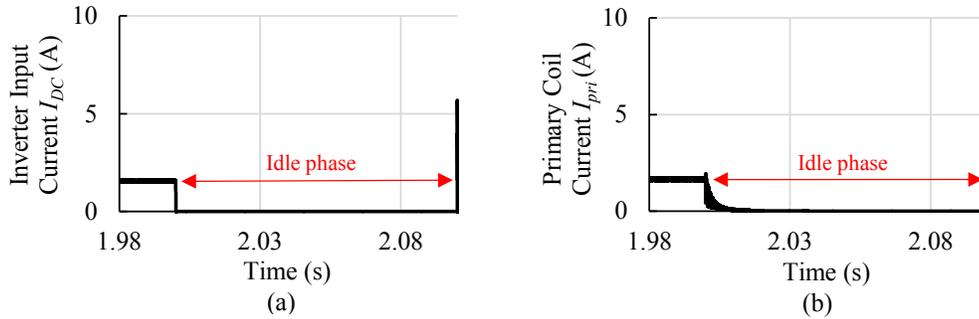
Fig. 4.31: (a) The grid current I_{DC} and (b) the primary coil current I_{pri} (RMS value) during the *idle phase*.
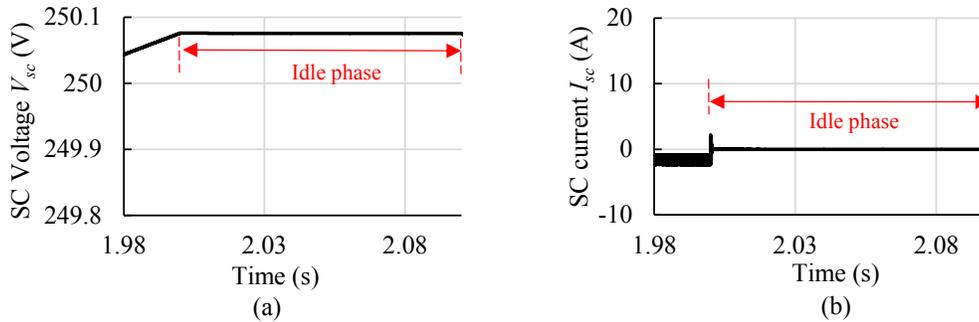
Fig. 4.32: (a) SC voltage V_{sc} and (b) SC current I_{sc} during the *idle phase*.

4.6.2.3   Charging Phase Simulation (G2V)

The *charging phase* is reached as soon as the system gets a VDS signal (at $t = 2.1$ s), indicating the arrival of an EV on top of the primary. Upon receiving this signal, the system immediately switches to the operating frequency of $f_s = 85$ kHz. Consequently, both the *track current controller* and the *grid current controller* are turned on.

The FFFB type control action from the *grid current controller* ensures that the grid

current ramps up to a reference value of $I_{DC,chg}$. This grid current reference at the *charging phase* depends on the chosen power buffering level, $F_{p,buffer}$. For the chosen case of 75% power buffering of the SC unit, the peak power rating of the grid is reduced by 75%. With this constraint, for a 25-kW DWPT system, the grid is expected to supply 10.4 kW, calculated from:

$$P_{avg} = P_{max}(1 - F_{p,buffer}) \tag{4.55}$$

For the *charging phase*, the average grid-current setpoint is then calculated to be 10.4 A, using the following equation:

$$I_{DC,chg} = \frac{P_{avg}}{V_{DC}} = \frac{P_{max}(1 - F_{p,buffer})}{V_{DC}} \tag{4.56}$$

As shown in Fig. 4.33(a), the inverter input current ramps and settles to a value of 10.4 A. The controller parameter K_p in (4.46) for the *charging phase* is chosen to be 1/120 for the FFFB type control action of the *grid current controller*. Throughout the DWPT cycle, this 10.4 A current level is approximately maintained at the grid side by the *grid current controller*. Effectively, this current level ensures a corresponding average of 25% of the DWPT power to the vehicle from the grid, whereas the SC unit supplies the remaining 75% of the DWPT power to the vehicle.

Fig. 4.33: (a) The grid current I_{DC} and (b) the primary coil current I_{pri} (RMS value) during the *charging phase* in G2V operation with FFFB type control action of the *grid current controller*.

As shown in Fig. 4.33(b), the *track current controller* makes the primary coil current settle to a regulated 30-A value. It can also be observed that this regulation is maintained throughout the *charging phase*.

From Fig. 4.33(a), it can be observed that the grid current tends to undergo a slight overshoot at the moment of the rising edge of the P_{out} profile and also a slight undershoot at the falling edge of the P_{out} profile due to the inability of the proportional feedforward controller to track the constant slop power load. The performance of grid current regulation during these two edges could be improved by deploying a differential control [102] in addition to the proposed proportional control for the feedback term in (4.46). However, adding a differential control generally makes the controller noise-prone and would increase the control complexity. Since the current variation is limited to a relatively low value of ± 1 A which corresponds to only 2.4% of the grid power, the differential type control is omitted in this design.

The G2V output power P_{out} profile delivered to the vehicle is shown in Fig. 4.34(a). Fig. 4.34(b) depicts the inverter output voltage V_{pi} and the primary coil current I_{pri} waveforms during the *charging phase*. It can be observed that the inverter operates in its *dual mode*, where the output voltage possesses both the AC component and DC components in order to achieve both the track current and grid current controls.
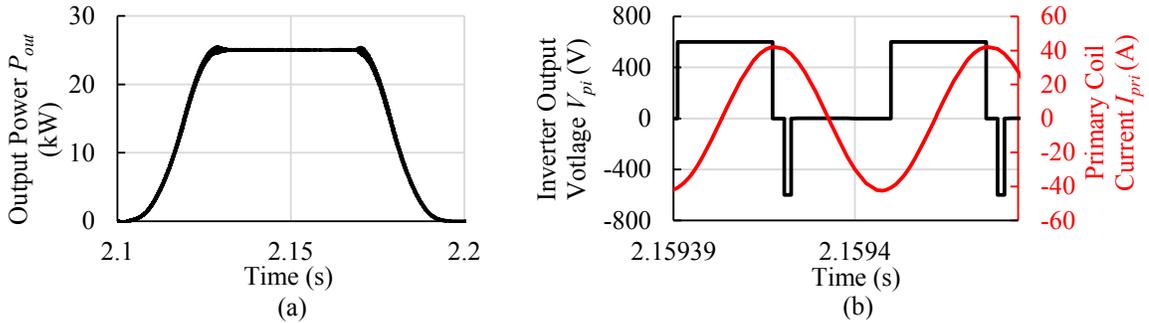
Fig. 4.34: (a) The output power P_{out} profile during the *charging phase* in G2V operation (b) the inverter output voltage V_{pi} and the primary coil current I_{pri} waveforms at one point during the *charging phase* with FFFB type control action of the *grid current controller*.

Fig. 4.35 illustrates the SC contribution in supplying the transient part of a DWPT load. It can be observed that the SC is dominantly discharged during the DWPT period with a discharging current of about 80 A. The end of a DWPT cycle is sensed by the controller as the moment when the SC current changes its direction and starts charging from the grid, as a result of the loss of DWPT load. At this point, the controller terminates the operation, and the *charging phase* is over.

Fig. 4.35: (a) SC voltage V_{sc} and (b) SC current I_{sc} during the *charging phase* in G2V operation with FFFB type control action of the *grid current controller*.

Alternatively, in case the *grid current controller* is designed to take a *bang-bang type* control action in the *charging phase*, it similarly starts together with the *track current controller* at the beginning of the *charging phase*. The controller starts applying the constant decremental duty cycle D_{dec} as soon as the I_{DC} starts increasing, indicating the arrival of DWPT load. The $I_{sc,lim}$ for the bang-bang controller can be roughly set corresponding to the buffering-level as follows:

$$I_{sc,lim} = \frac{P_{max}F_{p,buffer}}{V_{SC,init,chg}} \tag{4.57}$$

where $V_{SC,init,chg}$ is the V_{sc} setpoint corresponding to the beginning of the *charging phase*. With this limit, and with the controller parameter D_{dec}=0.05, the DWPT system simulation is carried out in G2V operation.

Fig. 4.36 illustrates the SC voltage and current during the *charging phase* with bang-bang type control. It can be observed that the SC is discharged during the DWPT period

with a constant current of about 80 A. The end of a DWPT cycle is sensed by the controller as the moment when the I_{DC} changes its direction and starts charging from the grid, as a result of the loss of DWPT load. At this point, the controller applies a negative D_{dec} to bring the SC current back to zero, and the *charging phase* is over. Fig. 4.37 shows the corresponding I_{DC} and I_{pri} profile.
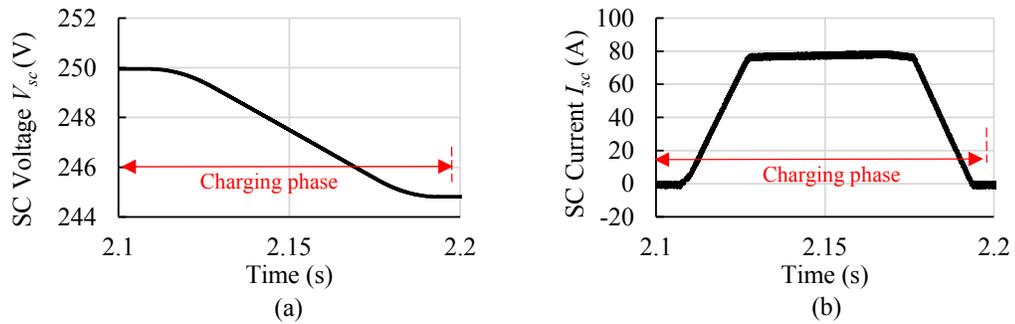
Fig. 4.36: (a) SC voltage V_{sc} and (b) SC current I_{sc} during the *charging phase* in G2V operation with bang-bang type control action of the *grid current controller*.
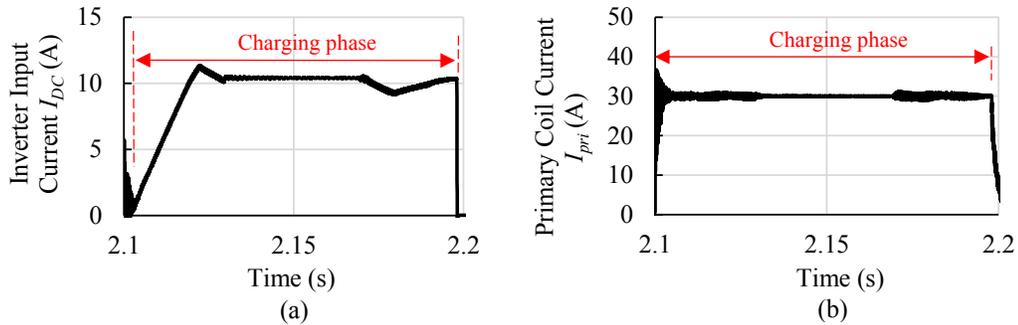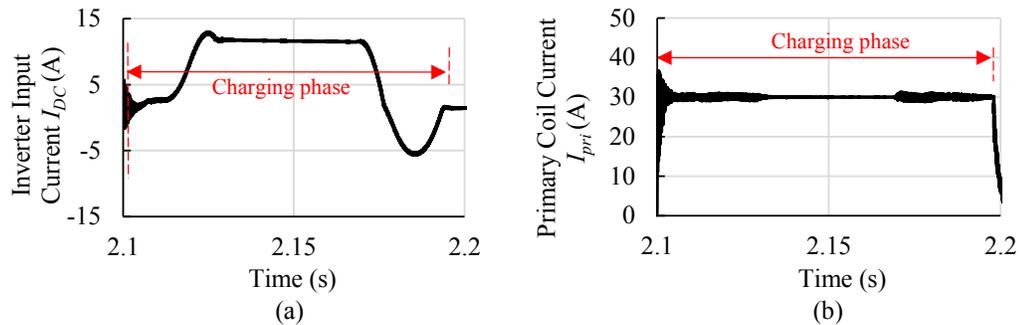

Fig. 4.37: (a) The grid current I_{DC} and (b) the primary coil current I_{pri} (RMS value) during the *charging phase* in G2V operation with bang-bang type control action of the *grid current controller*.

4.6.2.4 Charging Phase Simulation (V2G)

The proposed control method is capable of successfully operating in a V2G *charging phase*. To prove that, A V2G charging simulation is carried out with similar *precharge phase* and *idle phase* conditions as the G2V operation. At the beginning of the *charging phase*,

the system gets a notification by the VDS signal about the arrival of a vehicle. For the case of FFFB-type control implementation in the *charging phase*, *grid current controller* applies a negative 10.4-A current reference $I_{DC,chg}$ to the *grid current controller* in the *charging phase*. This way, the *grid current controller* ensures that the SC buffering unit captures 75% of the transient part of the DPWT power profile coming to the grid, while the grid still maintains a constant average charging current to the grid throughout the *charging phase*, as shown in Fig. 4.38(a). The *track current controller* operation works similar to the G2V operation, which is observed from Fig. 4.38(b).
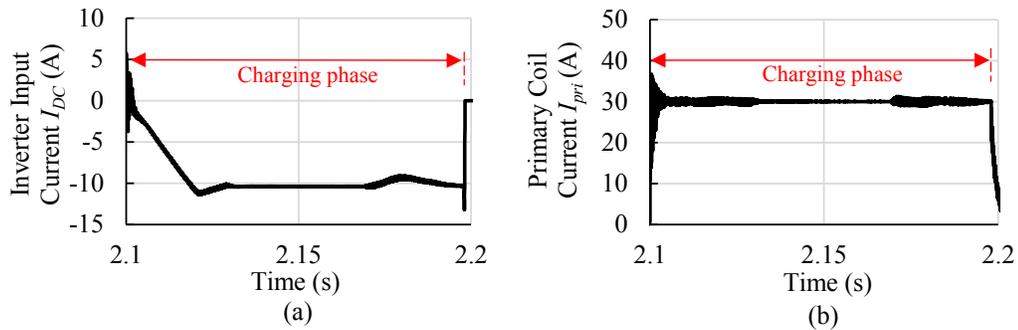
Fig. 4.38: (a) The grid current I_{DC} and (b) the primary coil current I_{pri} (RMS value) during the *charging phase* in V2G operation with FFFB type control action of the *grid current controller*.

Fig. 4.39 depicts the output power profile for the V2G power transfer. The negative value of the P_{out} power profile at the EV side proves that DPWT power is being transferred from the vehicle side to the grid side. Fig. 4.40 illustrates how the SC captures the transient V2G power throughout the *charging phase* by charging itself with a 70-A current at full rated power. At the end of the V2G cycle, the SC current changes its direction and starts discharging due to the loss of V2G power coming to the grid. At this point, the system senses the change in the direction of I_{sc} and terminates the *charging phase* operation.
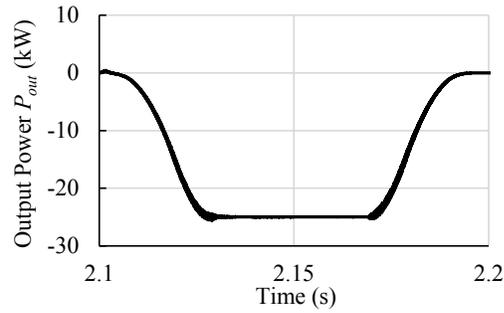
Fig. 4.39: The output power P_{out} profile during the charging phase in V2G operation with FFFB type *grid current controller*.
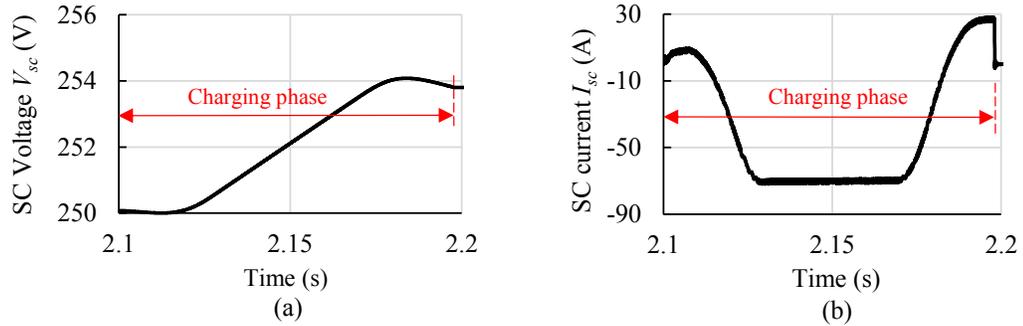
Fig. 4.40: (a) SC voltage V_{sc} and (b) SC current I_{sc} during the *charging phase* in V2G operation with FFFB type *grid current controller*.

Similarly, if a bang-bang type control action is implemented for the charging phase, *grid current controller* is set up with a $I_{sc,lim}$= -80 A for achieving 75% power-buffering. The simulation results are shown in Fig. 4.41 and Fig. 4.42.
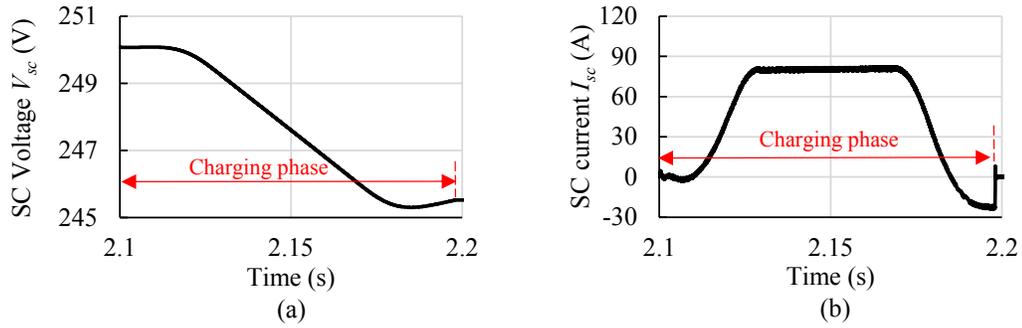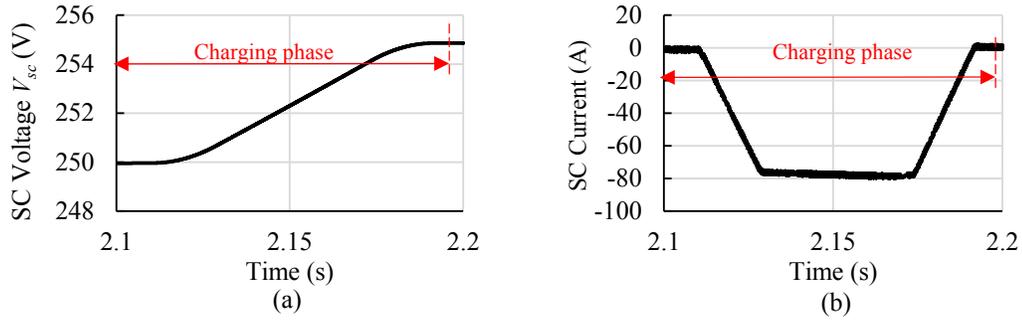
Fig. 4.41: (a) SC voltage V_{sc} and (b) SC current I_{sc} during the *charging phase* in V2G operation with bang-bang type control action of the *grid current controller*.
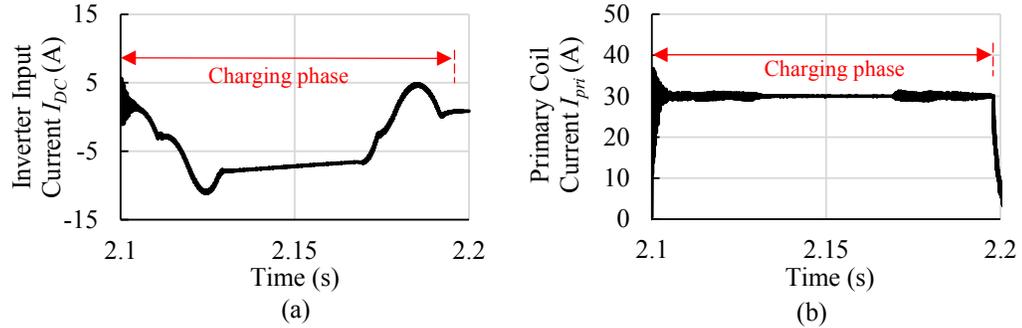
Fig. 4.42: (a) SC voltage V_{sc} and (b) SC current I_{sc} during the *charging phase* in V2G operation with bang-bang type control action of the *grid current controller*.

4.6.2.5 Effect of Different Power Buffering Levels

In order to compare the system's performances with different power buffering levels, two different cases of $F_{p,buffer}$ are considered, 75% and 87.5%. The same *grid current controller* is employed in both scenarios. However, to support a higher buffering level, an increased sizing of SC is recommended, as discussed in Section 4.4.1. In this case, to accommodate 87.5%, the SC unit is increased by 0.5 F. Similarly, at higher $F_{p,buffer}$ level, the SC current level and consequently, its ripple current would increase. For this reason, the choke inductance L is slightly increased to prevent SC ripple current from increasing and also to achieve better control at this higher power buffering level. Table 4.5 tabulates the buffering unit sizes finally adopted for simulations.

Table 4.5: Buffering unit parameters for different $F_{p,buffer}$ levels

$F_{p,buffer}$	C_{SC}	L
75%	1 F	0.7 mH
87.5%	1.5 F	1.1 mH

From (4.56), the reference $I_{DC,chg}$ for $F_{p,buffer}$=87.5% is calculated to be 5.2 A. With this constraint, a G2V simulation for $F_{p,buffer}$ =87.5% is carried out. Fig. 4.43(a) compares the inverter input currents for the two different buffering levels at the *charging phase* of the G2V operation. Fig. 4.43(b) compares the SC current levels for the two levels of power buffering at the *charging phase.* It is observed that the grid current is regulated at 5.2 A for the $F_{p,buffer}$ =87.5% case. Also, to ensure this reduced level of current at the inverter input side, the SC current increases, as shown in Fig. 4.43(b).
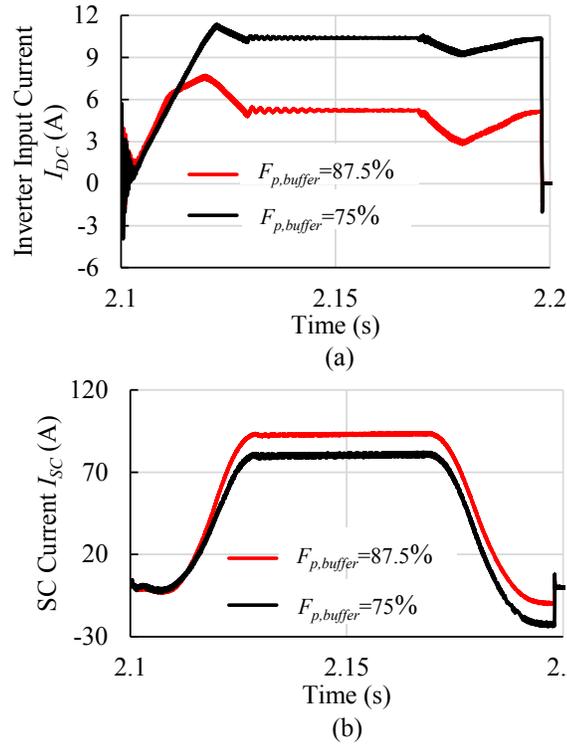
Fig. 4.43: Comparison of different power-buffering levels in the *charging phase* of a G2V operation: (a) inverter input current profile and (b) corresponding SC current profile.

Fig. 4.44 compares the inverter input current for the full DWPT cycle containing the *precharge phase*, *idle phase*, and *charging phase* for the two levels of $F_{p,buffer}$. The needed for $F_{p,buffer}$=87.5% is calculated to be 1.6 A, according to (4.54). At the precharge phase, 1.6 A current regulation is maintained for $F_{p,buffer}$=87.5% case, whereas a 1.5A level is maintained for $F_{p,buffer}$=75% case. There is no difference in the *idle phase*, as the system is turned off during this phase in both cases. Finally, the *charging phase* simulation results prove that a successful grid-side current and power reduction of 75% and 87.5% is achieved with the two respective simulation setups.
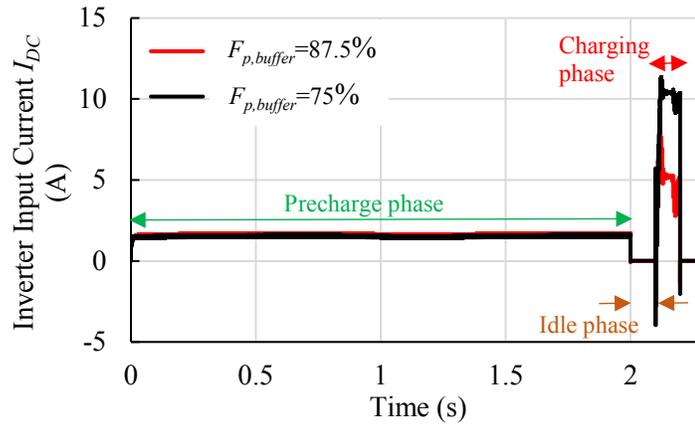
Fig. 4.44: The comparison of inverter input current profiles (G2V operation) for two different levels of (75% and 87.5%) grid-side energy buffering. The entire DWPT cycle is shown.

4.6.3 Comparison of the Proposed and Conventional DWPT Systems

To evaluate the advantages and disadvantages of the proposed 25-kW system compared to a conventional 25-kW DWPT system, the simulation results found from the two systems are analyzed in this subsection. Fig. 4.45 shows the inverter input current I_{DC} profile of the proposed system for a full G2V cycle containing the *precharge phase*, *idle phase*, and *charging phase*. A conventional DWPT system's input current profile for the same G2V operation is also plotted in Fig. 4.45, assuming similar conditions (T_{off}=2 s, v=50 mph, $l_{coil} = 2$ m). It can be observed from Fig. 4.45 that when the buffering unit is not employed, I_{DC} is zero throughout the T_{off} period, whereas the proposed system uses 1.5 A current

from the grid to precharge the SC buffering unit. In the *idle phase*, there is no difference between the two systems as in both systems the inverter is off. However, in the *charging phase*, the peak value of the inverter input current reduces from 44 A to 10.4 A in the case of the proposed system, as shown by the green arrow. Effectively, there is a significant 75% reduction of the peak value of I_{DC} in the proposed system compared to the conventional system of the same power rating. In effect, the proposed system buffers energy from the grid to charge the SC unit throughout the T_{off} period, and the SC utilizes that energy throughout the T_{on} period to reduce the peak I_{DC}. In other words, successful grid-side buffering is ensured, which is advantageous to the grid side.
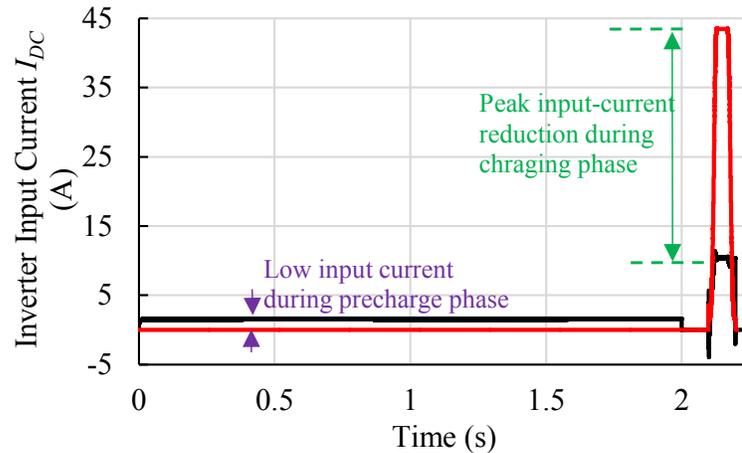
Fig. 4.45: Comparison of inverter input current profile (G2V mode) of the system without the buffering unit and with the 75%-buffered case of the proposed system.

The output power P_{out} profiles of a conventional 25-kW system and the proposed system are depicted in Fig. 4.46, where it is observed that the profiles are the same for both cases. This proves that the proposed system operation provides grid-side energy management while not compromising the power profile delivered to the vehicle.

Despite providing significant grid-side energy buffering benefits, the proposed system has some disadvantages. Fig. 4.47 compares the switch currents of the inverter while supplying a 25-kW G2V power to the EV. It can be observed that compared to the switch currents of a conventional system in Fig. 4.47(a) and (b), the peak switch current is increased in the
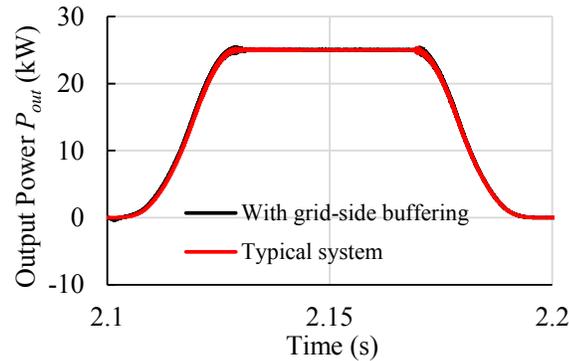
Fig. 4.46: The comparison of the output power P_{out} of the system without the buffering unit and with the 75%-buffered case of the proposed system.

case of the system with a buffering unit (Fig. 4.47(c) and (d)). Consequently, this would result in an increased level of stress and losses in the inverter switches.
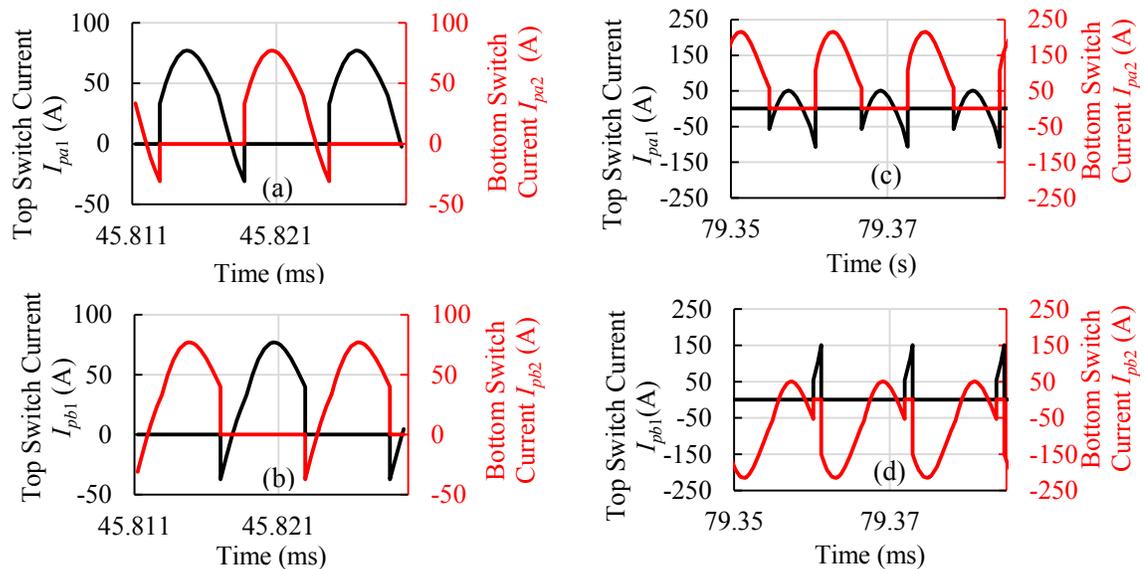
Fig. 4.47: The inverter switch currents in the systems without the buffering unit for (a) leg pa and (b) leg pb; the inverter switch currents in proposed system for (c) leg pa and (d) leg pb. Waveforms are taken during the rated 25-kW G2V power transfer.

Although the system suffers from increased switch-losses, the proposed solution for grid-side energy buffering is still advantageous, as the conventional system would require an extra power electronic converter unit (Fig. 4.48(a)) to achieve grid-side power-buffering,

which would add volume, cost and introduce its own power losses to the system.
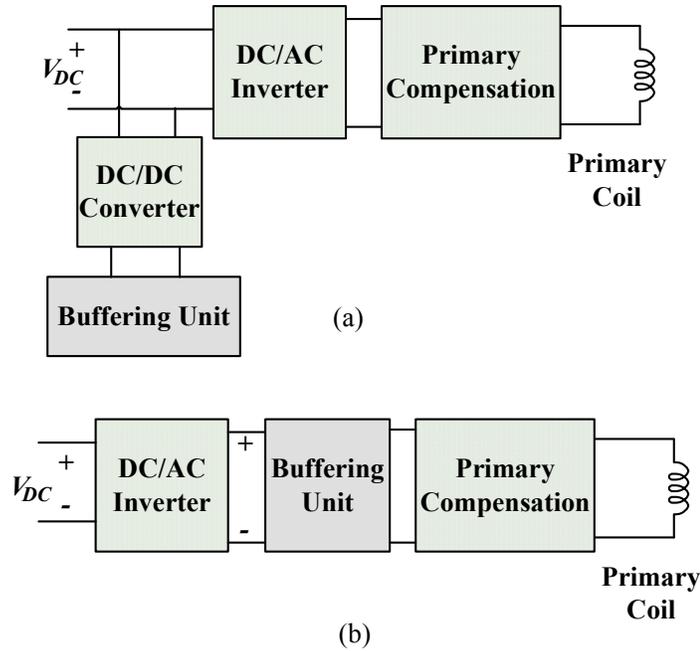
Fig. 4.48: (a) Conventional system with active grid-side energy buffering (b) proposed system with active grid-side energy-buffering

4.7 Experimental Results

In this section, the hardware and controller design of an experimental prototype are presented. For validating the functionality of the proposed grid-side energy management circuitry for G2V/V2G applications, an experimental hardware prototype is built. For implementing a proof-of-concept design, a benchtop setup is assembled. An overview of the system, followed by the details of each system component, is discussed. Afterward, the experimental results are presented, and the effectiveness of the proposed system is discussed.

4.7.1 System Overview

In EV roadways, a DWPT power profile's shape results from the M profile between the primary and secondary coils, as previously derived in (2.27).

However, in a stationary setup, M between primary and secondary is constant, and thereby, some other modulating parameter needs to be employed to produce the wanted

DWPT power profiles. In Chapter 2, it has been proved how DWPT power profile can be controlled by the secondary side control parameters ϕ_s or θ. Using either ϕ_s or θ angle profile at the bench setup, it becomes possible to emulate and test different types of power profile that correspond to different vehicle speeds and coil geometries. Due to this benefit, and also for the sake of easier test measurements, a benchtop setup is implemented.

Fig. 4.49 shows a simplified block diagram of the system hardware prototype. An OPAL-RT controller unit is used to implement the *track current controller* and *grid current controller*. These controllers are implemented using MATLAB Simulink blocks in the OPAL-RT device. Analog input/output channels are used to interface the controllers with the hardware.
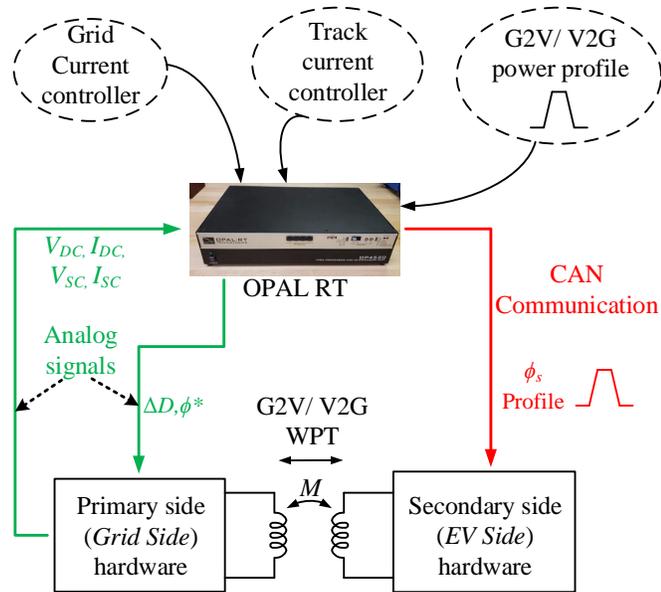
Fig. 4.49: System block diagram of the experimental prototype.

The *track current controller* senses the I_{pri} via an analog input channel and calculates ϕ_p^* which is then sent to the primary-side hardware via an analog output channel. Similarly, the *grid current controller* accepts V_{SC}, I_{SC}, and I_{DC} signals sent from the hardware to OPAL-RT's analog input channels. All four signals are measured at the hardware side using appropriate sensors, and a voltage equivalent of the sensed signal is then delivered to OPAL

inputs. Successively, OPAL-RT calculates and sends its control action ΔD via an analog output channel to the primary-side hardware. At the secondary, θ or ϕ_s profile is sent by OPAL to the secondary side hardware utilizing the Control Area Network (CAN) communication protocol to generate a desired DWPT power profile. With all these controllers implemented, the system is tested for different DWPT power profiles. The individual system components are discussed as follows.

4.7.1.1   OPAL-RT Unit

Prior to hardware implementation, the designed DWPT system is simulated using MATLAB Simulink environment. For faster and easier development of the experimental version of the two controllers without a complex microcontroller/FPGA coding, an OPAL-RT OP4520 Hardware-In-the-Loop (HIL) testing equipment [103] is utilized. OPAL-RT is capable of running controllers developed in Simulink environment on a dedicated real-time computing platform. This real-time platform facilitates the interfacing of the controllers with external hardware for HIL development. The controller interface with the external hardware is done using analog I/O channels provided in the OPAL-RT unit used for this experiment. With the OPAL-RT's real-time simulator, the controllers' functions can be rapidly evaluated in a testing environment, which facilitates rapid control prototyping (RCP), i.e., fast and smooth implementation/retuning of controllers throughout the system development stages. Fig. 4.50 shows the OP4520 model used for this application. Fig. 4.51 shows the controller implementation inside an OPAL-RT Simulink environment.

Fig. 4.50: OP4520 unit.
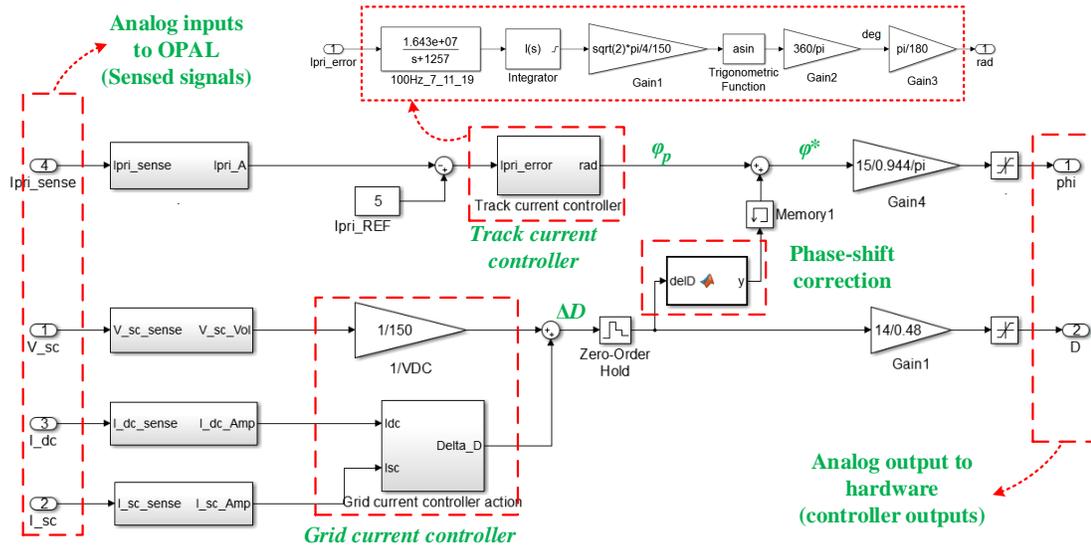
Fig. 4.51: The *track current controller* and *grid current controller* implemented in OPAL-RT simulator using the Simulink environment.

4.7.1.2 Inverter and Rectifier Unit

For the inverter at the primary-side and the active rectifier at the secondary side, Cree CCS050M12CM2 Silicon Carbide (SiC) Modules have been used. Each of these modules contains six high-speed, low-loss SiC MOSFETs. CGD15FB45P1 gate driver boards are used to drive the inverter and the rectifier modules. CGD15FB45P1 board is equipped with six isolated MOSFET drives. However, only four MOSFETs need to be driven in the inverter and the rectifier for this application. Accordingly, the other two MOSFETs of the modules are ensured to be always turned off using their respective gate signal inputs. The design of CGD15FB45P1 is directly soldered on the top of a CCS050M12CM2 SiC module, as shown in Fig. 4.52. This way, the unwanted trace inductances between the driver and the MOSFETs are minimized, which is a desirable feature for high-frequency applications.
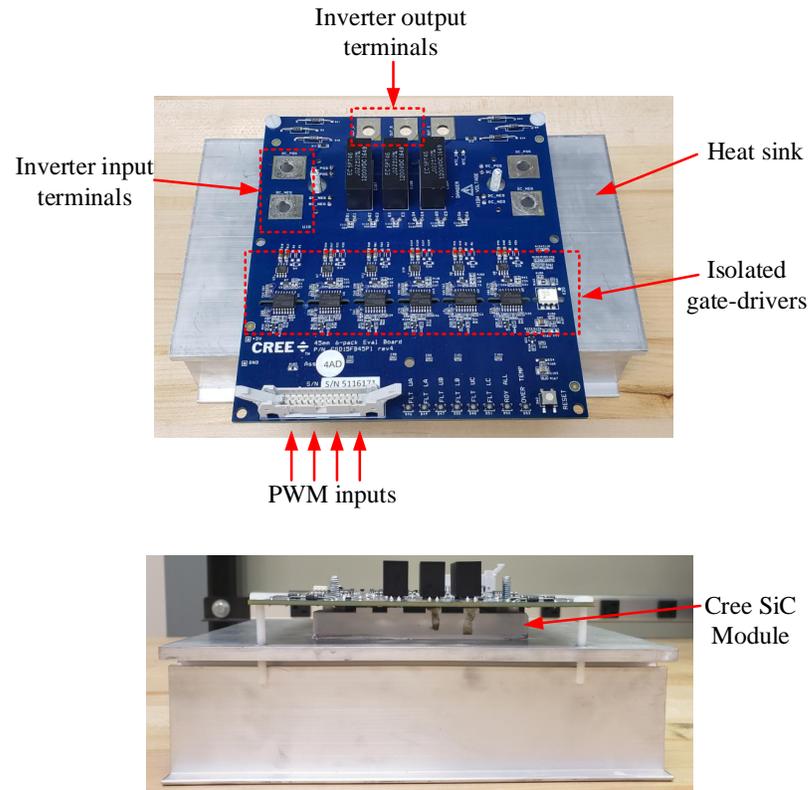
Fig. 4.52: Cree CGD15FB45P1 driver board and CCS050M12CM2 SiC module mounted on a heat-sink.

Some of the added features of this model include short circuit protection, over-temperature protection, and under-voltage protection. In addition, the module and the corresponding inverter can be reset by means of a *RESET* input, which provides the option to turn off the inverter intelligently during operation. Table 4.6 summarizes some of the key specifications of the driver and switch modules.

Table 4.6: Specifications of the Cree CCS050M12CM2 SiC module and the CGD15FB45P1 driver board

Parameter	Value
Gate driver supply voltage	15 V
Maximum switching frequency	250 kHz
Continuous drain current	59 A
Rated Drain-to-Source voltage	1200 V
On state switch-resistance	25 mΩ
Total gate charge	180 nC

4.7.1.3   Energy Bufering Unit

The buffering unit contains the choke inductor L and SC unit C_{SC}, as discussed in Section 4.1. A Maxwell BMOD0083 P048 B01 module available in the lab is used as the SC of the system prototype. A choke inductor capable of handling the desired charging/discharging current levels of the SC is selected. A 1-mH value of L is selected to provide adequate smoothening of the SC current. Fig. 4.53 shows the elements of the buffering unit.

Fig. 4.53: Elements of the energy buffering unit: Maxwell BMOD0083 P048 B01 SC module and a choke inductor.

The SC charging and discharging characteristics are tested in the lab environment. Fig. 4.54 shows a full charging/discharging characterization cycle of the SC module with a constant charging/discharging current of 1 A. Table 4.7 lists some of the operational specifications of the buffering unit elements.
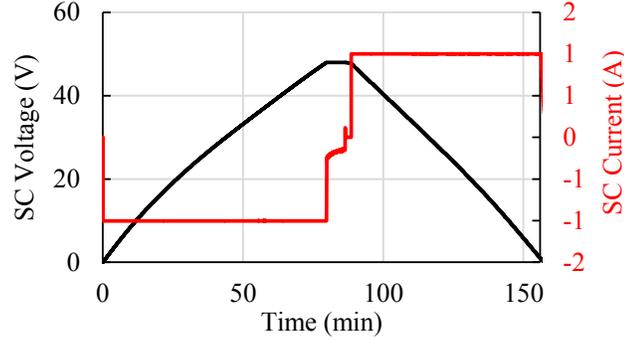
Fig. 4.54: Experimental characteristics of the Maxwell BMOD0083 P048 B01 module.

Table 4.7: Parameters of the energy buffering unit

Parameter	Value
Choke inductance	1 mH
Maximum current rating of choke	30 A
Capacitance of the SC	85 F
SC voltage rating	48 V
SC continuous current rating	61 A
SC ESR	12 mΩ

4.7.1.4 Sensing Coil Unit

In order to accurately profile the G2V/V2G DWPT power transfer between the grid and the vehicle, synchronization between those two is needed. Thereby, a sensing coil arrangement is deployed to sense the phase of the primary-side and synchronize the secondary side with the primary, accordingly. Details about synchronization requirements have already been discussed in Section 2.4.

The sensing coil should be magnetically decoupled from the secondary coil while being moderately coupled with the primary coil. It ensures that the sensing coil senses the primary-side phase without significantly affecting the normal operation of the secondary side. To ensure that, a sensing coil arrangement similar to the one presented in [104] and [105] is adopted. In this sensing coil arrangement, a specially designed bucking coil layout [106] is deployed. This layout ensures that the sensing coil is effectively decoupled from the secondary coil by means of flux cancelation caused by the alternating direction of turns of the sensing coil.

Fig. 4.55 shows the arrangement of the coil system, illustrating the winding structures and relative positions of the primary, secondary, and sensing coils. In this setup, the sensing coil is placed in between the primary and the secondary coil. However, an alternative layout is also possible where the sensing coil is situated above the secondary coil [105]. However, in that scenario, the Secondary coil should not have any ferrite structure above it.

It can be observed from Fig. 4.55 that coupling M_{23} between secondary and sensing coils is designed to be zero with the help of the alternating winding arrangement. Understandably, the coupling between primary and sensing coil M_{13} is non-zero.
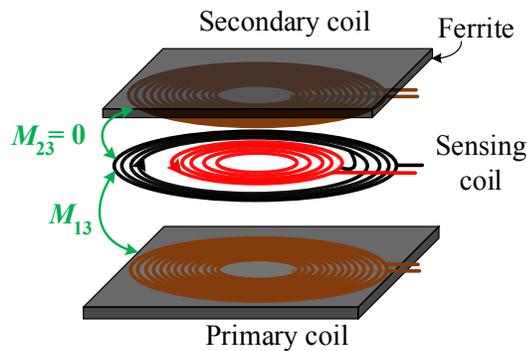
Fig. 4.55: The sensing coil structure configuration.

Fig. 4.56 shows the block diagram of the signal processing unit corresponding to the sensing unit. The primary coil induces open-circuit voltage V_{sense} at the sensing coil which is then processed through a zero-crossing detector and converted into a square-wave signal. This signal is further processed by a PLL. The output of the PLL is used as the external synchronization signal for the microcontroller at the secondary side. The ϕ_s or θ signals which shape the power profile are referenced with respect to the synchronization reference.
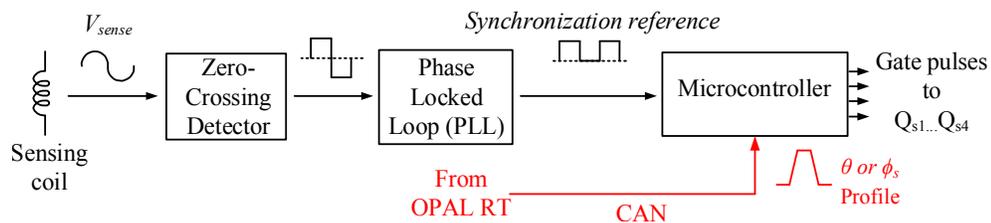
Fig. 4.56: The block diagram of the sensing coil and synchronization circuit.

Fig. 4.57 shows the primary, secondary and sensing coil for the experimental setup.
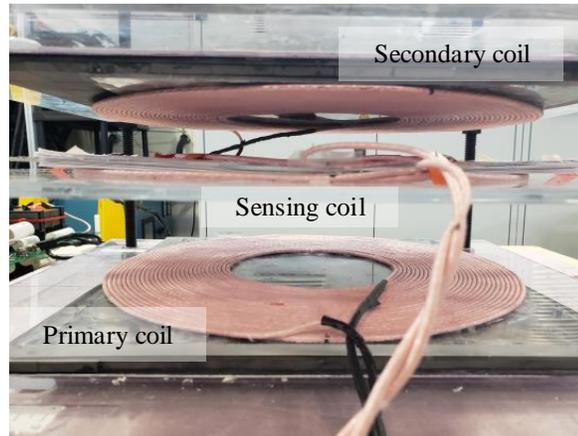
Fig. 4.57: Primary coil, secondary coil, and sensing coil of the experimental setup.

4.7.1.5 Compensation Circuit Design

The compensation circuits of the primary and secondary side is shown is Fig. 4.58. The LCC compensation scheme previously used in the 25-kW system simulation is adopted for the system prototype similarly. For the capacitors in the compensation circuits, Metallized Polypropylene (PP) type film capacitors from Cornell Dubilier Electronics are purchased due to their low ESR and ability to operate at high frequencies. For inductors, ETD59 cores with N87 material have been used. N87-type ferrite material offers high relative magnetic permeability (μ_e=1590) and can operate up to 100 kHz operation frequency, which makes it suitable for this application. For making the coil windings, the inductor windings, and also for interconnections between the compensation and the rest of the circuitry, Litz wire is used due to its reduced ESR at high frequencies. Table 4.8. summarizes the compensation circuit elements for the system tuned at 85 kHz frequency.
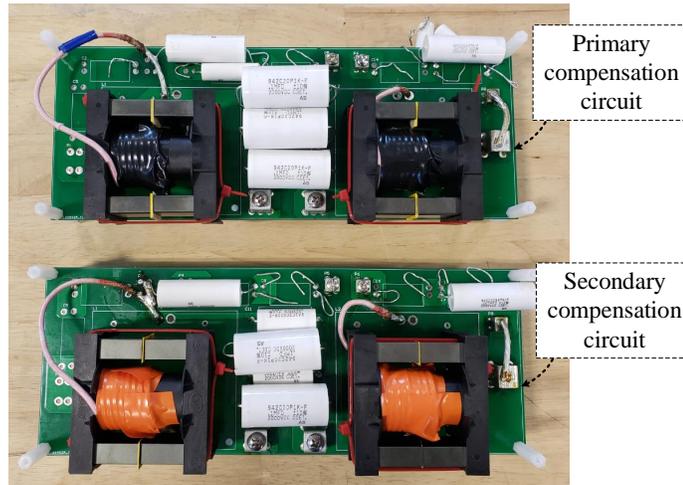
Fig. 4.58: Compensation circuits for the hardware prototype.

Table 4.8: Compensation circuit parameters of the experimental prototype

Parameter	Value
Primary coil inductance, L_{pri}	318.7 μH
Secondary coil inductance, L_{pri}	330.88 μH
Primary series inductance, L_{ps}	35.76 μH
Secondary series inductance, L_{ss}	57.4 μH
Primary series capacitance, C_{ps}	12.39 nF
Primary parallel capacitance, C_{pp}	98.04 nF
Secondary series capacitance, C_{ss}	12.82 nF
Secondary parallel capacitance, C_{sp}	61.084 nF

4.7.1.6   Power Supply Unit

To facilitate G2V/V2G charging, bidirectional power supplies are needed at the primary side as well as the secondary side. For the primary side, a Regatron bidirectional power supply is used. Regatron unit is supplied by a 480 V three-phase AC supply, and contains a transformer unit, followed by a three-phase rectifier unit and one or multiple TopCon DC/DC converters (TC.GSS) units. Each Topcon unit has 32-kW, 500-V, 80-A rating. In

the Regatron unit available in the lab, two of these TopCon units are connected in parallel which results in the rated values of the Regatron to be 500V, 160 A, and 64 kW. At the secondary side, a Gustav Klein (I-TS-3870) bidirectional and four-quadrant power supply is used. It requires a 3-phase 480V AC supply and is rated at 800 V, 1000 A, and 250 kW output. Fig. 4.58 shows the Regatron unit and the Gustav-Klein unit used for this application.

Regatron unit   Gustav-Klein unit
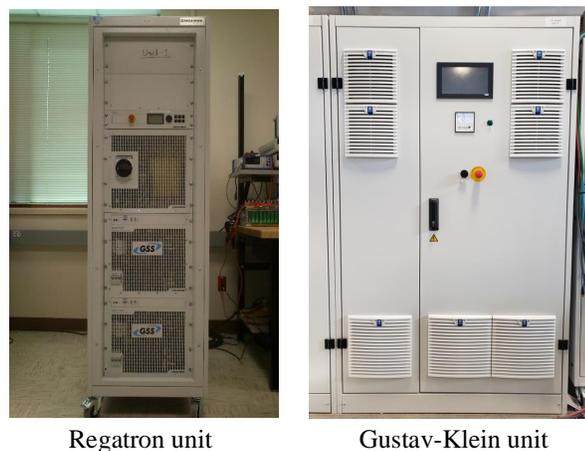
Fig. 4.59: Regatron and Gustav-Klein unit.

4.7.1.7 Microcontroller and Sensors

For both primary and secondary microcontrollers, TMS320F28035 units are used. TMS320F28035 is a 32-bit microcontroller with 60 MHz clock and 128KB FLASH program memory. This model offers a sufficient analog/digital I/Os and CAN communication interface, which is needed for this application. For voltage sensing, precision optically isolated voltage sensor ACPL-C870 is used due to its high gain accuracy $\pm0.5\%$. For DC-current sensing, HO 10-P/SP33 bidirectional hall-effect current sensors are used which has a measurement range of ±25 A. For AC-current sensing, 56T300C is used due to its high bandwidth (200 kHz) and 10-A measurement range, which is ideal for this application.

4.8 Experimental Results

In this section, the system operation of the hardware prototype is discussed in detail. *Track current controller* and *grid current controller* designs and their performance is discussed. The operation of the sensing coil arrangement and PLL circuitry is experimentally validated. Afterwards, the combined system operation is carried out with DWPT charging profile with and without the grid-side energy buffering, and the experimental results are presented, compared and summarized.

Fig. 4.60 shows the experimental setup of the hardware prototype. The setup can be identified as the association of 9 separate units. Unit A is the first unit following the input voltage (V_{DC}) terminals, and it contains DC capacitor bank, protection-fuse, and bleeder resistor.
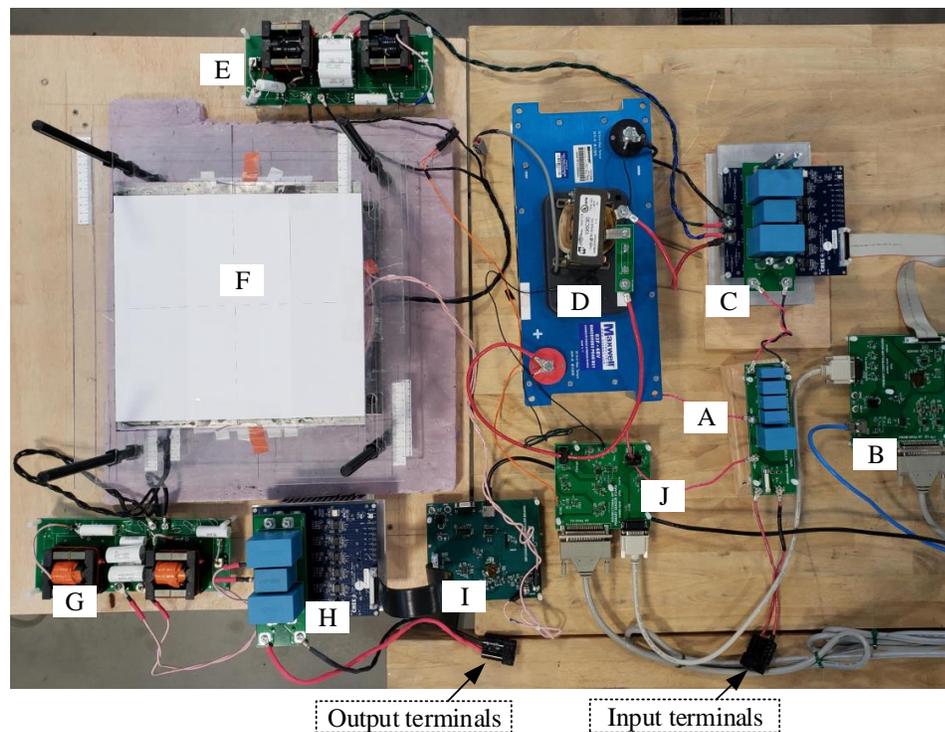
Fig. 4.60: Experimental setup for grid-side energy management.

Unit B is the microcontroller unit that takes command from OPAL-RT and sends gate

pulses to the inverter unit C. Energy buffering unit D and primary-compensation circuit E are connected parallelly at the output of the inverter. Unit F is the coil structure, containing primary, secondary and sensing coil shown earlier in Fig. 4.57. Unit G, H and I are the secondary compensation unit, the active-rectifier unit and the PLL unit, respectively. The output terminals are provided from the rectifier unit. Unit J is the primary-side sensing unit that senses I_{pri}, I_{sc} and V_{sc} and sends the values to OPAL-RT via the analog channels.

4.8.1 Track Current Controller Performance

For the experimental prototype, a *track current controller* is designed in OPAL-RT for a nominal operating current of 5 A and a bandwidth of 100 Hz. The *track current controller* is designed to operate at the *charging phase*, where the system operates at 85 kHz. The designed controller transfer function for the *track current controller* is given as follows:

$$G_c(s) = \frac{1.643e7}{s(s + 1257)} \tag{4.58}$$

Fig. 4.61 shows the response of the *track current controller* when the current reference is ramped up to 5 A within a 10-ms time period. At this testing phase, no buffering unit is installed on the system, and the inverter is operating with *AC mode* operation with no load.
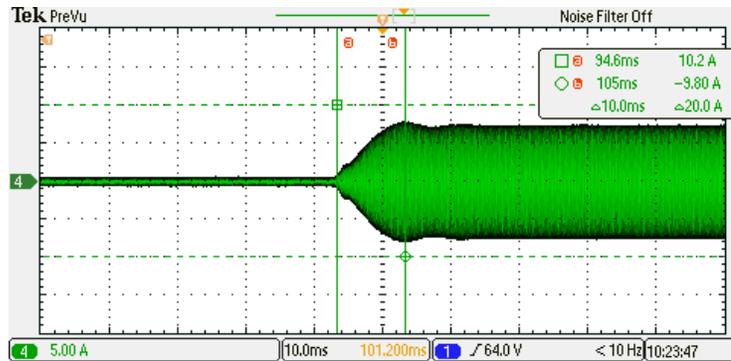
Fig. 4.61: *Track current controller* response to a 5-A ramp of the current-reference.

It can be observed that the primary coil current also ramps up in this 10-ms period, and settles to a well-regulated value afterward.

The regulated primary coil current waveform as well as the inverter output voltage waveforms are presented in Fig. 4.62. From the oscilloscope's *Cycle RMS* reading (C RMS) shown in Fig. 4.62, it can be observed that a regulated RMS value of 5 A for primary coil current is maintained. The nominal value of inverter phase-shift angle for this hardware setup is selected to be 90°, as evident from Fig. 4.62, as well.
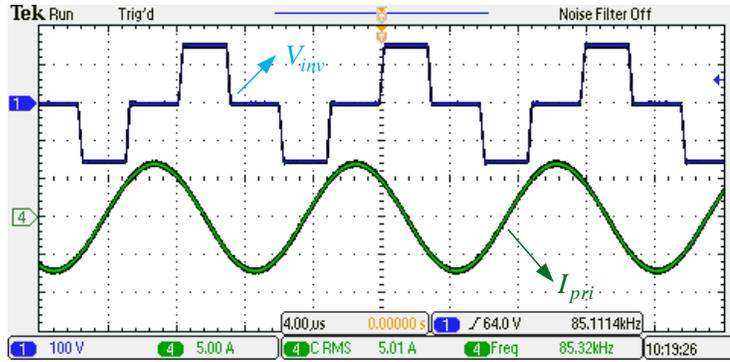
Fig. 4.62: The steady state waveform of the inverter output voltage, and regulated primary coil current.

4.8.2   Grid Current Controller Performance: Precharge Phase

After designing the *track current controller*, the *grid current controller* is also designed and implemented in OPAL-RT simulink environment. For the *precharge phase*, an FFFB type control implementation is chosen for the *grid current controller*. Furthermore, to decouple the *track current controller* and *grid current controller*, the phase-shift mapping function is also implemented in the OPAL-RT controller model. The mapping function for the selected operating ϕ_p=90° is given by:

$$\Delta\phi = 38.798\Delta D^4 - 1.1264\Delta D^3 + 3.343\Delta D^2 + 3.1795\Delta D + 0.0087 \qquad (4.59)$$

where $\Delta\phi$ is expressed in radian.

To evaluate the performance of the *grid current controller*, at first, a *precharge phase* scenario is chosen where the SC is precharged to a predefined voltage setpoint. A 1-A current reference is given to the *grid current controller* to precharge the SC. All the measurements of the *precharge phase* are recorded in real-time using OPAL-RT's *OpWriteFile* functional block. Fig. 4.63 shows the grid-current regulation in the *precharge phase* where it is observed that the inverter input current is fairly maintained at 1 A.
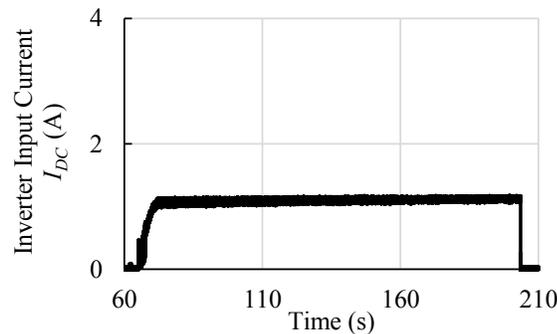
Fig. 4.63: Grid current regulation while precharging the SC from the grid.

The corresponding voltage and current profiles of SC are shown in Fig. 4.64. One can observe that the SC voltage linearly rises to about 32.5 V at which point the *grid current controller* terminates the precharging. Fig. 4.65 shows the inverter output voltage waveform in the *precharge phase*. As observed, the inverter is operating in *DC mode* operation in this phase, with a frequency of 140 kHz.
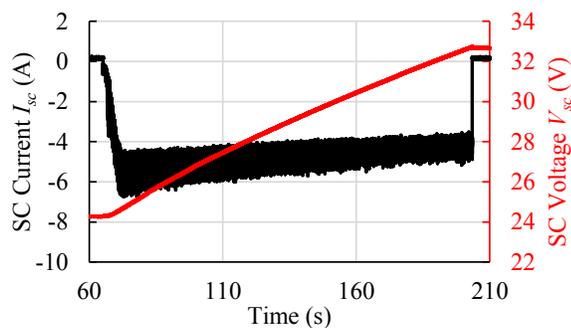
Fig. 4.64: SC current and voltage in the precharge phase.

The *precharge phase* can also be utilized to send the excess energy stored in SC back to the grid. This would be needed in the case when the SC captures DWPT energy from consecutive V2G power transfers and its voltage is increased beyond its operating limits. To prove the *grid current controller*'s bidirectional capability, a negative current reference of 0.6A is applied to the controller. The controller's regulation as well as the corresponding SC voltage and current waveforms are presented in Fig. 4.66 and Fig. 4.67 , respectively.
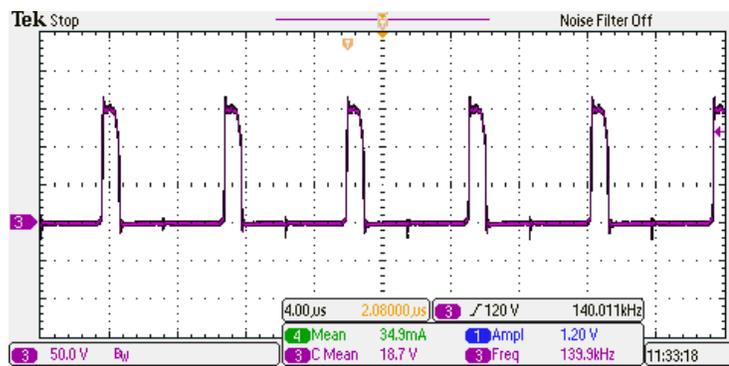
Fig. 4.65: The inverter output voltage during the precharge phase.
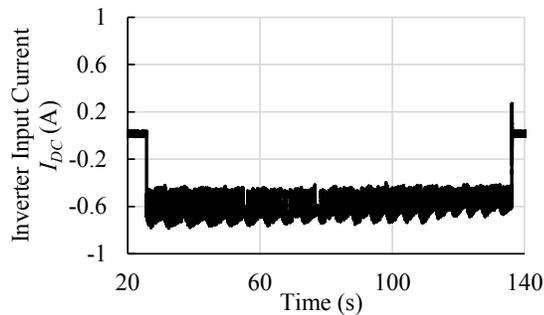
Fig. 4.66: Grid current regulation while precharging the grid from the SC.

Fig. 4.67 shows that the SC voltage linearly decreases until it reaches a predefined lower limit (24 V) at which point the *precharge phase* stops.
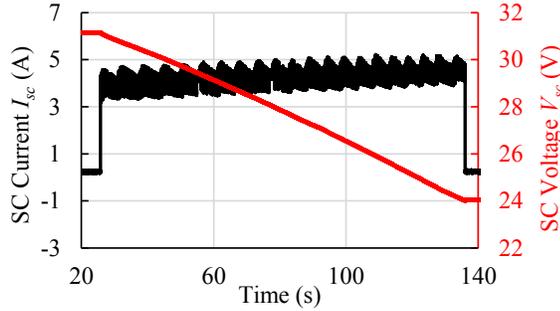
Fig. 4.67: SC current and voltage when SC is used to charge the grid during the *precharge phase.*

4.8.3 Sensing System and PLL Performance

Before running the *charging phase* tests with DWPT profiles, the sensing coil arrangement needs to be tested. Consequently, the sensing coil arrangement is placed in between the primary and secondary coil, as shown earlier in Fig. 4.57. The self-inductance of the sensing coil is designed to be 5 μH. The coil's distance from the primary coil is adjusted to ensure that the mutual inductance between primary coil and sensing coil M_{13} is a moderate value of 2.4 μH. However, as for any practical scenario, it is impossible to ensure the desired zero mutual inductance between the secondary coil and the sensing coil M_{23}. The experimental value of M_{23} for this system is 0.7 μH.

Using the sensing coil arrangement and the PLL circuitry discussed earlier, the synchornization reference frame is generated. Fig. 4.68 shows the operational waveform of the sensed signal, and the resultant synchronization pulsetrain at the output of the PLL circuitry. As one can observe, there is about 90° phase-shift between the sensed signal and the syncrhonization reference signal. This phase-shift results from the combined effect of the PLL chip and the latencies associated with the other ICs in the PLL circuitry.
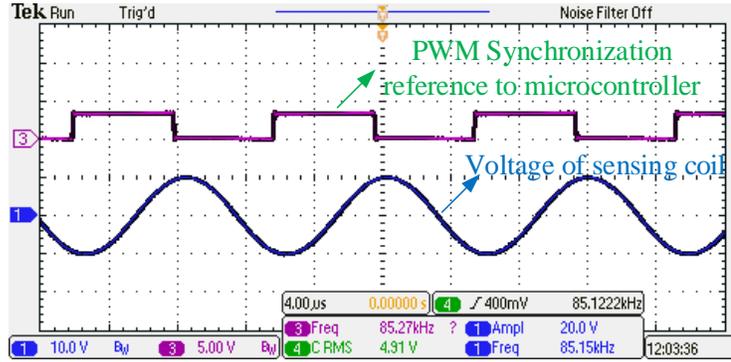
Fig. 4.68: Sensing coil voltage and the PWM synchronization pulsetrain input to the microcontroller.

For a successful DWPT system operation, it is important that this synchronization reference frame is generated and maintained constant over a wide range of voltages sensed by the PLL. This is due to the fact that when a vehicle is arriving on top of the primary coil, the PLL needs to start working as soon as the vehicle is starting to align with the primary coil. In this case, the M between primary and secondary coil, and consequently, the sensed voltage will be lower due to coil-misalignment. Nevertheless, the PLL circuitry should be able to sense this small but perceivable voltage, lock the frequency, and maintain a constant synchronization reference throughout the DWPT charging cycle. With the benchtop setup at hand, the PLL circuit's performance at different levels of sensed voltage is evaluated by varying the primary coil current I_{pri}. Varying I_{pri} is equivalent to varying the mutual inductance M, from the standpoint of the voltage induced in the sensing coil.

Fig. 4.69 shows that the primary coil current is varied from 1 A to 5 A with a step of 1 A. As can be seen from the experiments, the PLL circuit is able to successfully operate throughout the range of voltages corresponding to different coil currents. The PLL's phase-shift error with respect to the nominal phase-shift at rated operating condition (I_{pri}=5 A) is observed to be within $\pm 3.5°$. These results indicate that the PLL circuitry is able to operate throughout the varying sensed voltages without causing a significant shift of the synchronization reference frame.
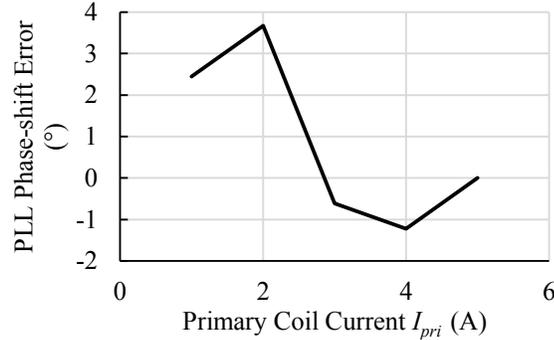
Fig. 4.69: The PLL phase-shift error at different levels of primary coil current.

4.8.4 System performance in Charging Phase

The performance of the experimental prototype with and without grid-side buffering is presented and compared in this section.

4.8.4.1 Charging Phase Without Grid-side Energy Buffering

Following the implementation of the PLL unit, different ϕ_s profiles are sent to the PLL unit via the CAN communication interface. The PLL unit successfully references the received ϕ_s profiles with respect to the synchronization-reference, consequently, emulating DWPT power profiles. With the generated DWPT profile, the experimental prototype is, at first, tested with the *charging phase* without the grid-side buffering operation. In other words, the ΔD command is made constant (V_{SC}/V_{DC}) to prevent SC from charging or discharging. This has been done to initially evaluate the *track current controller*'s performance in *dual mode* operation.

Fig. 4.70 shows three different G2V power profiles that were generated consecutively via the CAN command sent to the PLL unit. Both the input current I_{DC} and output current I_{out} profiles are captured in the oscilloscope. These profiles can be used as the basis of comparison to validate the effectiveness of the proposed grid-side power-buffering.
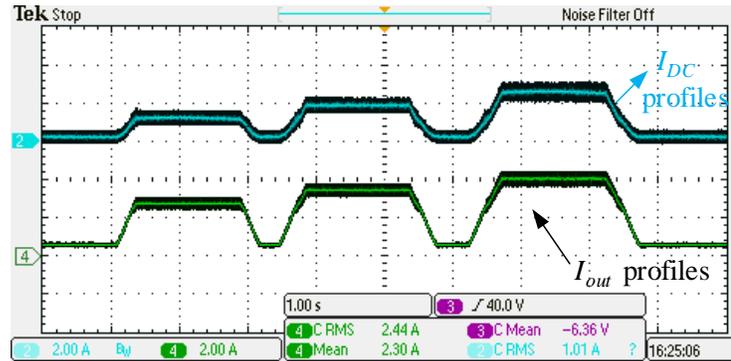
Fig. 4.70: Different G2V power profiles.

Fig. 4.71 shows the inverter output voltage V_{pi} and primary coil current I_{pri} in the *charing phase*. From the oscilloscope readings of the different conduction times at the inverter legs, it can be observed that the inverter is successfully operating in the *dual mode* with a constant DC voltage component of 18 V (corresponds to the SC voltage). However, even with the DC voltage component at the inverter output, the track current regulation of 5 A is maintained as can be observed from the oscilloscope reading. This proves the effectiveness of the phase-shift correction function implemented in OPAL-RT (4.59).
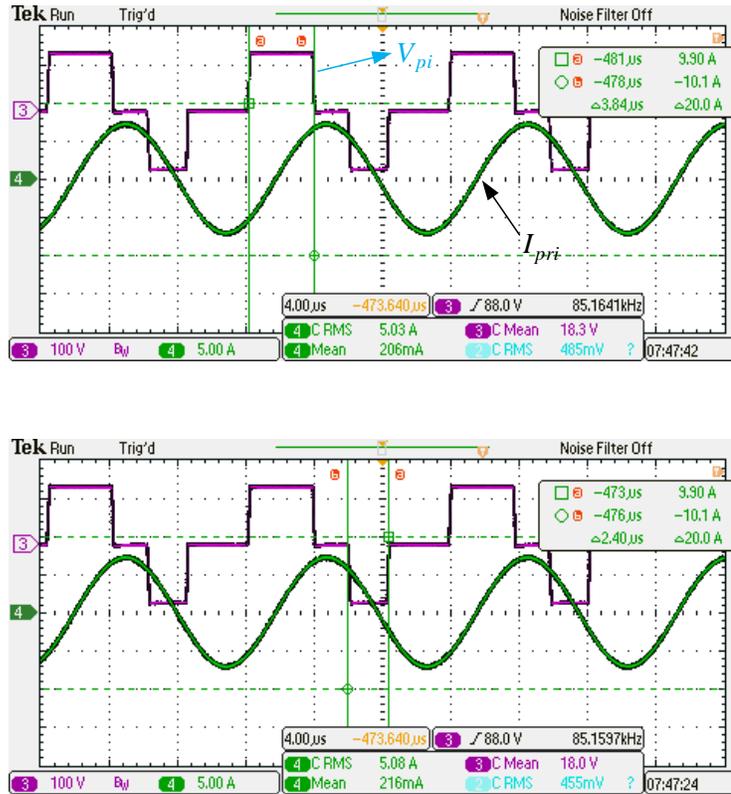
Fig. 4.71: Inverter output voltage V_{pi} and primary coil current I_{pri} during the *charing phase*.

4.8.4.2 Charging Phase With Grid-side Energy Buffering

Following the successful *dual mode* operation of the system with regulated track current in the *charging phase*, a bang-bang type control action is implemented in *grid current controller* for *charging phase* operation. The *track current controller* and the *grid current controller* together are run with a G2V DWPT load profile in the *charging phase* scenario. The DWPT load is profiled to have a peak output power P_{out} of 515 W. The system efficiency at this peak operating point is recorded to be 86%. Fig. 4.72(a) shows the corresponding input current I_{DC} and output current I_{out} profiles. In this scenario, the system is in *idle phase* until a triggering signal (which, in real-road scenario would be the VDS signal) is sent to the grid-side inverter, indicating the arrival of the vehicle. Immediately, the system begins to operate at *charging phase*, and turns on its controllers. Initially, the *grid current*

controller applies a very small ΔD (0.01), to ensure the SC unit does not discharge before the DWPT load starts ramping up. As soon as the DWPT load starts increasing, the I_{DC} starts increasing as well, consequently triggering the bang-bang control action. The *grid current controller* at this point applies a D_{dec} of 0.1. Consequently, the SC starts to heavily discharge with about 18 A current and its voltage starts decreasing (as shown in Fig. 4.73). When the DWPT load is leaving, the I_{DC} starts to drop to zero and then go negative, which triggers off the bang-bang control action. Consequently, the *grid current controller* stops discharging the SC, and the *charging phase* is over shortly afterward. Fig. 4.74 shows the *track current controller* regulation during the *charging phase*.
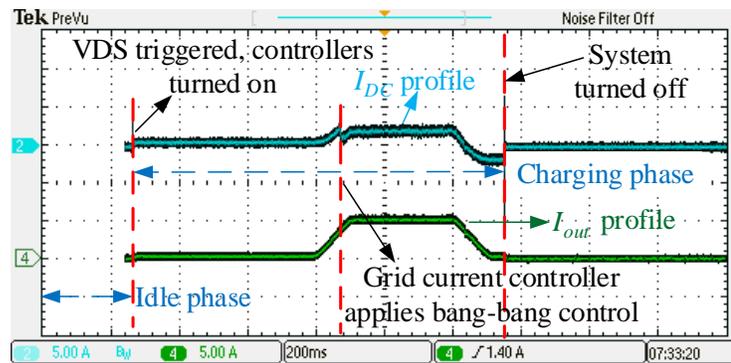
(a)
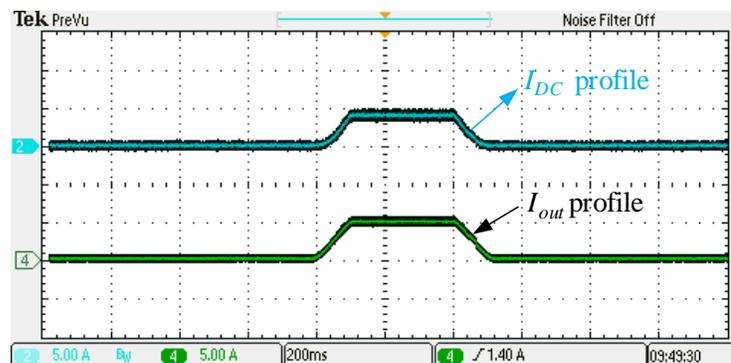
(b)

Fig. 4.72: Comparison of the inverter input current I_{DC} and output current I_{out} profile in the *charging phase* (a) with grid-side buffering (b) without the grid-side buffering.
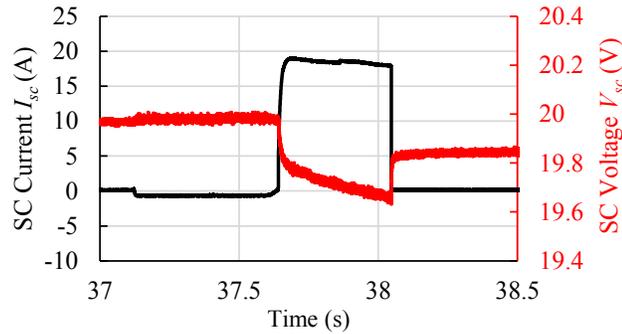
Fig. 4.73: SC voltage V_{sc} and current I_{sc} profile recorded by OPAL-RT during the *charging phase*.
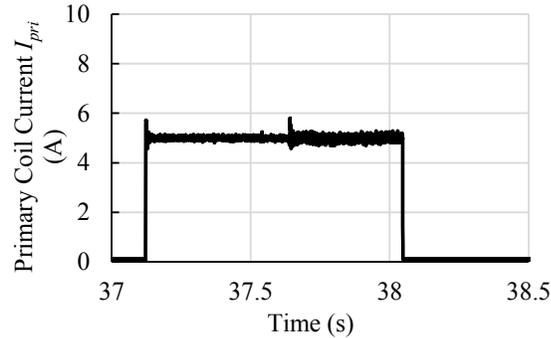
Fig. 4.74: Primary coil current I_{pri} recorded by OPAL-RT during the *charging phase*.

On a separate experiment, the same DWPT profile is run without applying the grid-side energy buffering. Fig. 4.72(b) shows the I_{DC} and I_{out} profiles of the experimental setup without the deployment of grid-side energy buffering. One can observe from the comparison shown in Fig. 4.72 that, in both cases, the output current profile I_{out} is essentially the same, suggesting the achievement of the same power output in both cases. However, in the case with grid-side buffering, the inverter input current profile I_{DC} in Fig. 4.72(b) has a reduced peak of 2 A, compared to the 4-A peak of I_{DC} at Fig. 4.72(a) without the buffering action. This proves an effective power-buffering level $F_{p,buffer}$ of 50% is experimentally achieved with this particular experiment, thereby validating the effectiveness of the proposed grid-side energy management for G2V DWPT application.

4.9 Summary

In this chapter, a DWPT system is proposed which is capable of grid-side energy management for DWPT applications on EV roadways. An energy buffering unit consisting of an SC and a choke inductance is introduced at the grid side, which can be actively controlled by the grid-side inverter, without requiring any additional power electronics. The size-optimization procedure of the buffering unit is presented. Detailed modeling of the proposed system is carried out and presented. Two separate controllers that work together are introduced for the proposed system, and their design procedures are discussed in detail. Simulation results and hardware design validations are provided. A comparison of the designed system's performance with conventional system performance is provided in order to prove the effectiveness of the proposed grid-side energy buffering control.

CHAPTER 5

EV-SIDE ENERGY MANAGEMENT FOR DWPT APPLICATIONS

Similar to the grid-side, the EV-side requires adequate energy management to mitigate the adverse effect of pulsating DWPT power profiles. EV battery's longevity can be adversely affected if the battery unit is exposed to high charging/discharging currents which would naturally happen in DWPT charging scenarios, and also during rapid acceleration/deceleration of the vehicle. In this chapter, an actively controlled Hybrid Energy Storage System (HESS) containing a battery and an SC unit is proposed for the EV systems. In addition, proposed Energy Management System (EMS) implements energy-buffering at the EV side which facilitates a lower level of average charging/discharging power to the battery while the SC absorbs the highly transient part of the DWPT power profile and the drivetrain power profile.

Section 5.1 presents a brief discussion of storage hybridization in EVs, and consequently, a battery-SC hybrid storage is proposed. The modeling of proposed HESS is discussed. Possible converter structures for controlling the HESS unit are presented, and consequently, a *full active parallel* architecture is selected to actively control the proposed HESS. In Section 5.2, the modeling of EV-drivetrain's propulsion power profile as well as different types of DWPT profiles are discussed. Section 5.3 discusses the system's controller designs in detail. To actively control the battery and SC unit of the HESS, two different controllers are designed. In addition, the EMS that would actively monitor and control the combined operation of the HESS and the EV is proposed and designed. Finally, a simulation model is built, combining all the modeled components of the system, and the simulation results are presented in Section 5.4. The chapter summary is given in Section 5.5.

5.1 Hybrid Energy Storage System for EVs

Traditionally, chemical batteries are used as the main and often the only energy storage

in EVs, due to the best trade-off in terms of energy and power density, dynamic, lifespan, weight, cost, and safety compared to other energy storage systems, such as fuel cells, super-capacitors, and flywheels [107], [108]. Due to battery cells' limited power density, exposure to very high charging and discharging currents in DWPT charging systems could generate more loss and reduce the lifespan of the battery module. To overcome these limitations, a Hybrid Energy Storage System (HESS) needs to be deployed.

In order to properly select the most suitable energy storage system for a given application, a Ragone plot [2] is typically used. Fig. 5.1 depicts a Ragone plot that compares different types of batteries, fuel cells, and capacitors according to their power density and energy density.
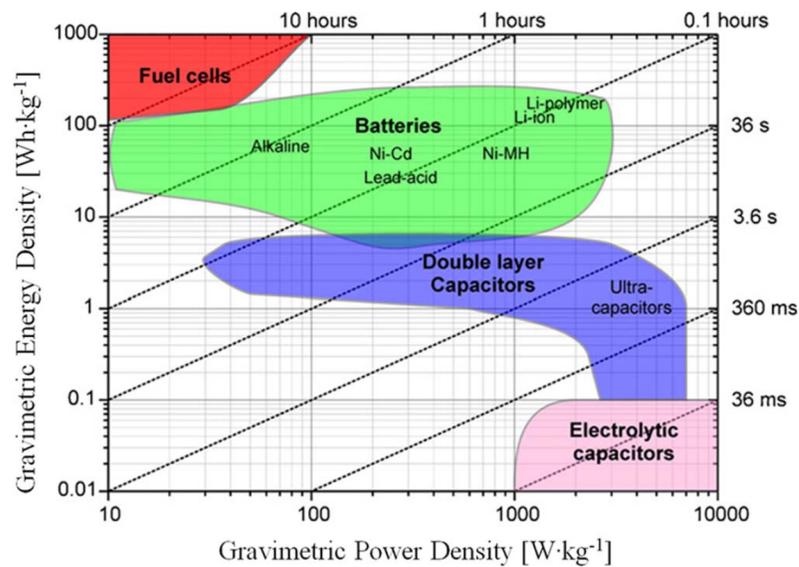
Fig. 5.1: Ragone plot [2].

It is observed from Fig. 5.1 that the Li-ion batteries have the highest energy density among the available battery technologies (up to 250 Wh/kg). However, they have relatively low power density (400-500 W/kg). Also, fuel cells only operate in a unidirectional power system, despite the fact that they have very high energy density [2]. Double-layer capacitors, or SCs, on the other hand, have extremely high power density (5000 W/kg) and a very low energy density (5 Wh/kg). Low internal resistance enables SCs to have high

charging/discharging efficiency even at high current levels [109]. According to the findings of Miller and Burk [110], SC has higher specific storage capabilities at all charge times less than 20 s; that means they have excellent DWPT-capturing and regenerative braking capability which is ideal for EV applications. Considering all these facts, a hybridization of battery and SC seems to match the high-performance requirements of DWPT-charged EV drivetrains. Thereby, this type of HESS is proposed in this dissertation. Moreover, an actively controlled HESS topology is selected for energy management of the incoming DWPT pulses to the vehicle. The storage system modeling and its active control method are discussed in details as follows:

5.1.1 Energy Storage Modeling

SC is characterized by internal resistance R_{SC} and its capacitance C_{SC}. A nonlinear capacitor model is adopted by including an additional voltage-dependent capacitance term. The model is presented in Fig. 5.2(a). Although more comprehensive models are reported in literature [111], the three-element model shown describes both power loss and energy storage capability of the SC with enough accuracy for most EMS algorithms. Battery is modeled by using internal charging/discharging resistance R_{bat}, and open-circuit voltage $V_{bat,oc}$ (Fig. 5.2(b)).
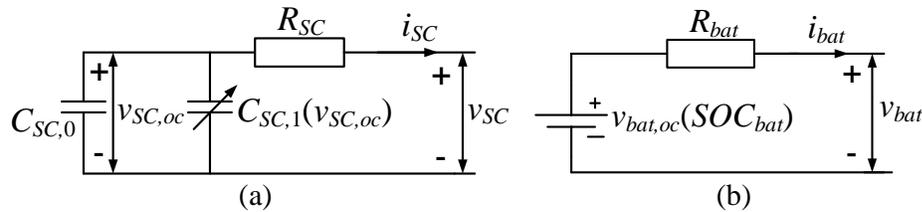
Fig. 5.2: (a) SC equivalent circuit (b) battery equivalent circuit (simplified).

In more detailed models, additional R-C branches are included in battery equivalent circuits. However, complex battery dynamic is usually much slower than the dynamic of the

powertrain or DWPT subsystem, and thereby can be neglected for this system. Selected SC and battery were characterized in the lab and were included in the EMS simulation model. For simulations, we have used the parameters of a 38-V 15-Ah Li-ion battery and parameters of a Maxwell BMOD0083 P048 B01 SC module. The experimental characteristic curves for SC and battery are shown in Fig. 5.3 and Fig. 5.4.
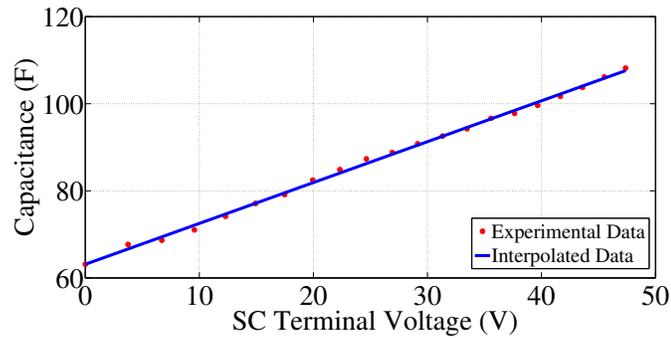
Fig. 5.3: SC characteristic curve.
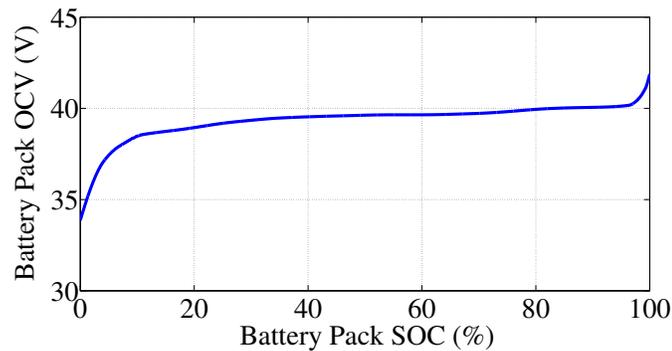
Fig. 5.4: Battery characteristic curve.

5.1.2 Converter Architecture

Different converter architectures have been investigated to manage and control battery-SC hybrid storage units [2], [112]. These architectures can be broadly divided into three categories: passive, semi-active, and active configurations.

(i) **Passive Parallel Configuration**

Fig. 5.5 shows a passive configuration. In this setup, the battery and SC unit are directly paralleled to supply the drivetrain.
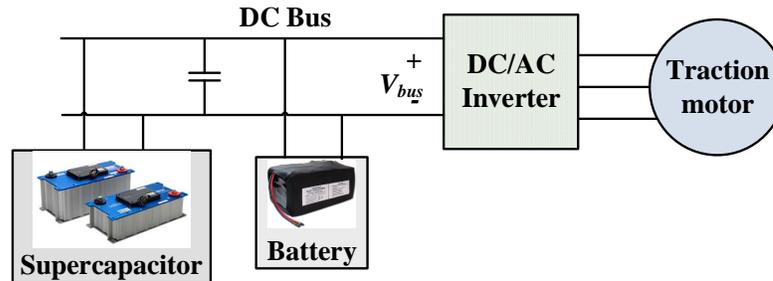
Fig. 5.5: Passive parallel structure of HESS.

Advantages:

    (a) It has the simplest architecture.

    (b) No power electronic converter is employed. As a result, the system facilitates low volume and cost.

Disadvantages:

    (a) SC operating voltage window is limited (SC voltage gets clamped by the battery). Thereby, SC is not fully utilized.

    (b) Energy sharing between the battery and SC not possible due to the lack of control.

    (c) Battery unit is directly placed across the drivetrain bus, thereby exposed to high charge/discharge currents from the drivetrain.

(ii) **Semiactive BFL Configuration**

Semiactive configurations are also known as partially decoupled configurations. In this setup, one of the energy storage is decoupled from the DC bus whereas the other storage unit is directly paralleled with the DC bus. BFL is known as the Battery Facing Load setup where the battery unit is paralleled with the DC bus, and the SC

unit is decoupled from the bus by a DC converter. This configuration is shown in Fig. 5.6(a).

(a)

(b)
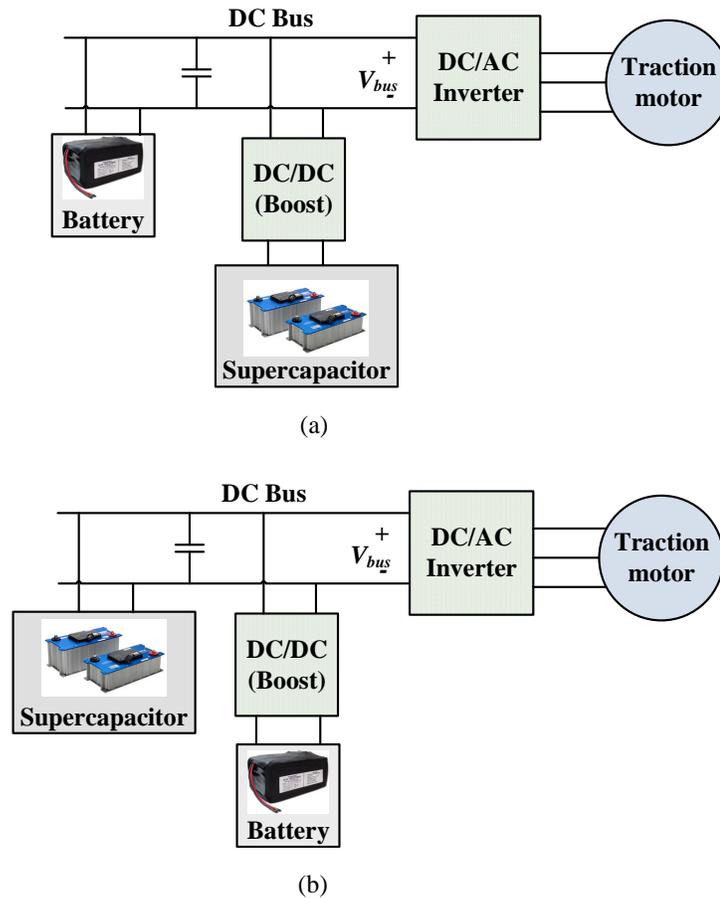
Fig. 5.6: Semiactive structure of HESS with (a) BFL configuration (b) SCFL configuration.

Advantages:

    (a) SC can be utilized since its voltage can vary in a wide range.

    (b) DC bus voltage does not undergo large variations as the battery is directly paralleled with it.

Disadvantages:

    (a) Large converter is needed to support high power charging/discharging of SC.

(b) Battery is exposed to large and fast variations of currents.

(iii) **Semiactive SCFL Configuration**

Fig. 5.6(b) shows the SCFL (SC Facing Load) configuration. In this setup, the SC is directly connected to the DC bus and the battery unit is decoupled from the bus by means of a DC converter.

Advantages:

(a) Battery is actively decoupled from the DC bus, therefore it becomes immune to high-frequency charge/discharge.

(b) SC absorbs the fluctuating pulsations at the bus.

(c) Converter size is smaller compared to BFL architecture.

(d) It facilitates less balancing issues for battery cells because battery voltage can be maintained lower than the SC voltage.

Disadvantages:

(a) DC bus might be exposed to large voltage fluctuations. An additional effort for proper control of bus voltage is needed, thereby.

(iv) **Active Series Configuration**

Active configuration corresponds to the architecture where both battery and SC are actively decoupled from the DC bus. This configuration generally requires more than one DC converters. Fig. 5.7(a) depicts the active series setup where these two DC converters are cascaded (in series).
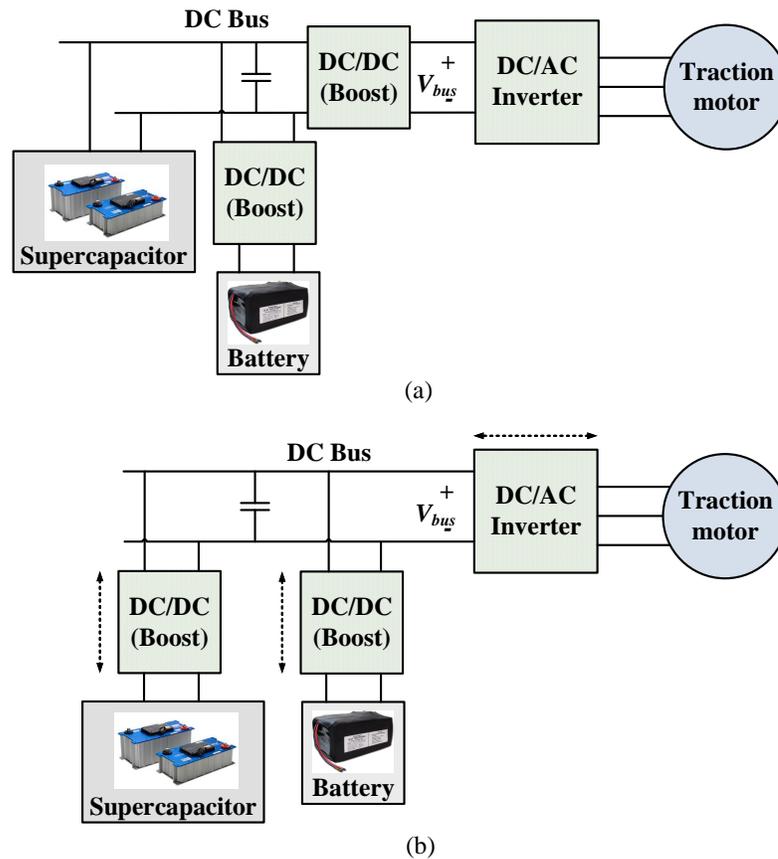
Fig. 5.7: Active structure of HESS with (a) active series configuration (b) active parallel configuration.

Advantages:

    (a) battery and SC are fully decoupled from DC bus.

Disadvantages:

    (a) Additional converter is added to the system, compared to semi-active configurations.

    (b) It results in reduced system efficiency due to two conversion stages between battery and drivetrain.

    (c) System might suffer potential stability problems associated with cascading of converters.

(v) **Active Parallel Configuration**

Fig. 5.7(b) depicts active parallel configurations where two DC converters are parallelly connected to the DC bus, fully decoupling both battery and SC unit.

Advantages:

    (a) Full control over battery-SC energy sharing is possible.

    (b) Independent selection of battery and SC unit is possible.

    (c) It facilitates longer battery life due to the battery's ability to operate at near-constant load.

Disadvantages:

    (a) System faces increased cost, volume requirements. It also requires additional control effort.

Along with the discussed types, there are other converter architectures for HESS available in the literature [113]. Carefully considering the system requirements, the full active parallel topology, depicted in Fig. 5.8 is selected for the HESS operation in DWPT environment. As can be observed, DWPT power is envisioned to be directly applied to the SC unit whereas the SC unit's DC converter could manage some part of the DWPT power to supply the drivetrain or charge the battery. Both converters are bidirectional, facilitating regenerative braking recuperation to charge the SC and/or the battery unit. Additionally, this active parallel approach increases controllability and redundancy of the HESS.
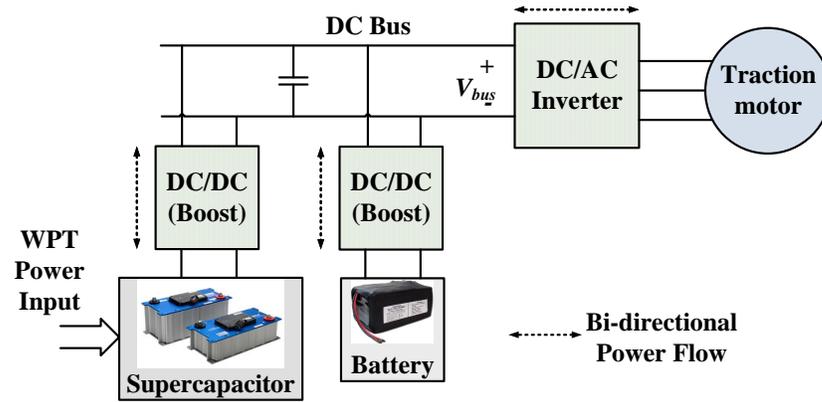
Fig. 5.8: Proposed HESS for DWPT-charged EV applications.

5.2 Powertrain Modeling

In this section, the modeling of EV drivetrain power-profile and different types of DWPT charging profiles are discussed in detail.

5.2.1 DWPT Charging Power Profile

Various factors contribute to the DWPT charging profile's power levels, shapes and sizes. Different coil geometry would result in different shapes of power profile, whereas different speed of the vehicle would cause the power profile to vary even with same coil geometry. Moreover, vehicle's misalignment to road embedded pads is a natural phenomenon that occurs while a vehicle is moving along the road, which tends to change the shape of the DWPT profile, too.

In this system, the effect of LonGitudinal Misalignment (LGM), LaTeralMisalignment (LTM), and variable speed of vehicle have been taken into account to match the DWPT charging scenario with the operating conditions as close as possible. Three WPT power profiles (Fig. 5.9) are created and simulated to test various operational scenarios. Power Profile I (PP-I) is adopted from WiTricity WIT-3300 [114] stationary charging WPT unit while maintaining the original power profile shape and considering perfect lateral alignment between the unit and the vehicle. It is assumed that the power delivery stops when the efficiency of the WIT-3300 unit drops below 70%. Power Profile II (PP-II) is derived from

the same WIT-3300 unit but assuming a 10-cm LTM between the vehicle and the road-embedded coil. Power Profile III (PP-III) is invented to represent longer coils structures, a trade-off between an elongated and a circular lumped coil.
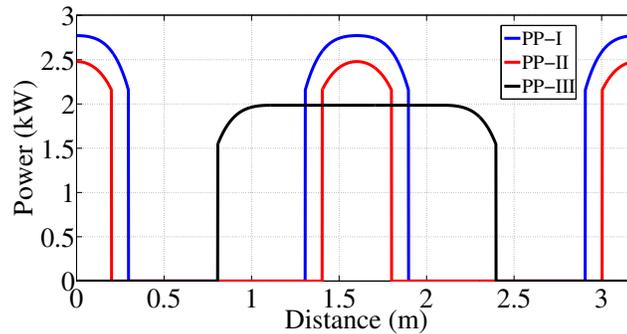
Fig. 5.9: Three different WPT pad power profiles (PP-I, PP-II, and PP-III).

Maximum power of PP-III is selected to provide identical average power as PP-I. Distance presented in Fig. 5.9 corresponds to one longitudinal period of PP-III and two periods of PP-I and PP-II. To create diversified road conditions, all three WPT power profiles (PP-I to PP-III) are joined together and combined with a section without WPT (as shown in Fig. 5.10), each of them covering one ECE-15 UDC cycle. The effect of varying velocity of the vehicle is taken into account while creating the complete profile. A lower velocity of vehicle would increase the amount of time taken to move from a particular WPT pad to the next pad, consequently resulting in wider power profile from that particular pad. This effect is further demonstrated in Fig. 5.11, where a zoomed-in segment of the complete WPT profile is shown. From about 20 s to 50 s of the travel time, the vehicle is at standstill position, which happens to be the case when the vehicle is directly on top of a WPT pad. That is why, during this period, the vehicle continues to receive constant amount of WPT power. After 50 s, the vehicle undergoes a rapid acceleration, which causes the successive pad's power profiles to last less and less, as observed in Fig. 5.11. One ECE-15 UDC cycle speed profile is shown in Fig. 5.12.
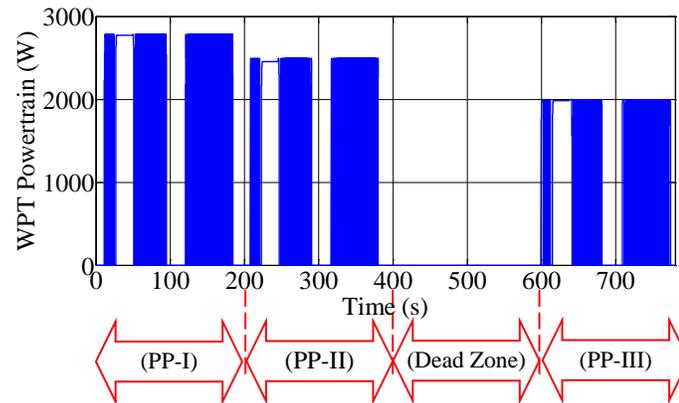
Fig. 5.10: Four-segment DWPT power profile.
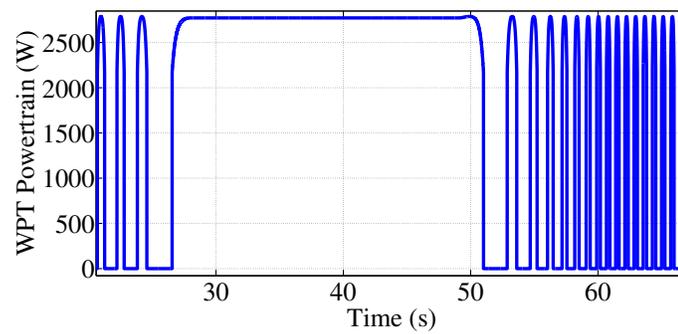
Fig. 5.11: Zoomed-in DWPT power profile to illustrate the effect of velocity on DWPT profile.
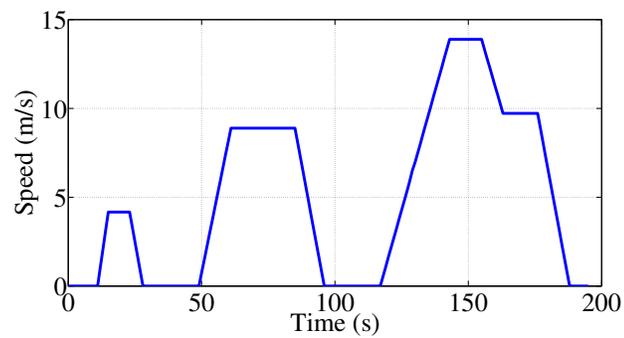
Fig. 5.12: ECE-15 UDC drive cycle.

5.2.2 EV Drivetrain Power Profile

Advanced Vehicle Simulator (ADVISOR) has been used to model the EV drive cycle and propulsion power profile. ADVISOR is a vehicular powertrain simulator originally developed by the National Renewable energy Lab (NREL) [3]. It can run in MATLAB Simulink environment to simulate different types of powertrains (series, parallel), different models of EVs, different drive cycles, etc. Fig. 5.13 illustrates a graphical user interface for selecting these parameters prior to running a simulation.
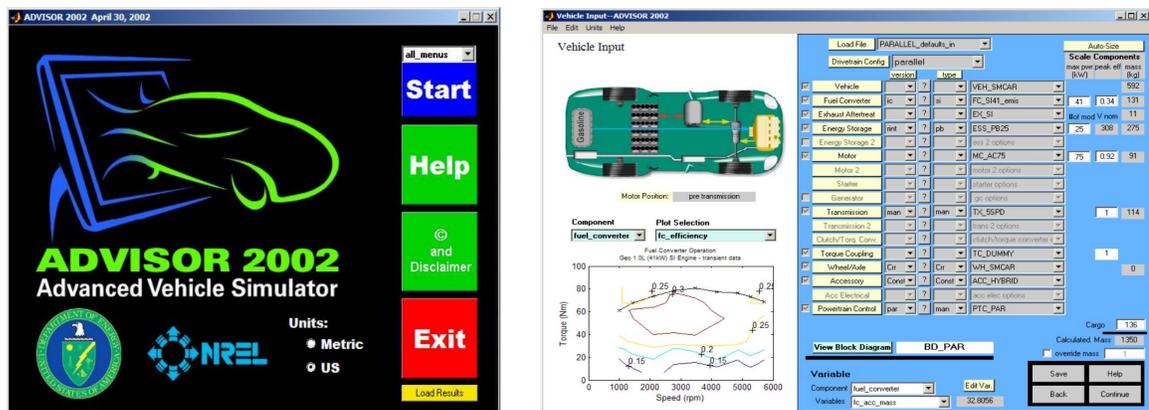
Fig. 5.13: Graphical User Interface (GUI) of ADVISOR [3], run from MATLAB.

A compact sized car and ECE-15 drive cycle are selected for running an ADVISOR simulation in order to get the propulsion power profile. A downscaled version of the drive-cycle and, consequently, a powertrain is taken in order to make a compatible EV system simulation with respect to the WIT-3300 DWPT profile previously discussed above. Fig. 5.14, and Fig. 5.15 depicts the speed and propulsion profile taken from the ADVISOR simulation.
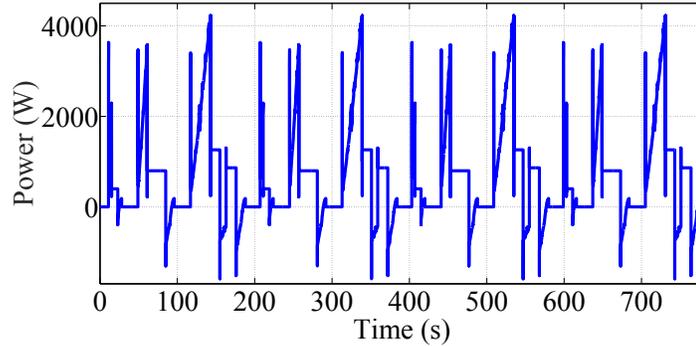
Fig. 5.14: Scaled-down propulsion power for 4 consecutive ECE-15 UDCs.
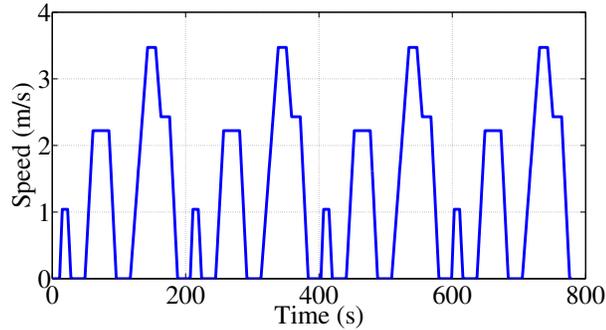
Fig. 5.15: Scaled-down speed for 4 consecutive ECE-15 UDCs.

5.3 Controller Design

In this section, two current-controllers' and one voltage regulator's design is carried out for the proposed full-active converter configuration. The desired features of the EMS are discussed, followed by its design procedure. Additionally, a bus-voltage regulation method is presented and the safety features of the EMS system are discussed, as well.

5.3.1 Converter Controller Design

Two bi-directional boost converters are deployed to separately control the battery and SC unit. Fig. 5.16 shows the circuit structure for both of the Boost converters, where V_{in} should be replaced by the terminal voltage of the battery and SC, respectively.

The small-signal model of the converter circuit is derived using AC equivalent circuit
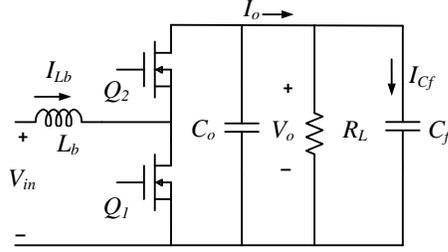
Fig. 5.16: Boost converter circuit.

modeling [98] approach. The detailed calculation is given in Section C.1. The "duty cycle to output current" transfer function for each converter is derived in Section C.1 as follows:

$$G_{iod}(s) = \frac{\hat{i}_o}{\hat{d}_{boost}}\bigg|_{\hat{v}_{dc}=0} = \frac{D'_{boost}V_0}{R} \frac{(1 - \frac{s}{\frac{D'_{boost}V_o}{I_L L}})(1 + \frac{s}{\frac{1}{C_f R}})}{s^2 L_b(C_o + C_f) + s\frac{L}{R_L} + D'^2_{boost}} \tag{5.1}$$

where, R_{Load} models the load, C_o is capacitance of the converter output filter, C_f is the DC-link capacitance, D_{Boost} is the converter duty cycle, L_{Boost} is boost converter's inductor and V_o is nominal value of the DC-link voltage.

To avoid interference and instability, converters are controlled to operate substantially faster than the dynamic of the EMS control loop and DWPT power input. The control bandwidth for both converters is chosen to be 10 kHz for this system, and the phase margin is designed to be 60°. With these constraints, the controller transfer functions are derived to be:

$$G_{c,bat}(s) = 12.69 \frac{(1 + \frac{s}{588.23})}{s(1 + \frac{s}{3.0303X10^5})} \tag{5.2}$$

$$G_{c,sc}(s) = 12.69 \frac{(1 + \frac{s}{1.0989X10^3})}{s(1 + \frac{s}{2.0833X10^5})} \tag{5.3}$$

Table 5.1 lists the parameters for HESS unit and the converter system.

Table 5.1: HESS and converter system parameters

Parameter	Value
Battery-converter power	750 W
Battery nominal voltage	38.4 V
Battery-converter inductance	74.17 μH
Battery-converter inductor resistance	7.5 mΩ
Battery-converter output filter capacitance	93.5 μF
Battery-converter switch on-resistance	2.8 mΩ
SC-converter power	1500 W
SC nominal voltage	42 V
SC-converter inductance	34.75 μH
SC-converter inductor resistance	4.05 mΩ
SC-converter output filter capacitance	146.5 μF
SC-converter switch on-resistance	2.8 m Ω
Bus capacitance	136 mF

Fig. 5.17 and Fig. 5.18 shows the openloop and controller tranfer function bode plots of the battery converter and SC converter, respectively. Fig. 5.19 and Fig. 5.20 depicts the loop gains and phase margins of the respective loops.
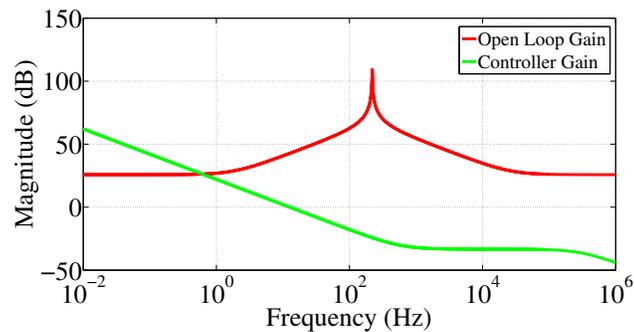
Fig. 5.17: Magnitude Bode plot of battery-converter openloop gain and controller transfer function.
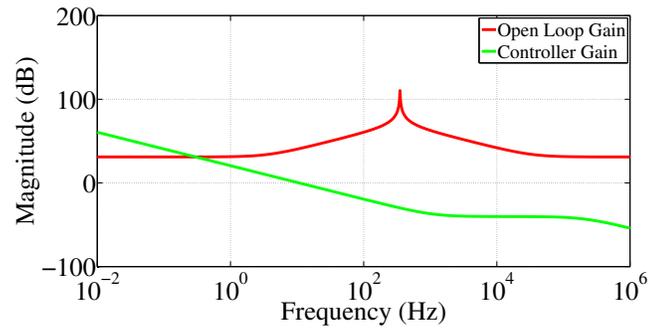
Fig. 5.18: Magnitude Bode plot of SC-converter openloop gain and controller transfer function.
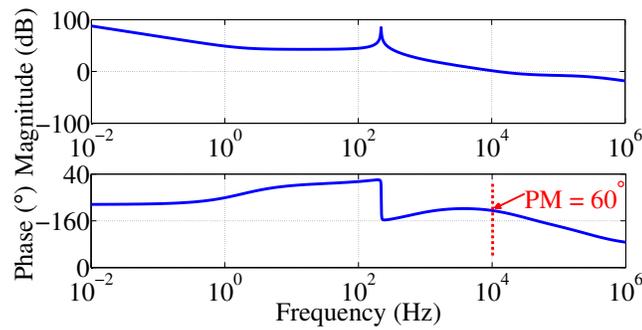
Fig. 5.19: Magnitude Bode plot of battery-converter compensated loop gain.
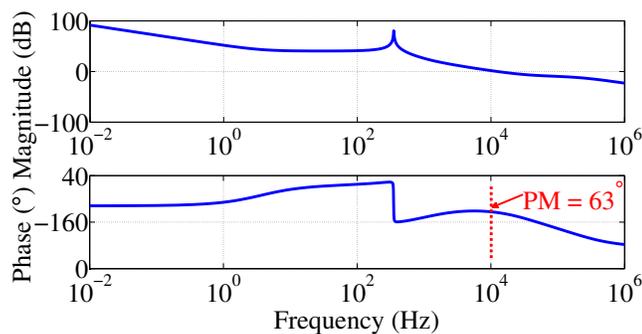
Fig. 5.20: Magnitude Bode plot of SC-converter compensated loop gain.

5.3.2 Energy Management System (EMS) Design

Fig. 5.21 illustrates the EMS block diagram for the system. The EMS has been designed
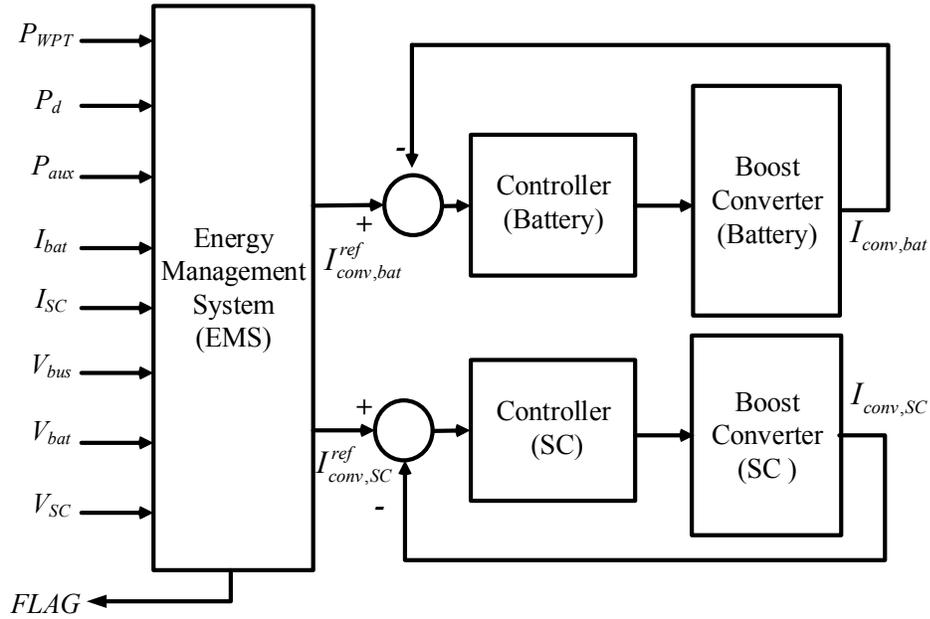
Fig. 5.21: EMS block diagram.

to ensure that SC can buffer the power delivered from the DWPT and also assist the battery in case of propulsion power transients, originated from acceleration/deceleration of the vehicle. Good SOH of the system is maintained by preventing both overcharging and over-discharging of batteries and SCs. EMS obtains the information about the demanded propulsion power P_d, the received WPT power P_{WPT}, and the required auxiliary power P_{aux} as inputs. Additionally, it takes the sensed voltages and currents of the battery (V_{bat}, I_{bat}) , SC (V_{SC}, I_{SC}) and bus measurements (V_{bus}, I_{bus}). Converter current references are the final output of the EMS which directly control the individual converter currents ($I_{conv,bat}$, $I_{conv,SC}$) taken from the battery and the SC, delivered to the propulsion system. Since the converter controllers are designed to be faster than the dynamics of the drivetrain and WPT profile, converter currents will accurately track their respective references under this assumption, i.e. :

$$I_{conv,bat} = I_{conv,bat}^{ref} \tag{5.4}$$

$$I_{conv,sc} = I_{conv,sc}^{ref} \tag{5.5}$$

which will eliminate the impact of the dynamic of current controllers on the EMS.

After carefully considering the requirements imposed by WPT applications on EV battery, the desired features of a HESS have been identified as follows:

(i) It should employ the operation of SC as an absorber and buffer for the power delivered from WPT system. Power bursts delivered periodically from the WPT system should be amortized by the SC.

(ii) It should provide the SC-assistance to the battery during drivetrain power transients so that the SC can shape, equalize and limit the battery power requirements by delivering an excessive amount of power during transients.

(iii) It should improve the energy efficiency by capturing regenerative braking energy. When the recuperated energy exceeds the amount manageable by the battery, SC should accept the excess energy and store it for some future use.

(iv) Controlled by an EMS, the HESS should assure long cycle life and good SoH of the battery and SC by preventing overcharging, overdischarging and excessive current ratings.

The salient features that add to the intelligence of the designed EMS are listed as follows:

5.3.2.1   FIR Filtering for SC Utilization of DWPT Charging

A Finite Impulse Response (FIR) filter is implemented to provide a moving average estimation of the power delivered by the WPT system. The output of the discrete FIR filter can be written as:

$$P_{WPT,FIR}(k) = \frac{1}{n} \sum_{i=k-n+1}^{k} P_{WPT}(i) \tag{5.6}$$

where k denotes the indices of the previously measured input power values. Instead of counting on the actual value of the power delivered from the WPT unit P_{WPT}, the EMS

algorithm continues calculations expecting that at a particular moment the averaged amount $P_{WPT,FIR}$ is available to support the propulsion and DC bus voltage, or charge the battery. That way, SC overcharging is prevented. In this study, an appropriate value of n is chosen so that it takes approximately 2 WPT segments to reach stable averaged value.

5.3.2.2 SC Utilization at High Frequency Load Variations

The initial current assigned to the SC controller converter is obtained after processing total current requirements through a first order high-pass filter:

$$\frac{I_{SC}(s)}{I_{\sum ES}(s)} = \frac{s}{s + \omega_{HP}} \tag{5.7}$$

where $\omega_{HP} = 2\pi f_{HP}$ is the filter corner angular frequency. This way, the SC will only be responsible for the high-frequency portion of the power demand and the operating current. Consequently, over a long period of time, WPT and battery will be providing the entire energy for the propulsion, while the SC will be serving as an energy buffer for WPT, and helping during high-rate transients. The selection of an adequate corner frequency is a challenging task since too low of a value may cause large SC voltage swings, while too high of a value would not utilize the full potential of the SC to screen the battery from the high-rate transitions. To determine the adequate value of ω_{HP}, power spectral density (periodogram) of the power demand signal P_d is used, and f_{HF} is selected so that the ratio of the P_d signal energy below and above the selected frequency *matches the energy capacity ratio* of the battery and the SC.

5.3.2.3 Bus Voltage Regulation

A Proportional (P) control is implemented to correct the discrepancy between the DC bus voltage reference $V_{bus,ref}$ and its actual value V_{bus}. However, instead of the voltage, bus capacitor energy $E_{bus}(t) = \frac{1}{2}C_0 V_{bus}(t)^2$ is selected as a controlled variable [115]. The energy calculation module introduces nonlinearity in the voltage control loop. However, the quadratic form of the voltage V_{bus} would penalize the deviation from reference voltage more

than the linear form, improving stability and response of the controller design.

$$I_{bus,ref} = K_{p,bus}\frac{1}{2}C_0(V_{bus,ref}^2 - V_{bus}^2) \tag{5.8}$$

Eq. (5.8) shows the additional current reference $I_{bus,ref}$ needed to be supplied by the HESS for bus voltage regulation. $I_{bus,ref}$ is added to the total propulsion current required by the drivetrain, and consequently, the EMS calculates the individual current references for the battery and SC unit. In other words, $I_{bus,ref}$ is shared by the battery and SC unit. For the system at hand, $K_{p,bus}$=5 was sufficient to maintain smooth regulation of V_{bus}.

5.3.2.4 Protection and Safety Features

The system is designed in a way so that the SC unit supplies the high-frequency variations of charging and discharging power profile while making sure the battery unit is operating safely. This, in turn, causes large variations to SC voltage, because SCs inherently have lower energy density. To prevent supercapacitor from overcharging or fully depleting, A safety factor is implemented and enforced by the action of EMS control. Derating factors for both charging (α_{SC}^{chg}) and discharging (α_{SC}^{dch}) are used to weigh the SC current reference depending on its SOC value. With this action, the SC would be less heavily discharged at low SOC values, and less heavily charged at high SOC values, which would prevent over-discharging and overcharging of SC, respectively.

The SC derating factor is shown in Fig. 5.22. It can be observed that the optimum SOC window where the SC is utilized with its full potential is 40%-90%. The discharging current detating takes places in the 30%-40% SOC window, and the charging current derating takes place in the 90%-95% SOC window. Outside these SOC ranges, SC operation are prevented as a protection measure to prevent damaging the unit.
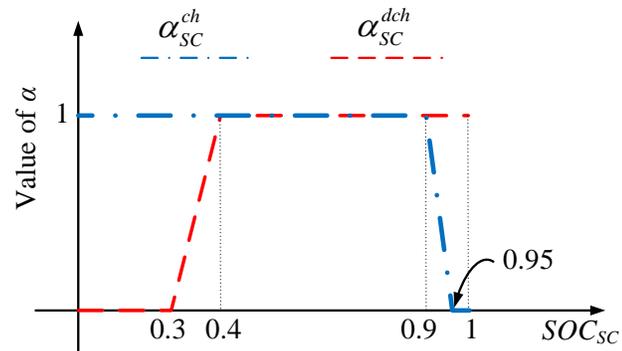
Fig. 5.22: SC current-derating factor vs. SOC.

5.4 Simulation Results

Upon modeling the different parts of the system, a complete simulation model is built using the MATLAB Simulink environment. With this propulsion profile, along with the DPWT charging profile, the EMS and the HESS-converter system is simulated for the entire drive time consisting of 4 consecutive ECE-15 cycles. The simulation results presented in Fig. 5.23 confirm successful operation of the EMS over the entire roadway section.
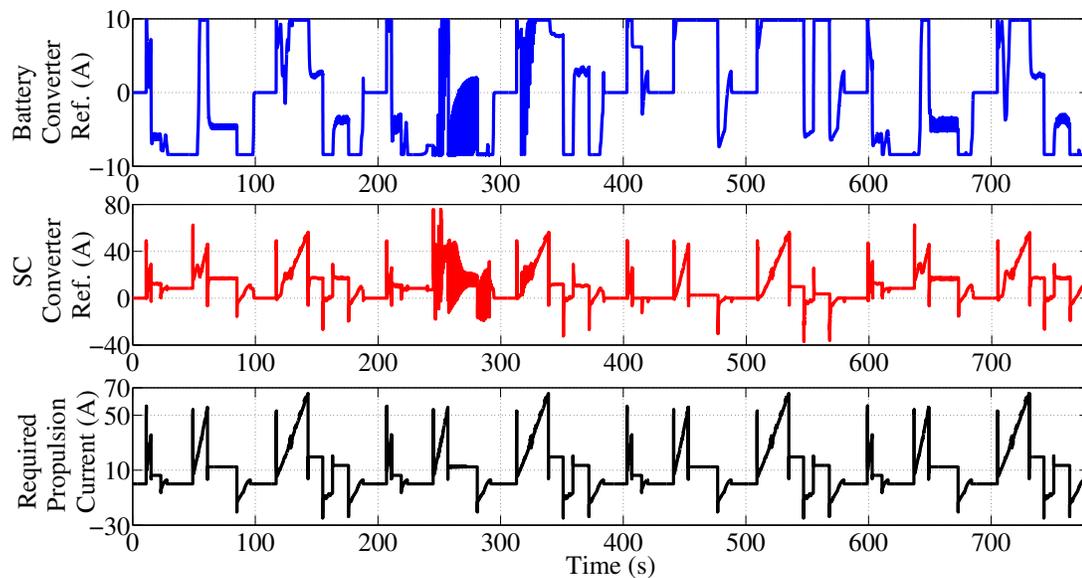
Fig. 5.23: Propulsion current and converter current references during four-segment test.

It is evident that the highly transient part of the powertrain is assigned to the SC unit, while the battery unit only supplies the slowly-varying part. The SC converter assigns up to 80A current to the SC unit, while the battery current is limited to 10A. This lower current limit imposed on battery prevents it from being exposed to harmful levels of charging/discharging current, thereby protecting the battery and helping it to last longer.

The overvoltage-flagging features of the EMS can be illustrated in Fig. 5.24. It shows that, at about 245 seconds, a flag signal is raised by the EMS. It happens because momentarily the EMS cannot handle a large amount of WPT energy as the battery reaches its charging current limit and the SC is also fully charged. Consequently, this increases the bus voltage momentarily. However, this problem can be easily prevented by temporarily limiting delivered wireless power to an acceptable level.
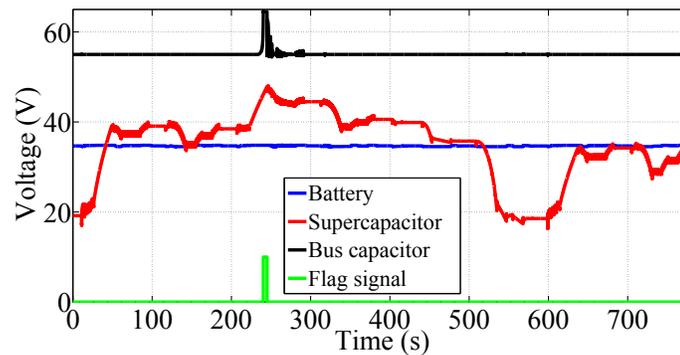
Fig. 5.24: Battery voltage, SC voltage, DC bus voltage, and flag signal during four-segment test.

To validate the undervoltage-flagging feature of the EMS, Fig. 5.25 illustrates the case when the EMS is tested by conducting a simulation over a single ECE-15 UDC ($T_{ECE} =195$ s) without the WPT pads available. It can be observed that despite the simulation starts with a nearly full SC since there is no DWPT available, the SC becomes almost depleted after 145 s, causing a flag to be raised. This problem can be prevented by increasing the size of the battery unit to support the entire power requirements of the vehicle. Alternatively, DWPT systems can be used to recharge the vehicle, in which case even a low-power battery

would be enough. To prove this, Fig. 5.26 shows the results for the same test, but now with PP-III employed to deliver power to the vehicle over the entire cycle. In this scenario, despite starting with low SOC, the SC and the battery gradually gain energy from the DWPT charging.
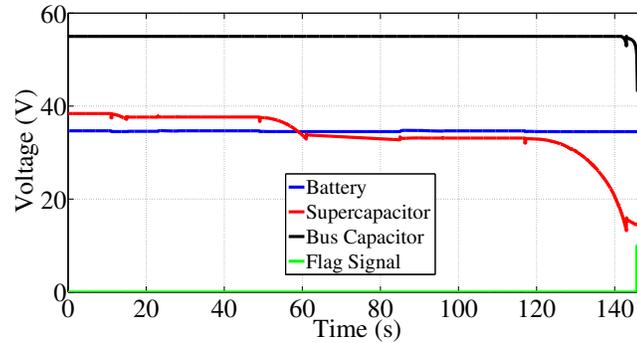
Fig. 5.25: Battery voltage, SC voltage, DC bus voltage and flag signal during dead-zone test with no DWPT.
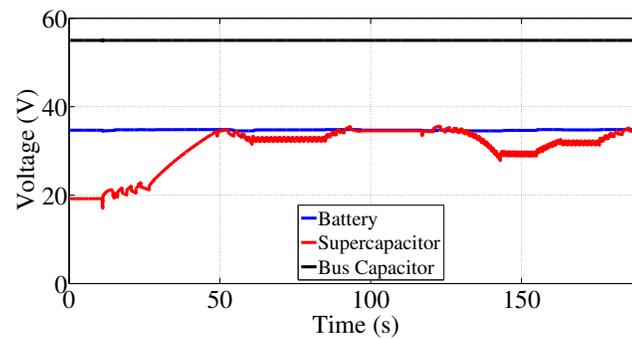
Fig. 5.26: Battery, SC, and DC bus voltages (during PP-III test).

5.5 Summary

In order to manage the DWPT charging profile received by the vehicle in a way that does not affect the EV battery, a hybrid energy storage system is proposed. The proposed storage system actively combines an SC unit with the existing EV battery unit. The storage unit is controlled with fully active parallel converter configuration which allows

independent selection of battery and SC unit. An energy management system is designed that uses the SC unit as a buffering unit for absorbing highly transient parts of the DWPT profile and drivetrain propulsion profile. Contrariwise, the battery unit only faces the low-frequency, filtered part of the DWPT power and drivetrain load, and thereby is operated within its recommended operating window. Additional protective features are employed in the energy management system. For example, the EMS ensures safe voltage limits for battery and SC to protect the units from dangerous operating conditions. Also, current scaling is imposed by the EMS to lightly charge/discharge the storage unit at high and low SOC levels, respectively. The proposed system has been adequately modeled to take care of different practical scenarios. A fairly detailed battery and SC equivalent modeling approach suitable for EV drivetrain application has been used. Different DPWT powertrain model has been discussed corresponding to lumped coil structures, elongated coil structure and misaligned coil structure. The effect of variable speed of the vehicle is also taken into account while modeling the DWPT powertrain. ECE-15 UDC is selected as a representative drive cycle, and the corresponding propulsion power is modeled with ADVISOR tool. Two current controller is designed for actively controlling the battery and SC unit, and controller design process is also discussed in detail. After modeling the system, the controller and the EMS, a full system simulation is run for 800s with 4 consequetive ECE-15 drive cycle. The simulation results have proved the effectiveness of the proposed hybrid energy storage and EMS algorithm and their ability to operate together in DWPT environment. The safety features of the EMS is also successfully tested in different simulation setups.

CHAPTER 6

CONCLUSION AND FUTURE WORKS

DWPT charging operation on EV roadways offers a safe and convenient charging option while eliminating the issue of range-anxiety. However, DWPT comes with the inherent disadvantages of grid-side and EV-side energy management issues, which has been addressed in this dissertation. Furthermore, a Vehicle Detection System (VDS) is proposed for DWPT roadways to ensure misalignment tolerant DWPT operation with enhanced safety features included. The summary of the contribution of this research is presented in Section 6.1, whereas the possible future research directions are discussed in Section 6.2.

6.1 Summary of Contribitions

The salient contributions of this dissertation are discussed in this section.

6.1.1 Vehicle Detection System and Integrated Operation with DWPT-charged EV Roadway

The primary role of a VDS is to initiate the DWPT controller at the time of the arrival of the EV on top of a primary coil. However, in this dissertation, several other important functionalities are added to the implemented VDS. The proposed VDS accurately calculates and communicates the measured vehicle LaTeral Misalignment (LTM) information to the DWPT controller to help it achieve misalignment-tolerance. Furthermore, a speed-detection capability is added to the VDS, to be used by the DWPT controller if needed. Moreover, the overall safety of the DWPT operation is enhanced by means of a Foreign Object Detection (FOD) system which implements emergency shutdown of the charger in case a potentially harmful object is detected on charging track. Finally a Driver feedback (DF) system is implemented to take into account the driver's or EMS's decision to activate/deactivate the charging. The speed and LTM information are also wirelessly transmitted and displayed to

the driver to assist the driver to achieve vehicle-to-track alignment. All these VDS-features are experimented with a 25-kW DWPT-charged E-bus system. The successful operation of the VDS in real-time DWPT operation validates its functionality.

6.1.2 Grid-side Energy Management for DWPT-Charged EV Roadway

DPWT charging cycles create pulsating power profiles at the powergrid side, which could expose the grid to possible frequency/voltage fluctuations and could cause grid-insatbility in worst-case conditions. In order to address this issue, a grid-side energy management strategy is proposed in this disseration. An energy buffering unit is proposed which works together with the proposed controller in order to achieve grid-side energy buffering, which reduces the grid-side DWPT pulsations. Optimum sizing of the energy buffering units are formulated. A downscaled hardware prototype is built and tested to validate the functionality of the proposed control strategy.

6.1.3 Energy Management of DWPT-Charged EV Energy Storage

EV batteries suffer from the loss of longevity due to their exposure to highly transient charging/discharging currents. DPWT charging inherently makes the EV battery unit more exposed to highly-pulsating charging-current profile. In order to manage the drivetrain power and the DWPT power so that the EV battery longevity is not compromised, a Hybrid Energy Storage System (HESS) and integrated Energy Management System (EMS) is proposed. The proposed HESS comprises of a battery unit and SC unit. The EMS ensures that the SC absorbs the highly transient part of the drivetrain power profile as well as the DWPT power profile, while the battery charges/discharges with a slowly varying power profile. Safe current and voltage limits are imposed on the battery and the SC unit, to ensure their respective recommended operating windows. The proposed EMS and HESS model is built in MATLAB Simulink enviroment. Successful operation of the system is observed while tested with consecutive ECE drive cycles and with different DWPT power profiles.

6.2 Future Works

In light of the research presented in this dissertation, possible directions for future research opportunities are identified and discussed in detail as follows.

6.2.1 Investigation of Control Methods for Grid-Side Energy Management for DWPT-charged Roadways

In the proposed grid-side energy management unit, two different controllers are employed to regulate the track current and the grid current. Depending on the control objective and the application, other types of control methods could be investigated. In the presented research, bang-bang control as well as P (Proportional) type FFFB control approach is implemented for controlling the grid-current, whether other types such as PD (Proportional Derivative), PID (Proportional Integral Derivative) type controller could be explored. Also, the efficiency comparison of the grid-controlled system with other conventional DWPT systems can be investigated.

Moreover, in the proposed model, an LCC compensation circuit is employed. It could be explored how the control method would change depending on different other types of compensation circuit topologies. Furthermore, the implemented grid current control method's controlling range is limited by the maximum duty cycle limit discussed in Section 4.5.3. Alternative control strategies can be investigated to reduce or eliminate this limitation.

6.2.2 Energy-Buffering Unit Optimization

For grid-side power-buffering on DWPT-charged roadways, an energy-buffering unit is proposed to be installed at the grid-side DWPT infrastructure. Similarly, this energy-buffering unit could be integrated inside EVs with the proposed control method for the onboard energy storage management, which would increase the longevity of EV battery units. Appropriate Sizing of the buffering unit with respect to the onboard battery size can be investigated, and the associated increase of battery lifetime could be explored.

From the SC-sizing analysis and calculations presented in Section 4.4.1, it is evident

that the rated voltage level of the SC unit should be considerably higher in order to reduce the losses of the system. However, this tends to increase the cost of the SC unit deployed. Investigations can be carried out to further optimize the DC-bus voltage level and the SC-voltage level by means of converter topology or control method. Also, several other factors could be considered to optimize the sizing of SC. For example, depending on the traffic size and the roadway segment size, the expected buffering level and consequently the sizing of SC unit should be different. Moreover, the SC sizing with respect to different drive-cycle conditions can be explored to maximize the utilization of the SC units. Furthermore, for a large scale infrastructure, the buffering unit installation, distribution, and associated economics as well as and feasibility analysis can be carried out.

6.2.3 Application of VDS for G2V/V2G Charging Scheduling and Optimization

The implemented VDS setup's application is limited to the G2V-type DWPT infrastructures. However, its functionality can be extended to bidirectional G2V/V2G charging infrastructures following the implementation of the proposed grid-side energy management strategy. For the systems where the grid-side and vehicle-side energy buffering units are employed, the VDS could be employed to schedule or negotiate the power buffering levels in order to further optimize the grid-side and vehicle-side energy management. Furthermore, this VDS and integrated bidirectional DWPT structures would facilitate the development of a more advanced V2V (Vehicle-to-Vehicle) charging infrastructure in future.

REFERENCES

[1] R. Tavakoli and Z. Pantic, "Analysis, design, and demonstration of a 25-kw dynamic wireless charging system for roadway electric vehicles," *IEEE Journal of Emerging and Selected Topics in Power Electronics*, vol. 6, no. 3, pp. 1378–1393, Sep. 2018.

[2] I. Aharon and A. Kuperman, "Topological overview of powertrains for battery-powered vehicles with range extenders," *IEEE Transactions on Power Electronics*, vol. 26, no. 3, pp. 868–876, March 2011.

[3] K. B. Wipke and M. R. Cuddy. (2014) Using an advanced vehicle simulator (advisor) to guide hybrid vehicle propulsion system development. [Online]. Available: https://www.nrel.gov/docs/legosti/fy96/21615.pdf

[4] N. Tesla, "Apparatus for transmitting electrical energy," U.S. Patent 1,119,732A, Dec. 1, 1914.

[5] G. A. Covic and J. T. Boys, "Inductive power transfer," *Proceedings of the IEEE*, vol. 101, no. 6, pp. 1276–1289, June 2013.

[6] A. W. Green and J. T. Boys, "10 khz inductively coupled power transfer-concept and control," in *1994 Fifth International Conference on Power Electronics and Variable-Speed Drives*, Oct 1994, pp. 694–699.

[7] J. T. Boys, G. A. Covic, and A. W. Green, "Stability and control of inductively coupled power transfer systems," *IEE Proceedings - Electric Power Applications*, vol. 147, no. 1, pp. 37–43, Jan 2000.

[8] Y. Jang and M. M. Jovanovic, "A contactless electrical energy transmission system for portable-telephone battery chargers," *IEEE Transactions on Industrial Electronics*, vol. 50, no. 3, pp. 520–527, June 2003.

[9] S. Y. R. Hui and W. W. C. Ho, "A new generation of universal contactless battery charging platform for portable consumer electronic equipment," *IEEE Transactions on Power Electronics*, vol. 20, no. 3, pp. 620–627, May 2005.

[10] W. X. Zhong, X. Liu, and S. Y. R. Hui, "A novel single-layer winding array and receiver coil structure for contactless battery charging systems with free-positioning and localized charging features," *IEEE Transactions on Industrial Electronics*, vol. 58, no. 9, pp. 4136–4144, Sept 2011.

[11] G. B. Joun and B. H. Cho, "An energy transmission system for an artificial heart using leakage inductance compensation of transcutaneous transformer," *IEEE Transactions on Power Electronics*, vol. 13, no. 6, pp. 1013–1022, Nov 1998.

[12] T. D. Dissanayake, A. P. Hu, S. Malpas, L. Bennet, A. Taberner, L. Booth, and D. Budgett, "Experimental study of a tet system for implantable biomedical devices," *IEEE Transactions on Biomedical Circuits and Systems*, vol. 3, no. 6, pp. 370–378, Dec 2009.

[13] H. Y. Leung, D. M. Budgett, and A. P. Hu, "Minimizing power loss in air-cored coils for tet heart pump systems," *IEEE Journal on Emerging and Selected Topics in Circuits and Systems*, vol. 1, no. 3, pp. 412–419, Sept 2011.

[14] R. Tavakoli and Z. Pantic, "Analysis, design and demonstration of a 25-kw dynamic wireless charging system for roadway electric vehicles," *IEEE Journal of Emerging and Selected Topics in Power Electronics*, vol. PP, no. 99, pp. 1–1, 2017.

[15] A. Azad, T. Saha, R. Zane, and Z. Pantic, "Design of hybrid energy storage systems for wirelessly charged electric vehicles," in *2015 IEEE 82nd Vehicular Technology Conference (VTC2015-Fall)*, Sept 2015, pp. 1–5.

[16] H. H. Wu, A. Gilchrist, K. Sealy, P. Israelsen, and J. Muhs, "A review on inductive charging for electric vehicles," in *2011 IEEE International Electric Machines Drives Conference (IEMDC)*, May 2011, pp. 143–147.

[17] C.-S. Wang, O. H. Stielau, and G. A. Covic, "Design considerations for a contactless electric vehicle battery charger," *IEEE Transactions on Industrial Electronics*, vol. 52, no. 5, pp. 1308–1314, Oct 2005.

[18] R. Tseng, B. von Novak, S. Shevde, and K. A. Grajski, "Introduction to the alliance for wireless power loosely-coupled wireless power transfer system specification version 1.0," in *2013 IEEE Wireless Power Transfer (WPT)*, May 2013, pp. 79–83.

[19] X. X. Tianjia Sun and Z. Wang, "Wireless power transfer for medical microsystems," [Ebrary version]. [Online], 2013. [Online]. Available: https://www.springer.com/us/book/9781461477013

[20] F. Lu, H. Zhang, H. Hofmann, and C. Mi, "A double-sided lclc-compensated capacitive power transfer system for electric vehicle charging," *IEEE Transactions on Power Electronics*, vol. 30, no. 11, pp. 6011–6014, Nov 2015.

[21] B. J. Limb, Z. D. Asher, T. H. Bradley, E. Sproul, D. A. Trinko, B. Crabb, R. Zane, and J. C. Quinn, "Economic viability and environmental impact of in-motion wireless power transfer," *IEEE Transactions on Transportation Electrification*, vol. 5, no. 1, pp. 135–146, March 2019.

[22] Z. Pantic, "Inductive power transfer systems for charging of electric vehicles," Ph.D. dissertation, North Carolina State University, Raleigh, NC, 2013.

[23] E. Bulut and M. C. Kisacikoglu, "Mitigating range anxiety via vehicle-to-vehicle social charging system," in *2017 IEEE 85th Vehicular Technology Conference (VTC Spring)*, June 2017, pp. 1–5.

[24] A. Govindaraj, "Design and characterization of various circuit topologies for battery/ultracapacitor hybrid energy storage systems," Master's thesis, North Carolina State University, Raleigh, NC, 2010.

[25] S. Ruddell, U. K. Madawala, D. J. Thrimawithana, and M. Neuburger, "A novel wireless converter topology for dynamic ev charging," in *2016 IEEE Transportation Electrification Conference and Expo (ITEC)*, June 2016, pp. 1–5.

[26] J. M. Miller, O. C. Onar, C. White, S. Campbell, C. Coomer, L. Seiber, R. Sepe, and A. Steyerl, "Demonstrating dynamic wireless charging of an electric vehicle: The benefit of electrochemical capacitor smoothing," *IEEE Power Electronics Magazine*, vol. 1, no. 1, pp. 12–24, March 2014.

[27] B. Kramer, S. Chakraborty, and B. Kroposki, "A review of plug-in vehicles and vehicle-to-grid capability," in *2008 34th Annual Conference of IEEE Industrial Electronics*, Nov 2008, pp. 2278–2283.

[28] N. Hatziargyriou, H. Asano, R. Iravani, and C. Marnay, "Microgrids," *IEEE Power and Energy Magazine*, vol. 5, no. 4, pp. 78–94, July 2007.

[29] H. Zhou, T. Bhattacharya, D. Tran, T. S. T. Siew, and A. M. Khambadkone, "Composite energy storage system involving battery and ultracapacitor with dynamic energy management in microgrid applications," *IEEE Transactions on Power Electronics*, vol. 26, no. 3, pp. 923–930, March 2011.

[30] J. M. Miller, P. T. Jones, J. M. Li, and O. C. Onar, "Ornl experience and challenges facing dynamic wireless power charging of ev's," *IEEE Circuits and Systems Magazine*, vol. 15, no. 2, pp. 40–53, Secondquarter 2015.

[31] U. K. Madawala and D. J. Thrimawithana, "A bidirectional inductive power interface for electric vehicles in v2g systems," *IEEE Transactions on Industrial Electronics*, vol. 58, no. 10, pp. 4789–4796, Oct 2011.

[32] E. Bulut and M. C. Kisacikoglu, "Mitigating range anxiety via vehicle-to-vehicle social charging system," in *2017 IEEE 85th Vehicular Technology Conference (VTC Spring)*, June 2017, pp. 1–5.

[33] C. Wang and H. Nehrir, "Power management of a stand-alone wind/photovoltaic/fuel-cell energy system," in *2008 IEEE Power and Energy Society General Meeting - Conversion and Delivery of Electrical Energy in the 21st Century*, July 2008, pp. 1–1.

[34] G. Pepermans, J. Driesen, D. Haeseldonckx, R. Belmans, and W. Dhaeseleer, "Distributed generation: Definition, benefits and issues," *Energy Policy*, vol. 33, no. 6, pp. 787–798, April 2005.

[35] J. Franz. (2017) California's electrical grid can't handle all the solar energy the state is producing. [Online]. Available: https://www.pri.org/stories/2017-07-20/california-s-electrical-grid-can-t-handle-all-solar-energy-state-producing

[36] M. Yilmaz and P. T. Krein, "Review of the impact of vehicle-to-grid technologies on distribution systems and utility interfaces," *IEEE Transactions on Power Electronics*, vol. 28, no. 12, pp. 5673–5689, Dec 2013.

[37] M. Kintner-Meyer, K. Schneider, and R. Pratt. (2007) Impacts assessment of plug-in hybrid vehicles on electric utilities and regional us power grids part 1: Technical analysis. [Online]. Available: https://www.ferc.gov/about/com-mem/5-24-07-technical-analy-wellinghoff.pdf

[38] F. Koyanagi and Y. Uriu, "A strategy of load leveling by charging and discharging time control of electric vehicles," *IEEE Transactions on Power Systems*, vol. 13, no. 3, pp. 1179–1184, Aug 1998.

[39] S. De Breucker, P. Jacqmaer, K. De Brabandere, J. Driesen, and R. Belmans, "Grid power quality improvements using grid-coupled hybrid electric vehicles pemd 2006," in *2006 3rd IET International Conference on Power Electronics, Machines and Drives - PEMD 2006*, April 2006, pp. 505–509.

[40] E. Keane and D. Flynn, "Potential for electric vehicles to provide power system reserve," in *2012 IEEE PES Innovative Smart Grid Technologies (ISGT)*, Jan 2012, pp. 1–7.

[41] A. Srivastava, B. Annabathina, and S. Kamalasadan, "The challenges and policy options for integrating plug-in hybrid electric vehicle into theelectric grid," *IEEE Transactions on Power Systems*, vol. 23, no. 3, pp. 83–91, Aug 2010.

[42] D. Steward. (2007) Critical elements of vehicle-togrid (v2g) economics. [Online]. Available: https://www.nrel.gov/docs/fy17osti/69017.pdf

[43] D. J. Thrimawithana, U. K. Madawala, and M. Neath, "A steady-state analysis of bidirectional inductive power transfer systems," in *2013 IEEE International Conference on Industrial Technology (ICIT)*, Feb 2013, pp. 1618–1623.

[44] C.-S. Wang, G. A. Covic, and O. H. Stielau, "Power transfer capability and bifurcation phenomena of loosely coupled inductive power transfer systems," *IEEE Transactions on Industrial Electronics*, vol. 51, no. 1, pp. 148–157, Feb 2004.

[45] N. A. Keeling, G. A. Covic, and J. T. Boys, "A unity-power-factor ipt pickup for high-power applications," *IEEE Transactions on Industrial Electronics*, vol. 57, no. 2, pp. 744–751, Feb 2010.

[46] W. Zhang and C. C. Mi, "Compensation topologies of high-power wireless power transfer systems," *IEEE Transactions on Vehicular Technology*, vol. 65, no. 6, pp. 4768–4778, June 2016.

[47] S. H. Lee and R. D. Lorenz, "Development and validation of model for 95 *IEEE Transactions on Industry Applications*, vol. 47, no. 6, pp. 2495–2504, Nov 2011.

[48] Y. Nagatsuka, N. Ehara, Y. Kaneko, S. Abe, and T. Yasuda, "Compact contactless power transfer system for electric vehicles," in *The 2010 International Power Electronics Conference - ECCE ASIA -*, June 2010, pp. 807–813.

[49] S. Y. Choi, B. W. Gu, S. Y. Jeong, and C. T. Rim, "Advances in wireless power transfer systems for roadway-powered electric vehicles," *IEEE Journal of Emerging and Selected Topics in Power Electronics*, vol. 3, no. 1, pp. 18–36, March 2015.

[50] J. Huh, S. W. Lee, W. Y. Lee, G. H. Cho, and C. T. Rim, "Narrow-width inductive power transfer system for online electrical vehicles," *IEEE Transactions on Power Electronics*, vol. 26, no. 12, pp. 3666–3679, Dec 2011.

[51] A. Zaheer, H. Hao, G. A. Covic, and D. Kacprzak, "Investigation of multiple decoupled coil primary pad topologies in lumped ipt systems for interoperable electric vehicle charging," *IEEE Transactions on Power Electronics*, vol. 30, no. 4, pp. 1937–1955, April 2015.

[52] G. A. Covic and J. T. Boys, "Modern trends in inductive power transfer for transportation applications," *IEEE Journal of Emerging and Selected Topics in Power Electronics*, vol. 1, no. 1, pp. 28–41, March 2013.

[53] G. A. Covic, M. L. G. Kissin, D. Kacprzak, N. Clausen, and H. Hao, "A bipolar primary pad topology for ev stationary charging and highway power by inductive coupling," in *2011 IEEE Energy Conversion Congress and Exposition*, Sep. 2011, pp. 1832–1838.

[54] M. Budhia, J. T. Boys, G. A. Covic, and C. Huang, "Development of a single-sided flux magnetic coupler for electric vehicle ipt charging systems," *IEEE Transactions on Industrial Electronics*, vol. 60, no. 1, pp. 318–328, Jan 2013.

[55] J. T. Boys and G. A. Covic, "The inductive power transfer story at the university of auckland," *IEEE Circuits and Systems Magazine*, vol. 15, no. 2, pp. 6–27, Secondquarter 2015.

[56] M. Budhia, G. A. Covic, and J. T. Boys, "Design and optimization of circular magnetic structures for lumped inductive power transfer systems," *IEEE Transactions on Power Electronics*, vol. 26, no. 11, pp. 3096–3108, Nov 2011.

[57] A. N. Azad, A. Echols, V. A. Kulyukin, R. Zane, and Z. Pantic, "Analysis, optimization, and demonstration of a vehicular detection system intended for dynamic wireless charging applications," *IEEE Transactions on Transportation Electrification*, vol. 5, no. 1, pp. 147–161, March 2019.

[58] J. Jang and M. Jovanovic, "Contactless electrical energy transmission systems," U.S. Patent 6 301 128 B1, Oct. 9, 2001.

[59] J. G. Meins and J. D. Sinsley, "Method and apparatus for supplying contactless power," U.S. Patent 6 515 878 B1, Feb. 4, 2003.

[60] L. Zhao, D. J. Thrimawithana, and U. K. Madawala, "Hybrid bidirectional wireless ev charging system tolerant to pad misalignment," *IEEE Transactions on Industrial Electronics*, vol. 64, no. 9, pp. 7079–7086, Sep. 2017.

[61] D. J. Thrimawithana, U. K. Madawala, and Y. Shi, "Design of a bi-directional inverter for a wireless v2g system," in *2010 IEEE International Conference on Sustainable Energy Technologies (ICSET)*, Dec 2010, pp. 1–5.

[62] D. J. Thrimawithana, U. K. Madawala, and M. Neath, "A synchronization technique for bidirectional ipt systems," *IEEE Transactions on Industrial Electronics*, vol. 60, no. 1, pp. 301–309, Jan 2013.

[63] D. Desai and S. Somani, "Instinctive traffic control and vehicle detection techniques," *International Journal of Scientific Engineering Research*, vol. 1, no. 1, Jan 2014.

[64] R. M. Tyburski, "A review of road sensor technology for monitoring vehicle traffic," *Institute of Transportation Engineers*, vol. 59, no. 8, Jan 1989.

[65] Ho Gi Jung, Dong Suk Kim, Pal Joo Yoon, and Jaihie Kim, "Parking slot markings recognition for automatic parking assist system," in *2006 IEEE Intelligent Vehicles Symposium*, June 2006, pp. 106–113.

[66] S. Birell, D. wilson, C. Yang, G. Dhadyalla, and P. Jennings, "A double-sided lcc compensation network and its tuning method for wireless power transfer," *Transportation Research Part C: Emerging Technologies*, vol. 58, no. D, pp. 721–731, September 2015.

[67] W. Ni, I. B. Collings, X. Wang, R. P. Liu, A. Kajan, M. Hedley, and M. Abolhasan, "Radio alignment for inductive charging of electric vehicles," *IEEE Transactions on Industrial Informatics*, vol. 11, no. 2, pp. 427–440, April 2015.

[68] Y. Gao, A. Ginart, K. B. Farley, and Z. T. H. Tse, "Uniform-gain frequency tracking of wireless ev charging for improving alignment flexibility," in *2016 IEEE Applied Power Electronics Conference and Exposition (APEC)*, March 2016, pp. 1737–1740.

[69] J. Franz. (2017) Wireless power transfer for light-duty plug-in/ electric vehicles and alignment methodology. [Online]. Available: https://www.sae.org/standards/content/j2954_201605/

[70] Q. Deng, J. Liu, D. Czarkowski, M. Bojarski, J. Chen, W. Hu, and H. Zhou, "Edge position detection of on-line charged vehicles with segmental wireless power supply," *IEEE Transactions on Vehicular Technology*, vol. 66, no. 5, pp. 3610–3621, May 2017.

[71] G. R. Nagendra, L. Chen, G. A. Covic, and J. T. Boys, "Detection of evs on ipt highways," *IEEE Journal of Emerging and Selected Topics in Power Electronics*, vol. 2, no. 3, pp. 584–597, Sep. 2014.

[72] S. Kim, A. Tejeda, G. A. Covic, and J. T. Boys, "Analysis of mutually decoupled primary coils for ipt systems for ev charging," in *2016 IEEE Energy Conversion Congress and Exposition (ECCE)*, Sep. 2016, pp. 1–6.

[73] Y. Gao, K. B. Farley, and Z. Tse, "A uniform voltage gain control for alignment robustness in wireless ev charging," *Energies*, vol. 5, no. 4, pp. 8355–8370, August 2015.

[74] K. Fotopoulou and B. W. Flynn, "Wireless power transfer in loosely coupled links: Coil misalignment model," *IEEE Transactions on Magnetics*, vol. 47, no. 2, pp. 416–430, Feb 2011.

[75] B. Z. Paul Green, Brian Cullinane and D. Smith. (2014) Typical values for driving performance with emphasis on the standard deviation of lane position: A summary of the literature. [Online]. Available: https://www.volpe.dot.gov/safety-management-and-human-factors/surface-transportation-human-factors/typical-values-driving

[76] J. L. Villa, J. Sallan, J. F. Sanz Osorio, and A. Llombart, "High-misalignment tolerant compensation topology for icpt systems," *IEEE Transactions on Industrial Electronics*, vol. 59, no. 2, pp. 945–951, Feb 2012.

[77] S. Li, W. Li, J. Deng, T. D. Nguyen, and C. C. Mi, "A double-sided lcc compensation network and its tuning method for wireless power transfer," *IEEE Transactions on Vehicular Technology*, vol. 64, no. 6, pp. 2261–2273, June 2015.

[78] N. Hasan, H. Wang, T. Saha, and Z. Pantic, "A novel position sensorless power transfer control of lumped coil-based in-motion wireless power transfer systems," in *2015 IEEE Energy Conversion Congress and Exposition (ECCE)*, Sep. 2015, pp. 586–593.

[79] H. H. Wu, A. Gilchrist, K. D. Sealy, and D. Bronson, "A high efficiency 5 kw inductive charger for evs using dual side control," *IEEE Transactions on Industrial Informatics*, vol. 8, no. 3, pp. 585–595, Aug 2012.

[80] Z. N. Low, J. J. Casanova, P. H. Maier, J. A. Taylor, R. A. Chinga, and J. Lin, "Method of load/fault detection for loosely coupled planar wireless power transfer system with power delivery tracking," *IEEE Transactions on Industrial Electronics*, vol. 57, no. 4, pp. 1478–1486, April 2010.

[81] K. H. S. Verghese, M. P. Kesler and H. T. Lou, "Foreign object detection in wireless energy transfer systems," U.S. Patent 2 013 036 947, Mar. 15, 2013.

[82] M. R. Sonapreetha, S. Y. Jeong, S. Y. Choi, and C. T. Rim, "Dual-purpose non-overlapped coil sets as foreign object and vehicle location detections for wireless stationary ev chargers," in *2015 IEEE PELS Workshop on Emerging Technologies: Wireless Power (2015 WoW)*, June 2015, pp. 1–7.

[83] N. Kuyvenhoven, C. Dean, J. Melton, J. Schwannecke, and A. E. Umenei, "Development of a foreign object detection and analysis method for wireless power systems," in *2011 IEEE Symposium on Product Compliance Engineering Proceedings*, Oct 2011, pp. 1–6.

[84] S. Fukuda, H. Nakano, Y. Murayama, T. Murakami, O. Kozakai, and K. Fujimaki, "A novel metal detector using the quality factor of the secondary coil for wireless power transfer systems," in *2012 IEEE MTT-S International Microwave Workshop Series on Innovative Wireless Power Transmission: Technologies, Systems, and Applications*, May 2012, pp. 241–244.

[85] W. Zhang, S. Wong, C. K. Tse, and Q. Chen, "Analysis and comparison of secondary series- and parallel-compensated inductive power transfer systems operating for optimal efficiency and load-independent voltage-transfer ratio," *IEEE Transactions on Power Electronics*, vol. 29, no. 6, pp. 2979–2990, June 2014.

[86] L. Chen, S. Liu, Y. C. Zhou, and T. J. Cui, "An optimizable circuit structure for high-efficiency wireless power transfer," *IEEE Transactions on Industrial Electronics*, vol. 60, no. 1, pp. 339–349, Jan 2013.

[87] S. B. Z. Pantic and S. M. Lukic, "Zcs *lcc*-compensated resonant inverter for inductive-power-transfer application," *IEEE Transactions on Industrial Electronics*, vol. 58, no. 8, pp. 3500–3510, Aug 2011.

[88] R. O. Duda and P. E. Hart, "Use of the hough transformation to detect lines and curves in pictures," *Communications of the ACM*, vol. 15, no. 1, pp. 11–15, Jan 1972.

[89] A. Jensen and A. Cour-Harbo, *Ripples in Mathematics*. New York, NY: Springer, 2001.

[90] V. Kulyukin and V. R. Sudini, "Real time vision-based lane detection on raspberry pi with 1d haar wavelet spikes," in *2017 Proc. of The International Multiconference of Engineers and Computer Scientists*, Mar 2017, pp. 15–17.

[91] A. Azad, Z. Pantic, and V. Kulyukin, "Misalignment tolerant dwpt charger for ev roadways with integrated foreign object detection and driver feedback system," in *IEEE Transportation Electrification Conference and Expo*, Jul. 2019.

[92] (2019) California driver handbook - vehicle positioning. [Online]. Available: https://www.dmv.ca.gov/portal/dmv/detail/pubs/hdbk+/merg_pass

[93] (2019) Keeping a safe following distance while driving. [Online]. Available: https://www.drive-safely.net/safe-following-distance/

[94] (2019). [Online]. Available: https://www.alliedelec.com/m/d/18664a71692af3be842bb3f7bb1b40de.pdf

[95] (2019). [Online]. Available: https://licaptech.com/lithium-ion-capacitors

[96] G. A. Covic, J. T. B. R. German, O. Briat, A. Sari, P. Venet, M. Ayadi, Y. Zitouni, and J. Vinassa, "Impact of high frequency current ripple on supercapacitors ageing through floating ageing tests," *Microelectronics Reliability*, vol. 53, no. 9-11, pp. 1643–1647, September 2013.

[97] I. Maxwell Technologies. (2019) Design considerations for ultracapacitors. [Online]. Available: https://www.maxwell.com/images/documents/technote_designinguide.pdf

[98] R. W. Erickson and D. Maksimovic, *Fundamentals of Power Electronics*. Norwell, MA: Kluwer Academic Publishers, 2001.

[99] H. Hao, G. A. Covic, and J. T. Boys, "An approximate dynamic model of lcl- *t*-based inductive power transfer power supplies," *IEEE Transactions on Power Electronics*, vol. 29, no. 10, pp. 5554–5567, Oct 2014.

[100] A. Azad and Z. Pantic, "Bidirectional grid-side power management in dwpt systems for ev charging applications," in *2019 IEEE Energy Conversion Congress and Exposition*, September 2019.

[101] ——, "A supercapacitor-based converter topology for grid-side power management in dynamic wireless charging systems," in *IEEE Transportation Electrification Conference and Expo*, July 2019.

[102] K. Ogata, *Modern Control Engineering.* Upper Saddle River, NJ: Prentice Hall, 2010.

[103] (2019). [Online]. Available: https://www.opal-rt.com/

[104] B. J. Varghese, T. Smith, A. Azad, and Z. Pantic, "Design and optimization of decoupled concentric and coplanar coils for wpt systems," in *2017 IEEE Wireless Power Transfer Conference (WPTC)*, May 2017, pp. 1–4.

[105] U. Pratik, B. J. Varghese, A. Azad, and Z. Pantic, "Optimum design of decoupled concentric coils for operation in double-receiver wireless power transfer systems," *IEEE Journal of Emerging and Selected Topics in Power Electronics*, vol. 7, no. 3, pp. 1982–1998, Sep. 2019.

[106] C. Moreland. (2006) Coil basics. [Online]. Available: https://www.geotech1.com/pages/metdet/info/coils.pdf

[107] S. M. Lukic, J. Cao, R. C. Bansal, F. Rodriguez, and A. Emadi, "Energy storage systems for automotive applications," *IEEE Transactions on Industrial Electronics*, vol. 55, no. 6, pp. 2258–2267, June 2008.

[108] A. Khaligh and Z. Li, "Battery, ultracapacitor, fuel cell, and hybrid energy storage systems for electric, hybrid electric, fuel cell, and plug-in hybrid electric vehicles: State of the art," *IEEE Transactions on Vehicular Technology*, vol. 59, no. 6, pp. 2806–2814, July 2010.

[109] A. F. Burke, "Batteries and ultracapacitors for electric, hybrid, and fuel cell vehicles," *Proceedings of the IEEE*, vol. 95, no. 4, pp. 806–820, April 2007.

[110] J. R. Miller and A. F. Burke. (2007) Electrochemical capacitors: Challenges and opportunities for real-world applications. [Online]. Available: https://www.electrochem.org/dl/interface/spr/spr08/spr08_p53-57.pdf

[111] L. Zubieta and R. Bonert, "Characterization of double-layer capacitors for power electronics applications," *IEEE Transactions on Industry Applications*, vol. 36, no. 1, pp. 199–205, Jan 2000.

[112] A. Ostadi, M. Kazerani, and S. Chen, "Hybrid energy storage system (hess) in vehicular applications: A review on interfacing battery and ultra-capacitor units," in *2013 IEEE Transportation Electrification Conference and Expo (ITEC)*, June 2013, pp. 1–7.

[113] J. Cao and A. Emadi, "A new battery/ultracapacitor hybrid energy storage system for electric, hybrid, and plug-in hybrid electric vehicles," *IEEE Transactions on Power Electronics*, vol. 27, no. 1, pp. 122–132, Jan 2012.

[114] (2014). [Online]. Available: https://www.greencarcongress.com/2014/09/20140902-witricity.html

[115] P. Thounthong and S. Rael, "The benefits of hybridization," *IEEE Industrial Electronics Magazine*, vol. 3, no. 3, pp. 25–37, Sep. 2009.

[116] A. P. Hu, "Selected resonant converters for ipt power supplies," Ph.D. dissertation, The University of Auckland, Auckland, NZ, 2001.

[117] C.-T. Chen, *Linear System Theory and Design.* Oxford, UK: Oxford University Press, 2012.

APPENDICES

APPENDIX A

A.1   Mutual Inductance Calculation of a Rectangular Loop

Two parallel wire segment are shown in Fig. A.1(a), where the distance between segments is D, their axial misalignment is m, and the segment lengths are l_1 and l_2.
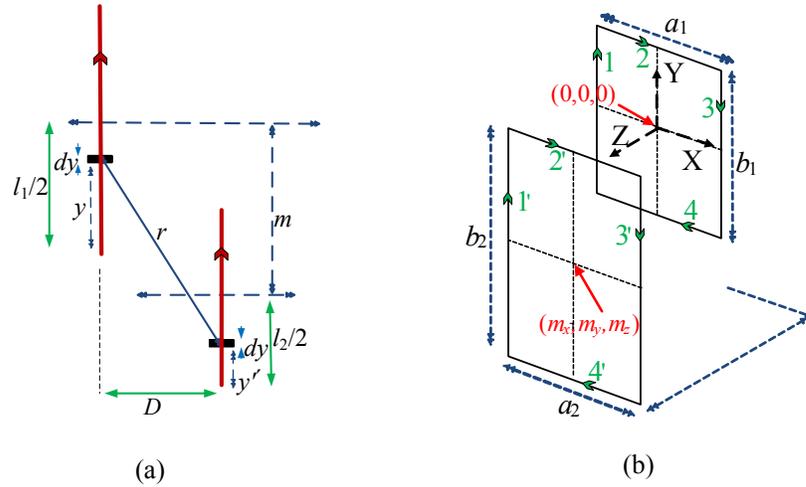
Fig. A.1: (a) Mutual inductance calculation of two parallel wire segments and (b) two parallel and misaligned rectangular coil turns.

After replacing the dot product of the two parallel infinitesimal vectors ds and ds' by their scalar product $dy.dy$, Neumann's formula (3.4) results in the double integral:

$$M = \frac{\mu_0}{4\pi} \int_0^{l_2} dy' \int_0^{l_1} \frac{dy}{r} \tag{A.1}$$

where

$$r = \sqrt{D^2 + (\frac{l_2}{2} - \frac{l_1}{2} + m + y - y')^2} \tag{A.2}$$

The solution of (A.1) can be written as:

$$M = \frac{\mu_0}{4\pi}[f(\frac{l_1}{2} + \frac{l_2}{2} - m) - f(\frac{l_1}{2} - \frac{l_2}{2} - m)] \tag{A.3}$$

where

$$\begin{aligned}
f(x) = l_1 \log(x - l_1 + \sqrt{D^2 + (l_1 - x)^2}) - \sqrt{D^2 + x^2} + \sqrt{D^2 + (l_1 - x)^2} \\
x \log \frac{l_1 - x + \sqrt{D^2 + (l_1 - x)^2}}{\sqrt{D^2 + x^2} - x}
\end{aligned} \tag{A.4}$$

Using (A.3) and (A.4), the mutual inductances between parallel sides of the two rectangular loops shown in Fig. A.1(b) can be readily found by taking into account the contribution of all parallel segments from different turns. Total mutual inductance could be calculated as an algebraic sum of all the mutual inductances as follows:

$$M_{total} = M_{11'} - M_{13'} + M_{22'} - M_{24'} - M_{31'} + M_{33'} - M_{42'} + M_{44'} \tag{A.5}$$

It is important to take into account the direction of current while calculating individual mutual inductances. The same direction of current (e.g., currents in segments 1 and 1') results in positive mutual inductances, whereas different current directions (e.g., segments 1 and 3) result in a negative value. Terms in (A.3) can be obtained by substituting the right combination of parameters l_1, l_2, D, and m in (A.1) and (A.2). For each pair of parallel conductors, these four parameters are listed in Table A.1.

Table A.1: Parameters for mutual inductance calculation of two rectangular coils

M	l_1	l_2	D	m
$M_{11'}$	b_1	b_2	$\sqrt{m_z^2 + 0.5(a_1 - a_2) + m_x}$	m_y
$M_{13'}$	b_1	b_2	$\sqrt{m_z^2 + 0.5(a_1 + a_2) + m_x}$	m_y
$M_{22'}$	a_1	a_2	$\sqrt{m_z^2 + 0.5(-b_1 + b_2) + m_y}$	m_x
$M_{24'}$	a_1	a_2	$\sqrt{m_z^2 + 0.5(-b_1 - b_2) + m_y}$	m_x
$M_{31'}$	b_1	b_2	$\sqrt{m_z^2 + 0.5(-a_1 - a_2) + m_x}$	m_y
$M_{33'}$	b_1	b_2	$\sqrt{m_z^2 + 0.5(-a_1 + a_2) + m_x}$	m_y
$M_{42'}$	a_1	a_2	$\sqrt{m_z^2 + 0.5(b_1 + b_2) + m_y}$	m_x
$M_{44'}$	a_1	a_2	$\sqrt{m_z^2 + 0.5(b_1 - b_2) + m_y}$	m_x

APPENDIX B

B.1 GSSA Modeling of WPT System

The GSSA modeling approach involves substituting the real-time domain variables with respective complex Fourier coefficient variables over a sliding time window [116]. In the following modeling approach, $< \, . \, >$ operator is used to symbolize the nth order complex Fourier coefficients.

Fig. B.1 represents a generalized GSSA model of a WPT system. For an accurate modeling, the capacitors' and inductances' losses have been modeled with respective series resistances. For example, R_{cpp}, R_{lps}, R_{lss}, and R_{csp} are modeled as the losses associated with C_{pp}, L_{ps}, L_{ss}, and C_{sp}, respectively. R_{lpri} represents the combined losses of C_{ps} and L_{pri}, whereas R_{lsec} represents the combined losses of C_{ss} L_{sec}. Similarly, the voltage source and EV battery losses are also modeled with series resistances R_{ldc} and R_{bat}, as shown in Fig. B.1.
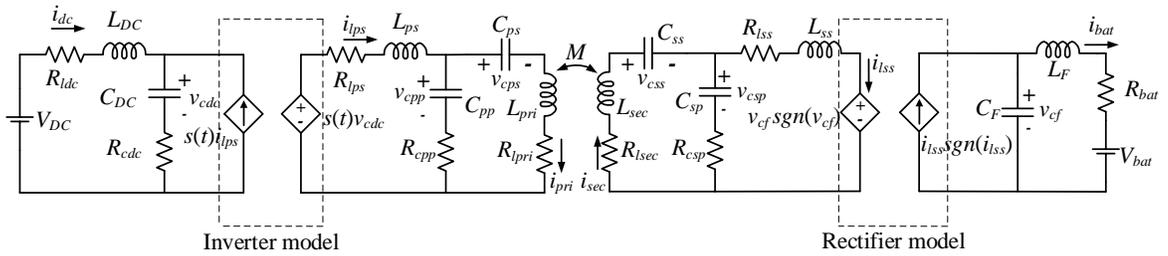

Fig. B.1: Generalized GSSA model of a WPT system.

An existance function [116] is employed to model the inverter circuit, defined by:

$$< s(t) >_n = \begin{cases} 0 & n = 0, 2, 4... \\ -\frac{2j}{n\pi} \sin \frac{\phi_p}{2} & n = 1, 3, 5... \end{cases} \tag{B.1}$$

In order to model the rectifier, a sign function [116] is employed, as follows:

$$< sgn(x) >_1 = \frac{2}{\pi} e^{\angle <x>_1} \tag{B.2}$$

With this modeling approach, the non-linear time-varying equations for the system states can be written as follows:

$$L_{ps} \frac{dL_{ps}}{dt} = s(t)v_{cdc} - i_{lps}R_{lps} - v_{cpp} - (i_{lps} - i_{pri})R_{cpp} \tag{B.3}$$

$$L_{pri} \frac{di_{pri}}{dt} = v_{cpp} + R_{cpp}(i_{lps} - i_{pri}) - i_{pri}R_{lpri} - v_{cps} + M\frac{di_{sec}}{dt} \tag{B.4}$$

$$C_{pp} \frac{dv_{cpp}}{dt} = i_{lps} - i_{pri} \tag{B.5}$$

$$C_{ps} \frac{dv_{cps}}{dt} = i_{pri} \tag{B.6}$$

$$L_{ss} \frac{di_{lss}}{dt} = R_{csp}(i_{sec} - i_{lss}) - i_{lss}R_{lss} - v_{csp} - v_{cf}sgn(v_{cf}) \tag{B.7}$$

$$L_{sec} \frac{di_{sec}}{dt} = -v_{css} - v_{csp} - R_{csp}(i_{sec} - i_{lss}) - i_{sec}R_{lsec} + M\frac{di_{pri}}{dt} \tag{B.8}$$

$$C_{sp} \frac{dv_{csp}}{dt} = i_{sec} - i_{lss} \tag{B.9}$$

$$C_{ss} \frac{dv_{css}}{dt} = i_{sec} \tag{B.10}$$

$$C_{DC} \frac{dv_{cdc}}{dt} = i_{dc} + s(t)i_{lps} \tag{B.11}$$

$$C_F \frac{dv_{cf}}{dt} = i_{lss}sgn(i_{lss}) - i_{bat} \tag{B.12}$$

Applying the first-order Fourier transformation operator $< . >_1$ to (B.3)-(B.12), the average state-space model of the circuit can be obtained.

The dynamics of the grid and the EV battery load could be neglected for a further simplified analysis with reduced number of states. With these assumptions, the *plant transfer function* for the proposed 25 kW system is be derived. While modeling the system, a typical *AC mode operation* is considered where inverter legs are operating with at constant duty cycles ($D_a = D_b = 0.5$) and with the phase shift modulation angle ϕ_p between the legs. The plant function is taken to be the transconductance G_{iv} between the primary coil current I_{pri} and the fundamental harmonic of the inverter output voltage $V_{pi,f}$. $V_{pi,f}$ can be defined as:

$$V_{pi,f} = \sqrt{2}\boldsymbol{V_{pi,1,rms}}sin\omega t \tag{B.13}$$

Simplified equivalent circuit models for the unloaded and loaded system are presented in Fig. B.2.
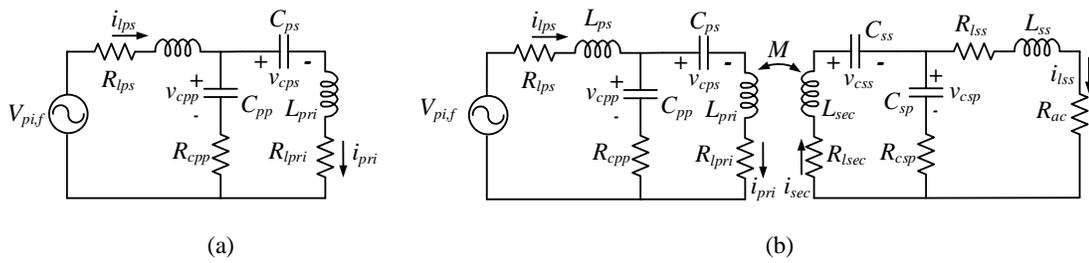

Fig. B.2: Simplified GSSA model of (a) unloaded system (b) loaded system.

For easier expressions in the calculation that follows, the following substitute variables are taken:

$$R_{cpp} + R_{lps} = R_1$$

$$R_{cpp} + R_{lpri} = R_2$$

$$R_{csp} + R_{lsec} = R_3 \tag{B.14}$$

$$R_{lss} + R_{csp} + R_{ac} = R_4$$

$$det = L_{pri}L_{sec} - M^2$$

The averaged state-space variables of the system can be expressed in complex form as shown below:

$$< i_{lps} >_1 = x_1 + jx_2$$

$$< i_{pri} >_1 = x_3 + jx_4$$

$$< v_{cpp} >_1 = x_5 + jx_6$$

$$< v_{cps} >_1 = x_7 + jx_8$$

$$< i_{lss} >_1 = x_9 + jx_{10} \tag{B.15}$$

$$< i_{sec} >_1 = x_{11} + jx_{12}$$

$$< v_{csp} >_1 = x_{13} + jx_{14}$$

$$< v_{css} >_1 = x_{15} + jx_{16}$$

A key property of $< . >$ operator used for GSSA modeling can be expressed as:

$$\frac{d < x >_k (t)}{dt} = < \frac{dx}{dt} >_k(t) - jk\omega_s < x >_k (t) \tag{B.16}$$

Applying (B.16) property on (B.3)-(B.12) and substituting into (B.15), the average state-space model of the system can be derived, and furthermore can be purturbed and linearized [98] to find the small-signal model expression in matrix form. The calculated state matrices are given as follows:

$$A = \begin{bmatrix} A_1 & A_2 \end{bmatrix}$$

where

$$A_1 = \begin{bmatrix}
-\frac{R_1}{L_{ps}} & \omega_s & \frac{R_{cpp}}{L_{ps}} & 0 & -\frac{1}{L_{ps}} & 0 & 0 & 0 \\
\omega_s & -\frac{R_1}{L_{ps}} & 0 & \frac{R_c}{L_{ps}} & 0 & -\frac{1}{L_{ps}} & 0 & 0 \\
\frac{R_{cpp}L_{sec}}{det} & 0 & -\frac{R_2 L_{sec}}{det} & \omega_s & \frac{L_{sec}}{det} & 0 & -\frac{L_{sec}}{det} & 0 \\
0 & \frac{R_{cpp}L_{sec}}{det} & -\omega_s & -\frac{R_2 L_{sec}}{det} & 0 & \frac{L_{sec}}{det} & 0 & -\frac{L_{sec}}{det} \\
\frac{1}{C_{pp}} & 0 & -\frac{1}{C_{pp}} & 0 & 0 & \omega_s & 0 & 0 \\
0 & \frac{1}{C_{pp}} & 0 & -\frac{1}{C_{pp}} & -\omega_s & 0 & 0 & 0 \\
0 & 0 & \frac{1}{C_{ps}} & 0 & 0 & 0 & 0 & \omega_s \\
0 & 0 & 0 & \frac{1}{C_{ps}} & 0 & 0 & -\omega_s & 0 \\
0 & 0 & 0 & 0 & 0 & 0 & 0 & 0 \\
0 & 0 & 0 & 0 & 0 & 0 & 0 & 0 \\
\frac{MR_{cpp}}{det} & 0 & -\frac{MR_2}{det} & 0 & \frac{M}{det} & 0 & -\frac{M}{det} & 0 \\
0 & \frac{MR_{cpp}}{det} & 0 & -\frac{MR_2}{det} & 0 & \frac{M}{det} & 0 & -\frac{M}{det} \\
0 & 0 & 0 & 0 & 0 & 0 & 0 & 0 \\
0 & 0 & 0 & 0 & 0 & 0 & 0 & 0 \\
0 & 0 & 0 & 0 & 0 & 0 & 0 & 0 \\
0 & 0 & 0 & 0 & 0 & 0 & 0 & 0
\end{bmatrix}$$

$$
A_2 =
\begin{bmatrix}
0 & 0 & 0 & 0 & 0 & 0 & 0 & 0 \\
0 & 0 & 0 & 0 & 0 & 0 & 0 & 0 \\
\frac{MR_{csp}}{det} & 0 & -\frac{MR_3}{det} & 0 & -\frac{M}{det} & 0 & -\frac{M}{det} & 0 \\
0 & \frac{MR_{csp}}{det} & 0 & -\frac{MR_3}{det} & 0 & -\frac{M}{det} & 0 & -\frac{M}{det} \\
0 & 0 & 0 & 0 & 0 & 0 & 0 & 0 \\
0 & 0 & 0 & 0 & 0 & 0 & 0 & 0 \\
0 & 0 & 0 & 0 & 0 & 0 & 0 & 0 \\
0 & 0 & 0 & 0 & 0 & 0 & 0 & 0 \\
-\frac{R_4}{L_{ss}} & \omega_s & \frac{R_{csp}}{L_{ss}} & 0 & \frac{1}{L_{ss}} & 0 & 0 & 0 \\
-\omega_s & -\frac{R_4}{L_{ss}} & 0 & \frac{1}{L_{ss}} & 0 & 0 & 0 & 0 \\
\frac{R_{csp}L_{pri}}{det} & 0 & -\frac{R_3L_{pri}}{det} & \omega_s & -\frac{L_{pri}}{det} & 0 & -\frac{L_{pri}}{det} & 0 \\
0 & \frac{R_{csp}L_{pri}}{det} & -\omega_s & -\frac{R_3L_{pri}}{det} & 0 & -\frac{L_{pri}}{det} & 0 & -\frac{L_{pri}}{det} \\
-\frac{1}{C_{sp}} & 0 & \frac{1}{C_{sp}} & 0 & 0 & \omega_s & 0 & 0 \\
0 & -\frac{1}{C_{sp}} & 0 & \frac{1}{C_{sp}} & -\omega_s & 0 & 0 & 0 \\
0 & 0 & \frac{1}{C_{ss}} & 0 & 0 & 0 & 0 & \omega_s \\
0 & 0 & 0 & \frac{1}{C_{ss}} & 0 & 0 & -\omega_s & 0
\end{bmatrix}
$$

$$
B = \begin{bmatrix} -\frac{1}{2L_{ps}} & 0 & 0 & 0 & 0 & 0 & 0 & 0 & 0 & 0 & 0 & 0 & 0 & 0 & 0 & 0 \end{bmatrix}^T
$$

$$
C = \begin{bmatrix} 0 & 0 & \frac{2X_3}{\sqrt{X_3^2+X_4^2}} & \frac{2X_4}{\sqrt{X_3^2+X_4^2}} & 0 & 0 & 0 & 0 & 0 & 0 & 0 & 0 & 0 & 0 & 0 & 0 \end{bmatrix}
$$

$$
D = \begin{bmatrix} 0 \end{bmatrix}
$$

where X_3 and X_4 are the steady-state values of x_3 and x_4.

For the unloaded case, however, the dynamics of the secondary circuit could be omitted, which results in a state-space having only 8 states (x_1 to x_8) instead of 16. In this scenario,

the state-space can be expressed as:

$$
A = \begin{bmatrix}
-\frac{R_1}{L_{ps}} & \omega_s & \frac{R_{cpp}}{L_{ps}} & 0 & -\frac{1}{L_{ps}} & 0 & 0 & 0 \\[6pt]
\omega_s & -\frac{R_1}{L_{ps}} & 0 & \frac{R_c}{L_{ps}} & 0 & -\frac{1}{L_{ps}} & 0 & 0 \\[6pt]
\frac{R_{cpp}L_{sec}}{det} & 0 & -\frac{R_2 L_{sec}}{det} & \omega_s & \frac{L_{sec}}{det} & 0 & -\frac{L_{sec}}{det} & 0 \\[6pt]
0 & \frac{R_{cpp}L_{sec}}{det} & -\omega_s & -\frac{R_2 L_{sec}}{det} & 0 & \frac{L_{sec}}{det} & 0 & -\frac{L_{sec}}{det} \\[6pt]
\frac{1}{C_{pp}} & 0 & -\frac{1}{C_{pp}} & 0 & 0 & \omega_s & 0 & 0 \\[6pt]
0 & \frac{1}{C_{pp}} & 0 & -\frac{1}{C_{pp}} & -\omega_s & 0 & 0 & 0 \\[6pt]
0 & 0 & \frac{1}{C_{ps}} & 0 & 0 & 0 & 0 & \omega_s \\[6pt]
0 & 0 & 0 & \frac{1}{C_{ps}} & 0 & 0 & -\omega_s & 0
\end{bmatrix}
$$

$$
B = \begin{bmatrix}
0 \\[6pt]
-\frac{1}{2L_{ps}} \\[6pt]
0 \\[6pt]
0 \\[6pt]
0 \\[6pt]
0 \\[6pt]
0 \\[6pt]
0
\end{bmatrix}
$$

$$
C = \begin{bmatrix} 0 & 0 & \frac{2X_3}{\sqrt{X_3^2 + X_4^2}} & \frac{2X_4}{\sqrt{X_3^2 + X_4^2}} & 0 & 0 & 0 & 0 \end{bmatrix}
$$

$$
D = \begin{bmatrix} 0 \end{bmatrix}
$$

Matrices A,B,C and D describes the small-signal no-load model of the system. Solving this no-load model using state-space to transfer function conversion [117], G_{vi} is calculated. Due to the complex form of the transfer function, its formula is not presented in the form of an equation.

B.2 Inverter-SC Unit: Small Signal AC analysis

In this section, small-signal AC analysis of the inverter and the SC circuit shown in Fig. B.3 is carried out. It is assumed that the inverter is operating with *dual mode operation* with a switching period T_s, as illustrated by the V_{pi} waveform shown in Fig. B.4. All switches and circuit elements are assumed to be ideal. All the signals are assumed to be time-variant for the sake of AC analysis. Within a switching period T_s, four distinct subintervals are identified that need to be addressed separately in order to derive the small signal AC model. These four subintervals are depicted in Fig. B.5.

Fig. B.3: Inverter circuit for DC analysis and small-signal AC analysis.

Fig. B.4: Single period of inverter output.

During $0 < t < d_1(t)$ subinterval Q_{p1}, Q_{p4} are ON and Q_{p2}, Q_{p3} are OFF. The time-varying state equations for this period are:
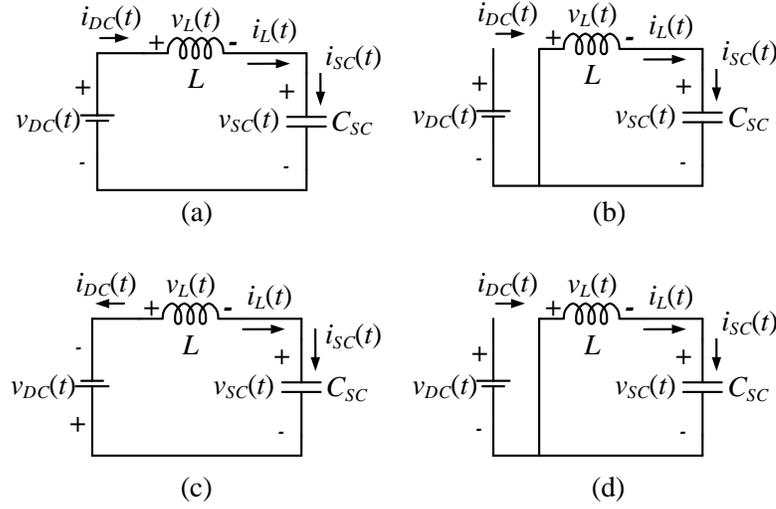
Fig. B.5: Inverter circuit during (a) $0 < t < d_1(t)$ subinterval (b) $d_1(t) < t < d_1(t) + d_2(t)$ subinterval (c) $d_1(t) + d_2(t) < t < d_1(t) + d_2(t) + d_3(t)$ subinterval (d) $d_1(t) + d_2(t) + d_3(t) < t < T_s$ subinterval.

$$v_L = L\frac{di_L(t)}{dt} = v_{DC}(t) - v_{SC}(t)$$

$$i_{SC} = C_{SC}\frac{dv_{SC}(t)}{dt} = i_L(t) \tag{B.17}$$

$$i_{DC}(t) = i_L(t)$$

During $d_1(t) < t < d_1(t) + d_2(t)$ subinterval Q_{p1}, Q_{p2} are ON and Q_{p3}, Q_{p4} are OFF. The time-varying state equations for this period are:

$$v_L = L\frac{di_L(t)}{dt} = -v_{SC}(t)$$

$$i_{SC} = C_{SC}(t)\frac{dv_{SC}}{dt} = i_L(t) \tag{B.18}$$

$$i_{DC}(t) = 0$$

During $d_1(t) + d_2(t) < t < d_1 + d_2(t) + d_3(t)$ subinterval Q_{p2}, Q_{p3} are ON and Q_{p1}, Q_{p4} are OFF. The time-varying state equations for this period are:

$$v_L = L\frac{di_L(t)}{dt} = -v_{DC}(t) - v_{SC}(t)$$

$$i_{SC} = C_{SC}\frac{dv_{SC}(t)}{dt} = i_L(t) \tag{B.19}$$

$$i_{DC}(t) = -i_L(t)$$

During $d_1(t) + d_2(t) + d_3(t) < t < T_s$ subinterval Q_{p3}, Q_{p4} are ON and Q_{p1}, Q_{p2} are OFF. The time-varying state equations for this period are:

$$v_L = L\frac{di_L(t)}{dt} = -v_{SC}(t)$$

$$i_{C_{SC}} = C_{SC}\frac{dv_{SC}(t)}{dt} = i_L(t) \tag{B.20}$$

$$i_{DC}(t) = 0$$

Replacing the signals with their low-frequency averaged values, one can calculate the low-frequency average of the system states over the period T_s as:

$$< v_L > = L\frac{d < i_L(t) >}{dt} = d_1(t)[< v_{DC}(t) > - < v_{SC}(t) >] - d_2(t) < v_{SC}(t) >$$
$$- d_3(t)[v_{DC}(t) + v_{SC}(t)] - [\Delta d(t) + d_4(t)]v_{SC}(t) \tag{B.21}$$

$$< i_{C_{SC}} > = C_{SC}\frac{d < v_{SC}(t) >}{dt} = < i_L(t) > \tag{B.22}$$

$$< i_{DC}(t) > = d_1(t) < i_L(t) > - d_3(t) < i_L(t) > \tag{B.23}$$

In order to simplify the expression of (B.21), the following equation could be utilized:

$$d_1(t) + d_2(t) + d_3(t) + \Delta d(t) + d_4(t) = 1 \tag{B.24}$$

Substituting (B.24) into (B.21) the following expression can be derived:

$$< v_L >= L\frac{d < i_L(t) >}{dt} = [d_1(t) - d_3(t)] < v_{DC}(t) > - < v_{SC}(t) > \tag{B.25}$$

Expressing each averaged signal as a sum of the quiescent value and an AC perturbation superimposed upon that signal, one can write:

$$d_3(t) = D_3 - \Delta\hat{d}$$

$$< v_{DC} >= V_{DC} + \hat{v}_{DC}$$

$$< v_{SC} >= V_{SC} + \hat{v}_{SC} \tag{B.26}$$

$$< i_L >= I_L + \hat{i}_L$$

$$< i_{DC} >= I_{DC} + \hat{i}_{DC}$$

Putting the perturbed signals of (B.26) into (B.25), the following expressions can be found:

$$L\frac{d\hat{i}_L}{dt} = [D_1 - (D_3 - \Delta\hat{d})][V_{DC} + \hat{v}_{DC}(t)] - V_{SC} - \hat{v}_{SC}(t) \tag{B.27}$$

In a similar way, substituting the perturbations of (B.26) into (B.23) results in:

$$I_{DC} + \hat{i}_{DC} = (D_1 - D_3 + \Delta\hat{d})(I_L + \hat{i}_L) \tag{B.28}$$

Since $D_1 - D_3 = \Delta D$ (Fig. B.4), (B.28) can be further simplified as:

$$I_{DC} + \hat{i}_{DC} = (\Delta D + \Delta\hat{d})(I_L + \hat{i}_L) \tag{B.29}$$

Equating DC terms of (B.27) and (B.29), the DC equivalent model equations could be derived as:

$$V_{SC} = \Delta D V_{DC}$$

$$I_{DC} = \Delta D I_L \tag{B.30}$$

Equating First order AC terms of (B.27) and (B.29) while neglecting higher-order AC terms, the AC equivalent model equations could be derived as:

$$L\frac{d\hat{i}_L}{dt} = \Delta D \hat{v}_{DC} + \Delta \hat{d} V_{DC} - \hat{v}_{SC}$$

$$\hat{i}_{DC} = \Delta D \hat{i}_L + \Delta \hat{d} I_L \tag{B.31}$$

From (B.31) the small-signal AC equivalent circuit is derived which is depicted in Fig. B.6.
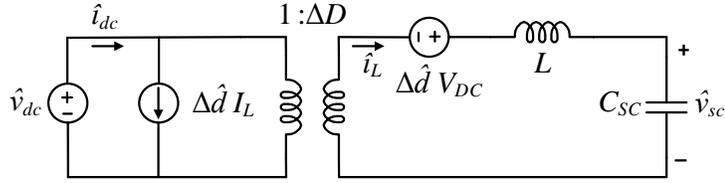

Fig. B.6: The small-signal AC equivalent circuit of inverter.

The *control to input current* transfer function can be derived from Fig. B.6 by setting $\hat{v}_{DC} = \hat{v}_{SC} = 0$, A simplified expression of this transfer function $G_{idc,d}$ is given as follows:

$$G_{idc,d} = \frac{\hat{i_{DC}}}{\Delta \hat{d}}\bigg|_{\hat{v}_{SC}=\hat{v}_{DC}=0} = I_L + \frac{\Delta D V_{DC}}{sL} = \frac{\Delta D V_{DC}}{L}\frac{(1 + \frac{s}{\frac{\Delta D V_{DC}}{LI_L}})}{s} \tag{B.32}$$

B.3 Choke Inductance's Current Ripple Calculation During Dual Mode Operation of Inverter

Fig. B.7 shows the waveform of the voltage v_L and current i_L across L during one full

switching period of the charging phase when the inverter is operating in dual mode. It can be observed that, during different subintervals of the switching period of T_s, v_L can be written as:
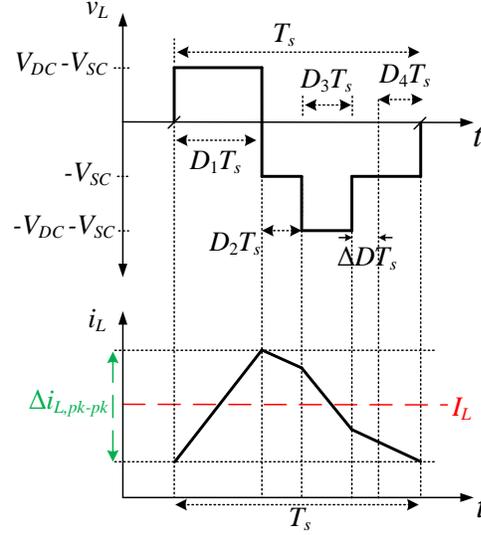

Fig. B.7: Voltage and current waveform of choke inductance L during a single period T_s in dual mode operation.

$$\frac{di_L}{dt} = \frac{V_{DC} - V_{SC}}{L}; 0 < t < D_1 T_s \tag{B.33}$$

$$\frac{di_L}{dt} = \frac{-V_{SC}}{L}; D_1 T_s < t < (D_1 + D_2) T_s \tag{B.34}$$

$$\frac{di_L}{dt} = \frac{-V_{DC} - V_{SC}}{L}; (D_1 + D_2) T_s < t < (D_1 + D_2 + D_3) T_s \tag{B.35}$$

$$\frac{di_L}{dt} = \frac{-V_{SC}}{L}; (D_1 + D_2 + D_3) T_s < t < T_s \tag{B.36}$$

From the waveform of i_L in Fig. B.7, it can be observed that the inductor current

increases in subinterval $D_1 T_s$ only, and decreases in all the other three subintervals. Thereby, for the peak-to-peak ripple calculation, the $D_1 T_s$ subinterval can be used. Furthermore, the change in i_L with respect to time can be approximated as linear during this subinterval, and thereby can be re-written as:

$$L = \frac{(V_{DC} - V_{SC})D_1 T_s}{\Delta i_{L,pk-pk}} \tag{B.37}$$

where is expressed as the total peak-to-peak ripple, as can be observed from Fig. B.7.

APPENDIX C

C.1 Boost Converter: Small Signal AC Analysis

In this section, small-signal AC analysis of the boost circuit shown in Fig. C.1 is carried out. It is assumed that the Boost converter is operating at a duty cycle D_{boost} and with a switching period T. All switches and circuit elements are assumed to be ideal. All the signals are assumed to be time-variant for the sake of AC analysis.
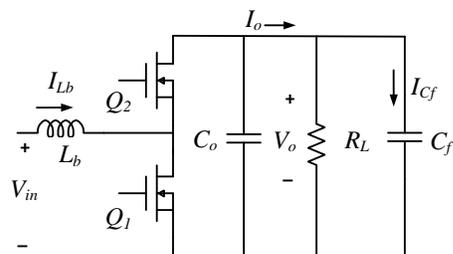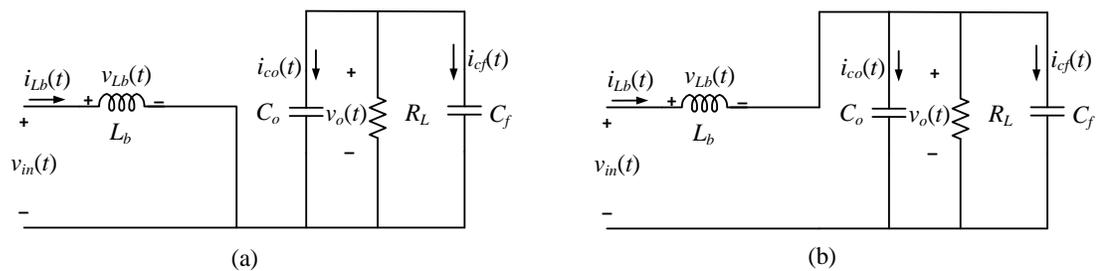

Fig. C.1: Boost converter circuit.

Within a switching period of T, two distinct subintervals are identified that need to be analyzed separately in order to derive the small-signal AC model. These two subintervals are depicted in Fig. C.2.

Fig. C.2: Boost converter circuit at (a) $0 < t < d_{boost}(t)$ subinterval (b) $d_{boost}(t) < t < T$ subinterval.

During $0 < t < d_{boost}(t)$, Q_1 is ON and Q_2 is OFF (Fig. C.2(a)). The time-varying state equations for this period are:

$$v_{Lb}(t) = L_b \frac{di_{Lb}(t)}{dt} = v_{in}(t)$$

$$i_{Co}(t) = C_o \frac{dv_o(t)}{dt} = -\frac{v_0(t)}{R_L} - i_{Cf}(t) \tag{C.1}$$

During $d_{boost}(t) < t < T$ subinterval, Q_2 is ON and Q_1 is OFF. The time-varying state equations for this period are:

$$v_{Lb}(t) = L_b \frac{di_{Lb}(t)}{dt} = v_{in}(t) - v_0(t)$$

$$i_{Co}(t) = C_o \frac{dv_o(t)}{dt} = i_L(t) - \frac{v_0(t)}{R_L} - i_{Cf}(t) \tag{C.2}$$

Replacing the signals with their low frequency averaged values, one can calculate the low-frequency average of the system states over the period T as:

$$<v_{Lb}(t)> = L_b \frac{d<i_{Lb}(t)>}{dt} = d_{boost}(t) <v_{in}(t)> + d'_{boost}(t) <v_{in}(t)> - d'_{boost}(t) <v_o(t)> \tag{C.3}$$

$$<i_{Co}(t)> = C_o \frac{d<v_c(t)>}{dt} = d_{boost}(t)(-\frac{<v_0(t)>}{R_L} - <i_{Cf}(t)>) + d'_{boost}(t)(<i_L(t)>$$

$$-\frac{<v_0(t)>}{R_L} - <i_{Cf}(t)>) \tag{C.4}$$

Using $d_{boost}(t) + d'_{boost}(t) = 1$, (C.3) and (C.4) can be further simplified as follows:

$$<v_{Lb}(t)> = L_b \frac{d<i_{Lb}(t)>}{dt} = <v_{in}(t)> - d'_{boost}(t) <v_o(t)> \tag{C.5}$$

$$< i_{Co}(t) >= C_o \frac{d < v_{co}(t) >}{dt} = -\frac{< v_0(t) >}{R_L} - < i_{Cf}(t) > + d'_{boost}(t) < i_L(t) > \qquad \text{(C.6)}$$

Expressing each averaged signal as a sum of the quiescent value and an AC perturbation superimposed upon that signal, one can write:

$$d_{boost}(t) = D_{boost} + \hat{d}_{boost}$$

$$d'_{boost}(t) = D'_{boost} - \hat{d}_{boost}$$

$$< v_{in} >= V_{in} + \hat{v}_{in}$$

$$< v_o >= V_o + \hat{v}_o \qquad \text{(C.7)}$$

$$< i_{Lb} >= I_{Lb} + \hat{i}_{Lb}$$

$$< i_{co} >= I_{co} + \hat{i}_{co}$$

$$< i_{cf} >= I_{cf} + \hat{i}_{cf}$$

Putting the perturbed signals of (C.7) into (C.5), the following expression can be found:

$$L\frac{d\hat{i}_{Lb}}{dt} = V_{in} - D'_{boost}V_o + \hat{v}_{in} + \hat{d}_{boost}V_o - D'_{boost}\hat{v}_o + \hat{d}_{boost}\hat{v}_o \qquad \text{(C.8)}$$

In a similar way, putting the signal perturbations of of (C.7) into (B.23) results in:

$$I_{co} + \hat{i}_{co} = C_o\frac{d\hat{v}_o}{dt} = -\frac{V_o}{R} - I_{Cf} + I_L D'_{boost} - \frac{\hat{v}_o}{R_L} - \hat{i}_{cf} + D'_{boost}\hat{i}_{Lb} - \hat{d}_{boost}I_L - \hat{i}_{Lb}\hat{d}_{boost} \quad \text{(C.9)}$$

Equating DC terms of (C.8) and (C.9), the DC equivalent model equations could be derived as:

$$V_o = \frac{V_{in}}{D'_{boost}}$$
$$I_L = \frac{I_o}{D'_{boost}}$$

(C.10)

Equating First order AC terms of (C.8), (C.9) , and neglecting higher-order terms, the AC equivalent model equation could be derived as:

$$L\frac{d\hat{i}_{Lb}}{dt} = \hat{v}_{in} - D'_{boost}\hat{v}_o + \hat{d}_{boost}V_o$$
$$\hat{i}_{co} = -\frac{\hat{v}_o}{R_L} - \hat{i}_{cf} + D'_{boost}\hat{i}_{Lb} - \hat{d}_{boost}I_L$$

(C.11)

From (C.11), the small-signal AC equivalent model of the boost converter circuit is derived which is shown in Fig. C.3.
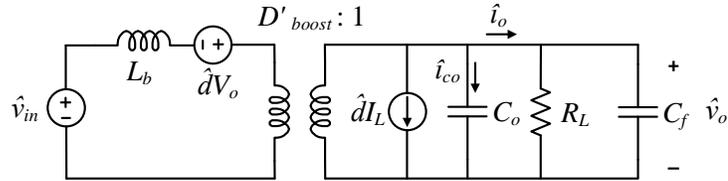

Fig. C.3: Small-signal AC equivalent model of the Boost converter circuit.

The small-signal expression of the output current can be written as:

$$\hat{i}_o = D'_{boost}\hat{i}_{Lb} - \hat{d}_{boost}I_L - \hat{i}_{co}$$

(C.12)

The *control-to-output current* transfer function can be derived from (C.11), (C.12) by setting $\hat{v}_{in} = 0$. It can be expressed as follows:

$$G_{iod}(s) = \frac{\hat{i}_o}{\hat{d}_{boost}}\bigg|_{\hat{v}_{dc}=0} = \frac{D'_{boost}V_0}{R} \frac{(1 - \frac{s}{\frac{D'_{boost}V_o}{I_L L}})(1 + \frac{s}{\frac{1}{C_f R}})}{s^2 L_b(C_o + C_f) + s\frac{L}{R_L} + D'^2_{boost}}$$

(C.13)

CURRICULUM VITAE

Ahmed Nasim Azad

Journal Articles

- Analysis, Optimization, and Demonstration of a Vehicular Detection System Intended for Dynamic Wireless Charging Applications, Ahmed N. Azad, Allon Echols, Vladimir A. Kulyukin, Regan Zane and Zeljko Pantic, *IEEE Transactions on Transportation Electrification*, vol. 5, no. 1, pp. 147-161 , 2019.

- A Smart Autonomous WPT System for Electric Wheelchair Applications with Free-Positioning Charging Feature, Ahmed Azad, Reza Tavakoli, Ujjwal Pratik, Benny Varghese, Calvin Coopmans and Zeljko Pantic, *IEEE Journal of Emerging and Selected Topics in Power Electronics*, Early access, 2018.

- Optimum Design of Decoupled Concentric Coils for Operation in Double-Receiver Wireless Power Transfer Systems, Ujjwal Pratik, Benny J. Varghese, Ahmed Azad and Zeljko Pantic, *IEEE Journal of Emerging and Selected Topics in Power Electronics*, 2019.

Patents

- Vehicle Misalignment Measurement and Compensation in Dynamic Wireless Charging Applications, Zeljko Pantic, Ahmed Azad and Reza Tavakoli, patent filed, September, 2018.

Conference Papers

- Bidirectional Grid-Side Power Management in DWPT Systems for EV Charging Applications, Ahmed Azad, and Zeljko Pantic, in *Proc. IEEE Energy Conversion Congress and Expo (ECCE)*, 2019, accepted.

- A Supercapacitor-Based Converter Topology for Grid-Side Power Management in Dynamic Wireless Charging Systems, Ahmed Azad, and Zeljko Pantic, in *IEEE Transportation Electrification Conference and Expo (ITEC)*, 2019, in press.

- Misalignment Tolerant DWPT Charger for EV Roadways with Integrated Foreign Object Detection and Driver Feedback System, Ahmed Azad, Vladimir Kulyukin, and Zeljko Pantic, in *IEEE Transportation Electrification Conference and Expo (ITEC)*, 2019, in press.

- DAB-based WPT Charger with Integrated Battery Management System for Fast Charging of Mobility Devices, Ahmed Azad, Chakridhar Reddy Teeneti, Regan Zane and Zeljko Pantic, in *IEEE Transportation Electrification Conference and Expo (ITEC)*, 2019, in press.

- Design and optimization of decoupled concentric and coplanar coils for WPT systems, Benny J. Varghese, Trent Smith, Ahmed Azad, and Zeljko Pantic, in *IEEE Wireless Power Transfer Conference (WPTC)*, 2017.

- Design of Hybrid Energy Storage Systems for Wirelessly Charged Electric Vehicles, Ahmed Azad, Tarak Saha, Regan Zane and Zeljko Pantic, in *IEEE Vehicular Technology Conference (VTC2015-Fall)*, 2015.